

การพัฒนาท่อนำคลื่นเออร์มานีเยมรีขวลงแบบสมมาตรเพื่อใช้เป็นอุปกรณ์รับรู้อาร์เคมิ  
สำหรับงานวิเคราะห์ระดับจุลภาค



นางสาวจิตรารักษ์ วงศ์วิวัฒน์

สถาบันวิทยบริการ  
จุฬาลงกรณ์มหาวิทยาลัย

วิทยานิพนธ์นี้เป็นส่วนหนึ่งของการศึกษาตามหลักสูตรปริญญาวิทยาศาสตรดุษฎีบัณฑิต

สาขาวิชาเคมี ภาควิชาเคมี

คณะวิทยาศาสตร์ จุฬาลงกรณ์มหาวิทยาลัย

ปีการศึกษา 2547

ISBN 974-17-6390-5

ลิขสิทธิ์ของจุฬาลงกรณ์มหาวิทยาลัย

DEVELOPMENTS OF SYMMETRICALLY TAPERED  
GERMANIUM WAVEGUIDES AS CHEMICAL SENSORS  
FOR MICROANALYSIS



Miss Jitraporn Vongsvivut

สถาบันวิทยบริการ  
จุฬาลงกรณ์มหาวิทยาลัย

A Dissertation Submitted in Partial Fulfillment of the Requirements  
for the Degree of Doctor of Philosophy in Chemistry

Department of Chemistry

Faculty of Science

Chulalongkorn University

Academic Year 2004

ISBN 974-17-6390-5



จิตรภรณ์ วงศ์วิวัฒน์: การพัฒนาท่อนำคลื่นเยอรมาเนียมเรียวยาวแบบสมมาตรเพื่อใช้เป็นอุปกรณ์รับรู้สารเคมีสำหรับงานวิเคราะห์ระดับจุลภาค (DEVELOPMENTS OF SYMMETRICALLY TAPERED GERMANIUM WAVEGUIDES AS CHEMICAL SENSORS FOR MICROANALYSIS) อาจารย์ที่ปรึกษา: ผศ. ดร. สนอง เอกสิทธิ์, อาจารย์ที่ปรึกษาร่วม: PROFESSOR MARK S. BRAIMAN, 146 หน้า. ISBN 974-17-6390-5.

ได้ทำการประดิษฐ์ท่อนำคลื่นอินฟราเรดแบบระนาบแบนอย่างสมมาตรขึ้นจากชั้นของเยอรมาเนียมผลึกเดี่ยวที่เคลือบด้วยซิงก์ซัลไฟด์ และฝังลงในอีพอกไซด์เรซินซึ่งทำหน้าที่เป็นตัวรองรับ จากนั้นขัดผิวหน้าด้านระนาบออกจนกระทั่งได้ความหนาบริเวณกึ่งกลางที่บางที่สุดในระดับต่ำกว่า 30 ไมโครเมตร ดังที่คาดไว้โดยทฤษฎีกล่าวคือสภาพไวเชิงพื้นผิวมีค่าเพิ่มขึ้นเมื่อความหนาของบริเวณที่บางที่สุดลดลง อันเนื่องมาจากการเพิ่มค่าพลังงานคลื่นอิวานเนสเซนท์ ณ ส่วนที่บางที่สุดของท่อนำคลื่น สภาพไวเชิงพื้นผิวนี้ให้ค่าที่เหนือกว่าผลซึ่งได้รับจากอุปกรณ์เสริมเยอรมาเนียมแอทเทินนูเอตโทเทลรีเฟล็กชันในเชิงพาณิชย์สำหรับสารตัวอย่างหลายประเภท อันได้แก่ ฟิล์มบาง (น้ำหนัก < 10 นาโนกรัม) และตัวทำละลายระเหยง่ายในปริมาณน้อย (< 1 ไมโครลิตร) การเปลี่ยนแปลงเชิงโครงสร้างซึ่งถูกเหนี่ยวนำด้วยแสงในโพรตีนแบคทีเรียโอโรคอปซินที่มีปริมาณเพียงแค่ 50 พิโคโมล (~ 1 ไมโครกรัม) สามารถตรวจวัดได้โดยการใช้ท่อนำคลื่นนี้ อีกทั้งท่อนำคลื่นรับรู้ยังสามารถแสดงให้เห็นถึงองค์ประกอบบนพื้นผิวของเส้นผมมนุษย์เพียงเส้นเดียว อันจะนำไปสู่การใช้เป็นเครื่องมือสำหรับวิเคราะห์เส้นใยในเชิงนิติเวชศาสตร์ นอกเหนือจากนี้ผลจากการคำนวณทางเดินของรังสีในเชิงทัศนศาสตร์ชี้ให้เห็นว่ามุมการแพร่ ณ ตำแหน่งกึ่งกลางที่บางที่สุดแสดงถึงอิทธิพลแบบไม่เป็นเชิงเส้นอย่างชัดเจนต่อมุมและระยะในแนวตั้งของรังสีขาเข้า ปรากฏการณ์นี้มีแนวโน้มให้เกิดการก่อกวนอย่างไม่มีประสิทธิภาพของแสงขาเข้าเพื่อเข้าสู่รูปแบบการเดินทางแบบนอกแกน ซึ่งเป็นรูปแบบที่เป็นประโยชน์มากที่สุดสำหรับอิวานเนสเซนท์เวฟสเปกโทรสโกปี เมื่อเปรียบเทียบกับแหล่งกำเนิดแสงวัตต์ค่าพบว่าความส่องสว่างที่มากกว่าของรังสีซินโครตรอนอินฟราเรดนำไปสู่ค่าการส่งผ่านพลังงานในระดับเดียวกัน แต่ปริมาณแสงในรูปแบบการเดินทางที่เกิดขึ้นได้จะถูกจำกัดให้น้อยลง อย่างไรก็ตามการเร้าที่จำเพาะต่อมุมเช่นนี้เป็นผลให้เกิดลักษณะของคลื่นแทรกสอดที่ชัดเจนในสเปกตรัมการส่งผ่าน ซึ่งจะจำกัดการใช้ประโยชน์ของรังสีซินโครตรอนกับท่อนำคลื่นบางประเภทนี้

ภาควิชา.....เคมี.....ลายมือชื่อนิติต.....  
 สาขาวิชา.....เคมี.....ลายมือชื่ออาจารย์ที่ปรึกษา.....  
 ปีการศึกษา.....2547.....ลายมือชื่ออาจารย์ที่ปรึกษาร่วม.....

# # 4273804623 : MAJOR CHEMISTRY

KEY WORDS: TAPERED GERMANIUM WAVEGUIDES / EVANESCENT WAVE SENSOR / THROUGHPUT / SENSITIVITY / NUJOL / BACTERIORHODOPSIN / HAIR ANALYSIS / SYNCHROTRON IR RADIATION

JITRAPORN VONGSVIVUT: DEVELOPMENTS OF SYMMETRICALLY TAPERED GERMANIUM WAVEGUIDES AS CHEMICAL SENSORS FOR MICROANALYSIS. THESIS ADVISOR: ASST. PROF. SANONG EKGASIT, PH.D., THESIS CO-ADVISOR: PROF. MARK S. BRAIMAN, PH.D. 146 pp. ISBN 974-17-6390-5.

Symmetrically tapered planar infrared (IR) waveguides have been fabricated from a ZnS-coated piece of single-crystalline germanium (Ge), embedded in an epoxide resin as a supporting substrate. The planar surface was subsequently ground to the thickness at the central minimum of  $< 30 \mu\text{m}$ . As predicted by theory, the surface sensitivity increases with decreasing thickness of the tapered region by maximizing the amount of evanescent wave energy present at the thinnest part of the waveguide. The surface sensitivity is superior to that obtained with a commercial Ge attenuated total reflection (ATR) accessory for several types of sample, including thin films ( $< 10 \text{ ng}$ ) and small volumes ( $< 1 \mu\text{L}$ ) of volatile solvents. By using the waveguides, light-induced structural changes in the protein bacteriorhodopsin (bR) were observable using samples as small as  $\sim 50 \text{ pmol}$  ( $\sim 1 \mu\text{g}$ ). Such waveguide sensors can also reveal the surface compositions on a single human hair, pointing to its promise as a tool for forensic fiber analysis. In addition, ray-optic calculations indicate that the propagation angle at the central minimum has a strong non-linear dependence on both angle and vertical position of the input ray. This results in rather inefficient coupling of input light into the off-axis modes that are most useful for evanescent-wave spectroscopy. As compared to a blackbody source, the much greater brightness of synchrotron IR radiation allows a similar total throughput, but restricted to a smaller fraction of the allowed waveguide modes. However, such angle-selective excitation results in a strong oscillatory interference pattern in the transmission spectra, which limits the use of synchrotron radiation with the thin waveguides.

Department.....Chemistry.....Student's signature.....  
 Field of study.....Chemistry.....Advisor's signature.....  
 Academic year.....2004.....Co-advisor's signature.....

## ACKNOWLEDGEMENTS

The financial support from the Thailand Research Fund (TRF) through the Royal Golden Jubilee (RGJ) Ph.D. Program (Grant No. PHD/0004/2543) to Jitraporn Vongsvivut and Dr. Sanong Ekgasit is gratefully acknowledged.

I would like to express my sincere gratitude to Associate Professor Dr. Sirirat Kokpol, Associate Professor Dr. Supot Hannongbua, Associate Professor Dr. Mana Sriyuthasak, Assistant Professor Dr. Thawachai Tantulani, and Assistant Professor Dr. Toemsak Srikehrin, for the insightful suggestions and contribution as thesis committee.

Gratefully thanks to my thesis co-advisor, Professor Mark S. Braiman, for the invaluable guidance and his strong efforts in training and providing me such a warm hospitality during my stay in the USA. I am also thankful to John W. Chabot (Syracuse University) and William F. Kutz (K & S Optics) for their substantial assistance in the fabrication process. The technical and instrumental supports from Dr. Nebojsa Marinkovic at U2B beamline (NSLS at BNL) are truly appreciated.

Exceptional acknowledgement to Professor Yukihiro Ozaki for the great opportunity of doing research in Japan. His patience and professionalism dedicated to our collaborative project are gratefully impressive.

In essence, the research would never be successfully completed without the excellent advice and pioneering spirit from my thesis advisor, Assistant Professor Dr. Sanong Ekgasit, whose trust and scientific excitement inspire me in the most important moments of making right decisions. I have greatly enjoyed the innovative and challenging atmosphere in his laboratory. His translation of cares into action, guidance, and understanding are deeply thankful.

Warmest thanks to my friends and colleagues at the Sensor Research Unit (Thailand) and at Syracuse University (USA), as well as at Ozaki's Group (Japan) for the everlasting friendship and spiritual supports throughout the time of study.

Above all, I am profoundly grateful to my wonderful parents and the endearing family for their patient love, perpetual encouragement, and overwhelming support.

## CONTENTS

	Pages
ABSTRACT IN THAI.....	iv
ABSTRACT IN ENGLISH.....	v
ACKNOWLEDGEMENTS.....	vi
LIST OF FIGURES.....	xi
LIST OF TABLES.....	xviii
LIST OF ABBREVIATIONS.....	xix
LIST OF SYMBOLS.....	xx
CHAPTER I INTRODUCTION.....	1
1.1 Mid-IR Optical Sensors: Promising Tools for Microanalysis.....	1
1.2 Evanescent-Wave Spectroscopy: A Basic Sensing Principle.....	2
1.3 Basic Considerations on Mid-IR Sensing Systems.....	4
1.3.1 Materials for Mid-IR Optics.....	4
1.3.2 Design for the Optical Configuration.....	5
1.3.2.1 Intensity of IR Light Sources.....	6
1.3.2.2 Selection of Mid-IR Detectors.....	7
1.3.2.3 Dimension of the Waveguide.....	8
1.4 Historical Developments of Thin Tapered Ge Waveguides.....	9
1.5 Scope of the Research.....	11
1.6 Objectives of the Research.....	12
CHAPTER II THEORETICAL BACKGROUND.....	13
2.1 Fundamentals of Light Propagation.....	13
2.1.1 Snell's Law: A Principle of Light Reflection and Refraction.....	14
2.1.2 The Evanescent Field at Total Internal Reflection.....	15

	Pages
2.2 An Introduction to Slab Waveguides.....	17
2.2.1 Ray Optics and Guided Modes in Slab Waveguides.....	19
2.2.2 Geometrical Optics Treatment of Slab Waveguide.....	20
2.3 Realistic Calculation for Design of the Supported Planar Ge Waveguide.....	23
2.3.1 Calculation of Cut-off Thickness of Ge Waveguide.....	24
2.3.2 Investigation of the Transmitted Throughput.....	25
2.3.3 Feasibility Calculation A: Size of Relative Absorption Changes.....	26
2.3.4 Feasibility Calculation B: Detection of Signals.....	30
2.4 A Brief Description of Synchrotron Radiation.....	30
2.4.1 Origin of the Synchrotron.....	30
2.4.2 Synchrotron Facility at National Synchrotron Light Source.....	31
2.4.3 Synchrotron Characteristics.....	33
 CHAPTER III EXPERIMENTAL SECTION.....	 35
3.1 Fabrication of the Tapered Quasi-Planar Waveguides and Its Optics.....	35
3.1.1 Materials and Equipment.....	35
3.1.2 Instruments.....	36
3.1.3 Fabrication Procedure.....	36
3.1.4 Thickness Determination Based on Interference Fringes.....	38
3.1.5 Optical Alignment of the Tapered Waveguide.....	41
3.2 Potential Applications of the Tapered Quasi-Planar Ge Waveguides.....	41
3.2.1 Samples of Interest.....	41
3.2.2 Instruments for Data Acquisition.....	42
3.2.3 Default Instrumental Parameters.....	42
3.2.4 Experimental Procedure.....	43
3.2.4.1 Preparation of D96N-bR Films for Light-Dark Experiments.....	44



	Pages
3.3 Characterization of the Waveguides with Synchrotron IR Radiation.....	45
3.3.1 Sample of Interest.....	45
3.3.2 Instruments for Data Acquisition.....	45
3.3.3 Default Instrumental Parameters.....	45
3.3.4 Experimental Procedure.....	46
3.4 Ray-Tracing Calculations.....	47
3.4.1 Software and Requirements.....	47
3.4.2 Strategic Approach.....	47
 CHAPTER IV RESULTS AND DISCUSSION.....	 49
 4.1 Symmetrically Tapered <30- $\mu$ m-thick Quasi-Planar Ge Waveguides and Their Coupling Efficiency.....	 49
4.1.1 Dependence of Total Throughput on Coupling Efficiency.....	51
4.1.2 Variation of Waveguide Thickness.....	53
4.1.3 Variations in Optical Coupling with Sample.....	56
4.1.3.1 Sampling Length of the Sample.....	56
4.1.3.2 Quality of the Polished Sensing Surface.....	58
4.1.3.3 Effects of Central Beam Blocking.....	59
4.1.3.4 Effects of Detector Dimensions.....	61
4.2 Applications and Comparisons with a Commercial Ge ATR Accessory.....	63
4.2.1 Small Volumes of Volatile Solvents.....	63
4.2.2 Small Quantities of Non-Volatile Thin Films.....	66
4.2.3 Light-Dark Difference Spectra of Biological Film Samples.....	67
4.2.4 Hair Analysis.....	70
4.3 Ray-Tracing Calculations of Supported Ge Waveguides.....	72
4.3.1 Ray Tracing of Cylinder-Planar Waveguides.....	72
4.3.1.1 Contour Features of Cylinder-Planar Waveguide at High Resolution.....	 83

	Pages
4.3.2 Ray Tracing for Waveguides with a More Complicated (Gaussian) Curved Surface.....	86
4.4 Characterization of Supported Cylinder-Planar Ge Waveguides with Synchrotron IR Radiation.....	93
4.4.1 Throughput Measurements with Synchrotron IR Radiation.....	93
4.4.2 Angle Dependence of Throughput and Absorbance Signals with Synchrotron IR Radiation.....	96
4.4.3 Oscillatory Signal on Absorbance Spectra Measured with Synchrotron IR Radiation.....	99
CHAPTER V CONCLUSIONS.....	103
5.1 Symmetrically Tapered <30- $\mu$ m-thick Quasi-Planar Ge Waveguides as Chemical Sensors for Microanalysis.....	103
5.2 Characterization of Supported Cylinder-Planar Ge Waveguides with Synchrotron IR Radiation.....	104
5.3 Ray-Tracing Calculations of Supported Ge Waveguides.....	105
REFERENCES.....	106
APPENDICES.....	112
Appendix A Publication I.....	113
Appendix B Publication II.....	124
Appendix C Ray-Tracing Program.....	134
CURRICULUM VITAE.....	145

## LIST OF FIGURES

	Pages
1.1 Simple illustration of TIR condition present inside a planar waveguide used as an IRE. The respective symbols $n_1$ , $n_2$ refer to refractive indices of the corresponding waveguide and sample; $\theta$ is angle of incidence; $l$ , $t$ are length and thickness of the waveguide, respectively.....	3
1.2 (A) Design of the supported planar Ge waveguide used for evanescent-wave sensing. The relative thickness of the different layers is not to scale. (B) Optical diagram of the microscope and waveguide, showing ~12-mm separation of focal points of the objective and condensing optical elements.....	9
1.3 Schematic diagram of a modified planar Ge waveguide and its coupling to an MCT detector located at right. Focused input light shown at left is typically from an FT-IR spectrometer.....	10
1.4 Proposed dimension of a novel MIR evanescent-wave sensor. Left shows the side projection of the symmetrically tapered <30- $\mu$ m-thick waveguide supported by an epoxide substrate, with its end view depicted at right.....	11
2.1 Propagation of a linearly polarized electromagnetic wave in the direction of propagation.....	13
2.2 Reflection and refraction of a plane wave at a dielectric interface based on Snell's Law.....	14
2.3 Schematic illustration of an evanescent-wave sensor under the TIR condition ( $n_1$ , $n_2$ , refractive indices of the respective waveguide and sample; $\alpha$ , angle of incidence; $E$ , exponentially decaying evanescent field; $d_p$ , penetration depth)...	16
2.4 A typical dielectric slab waveguide. Guidance occurs through TIR condition when the entering angle of the light is within a range of the acceptance cone angle ( $\theta_m$ ).....	17
2.5 Zig-zag ray-optical trajectory of "modes" propagating along a dielectric slab waveguide.....	20

2.6	Illustration of the phase condition that leads to the eigenvalue equation. All rays that travel in the same direction belong to the same plane wave.....	22
2.7	A plot of power attenuation ( $\log(\Delta P/P_0N)$ ) by amide (I) absorption as a function of the waveguide thickness $t$ (in $\mu\text{m}$ ).....	28
2.8	Schematic of synchrotron radiation produced by a relativistic particle. (A) An electron is accelerated in a magnetic field with a circular motion. (B) Electric field as a function of time $t$ at the observer. (C) Fourier transform of (B) which yields a broadband spectrum.....	31
2.9	Diagram of the synchrotron at NSLS/BNL showing the (A) electron source, (B) linear accelerator, and (C) booster ring, as well as the VUV storage ring and beamlines.....	32
3.1	Experimental outline of the fabrication procedure of the symmetrically tapered $<30\text{-}\mu\text{m}$ -thick quasi-planar Ge waveguides.....	37
3.2	Reflections at the front and the back of a thin Ge film resulting in the oscillatory interference fringes.....	39
3.3	FT-IR single-beam spectrum obtained from IR microscopy, by impinging the incident IR beam transverse the thinnest central part of the waveguide's sensing surface. <b>Inset:</b> Expanded range of the periodic oscillatory interference pattern.....	39
3.4	Symmetrical spikes in a FT-IR interferogram used for determination of the waveguide thickness.....	40
3.5	Optical layout of a symmetrically tapered $<30\text{-}\mu\text{m}$ -thick Ge waveguide with respect to IR source and detector. Incident light, indicated at left, is typically generated from a standard Globar <sup>TM</sup> source of an FT-IR spectrometer, and the output is coupled onto a liquid-N <sub>2</sub> -cooled MCT immersion detector placed as close as possible to the exit end of the waveguide. The detector window, outside the lens, is not shown.....	41

4.1	FT-IR single-beam spectra observed during an alignment procedure of a symmetrically tapered 14- $\mu\text{m}$ -thick Ge waveguide. All spectra were collected with 1-minute scans. The $y$ -axis scale stands for arbitrary intensity units, which are the same for all plots shown here.....	52
4.2	FT-IR single-beam spectra of symmetrically tapered Ge waveguides with different thicknesses (i.e., 7, 14, 22, and 27 $\mu\text{m}$ from lower to upper lines, respectively). All spectra were collected with 1-minute scans and under identical conditions. The $y$ -axis scale stands for arbitrary intensity units, which are the same for all plots shown here. <b>Inset:</b> Plot of the detected intensity at 1850 $\text{cm}^{-1}$ as a function of the waveguide thickness.....	54
4.3	ATR FT-IR Spectra of 1- $\mu\text{L}$ water droplet, covering an $\sim 1 \text{ mm}^2$ sensing area, acquired by using symmetrically tapered Ge waveguides with different thicknesses (i.e., 7, 14, 22, and 27 $\mu\text{m}$ from upper to lower lines, respectively). <b>Inset:</b> Plot between the logarithm of the absorption intensity at 3400 $\text{cm}^{-1}$ ( $\log(A_{3400})$ ), due to the O-H stretching vibration, vs. the logarithm of waveguide thickness ( $\log(t)$ ).....	55
4.4	ATR FT-IR Spectra of water droplets with different lengths contacting the sensing surface of the waveguide. (A) Spectra were obtained by using a 7- $\mu\text{m}$ -thick Ge waveguide, with sampling lengths of 1, 4, 7, 9, and 12 mm from lower to upper lines, respectively; (B) spectra acquired with 27- $\mu\text{m}$ -thick waveguide with sampling lengths of 1, 3, 5, 7, 10, 12, 15, 18, and 20 mm from lower to upper lines, respectively. All spectra were taken with 1-minute scans. <b>Insets:</b> Plot of the absorption intensity at 3400 $\text{cm}^{-1}$ ( $A_{3400}$ ), vs. the sampling length (mm) with a constant width of the waveguide (i.e., 1 mm), for different waveguide thicknesses.....	57
4.5	Effect of the surface quality on absorbance spectral features observed from a 1-cm-diameter water droplet sample. These spectra were collected by using a 100- $\mu\text{m}$ -thick tapered Ge waveguide with 45 $^\circ$ bevel angle at both ends with 1-minute scans.....	58

4.6	Effect of central beam blocking on absorption intensity of 1-mm-diameter (= 1 $\mu$ L) water droplet investigated by (A) 14- and (B) 22- $\mu$ m-thick Ge waveguides with 5-minute scans. Thick lines represent results with the blocked beam in comparison to those with unblocked one (thin lines).....	60
4.7	Effect of size of the detector element on spectral SNR measured from a 1-mm-diameter (= 1 $\mu$ L) water droplet. Both spectra were collected by using 5-minute scans with a 14- $\mu$ m-thick Ge waveguide, but with different lensed detectors carrying MCT active elements either 0.50 or 0.15 mm on a side, as indicated.....	62
4.8	Comparison of absorption intensities of 1-mm-diameter (= 1 $\mu$ L) water droplet observed by 14- $\mu$ m-thick tapered Ge waveguide to that with a commercial macroscopic ATR accessory. Both spectra represent 5-minute scan times.....	63
4.9	ATR FT-IR spectra of some volatile solvents in a few $\mu$ L of applied volume. Data were acquired by a 14- $\mu$ m-thick tapered Ge waveguide with 64 scans.....	65
4.10	ATR FT-IR spectra of Nujol thin films with different quantities deposited on the sensing surface, i.e., (A) 850 ng and (B) 85 ng. The thick lines represent the results observed by a 14- $\mu$ m-thick tapered Ge waveguide, while the thin one was collected with the commercial ATR accessory. All spectra were taken after hexane was completely evaporated, and with 5-minute scan times...	66
4.11	(A) ATR FT-IR spectrum of D96N-bR film with a total amount of 1.25 pmol (37.5 ng) of protein. The spectrum was acquired with a 14- $\mu$ m-thick tapered Ge waveguide with 5-minute scan times. (B,C) ATR FT-IR difference spectra of D96N-bR using light-dark subtraction at room temperature (25°C): (B) 128 averaged data sets, total measurement time ~4 h, using 14- $\mu$ m-thick tapered Ge waveguide and 50 pmol protein; (C) 64 averaged data sets, total measurement time ~2 h, using the commercial ATR accessory and 15 nmol protein.....	69

4.12	Baseline-corrected ATR FT-IR spectra of single hairs (upper thin line) taken from two different people: (A) an African-West Indian female, and (B) a Caucasian male. The lower (thick line) spectrum in each sub-figure represents the styling gel applied earlier in the day by each person (i.e., Magnificent <sup>®</sup> Hair Food manufactured by Magnificent Products Division, Memphis, TN, for donor A; and Aussie Mega Styling Gel <sup>®</sup> manufactured by Redmond Products, Inc. Dist., Stamford, CT, for donor B). Films were dried ~1 h prior to spectral measurement. All spectra were acquired with a 14- $\mu$ m-thick tapered Ge waveguide with 5-minute scans.....	71
4.13	Typical calculated reflection pattern of a light ray propagating through a symmetrically tapered cylinder-planar waveguide with a total length $L$ of 70 mm, a circular radius $R$ of 300 mm for the cylinder surface, and a minimum thickness $t$ of 10 $\mu$ m. Note that the exaggerated vertical scale in both the main figure and the inset results in distorted apparent reflection angles.....	73
4.14	Plot of the calculated number of total internal reflections vs. vertical distance ( $y$ ) of the impinging ray from the upper planar surface of a 70-mm-long, symmetrically-tapered, cylinder-planar waveguide with a minimum thickness of 10 $\mu$ m. The light rays are assumed to enter the waveguide on-axis ( $\theta = 0^\circ$ ).....	75
4.15	Summary of results of 10,251 ray-trace calculations on each of three different cylinder-planar waveguide sensors, all having a circular radius $R$ of 300 mm but different minimum thicknesses $t$ (i.e., 14, 27, and 50 $\mu$ m) as indicated.....	76
4.16	Sensing-angle plots for rays impinging on the entrance faces of 14- $\mu$ m-thick cylinder-planar waveguides with different values of circular radius $R$ (i.e., 300, 600, 1200, 2400, and 4800 mm) as indicated. As in Figure 4.15, $z$ -axis contours are always calculated at $5^\circ$ intervals. The color bar shown at right is applicable to all plots.....	80

4.17	(Upper) Plot of calculated total étendue (■) and high-sensing-angle étendue (●) of a 14- $\mu\text{m}$ -thick cylinder-planar waveguide vs. curvature radius $R$ of the bottom cylinder surface. (Lower) Ratio of the high-sensing-angle étendue to the total étendue as a function of the curvature radius $R$ , based on plots in the upper part of the figure.....	82
4.18	Ray-trace calculations at the higher resolution of incoming angle $\theta$ on each of cylinder-planar waveguides, having a circular radius $R$ of 300 mm, with different minimum thicknesses $t$ (i.e., 14, 27, and 50 $\mu\text{m}$ ) as indicated.....	84
4.19	Sensing-angle plots at the higher resolution of incoming angle $\theta$ for rays impinging on the entrance faces of 14- $\mu\text{m}$ -thick cylinder-planar waveguides with different values of circular radius $R$ (i.e., 300, 600, 1200, 2400, and 4800 mm) as indicated.....	85
4.20	Changes in Gaussian curvatures of the bottom surface observed for 14- $\mu\text{m}$ -thick waveguides with increasing $w$ values (i.e., 16, 64, 256, and 1024 mm) from lower to upper lines, respectively, at a fixed $e$ of 2 mm. The circular arc of $R = 300$ mm with the same center thickness $t = 14$ $\mu\text{m}$ is shown as a reference curve on the top. The ray traces were simulated using the distance away from the flat sensing surface ( $y$ ) of 0.2 mm and an impinging $\theta = 0^\circ$ .....	88
4.21	Contour plots of Gaussian-planar waveguides with identical variables as those in Figure 4.20, in comparison to that of cylinder-planar waveguide with $R = 300$ mm shown on the top. The $z$ -axis contours are calculated at $5^\circ$ intervals as represented by the color bar at right.....	90
4.22	Sensing-angle plots of rays impinging on each of three different Gaussian-planar waveguides, having the same length (70 mm) but different central thicknesses (i.e., 14, 27, and 50 $\mu\text{m}$ ) as indicated. Contours in each column reflect Gaussian-planar waveguides with (left) 2-mm-high and (right) 1-mm-high entrance ends, which correspond to the respective ray-trace pattern shown on the top. The $5^\circ$ -interval color bar at right is applicable to all plots...	92



- 4.23 FT-IR single-beam spectra of (A) a 14- $\mu\text{m}$ -thick and (B) a 27- $\mu\text{m}$ -thick Ge waveguides observed with synchrotron IR radiation, compared to those observed with a standard blackbody (Globar<sup>TM</sup>) source. With each waveguide thickness, two different on-axis setups were examined: (i) using the external output port; and (ii) using the internal sample compartment..... 95
- 4.24 Correlation of changes in % total energy throughput and absorption intensity of a 1-mm-diameter water droplet observed at different external incident angles by using the synchrotron IR radiation with a 27- $\mu\text{m}$ -thick Ge waveguide. The +/- signs indicated on the x-axis represent the direction from where the input light was focused, i.e., below (-) and above (+) the waveguide plane, as presented in black and white columns, respectively. The throughput value observed at each input angle was ratioed to the reference value of the total transmission detected with no input angle (0°) when the light was directed on-axis shown in the last (shaded) column. Numbers indicated over the columns are the actual absorption intensities..... 97
- 4.25 Comparison of evanescent-wave absorbance spectra measured with a 14- $\mu\text{m}$ -thick Ge waveguide, by using either synchrotron IR radiation (bold lines) or a standard blackbody (Globar<sup>TM</sup>) source (thin lines). Samples were water droplets covering either (A) 1 mm or (B) 10 mm of the central part of the waveguide's sensing surface..... 99

**LIST OF TABLES**

Pages

3.1 Physical and optical properties of crystalline Ge..... 35



สถาบันวิทยบริการ  
จุฬาลงกรณ์มหาวิทยาลัย

**LIST OF ABBREVIATIONS**

Al <sub>2</sub> O <sub>3</sub>	: aluminum oxide
ATR	: attenuated total reflection
BNL	: Brookhaven National Laboratory
bR	: bacteriorhodopsin
D96N-bR	: D96N mutant of bacteriorhodopsin
DTGS	: deuterated triglycine sulfate
CVD	: chemical vapor deposition
EWS	: evanescent-wave spectroscopy
FT-IR	: Fourier transform infrared
Ge	: germanium
IR	: infrared
IRE	: internal reflection element
KRS-5	: thallos bromide iodide
MCT	: mercury cadmium telluride
MIR	: mid infrared
μm	: micron
NA	: numerical aperture
ng	: nanogram
NIR	: near infrared
NSLS	: National Synchrotron Light Source
ORV	: optical retardation velocity
SiC	: silicon carbide
SNR	: signal-to-noise ratio
TE	: transverse electric
TIR	: total internal reflection
TM	: transverse magnetic
TRIS	: tris(hydroxymethyl)aminomethane
ZnS	: zinc sulfide
ZnSe	: zinc selenide

## LIST OF SYMBOLS

$A$	: absorbance
$A_D$	: detector area
$d_p$	: penetration depth
$D^*$	: specific detectivity
$f$	: focal length
$L$	: length of the waveguide
$n$	: refractive index
$N$	: number of internal reflections
$R$	: curvature radius
$R^2$	: correlation coefficient
$t$	: minimum (central) thickness of the waveguide
$T$	: temperature
$U$	: spectral energy density
$x$	: distance measured horizontally from the entrance end of the waveguide
$y$	: vertical distance measured downward from the flat sensing surface
$\theta$	: angle of incidence (in air)
$\theta'$	: initial angle inside the waveguide
$\theta_c$	: critical angle
$\varphi$	: maximum sensing angle
$\Theta$	: throughput
$\xi$	: throughput efficiency
$\bar{\nu}$	: wavenumber
$\Delta\bar{\nu}$	: spectral resolution

# CHAPTER I

## INTRODUCTION

Methods for the structural characterization of samples in small quantities have gained significant interest over the past years. Fourier transform infrared (FT-IR) spectroscopy is one of the most often used spectroscopic tools to resolve structural compositions, due to highly molecular specific fingerprints present in vibrational spectra. The instrumental evolution of the FT-IR technique, accompanied by the developments of both new accessories and auxiliary optics, is continually being advanced in order to allow one to access a wide range of different samples [1]. However, the relatively high limits of detection in most general systems obtained by the traditional infrared (IR) technique have been insufficient for characterizing a tiny amount of sample (i.e.,  $\leq$  ng level). As a consequence, methods for increasing the sensitivity are of substantial interest.

### 1.1 Mid-IR Optical Sensors: Promising Tools for Microanalysis

Chemical sensor technology is one of the fastest growing research fields and can be identified as a key technological area in modern analytical chemistry. Attempts to develop compact chemical sensors based on optical fibers and other types of miniature waveguides have been driven by increasing demands to handle very small-sized samples in microanalysis and trace analysis. In modern technology, the greatest progress in the development of waveguide sensors based on vibrational spectroscopy has been focused in the near infrared (NIR), due to greater manufacturing experience with silica and other optical glasses that transmit in the visible and NIR regions [2–4]. Because of the minimal loss of light during transmission and their superb flexibility, these silica-based glasses have contributed to success of NIR and Raman spectroscopies, particularly in the fields of process analytical chemistry and remote sensing applications. As compared to the overtones and combination bands in the NIR spectral range, the significantly stronger and more readily interpreted fundamental absorption bands in the mid-infrared (MIR) region

turn out to provide a substantial advantage for chemical sensing analysis. In general, the fundamental vibrational bands in MIR range are 10–1000 times stronger than those in NIR spectra. With this in consideration, various kinds of MIR optical sensors have been demonstrated to be a potentially powerful chemical sensing tool with applications ranging from environmental monitoring to process analysis and clinical diagnostics, as seen in many publications over the past few years [5–18]. Nevertheless, further improvements in the design and optical configuration of alternative MIR waveguide sensors are still desirable in order to meet current needs in trace analyses.

## 1.2 Evanescent-Wave Spectroscopy: A Basic Sensing Principle

Whether a cylindrical optical fiber or a planar waveguide in various shapes is utilized as a chemical sensor, the technique can generally be referred to as either attenuated total reflection (ATR) or evanescent-wave spectroscopy (EWS) [19]. The phenomenon of total internal reflection (TIR) was first experimentally and theoretically explored by Harrick in 1960 [20]. Since then, the theory has been continually developed, and practical usage of ATR accessories in various configurations has grown enormously. To date, the technique has successfully become a widespread method in MIR spectroscopy, for both qualitative and quantitative measurements.

With this technique, the waveguide can be regarded as an internal reflection element (IRE) wherein the incident light experiences TIR conditions at the interface of two media with different refractive indices. In theory, TIR occurs when light traveling in an optically denser waveguide approaches into a rarer medium (i.e.,  $n_1 > n_2$ ) with an incident angle larger than the critical angle of which equals to  $\theta_c = \sin^{-1}\left(\frac{n_2}{n_1}\right)$ , as depicted in Figure 1.1.

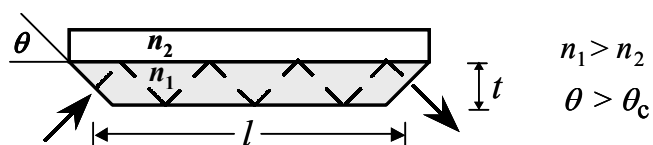


**Figure 1.1** Simple illustration of TIR condition present inside a planar waveguide used as an IRE. The respective symbols  $n_1$ ,  $n_2$  refer to refractive indices of the corresponding waveguide and sample;  $\theta$  is angle of incidence;  $l$ ,  $t$  are length and thickness of the waveguide, respectively.

At each reflection, the evanescent wave penetrates a fraction of the wavelength beyond the high-index waveguide into the lower-index sample layer. It decays exponentially within a shallow region, defined as the penetration depth ( $d_p$ ). For MIR light, the penetration depth is generally in the range of 0.5–5  $\mu\text{m}$  depending on both experimental conditions (e.g., angle of incidence) and material characteristics (i.e., refractive indices of waveguide and sample) [21]. As the name ‘ATR’ implies, the measured absorption spectrum under this certain condition is the result of attenuation of the evanescent wave accompanying an incident IR beam traveling through the high-index waveguide. In consequence, only a thin layer of the sample is probed. The mechanism of evanescent-wave sensors therefore relies on the electromagnetic component of the reflected light at the sensing surface of a waveguide to excite only the signal events localized at that surface. The nature of the surface evanescent field makes the ATR technique (or EWS) a powerful surface-sensitive chemical sensor.

Based on simple geometrical considerations, the number of total internal reflections inside a planar waveguide can be estimated by the following expression.

$$N = \frac{l}{t} \cot \theta \quad (1.1)$$

where  $N$  is the calculated number of internal reflections observed for a planar waveguide having the length  $l$  and thickness  $t$ . The angle of incidence,  $\theta$ , corresponds to that shown in Fig. 1.1.

Equation 1.1 implies that decreasing the waveguide thickness increases the total number of reflections at the sensing surfaces. This results in an increase in the effective path length of the evanescent, and the sensitivity observed by the waveguide is consequently enhanced. Therefore, miniaturization of the waveguide permits smaller amounts of samples to be detected. This advantage arises from the fact that, although the sampling area is smaller, the light experiences a larger number of reflections per unit length of the waveguide. It would be desirable to observe how far this advantage could be extended (i.e., how thin a waveguide could be made) and how strong the absorbance can be enhanced.

### **1.3 Basic Considerations on Mid-IR Sensing Systems**

#### **1.3.1 Materials for Mid-IR Optics**

Development of MIR waveguides imposes strong requirements on the high-quality light-guiding materials. In principle, the desired optical and physical characteristics of MIR waveguides include transparency over the IR spectral region of 400–4000  $\text{cm}^{-1}$  (i.e., 2.5–25  $\mu\text{m}$ ), mechanical strength, chemical and thermal stabilities, as well as flexibility. Despite the large number of IR-transparent substances, there is yet no commercial material that answers all these demands, and its fabrication is in practice extremely difficult. Therefore, a study of the potential of existing materials prior to the manipulation process is strongly recommended in order to achieve certain specifications of waveguide design.

In fact, MIR optical sensors have been reportedly fabricated from several IR-transparent materials with high refractive index and low attenuation values, such as germanium (Ge), zinc selenide (ZnSe), thallos bromide iodide (KRS-5), and chalcogenide [22–33]. Fragility and comparatively low hardness and thermal stability are in practice the most essential drawbacks of these vitreous materials, and thereby cause significant difficulties in fabrication process. The properties of hardness and brittleness thus play a significant role in the preparation procedure of these materials, and in the resistance to surface damage through usage and breakage



due to misuse. Accordingly, the strategy for waveguide fabrication turns to be the most important aspect for implementing these vitreous materials.

Regarding this research study, single-crystalline Ge, with a relatively high refractive index ( $n_{\text{Ge}} = 4.0$ ), has been the material of interest. As mentioned above, the relevant difficulties in fabricating Ge as a thin waveguide are its brittleness and the lack of sufficient mechanical strength, which together seem to preclude fabrication of a freestanding Ge waveguide <1 mm in thickness. However, its excellent property of chemical inertness, particularly with biochemical molecules in picomolar quantities, is an impetus for choosing this substance. For development studies, an additional advantage of this material is the presence of characteristic high- and low-frequency Ge cut-offs at 5200 and 670  $\text{cm}^{-1}$ , respectively. These cut-off frequencies provide useful evidence for the propagation of broadband IR light genuinely through the waveguide.

### 1.3.2 Design for the Optical Configuration

The performance of an optical system can be indicated in terms of signal-to-noise ratio (SNR) of an acquired spectrum. The SNR is typically defined as the signal level of a blank “100% line” divided by the noise level. In most circumstances, users are rather interested in SNR performance when the absorbance of analyte is compared to the noise level of the system. In theory, the SNR of a spectrum measured using a commercially available FT-IR spectrometer can be evaluated based on a formula given by Griffiths and de Haseth [1]:

$$\text{SNR} = \frac{U_{\bar{\nu}}(T) \cdot \Theta \cdot \Delta \bar{\nu} \cdot t^{1/2} \cdot \xi \cdot D^*}{(A_{\text{D}})^{1/2}} \quad (1.2)$$

where  $U_{\bar{\nu}}(T)$  represents the spectral energy density at wavenumber  $\bar{\nu}$  from a blackbody source at a temperature  $T$ . This energy is received at a detector through an interferometer in a measurement time  $t$  (in seconds) having a throughput  $\Theta$ , a resolution  $\Delta \bar{\nu}$ , and an efficiency  $\xi$ , in unit wavenumber interval. The variables  $D^*$  and  $A_{\text{D}}$  are the specific detectivity and the detector area, respectively.

In accordance, one strategy to gain an optimum SNR for a sensing system is to maximize the amount of optical throughput detected. This strongly requires advances in design of optical configuration for a particular coupling method. In principle, the optical configuration of a MIR sensing system depends on two fundamental factors—overall optical throughput and the magnitude of the chemical signature (i.e., absorbance signal achieved by a particular waveguide sensor). From a practical point of view, these parameters can be categorized into several schemes including the specifications of the light source and detector, as well as the dimensions of the waveguide.

### 1.3.2.1 Intensity of IR Light Sources

An optical scheme for the waveguide's setup requires a source of intense multi-wavelength IR radiation to provide adequate intensity incident into the waveguide. For this particular application, an ideal source of IR radiation should have a high intensity distributed over a small area and a narrow range of input angles. In general, the most commonly used source in modern FT-IR spectrometers is a standard blackbody IR source made of a silicon carbide rod (i.e., frequently known by the trade name Global<sup>TM</sup>). The radiated power produced by a Global<sup>TM</sup> source is constant with time. This component thus causes a small effect on the relative performance between the two instruments, and thereby limits the throughput improvement that can be made by sources.

However, a distinct improvement is available because of the intrinsic high brightness of the synchrotron IR radiation (i.e., 10–1000 times greater than the Global<sup>TM</sup>). Because the synchrotron-generated IR light is by nature emitted into a narrow range of angles due to its small effective source size, sample areas as small as a few  $\mu\text{m}^2$  can be potentially probed. Using synchrotron radiation, the entire input beam is expected to pass through the small input end of thin waveguides ( $\sim 1 \text{ mm}^2$ ), resulting in a substantial increase in total throughput detected. With this in consideration, a combination of the synchrotron IR

radiation and thin waveguides becomes a prospect for improving waveguide's performance.

### 1.3.2.2 Selection of Mid-IR Detectors

One of the most important elements of an IR spectrometer is the component responsible for detecting IR energy. The responsive element inside an IR detector works by changing the incoming radiation into an electrical signal. The sensitivity of IR detectors is fundamentally expressed in terms of the specific detectivity ( $D^*$ ), which is often used as the first criterion in a comparison of the performance of different IR detector types. Briefly,  $D^*$  is equivalent to the SNR of a detector of unit area in a unit bandwidth when a 1 W radiant power is incident onto the detector element. The basic type of detectors equipped in most commercial FT-IR spectrometers is a deuterated triglycine sulfate (DTGS) pyroelectric detector that responds directly to temperature changes due to exposure to the incoming radiation. Nonetheless, a more sensitive detector is often required, particularly for the low-throughput conditions that apply with thin waveguides. A mercury cadmium telluride (MCT) photoconductive detector measuring the mobility of free-charged carriers therefore becomes a good detector choice. Basically, photoconductive detectors have two significant advantages over pyroelectric (thermal) detector. Firstly, they respond over a narrower part of the spectrum, resulting in lower thermal background noise and thereby a higher  $D^*$ . Secondly, the photoconductive detectors have much faster response times (i.e., typically 1  $\mu$ s) as compared to a pyroelectric detector, which is restricted to slower than 1 ms [34].

Due to the fact that IR photons produced by a typical Globar<sup>TM</sup> source are low in energy and only a small amount of light can pass through a thin waveguide, a liquid-nitrogen-cooled MCT detector must be utilized for acquiring the maximum possible  $D^*$ . For an even further improvement of the waveguide performance, use of a MCT detector with a smaller detector element in theory would give rise to a better spectral SNR.

### 1.3.2.3 Dimension of the Waveguide

Among a various shapes of IREs commercially available, the horizontally mounted ATR accessory is in wide use due to its ease in sampling procedure for both liquids and solids. MIR prisms having trapezoidal or parallelogram cross-sections, and dimensions on the order of  $50 \text{ mm} \times 20 \text{ mm} \times 2 \text{ mm}$ , are thus chosen for most ATR measurements. These macroscopic waveguides typically have throughputs matched to commercial FT-IR spectrometers. On the other hand, miniature waveguides and IR fiber optics have much lower throughputs than those of macroscopic prisms. The throughput restriction somewhat complicates the application of thin waveguides with commercial FT-IR spectrometers. Nevertheless, when properly coupled to a small-area (low-noise) MCT detector, these thin waveguides apparently display the advantage of permitting minute amounts of sample to be sensed. This advantage arises from the fact that, although the surface-sensing area is smaller, the light experiences a larger number of internal reflections per unit length of waveguide, and this yields a concomitant increase in evanescent path length. Therefore, the low throughput can be compensated by an increase in number of internal reflections, and also the use of a suitable MCT detector. An additional improvement in spectral quality can be obtained simply by increasing acquisition time.

The main purpose of this study is focused on enhancing the sensitivity of a sensing system by optimizing the waveguide design. Reducing the cross-sectional area of a planar waveguide tends to increase the fraction of the total energy carried in the evanescent wave by means of increasing the number of total internal reflections. Superior sensitivity is thus expected for thinner waveguides. As mentioned above, such a strategy causes a certain decrease in amount of light detected. The additional challenge for achieving an optimal performance of the thin waveguide is also to maintain an adequate energy throughput of the thin waveguides as their thickness is reduced.

#### 1.4 Historical Developments of Thin Tapered Ge Waveguides

Methods of fabricating supported thin planar Ge waveguides have been reported by Braiman and his co-workers [22–29]. Starting in 1997, Braiman *et al.* theoretically developed a model, based on the optical theory of the miniature planar slab Ge waveguide, in order to estimate the optimal dimensions for Ge performing as a multiple-reflection IRE with high sensitivity [23–24]. Later on, the  $\sim 50\text{-}\mu\text{m}$ -thick supported planar Ge waveguides were practically introduced as a chemical tool with applications for biomolecules [25–27]. Figure 1.2 schematically presents the proposed design of the thin planar waveguide supported by a ZnS substrate, and also a diagram of the optical layout that was used to achieve the direct broadband coupling.

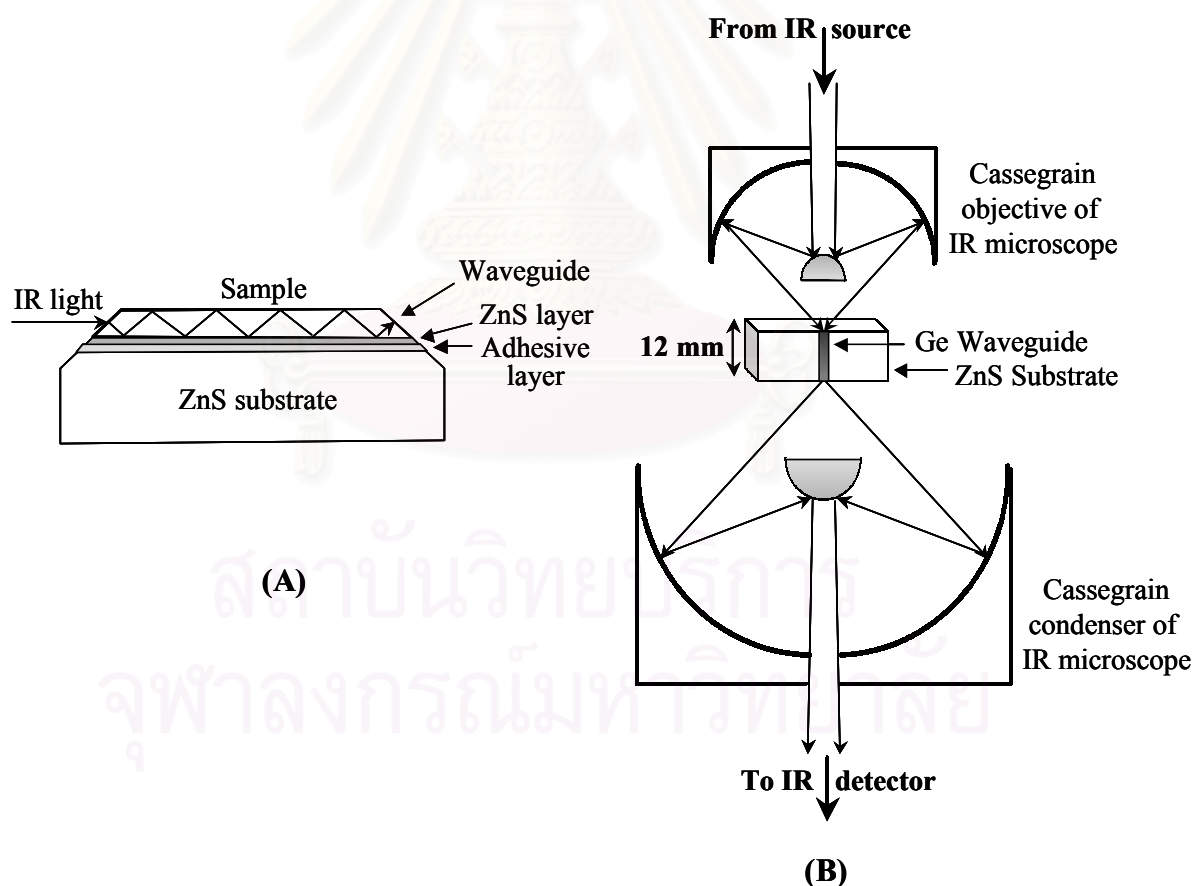


**Figure 1.2** (A) Design of the supported planar Ge waveguide used for evanescent-wave sensing. The relative thickness of the different layers is not to scale. (B) Optical diagram of the microscope and waveguide, showing  $\sim 12\text{-mm}$  separation of focal points of the objective and condensing optical elements.

The observed spectral results clearly revealed a significant increase in surface sensitivity achieved by such thin waveguides, but the use of an IR microscope as a focusing optic required mounting of the waveguide in a vertical direction, providing a substantial restriction on sample handling. Furthermore, the maximum adjustable distance between the focal points of objective and condenser in commercial FT-IR microscopes limited the waveguide length to the range of <12 mm.

In order to get rid of an IR microscope, Braiman *et al.* further created the new configuration of 30–50- $\mu\text{m}$ -thick tapered Ge waveguide [28]. As seen in Figure 1.3, the top surface of the waveguide is a cylindrical sector, while the bottom is flat with a thin ZnS cladding layer. With this design, the waveguide was cemented onto a rigid quartz substrate. Comparing to the previous scheme, the development clearly made the sample handling easier in horizontal arrangement. The setup could be simply operated in the same manner as those commercial ATR accessories.

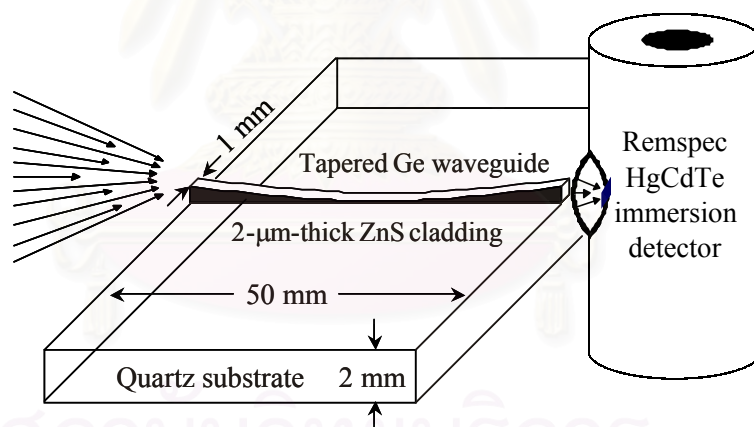


**Figure 1.3** Schematic diagram of a modified planar Ge waveguide and its coupling to an MCT detector located at right. Focused input light shown at left is typically from an FT-IR spectrometer.

However, this type of a modified planar waveguide presented some disadvantages. Special care is required because the waveguide is very susceptible to damage during grinding and polishing. Samples also have a tendency to fall “off” the elevated waveguide. In the end, the observed sensitivity was still inadequate to be considered as a technique for trace analysis.

## 1.5 Scope of the Research

In this work, we have proposed and developed a new design of symmetrically tapered Ge waveguides with the central minimum in the range of 7–30  $\mu\text{m}$ , as demonstrated in Figure 1.4 [33]. Tapering in this manner allows the use of common focusing optical elements without an IR microscope. Substantially higher total energy throughput, compared to previous studies, could be expected with very simple optical alignment procedures. As can be seen, the tapered waveguides have a planar upper surface and a gently curved lower surface that is parallel to the upper surface only near the line segment corresponding to the thinnest region of the waveguide. Due to the lack of a planar lower surface, these waveguides do not meet the standard definition of planar waveguides. But because of the near-parallelism at the sensing region, we refer to them as “quasi-planar”.

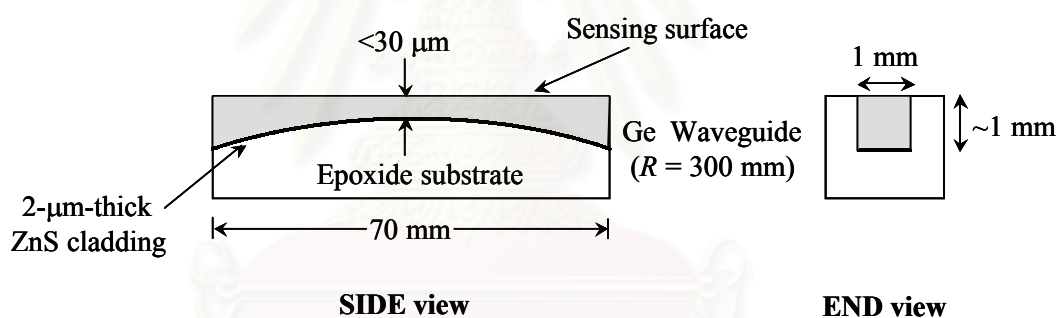


**Figure 1.4** Proposed dimension of a novel MIR evanescent-wave sensor. Left shows the side projection of the symmetrically tapered  $<30\text{-}\mu\text{m}$ -thick waveguide supported by an epoxide substrate, with its end view depicted at right.

With such a thin dimension, the central minimum with a thinnest thickness (i.e., 7–30  $\mu\text{m}$ ) is expected to result in enhanced absorption intensity of small-sized samples, through an increase in the detected absorption intensity per unit area of sample-waveguide contact. These include a number of potential new applications for the waveguide sensors: light-dark difference spectroscopy of picomolar quantities of the purple membrane protein, bacteriorhodopsin (bR); as well as the non-destructive sampling of surface layers of short pieces of human hair.

Because of the inferior spectral SNR that results from a substantial decrease in total throughput, another goal addressed in the current work was to maintain adequate energy throughput of IR light, in order to take a full advantage of the high surface sensitivity. In this regard, a combination of synchrotron-based IR spectroscopy with the symmetrically tapered Ge waveguides would create a new opportunity for analyzing tiny samples with improved spectral quality. Understanding how the thin waveguides functions with a high throughput of synchrotron light source turned to be of crucial interest.

The reasons for the discrepancy between the theoretical and observed performance of such waveguides were theoretically investigated in more detail. In an attempt to accomplish the goal, a systematic approach was carried out both using ray-tracing calculations and by using broadband synchrotron IR radiation to perform mode-specific measurements. In addition, future directions for the development of waveguide sensors could be predicted according to results with the ray-optic calculations.

## **1.6 Objectives of the Research**

1. To develop symmetrically tapered <math><30\text{-}\mu\text{m}</math>-thick Ge waveguides as chemical sensors for very small-sized samples using FT-IR spectroscopy.
2. To investigate the discrepancy between the theoretical and observed performance of the waveguides through a ray-optics calculation, using MATLAB<sup>®</sup> software.
3. To determine how the tapered waveguides function under the high-intensity illumination of the synchrotron IR radiation, in comparison to a standard Global<sup>™</sup> source, in order to improve throughput of the thin waveguides.



## CHAPTER II

### THEORETICAL BACKGROUND

The study of light is perhaps one of man's oldest scientific endeavors. Ancient philosophers speculated about its nature and were familiar with the concepts of reflection, refraction, as well as the rectilinear propagation of light. However, the early studies of light, up to the time of Galileo Galilei (1564–1642), were more philosophical than scientific [35]. The power of the experimental method in optics was subsequently demonstrated and the field of classical optics was elevated to the level of a science. Nowadays, there have been numerous scientific milestones achieved in the process of developing modern light-wave technology. In an effort to motivate a significant development in the area of integrated optics, the fundamental concepts are essentially crucial to gain an insightful understanding of electromagnetic field theory at optical frequencies.

#### 2.1 Fundamentals of Light Propagation

Light is by nature an electromagnetic wave produced by the vibration of an electric charge. In its simplest monochromatic form, light can be represented as polarized, oscillating electric and magnetic fields that propagate in space, as depicted in Figure 2.1 [36].

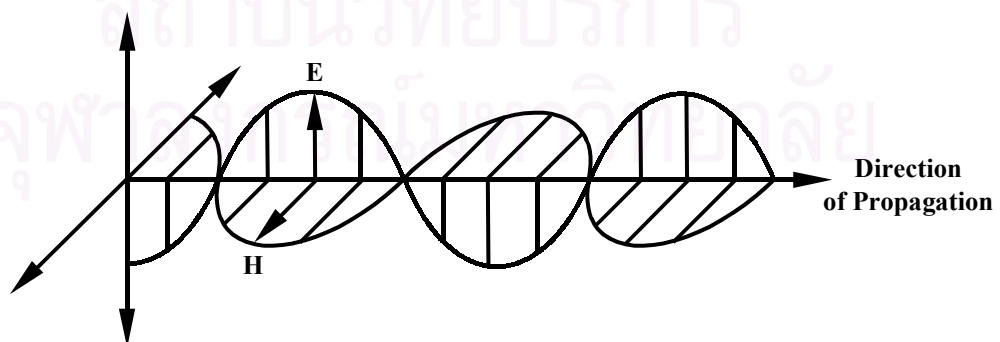


**Figure 2.1** Propagation of a linearly polarized electromagnetic wave in the direction of propagation.

The electric (**E**) and magnetic (**H**) vectorial components are orthogonal to each other and to the direction of propagation. In unpolarized light, the electric component **E** is randomly oriented in an infinite number of directions, but remains always perpendicular to the direction of propagation.

### 2.1.1 Snell's Law: A Principle of Light Reflection and Refraction

When an electromagnetic radiation strikes a boundary between two media with different refractive indices (i.e., a dielectric interface), refraction and reflection occurs. The law that governs the reflection process requires that the angle of incidence be equal to the angle of reflection. In this case, reflection is specular. If electromagnetic radiation passes from one medium to another that has a different refractive index, a sudden change of beam direction takes place because of the differences in propagation velocity through two media. If light propagates through an incident medium with refractive index  $n_1$  and enters a medium with refractive index  $n_2$  (see Figure 2.2), the light path will be changed and the extent of refraction is given by the following expression, known as Snell's law [36]:

$$n_1 \sin \alpha_1 = n_2 \sin \alpha_2 \quad (2.1)$$

where  $\alpha_1$  and  $\alpha_2$  are the angles of incidence and refraction, respectively.

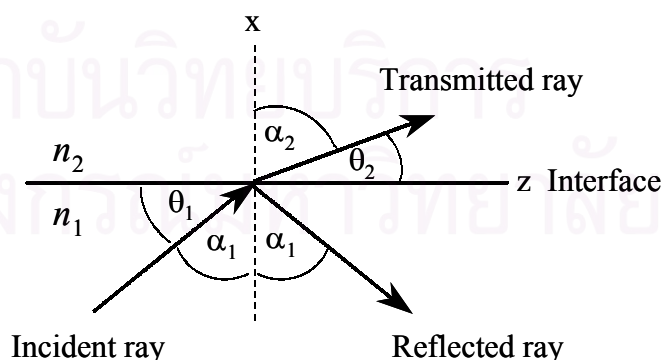


**Figure 2.2** Reflection and refraction of a plane wave at a dielectric interface based on Snell's Law.

### 2.1.2 The Evanescent Field at Total Internal Reflection

The phenomenon of total internal reflection (TIR) occurs when light traveling in an optically dense medium strikes the boundary of a second medium with a relatively lower refractive index (i.e.,  $n_1 > n_2$ ), at a certain angle greater than the critical angle. Based upon the definition of angles in Figure 2.2, the critical angle with respect to the normal of a dielectric interface ( $\alpha_{1c}$ ) is defined by Eq. 2.2. Under this circumstance, the refracted angle  $\alpha_2$  equals  $90^\circ$ , indicating that no light beam emerges on the opposite side of the optically rarer medium 2. Therefore, only light incident on a high-index prism at angles exceeding the critical angle will be totally reflected. However,  $\alpha_2$  can never reach  $90^\circ$  if the values of  $n_1$  and  $n_2$  are interchanged (i.e.,  $n_1 < n_2$ ). In another word, there is no critical angle when the wave is incident from the low-index side.

$$\alpha_{1c} = \sin^{-1}\left(\frac{n_2}{n_1}\right) \quad (2.2)$$

In practice, a variety of MIR optical materials with high refractive indices have been utilized as an IRE for supporting light propagation (or the so-called *waveguide*). When light undergoes the TIR condition, an electromagnetic component of the light extends from the surface of high-index waveguide ( $n_1$ ) into the lower-index medium ( $n_2$ ). This electromagnetic field, known as the *evanescent wave*, decays exponentially within a limited region into the adjacent lower-index sample, as illustrated in Figure 2.3.

The penetration depth ( $d_p$ ) of the evanescent wave is defined as the depth at which the amplitude of the radiation drops to  $1/e$  of its initial value at the interface, as given by Eq. 2.3 [19]. It should be noted that the penetration depth is about one-tenth the wavelength in the denser medium near grazing incidence ( $\alpha \sim 90^\circ$ ) for high-index materials, but becomes infinitely large as  $\alpha$  approaches  $\alpha_{1c}$ . At a fixed angle, the penetration depth is larger for a closer index matching (i.e., as  $n_2/n_1 \rightarrow 1$ ). The penetration depth is also proportional to wavelength and hence is greater at longer wavelengths.

$$d_p = \frac{1}{2\pi\nu n_1 \left( \sin^2 \alpha - (n_2/n_1)^2 \right)^{1/2}} \quad (2.3)$$

where  $d_p(\alpha, \nu)$  is the penetration depth which depends on both experimental conditions (e.g., angle of incidence  $\alpha$ ) and material characteristics (i.e., refractive indices  $n_1$  and  $n_2$ ).

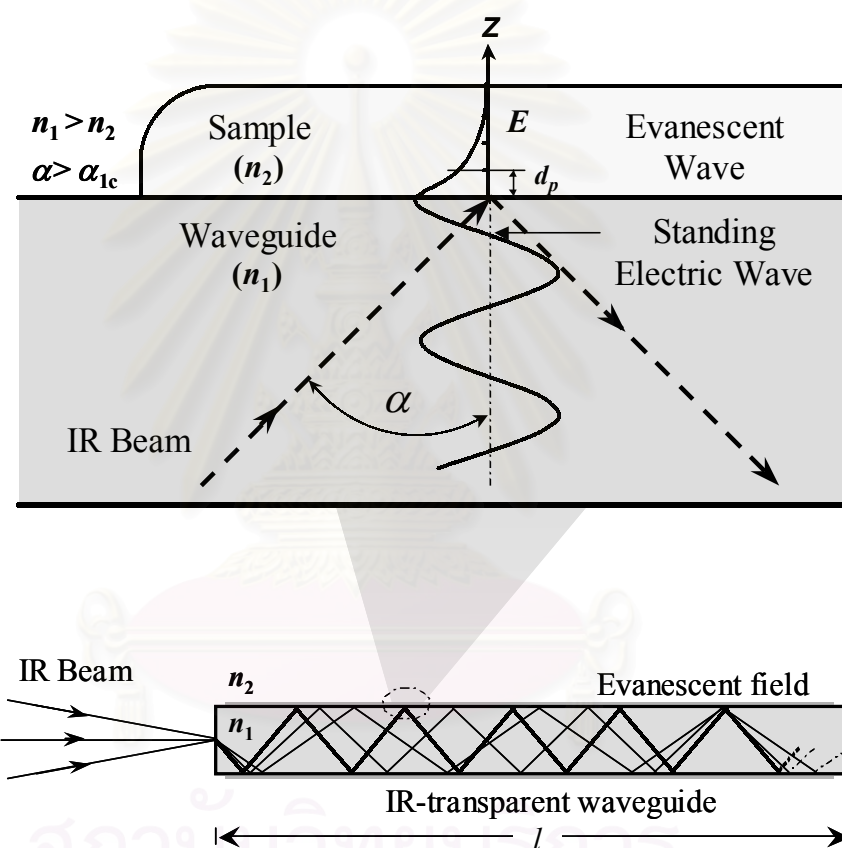


**Figure 2.3** Schematic illustration of an evanescent-wave sensor under the TIR condition ( $n_1$ ,  $n_2$ , refractive indices of the respective waveguide and sample;  $\alpha$ , angle of incidence;  $E$ , exponentially decaying evanescent field;  $d_p$ , penetration depth).

In accordance, any absorbing species locating in close proximity to the dielectric interface will interact with the evanescent field, resulting in wavelength-dependent light loss of the guided light. Changes in the intensity of the guided light provide the qualitative and quantitative information about species present at the interface.

The technique, known as either ATR or EWS, is thus capable of detecting optical events at the boundary with relatively little interference from the bulk solution. Because of the surface-selective nature of the evanescent wave, ATR spectroscopy has become a powerful analytical technique for surface analysis.

## 2.2 An Introduction to Slab Waveguides

The principle of optical confinement using a high dielectric material is based upon the phenomenon of TIR. Figure 2.4 demonstrates schematically the features of an optical dielectric slab waveguide in the form of a three-layer planar guide. As shown, a thin core region of the guiding material is assumed to have refractive index  $n_1$ , and is supported on a thicker, lower-index substrate with refractive index  $n_2$ . The refractive index of the medium above the core is indicated as  $n_3$ . The refractive index  $n_3$  may be unity if the region above the core is air ( $n_{\text{air}} = 1.0$ ), or it may have some other value if the guiding region of index  $n_1$  is covered by an additional low-index layer. The difference in refractive indices between the waveguide and surrounding media enables both the upper and lower interfaces to effectively act as a mirror to propagate the light through TIR condition. In order to achieve true mode guidance, it is necessary that  $n_1$  must be larger than  $n_2$  and  $n_3$  (i.e.,  $n_1 > n_2 \geq n_3$ ). Under certain circumstances, the light will continually bounce between two interfaces for the full length of a waveguide.

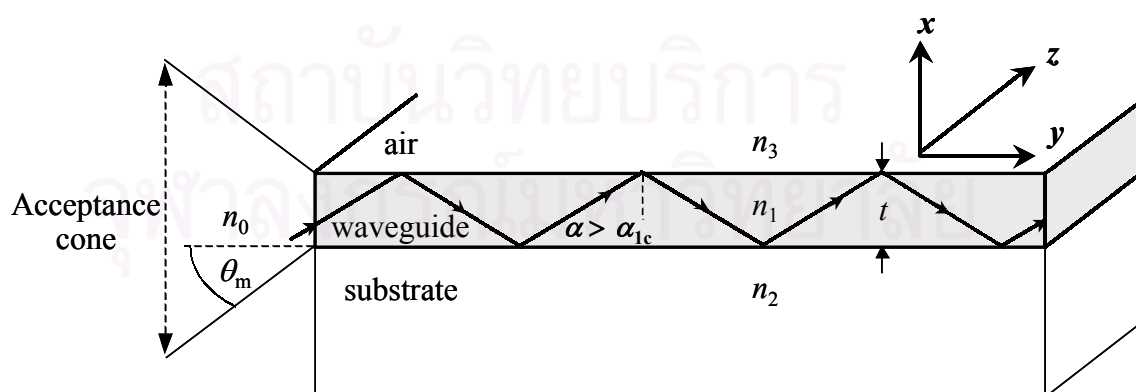


**Figure 2.4** A typical dielectric slab waveguide. Guidance occurs through TIR condition when the entering angle of the light is within a range of the acceptance cone angle ( $\theta_m$ ).

If  $n_2 = n_3$ , such a model is commonly referred to as a *symmetric* slab waveguide. In case  $n_2 \neq n_3$ , this geometry is on the other hand described as an *asymmetric* slab waveguide. By a comparison, the lowest-order mode of a symmetric waveguide does not have a cut-off frequency, indicating that this mode in principle can propagate at arbitrarily low frequencies (long wavelengths). On the contrary, all modes of asymmetrical slabs become cut-off if the frequency of operation is sufficiently low.

It is noteworthy that light undergoes TIR at the dielectric interface only if two basic conditions are fulfilled: (1) the light from high-index medium strikes the interface at an angle greater than the critical angle; and (2) the angles of the light entering the waveguide should be within the *acceptance cone*, as given in Figure 2.4. The acceptance cone angle ( $\theta_m$ )—the maximum input half-angle that could support light propagation into a waveguide—is generally referred to its numerical aperture (NA), which is defined by Eq. 2.4. This parameter indicates the efficiency of light collection into a waveguide. A high NA suggests a wide acceptance cone and thereby a better light gathering capabilities of a waveguide. Note that a typical NA value for a high-quality glass fiber is 0.55, nevertheless most sensing fibers possess values in a range of 0.22–0.66 [37].

$$\text{NA} = n_0 \sin \theta_m = \sqrt{n_1^2 - n_2^2} \quad (2.4)$$

where  $n_0$  is the refractive index of the external medium from which the light enters;  $\theta_m$  is acceptance cone angle; and  $n_1, n_2$  are the refractive indices of the waveguide and its cladding, respectively.

Another crucial variable in an evanescent-wave sensor is the dimensionless waveguide parameter  $V$ , as expressed in Eq. 2.5. The  $V$ -number determines the number of modes of each polarization (TE, transverse-electric; or TM, transverse-magnetic) capable of propagating at the longest wavelength in the desired spectral region inside a waveguide.

$$\begin{aligned}
 V &= 2\pi \frac{t}{\lambda_0} \sqrt{n_1^2 - n_2^2} \\
 &= 2\pi \frac{t}{\lambda_0} \times \text{NA}
 \end{aligned} \tag{2.5}$$

where  $t$  is the thickness of the waveguide, and  $\lambda_0$  is the free-space wavelength of the light.

### 2.2.1 Ray Optics and Guided Modes in Slab Waveguides

Dielectric slabs are the simplest optical waveguides. Guided and radiation modes of slab waveguides can thus be described by simple mathematical expressions. The study of slab waveguides thus serves as a valuable fundamental to the entire field of dielectric optical waveguides, and is often useful in gaining an understanding of the waveguiding properties of more complicated dielectric waveguides used for light guidance in integrated optics applications. Consider an incident coherent light at an angle  $\alpha$  between the wave normal and the normal to the interface in a slab waveguide, as defined by Figure 2.4. The critical angles at both upper and lower interfaces, are respectively,

$$\alpha_{\text{upper}} = \sin^{-1}(n_3/n_1) \tag{2.6}$$

$$\alpha_{\text{lower}} = \sin^{-1}(n_2/n_1) \tag{2.7}$$

On the basis of these two critical angles, three possible ranges of the incident angle  $\alpha$  exist: (1)  $\alpha_{\text{lower}} < \alpha < 90^\circ$ , (2)  $\alpha_{\text{upper}} < \alpha < \alpha_{\text{lower}}$ , and (3)  $\alpha < \alpha_{\text{upper}}$  [38]. Three different zig-zag ray-optical pictures, based upon the incident angle  $\alpha$ , are illustrated in Figure 2.5. When  $\alpha_{\text{lower}} < \alpha < 90^\circ$ , the light is confined in the guiding layer by the TIRs at both upper and lower interfaces and propagated along the zig-zag path (Figure 2.5a). If the waveguide material is lossless, the light can propagate without attenuation. This case corresponds to a *guided mode*, which plays an important role in integrated optics. On the other hand, when  $\alpha_{\text{upper}} < \alpha < \alpha_{\text{lower}}$

(Figure 2.5b), the light is totally reflected at the upper interface while it escapes from the guiding layer through the cover, according to Snell's law, because  $\alpha < \alpha_{\text{lower}}$ . This light is a *substrate radiation mode* whose amplitude decreases significantly along the propagation direction. The case of  $\alpha < \alpha_{\text{upper}}$  also leads to a *substrate-clad radiation mode* that radiates to both the cover and the substrate (Figure 2.5c)

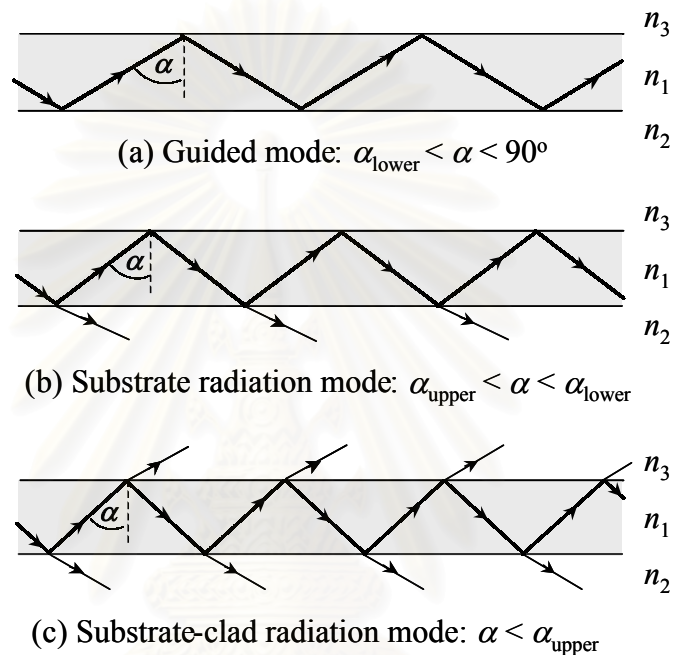


**Figure 2.5** Zig-zag ray-optical trajectory of “modes” propagating along a dielectric slab waveguide.

### 2.2.2 Geometrical Optics Treatment of Slab Waveguides

The simplest description of the propagation of light in a waveguide is in terms of ray-optics. Geometrical (or ray) optics describes the propagation of light fields by defining rays as the lines that follow a straight path across the surfaces of constant phase of the light field (in homogeneous optical medium) at right angles. Light rays have intuitive appeal since a narrow beam of light is a good approximation to the more abstract notion of light rays.

As previously mentioned in Eq. 2.1, Snell's law was introduced to relate the angles with respect to the normal to a dielectric interface. For ray-optic calculations,



it turns to be more general to use the angle between the ray and the dielectric interface, as indicated by the symbol  $\theta$ . Using the definition of the angles shown in Figure 2.2, the formulas of Snell's law and the critical angle can be transformed into the following expressions, respectively [39].

$$n_1 \cos \theta_1 = n_2 \cos \theta_2 \quad (2.8)$$

$$\cos \theta_{1c} = n_2/n_1 \quad (2.9)$$

If  $n_1 > n_2$ , it is apparent from Eq. (2.8) that there is no real angle  $\theta_2$  if  $n_1 \cos \theta_1 > n_2$ . The absence of a real angle can be interpreted as the TIR condition.

In fact, a straight light ray is associated with a plane wave. Ray optics does not include the description of the phase of the light field. However, the notion of the optical path length, which is defined by the actual length times the refractive index of the medium, provides an option to combine a phase to the light ray. A ray of length  $s$  has traveled an optical path length  $n_1 s$  in the guiding layer (medium 1). Its phase relative to the starting point at  $s = 0$  can be defined as  $\phi = -n_1 k s$  (the minus sign is required since the time dependence  $e^{i\omega t}$ ) with the free space propagation constant of plane waves,

$$k = 2\pi/\lambda \quad (2.10)$$

Nevertheless, a plane wave or a ray accumulates a phase shift not only by traveling in space but also by reflection from a dielectric interface. For a plane wave that is polarized with its electric-field vector parallel to the interface, the reflection coefficient  $r$  at the dielectric interface is defined by the following equation:

$$r = \frac{B}{A} = \frac{(n_1^2 k^2 - \beta^2)^{1/2} - (n_2^2 k^2 - \beta^2)^{1/2}}{(n_1^2 k^2 - \beta^2)^{1/2} + (n_2^2 k^2 - \beta^2)^{1/2}} \quad (2.11)$$

where

$$\beta = n_1 k \cos \theta_1 \quad (2.12)$$

For  $\theta_1 > \theta_{1c}$ , the reflection coefficient  $r$  given by Eq. 2.11 is real and positive. Therefore, no additional phase change occurs on reflection from the medium with index  $n_2$ . For  $\theta_1 < \theta_{1c}$ , TIR takes place at the dielectric interface. In this case,  $r$  is complex because the second square root in numerator and denominator of Eq. 2.11 is negative imaginary. The negative sign is necessary since a decaying instead of a growing wave must result in medium 2. Under TIR condition, a wave that is polarized with its electric-field vector parallel to the waveguide surface but perpendicular to the direction of propagation (TE; transverse-electric incidence), suffers a phase shift:

$$\text{TE mode:} \quad \phi = -2 \arctan \left[ \frac{(\beta^2 - n_2^2 k^2)^{1/2}}{(n_1^2 k^2 - \beta^2)^{1/2}} \right] \quad (2.13)$$

For a wave polarized with its magnetic vector parallel to the waveguide surface (TM; transverse-magnetic incidence), the phase shift is given by:

$$\text{TM mode:} \quad \phi = -2 \arctan \left[ \frac{(n_1^2/n_2^2)(\beta^2 - n_2^2 k^2)^{1/2}}{(n_1^2 k^2 - \beta^2)^{1/2}} \right] \quad (2.14)$$

The combination of ray optics and the theory of plane wave reflection at dielectric interfaces enables us to discuss mode guidance in the slab waveguide and derive the eigenvalue equation for propagation constants of the guided modes. Figure 2.6 shows the phase fronts of the plane waves as represented by dashed lines. The ray AB is assumed to have suffered no reflection. In contrast, the longer ray CD belonging to the reflected wave has suffered two TIRs as it travels from the phase front through A and the phase front through B.

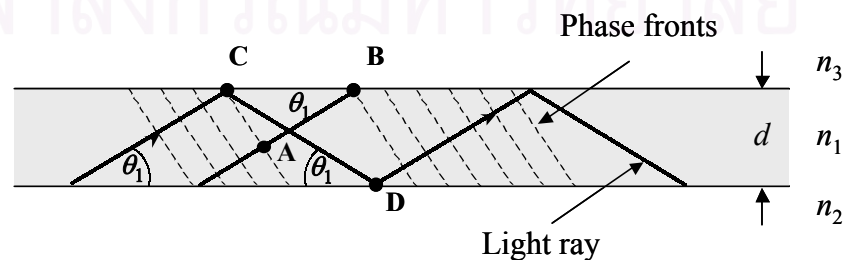


**Figure 2.6** Illustration of the phase condition that leads to the eigenvalue equation. All rays that travel in the same direction belong to the same plane wave.

The two TIRs result in phase changes  $\phi_3$  and  $\phi_2$  that represent the reflections from the interface with region 3 and region 2, respectively. The condition that both rays contribute to the same plane waves can thus be expressed by the following relationship.

$$n_1(s_2 - s_1)k + \phi_2 + \phi_3 = 2N\pi \quad (2.15)$$

where  $s_1, s_2$  are the distances between AB and CD, respectively;  $N$  is an integer number. Such a relation is known as an *eigenvalue equation*, which determines the allowed ray angles or the value of eigenvalue  $\beta$  through Eq. 2.12. The derived eigenvalue equations for two possible polarizations are expressed as follows [39].

$$\text{TE wave:} \quad \tan \kappa d = \kappa(\gamma + \delta) / (\kappa^2 - \gamma\delta) \quad (2.16)$$

$$\text{TM wave:} \quad \tan \kappa d = n_1^2 \kappa (n_3^2 \gamma + n_2^2 \delta) / (n_2^2 n_3^2 \kappa^2 - n_1^4 \gamma \delta) \quad (2.17)$$

where,

$$\kappa = (n_1^2 k^2 - \beta^2)^{1/2} = n_1 k \sin \theta_1$$

$$\gamma = (\beta^2 - n_2^2 k^2)^{1/2} = [(n_1^2 - n_2^2)k^2 - \kappa^2]^{1/2}$$

and

$$\delta = (\beta^2 - n_3^2 k^2)^{1/2} = [(n_1^2 - n_3^2)k^2 - \kappa^2]^{1/2}$$

### 2.3 Realistic Calculation for Design of the Supported Planar Ge Waveguide

Although the theory of optical waveguides, as described in Section 2.2, is of importance to gain an understanding of the waveguiding properties, those complex mathematical expressions however are unlikely to allow one to perceive its uses in practice. It would thus be very useful to demonstrate the application of the optical theories for designing and evaluating the performance of a particular waveguide sensor. The theoretical design of a model planar Ge waveguide described herein is based upon calculations published by Braiman and Plunkett in 1997 [16]. Such miniature planar waveguides were intended to detect evanescent-wave spectra of small areas of biomolecular films.

A generalized planar waveguide design is as shown previously in Figure 2.4. The waveguide itself is a layer of Ge ( $n_1 = 4.0$ ) sandwiched between materials of lower refractive indices. At the sensing region of the waveguide (of length  $l$ , width  $w$ , and thickness  $t$ ), these outer materials consist of aqueous solution (used as a sample) on the sensing side ( $n_3 = 1.35$ ), and ZnS ( $n_2 = 2.26$ ) on the substrate side. Therefore, this model waveguide can be considered as an asymmetrical slab. The NA of this waveguide can be determined, according to Eq. 2.4, to be  $\sqrt{(4.0)^2 - (2.26)^2} = 3.3$ .

### 2.3.1 Calculation of Cut-off Thickness of Ge Waveguide

The cut-off condition for a slab waveguide is derived from the critical angle at which TIR is lost at a plane dielectric interface. Because the width of the sensing region is much greater than its thickness (i.e., 1–2 mm vs. 10  $\mu\text{m}$ ), such a waveguide can be treated as an infinite planar slab. Due to its asymmetrical characteristics, we must confirm that the waveguide is sufficiently thick to allow the propagation of every wavelength in the region of interest (i.e., MIR light should not be completely cut off). Cut-off occurs only when  $N$ , the number of modes of each polarization (TE or TM) capable of propagating at the longest wavelength in the desired spectral region, becomes 0.  $N$  can be calculated in terms of the dimensionless waveguide parameter  $V$  (see Eq. 2.5), by the following equation [39]:

$$N \cong \left( \frac{1}{\pi} \right) \left\{ V - \arctan \left[ \frac{\eta \sqrt{1 - (n_{32})^2}}{\sqrt{(n_{12})^2 - 1}} \right] \right\} \quad (2.18)$$

where  $n_{32} = n_3/n_2$  ( $n_3$  is equal to the lower outside index of refraction, which is  $\sim 1.35$  for  $\text{H}_2\text{O}$ ); and  $n_{12} = n_1/n_2$ . The variable  $\eta$  equals 1 for TE modes, while  $\eta$  equals  $(n_{13})^2$  for TM modes. Note that the number of allowed modes must be integral; the value given by the right side of Eq. 2.18 must simply be raised to the next higher integer to give the exact value of  $N$ .

The cut-off thickness is determined by setting  $N \leq 0$  in Eq. 2.18. For a Ge waveguide sandwiched between an aqueous solution (H<sub>2</sub>O) and ZnS, the cut-off thickness for light with a wavelength (*in vacuo*) for  $\lambda_0 = 10 \mu\text{m}$ , or  $1000 \text{ cm}^{-1}$ , will be  $0.14 \mu\text{m}$  for TE modes and  $0.36 \mu\text{m}$  for TM modes. Thus, at a thickness above  $0.36 \mu\text{m}$ , both TE- and TM-polarized lights are capable of propagating through the waveguide. Equation 2.18 additionally indicates that  $N_{\text{TE}}$  and  $N_{\text{TM}}$  each increase by 1 for every increment of  $\lambda_0 / \left(2 \times \sqrt{n_1^2 - n_3^2}\right)$  in thickness. It is noteworthy that analogous formulas for numbers of modes propagating through a ‘non-infinite’ waveguide are more complicated [39], but lead to qualitatively similar results. In particular, the total number of allowed modes of a slab waveguide at a particular frequency is approximately proportional to the product of  $(w \times t)$ , even when one of the dimensions is somewhat smaller than the wavelength *in vacuo*.

### 2.3.2 Investigation of the Transmitted Throughput

The maximum amount of light that can be transmitted from the broadband (blackbody) source through a waveguide is expected to be proportional to the number of allowed propagation mode. To investigate this behavior, consider a transparent waveguide with both planar endfaces in contact with blackbodies of infinite surface area. Assume that both blackbodies have refractive index  $n_1$  matching to that of the waveguide, and that both are at a high temperature  $T$ . Generally speaking, this direct-coupling arrangement would be expected to transmit, in both directions through the waveguide, the maximum possible amount of broadband power for any coupling of a blackbody source at the same temperature to the same waveguide. A standard quantum-field theoretical extension of Plank’s principle states that a fixed amount of energy,  $h\nu \left(e^{h\nu/kT} - 1\right)$ , will be present in each electromagnetic mode having a particular frequency  $\nu$ . The maximum blackbody power that can be transmitted by a waveguide with  $N$  propagation modes at a frequency  $\nu$  is then  $h\nu N u_{\text{ave}} \left(e^{h\nu/kT} - 1\right)$ , where  $u_{\text{ave}}$  is the average group velocity of all the allowed propagation modes. The latter quantity is roughly constant with waveguide thickness, even down to the single-mode regime. As a consequence,

the maximum light power at each wavelength that can be transmitted from a blackbody source through a Ge dielectric waveguide should be proportional to the waveguide's cross-sectional area, even down to a little below 1  $\mu\text{m}$  for MIR light. This statement is thus equally true for miniature waveguides as for the in-air sample beam focus of traditional IR spectrometers [1]. Its accuracy depends, of course, on the assumption that an optical coupling method between broadband source and waveguide is used that is equally efficient for all allowed propagation modes of the waveguide.

### 2.3.3 Feasibility Calculation A: Size of Relative Absorption Changes

To ascertain the feasibility of the proposed waveguide, the fractional absorption of light propagating through the waveguide by IR-absorbing species in contact with the sensing surface, and its dependence on the waveguide thickness, were estimated. The temporal rate of energy absorption per molecule is proportional to the square of the dot product of a molecular vibrational transition dipole moment and the electric field vector  $\mathbf{E}$ . Alternatively, it is equal to  $(1/4\pi)c\sigma E^2 \cos^2 \phi$ , where  $E^2 = \mathbf{E} \cdot \mathbf{E}$  is expressed in cgs units ( $\text{erg cm}^{-3}$ ),  $\phi$  is the angle between the transition dipole moment and  $\mathbf{E}$ , and  $\sigma$  is the cross section for a particular IR absorption band of the absorbing species. Assuming that all  $N$  molecules are at the same distance from the sensor surface, the same value of  $E$  can be applied to the equation of total temporal rate of energy absorption in a TE mode, as expressed in Eq. 2.19. The variable  $\theta$  represents the angle that the transition dipole moment makes with the waveguide normal.

$$\Delta P = 1/8\pi Nc\sigma E^2 \sin^2 \theta \quad (2.19)$$

If these molecules absorb only weakly (e.g., less than 1% of the total power passing through the waveguide), the fractional loss of optical power is given by  $\Delta P$  divided by the input power transmission  $P_0$  through the Ge waveguide and surrounding dielectrics. The resulting expression includes the ratio  $E^2/P_0$ . This ratio depends on what types of mode(s) are carrying the light intensity.

For the lowest-order TE mode, the final result for the power attenuation due to  $N$  absorbing molecules located at a distance  $x$  from the sensor surface is,

$$\frac{\Delta P}{P_0} \approx N \sin^2 \theta \frac{\sigma \lambda_0^2 \exp(-2x/d_p)}{\pi^2 w t d_p (t + 2d_p) (n_1^2 - n_3^2) \left[ \left( \frac{\lambda_0}{2\pi d_p} \right)^2 + n_3^2 \right]^{1/2}} \quad (2.20)$$

where  $w$  and  $t$  are the width and thickness of the sensing region, and  $d_p$  is the penetration depth of the evanescent field into the sensed medium, defined by  $d_p \approx t \left( \sqrt{1+V^2} - 1 \right)^{-1}$ . As a waveguide gets thicker ( $V \gg 1$ ), this formula is reduced to  $d_p \approx t/V = \lambda_0 / 2\pi \sqrt{n_1^2 - n_3^2}$ . Since the lowest-order mode in a thick waveguide corresponds to glancing internal reflection ( $\theta \rightarrow 90^\circ$ ), the preceding formula for  $d_p$  coincides with that obtained from the standard formula for ATR spectroscopy in Eq. 2.3 [19].

For the highest-order mode (i.e., modes propagating near to the critical angle) where the attenuation is expected to be the greatest, only the thick waveguide limit is considered. By assuming that the light is propagating right at the critical angle, Eq. 2.20 must be replaced by the following, derivable either from Marcuse [39] or from the standard ATR equations in Harrick [19]:

$$\frac{\Delta P}{P_0} \approx V \sin^2 \theta \frac{2\sigma \exp(-2x/d_p)}{n_3 w t} \quad (2.21)$$

It is well established that, for ATR spectroscopy, the measured absorption due to a thin-film coating on a multiple-reflection ATR prism is expected to go as  $1/t$ , because of the increase in the number of reflections as  $t$  decreases. Indeed, the appearance of several factors of  $t$  in the denominator of Eq. 2.20 indicates that  $\Delta P/P_0$  can be made to increase monotonically without limit as  $t$  is reduced to 0. However, this assumption does not take into account that  $V$  depends on  $t$ , and therefore, so does  $d_p$ . In fact, it is expected that as  $t \rightarrow 0$ ,  $d_p \rightarrow \infty$ , even for the lowest-order mode.

Taking into account this dependence of  $d_p$  on  $t$ , it is found that, for the lowest-order TE mode, the fractional absorption function  $\Delta P/P_0$  has a limit of 0 as the waveguide thickness  $t$  approaches either 0 or  $\infty$ . This observation is shown in Figure 2.7, which gives the calculated value of  $\Delta P/P_0$  due to attenuation of  $\sim 6\text{-}\mu\text{m}$  light by amide (I) absorption of protein molecules, which is assumed to be within several nm of the water-sensor interface and oriented parallel to it. The attenuation  $\Delta P/P_0$  was calculated under the assumption of a Ge waveguide  $200\ \mu\text{m}$  in width. Curves represent both the lowest-order TE mode (Eq. 2.20) and the TE light propagating at the critical angle in the thick-waveguide limit (Eq. 2.21). The absorption cross section  $\sigma$  was assumed to be  $4 \times 10^{-10}\ \mu\text{m}^2$  on the basis of an approximate value of  $\varepsilon = 1000\ \text{M}^{-1}\ \text{cm}^{-1}$  for the amide (I) vibration.

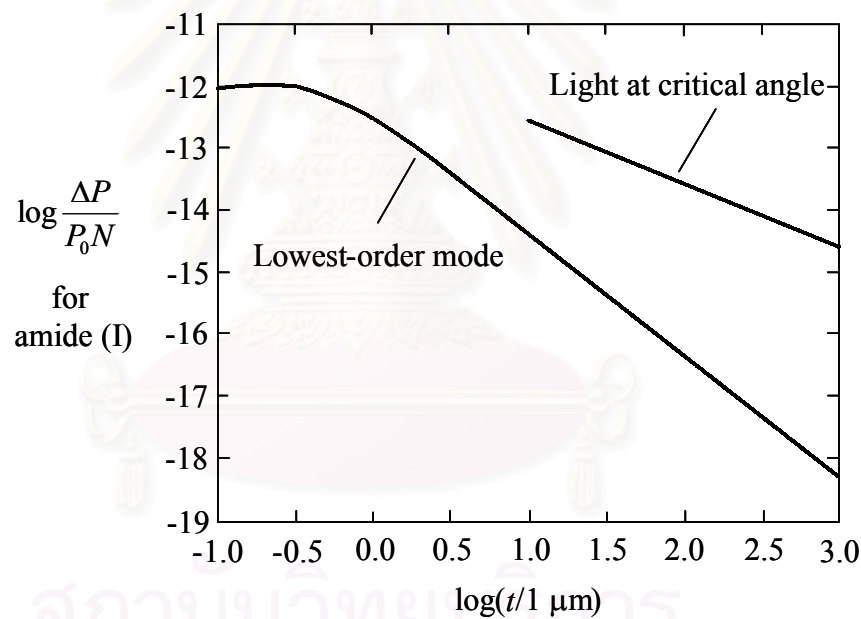


**Figure 2.7** A plot of power attenuation ( $\log(\Delta P/P_0N)$ ) by amide (I) absorption as a function of the waveguide thickness  $t$  (in  $\mu\text{m}$ ).

The curves reveal the limits for the lowest- and highest-order TE modes that can be propagated through a waveguide of any particular wavelength. The actual fractional attenuation is expected to be an average of the attenuations of all allowed individual modes, and thus to lie somewhere between the two plotted curves. As can be seen, a maximum in the average attenuation occurs within the single-mode



regime, where curves for the lowest- and highest-order modes must coincide. For a Ge waveguide in contact with aqueous medium, this maximum occurs for a thickness of  $t \approx 0.5 \mu\text{m}$ . Assuming  $N$  protein molecules are present within  $\sim 10$  nm of the sensing surface, Eq. 2.20 gives an expected value of  $3 \times 10^{-13} N$  for attenuation of the TE portion of the light passing through a 1- $\mu\text{m}$ -thick Ge sensor. In contrast, for a macroscopic 1-mm-thick, 10-mm-wide ATR plate, Eq. 2.21 predicts an attenuation of  $6 \times 10^{-17} N$ , which is  $\sim 5000$ -fold less than that obtained with a waveguide of optimal thickness.

Equations for TM modes are more complicated [39]. Indeed, Harrick showed that, in the case of a simple dielectric interface, the field right at the critical angle for TM mode exceeds that of TE mode by exactly a factor of  $n_1/n_3$  (i.e., 2.2) [19]. This condition results in a nearly 5-fold increase in  $\Delta P/P_0$  relative to the lowest-order TE mode. This observation implies that almost a 5-fold greater absorbance is expected for groups with transition dipole moments oriented perpendicular to the waveguide surface. An additional 2-fold enhancement is expected for such perpendicular groups, because the free rotation in the plane of protein membrane does not cause any of their transition moments to become unaligned with the electric-field vector. Accordingly, the fractional absorption  $\Delta P/P_0$  of the TM portion is then given by  $3 \times 10^{-12} N$ , for  $N$  protein molecules oriented perpendicular to the waveguide surface.

If the light traveling through the waveguide is unpolarized (i.e., equal power is carried in TE and TM modes), then a transient change in orientation of protein molecules at the surface should be accompanied by a change in total IR transmission. For  $N$  protein molecules undergoing a full  $90^\circ$  rotation from perpendicular to parallel to the molecular plane, the signal should be:

$$\frac{\Delta P}{P_0} \approx \frac{1}{2} \left[ (3 \times 10^{-12}) - (3 \times 10^{-13}) \right] N \approx 1.5 \times 10^{-12} N$$

### 2.3.4 Feasibility Calculation B: Detection of Signals

In an effort to evaluate the efficiency of using such a waveguide in combination with a commercially available FT-IR spectrometer under extensive signal averaging, the parameter SNR should be determined based on the formula given by Griffiths and de Haseth [1].

Referring to Eq. 1.2, the blackbody radiation intensity  $U_{\bar{\nu}}(T)$  for a source temperature  $T = 1500$  K in the range of  $1650 \text{ cm}^{-1}$  (i.e., amide (I) vibration) is  $1.4 \text{ mW}/(\text{cm}^2 \text{ sr cm}^{-1})$ ; the throughput  $\Theta$  for our model waveguide is  $7.5 \times 10^{-5} \text{ cm}^2 \text{ sr}$  (the product of the input area for a  $5\text{-}\mu\text{m}$ -thick,  $1000\text{-}\mu\text{m}$ -wide planar waveguide and the solid angle of the  $\text{NA} = 0.5$  focusing optic); the resolution  $\Delta\bar{\nu}$  is set at  $8 \text{ cm}^{-1}$ ; the detectivity  $D^*$  of our cooled MCT detector is  $5 \times 10^{10} \text{ cm W}^{-1} \text{ Hz}^{1/2}$  with its active area  $A_D$  of  $(100 \mu\text{m})^2$ . If a realistic spectrometer efficiency  $\xi$  is assumed to be 0.1, then the estimated SNR should be  $3 \times 10^7$  after a measurement time  $t$  of  $10^3$  s. This estimate readily suggests an adequate margin to detect signals of several parts per million.

## 2.4 A Brief Description of Synchrotron Radiation

### 2.4.1 Origin of the Synchrotron

Electron-particle accelerators can produce very bright beams of IR radiation [40]. The passing of an electron produces an electric field varying in time. As illustrated in Figure 2.8 (A), an electron is circulating relativistically in a storage ring with a velocity close to the speed of light in vacuum (i.e.,  $\sim 3.0 \times 10^8 \text{ m s}^{-1}$ ), generating a sharp pulse of  $\Delta t$ . Owing to the relativistic motion, the electric field is pointed in a forward direction into an angle of  $1/\gamma$ , where  $\gamma$  is a ratio of the mass of the electron to its rest mass. As a consequence, a directional and concentrated radiation, so-called synchrotron radiation, is emitted. By using the Fourier transform theorem, the intensity as a function of  $1/\text{time}$  (or frequency) can be obtained in terms of a broadband spectrum (see Figure 2.8 (B,C)). In principle, the wavelength

indicated by the vertical dashed line, in Figure 2.8 (C), can be estimated by the product of the light velocity in vacuum and the pulse width ( $\Delta t$ ). It is also noteworthy that the spectrum extends to longer wavelengths with only a slow falloff.

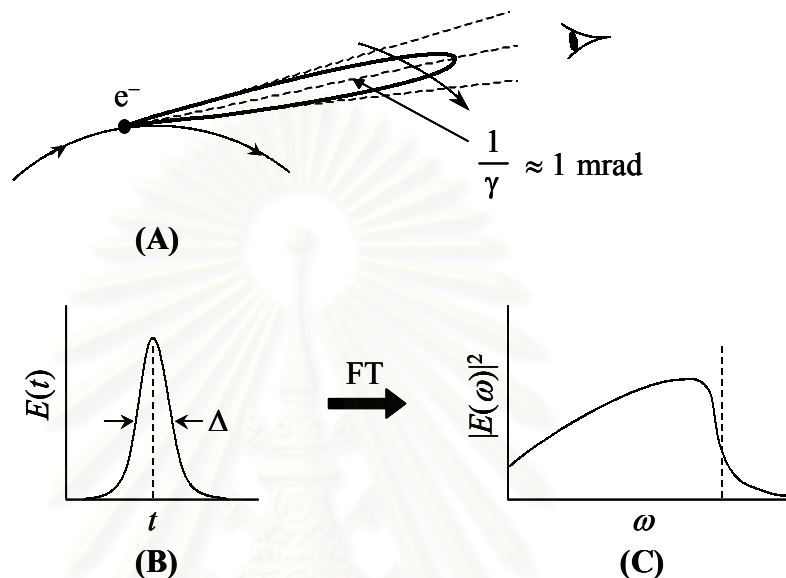


**Figure 2.8** Schematic of synchrotron radiation produced by a relativistic particle. (A) An electron is accelerated in a magnetic field with a circular motion. (B) Electric field as a function of time  $t$  at the observer. (C) Fourier transform of (B) which yields a broadband spectrum.

#### 2.4.2 Synchrotron Facility at National Synchrotron Light Source

Nowadays, facilities for synchrotron IR radiation can be found around the globe, serving to produce light for scientific communities. The National Synchrotron Light Source (NSLS) of Brookhaven National Laboratory (BNL) in Upton (NY) presently operates six IR beamlines, making it a premier synchrotron facility for IR investigations. For a practical point of view, Figure 2.9 depicts the NSLS synchrotron facility. Electrons from an electron source (A) are initially accelerated by the radio-frequency cavities in a linear accelerator (B), to energy of  $\sim 75 \text{ MeV}$ , prior to entering into a booster ring (C). At the booster ring, they are continually accelerated to a higher energy state of  $\sim 750 \text{ MeV}$ , and then injected into either an X-ray storage ring or, for the IR region, a vacuum ultraviolet (VUV) storage ring.

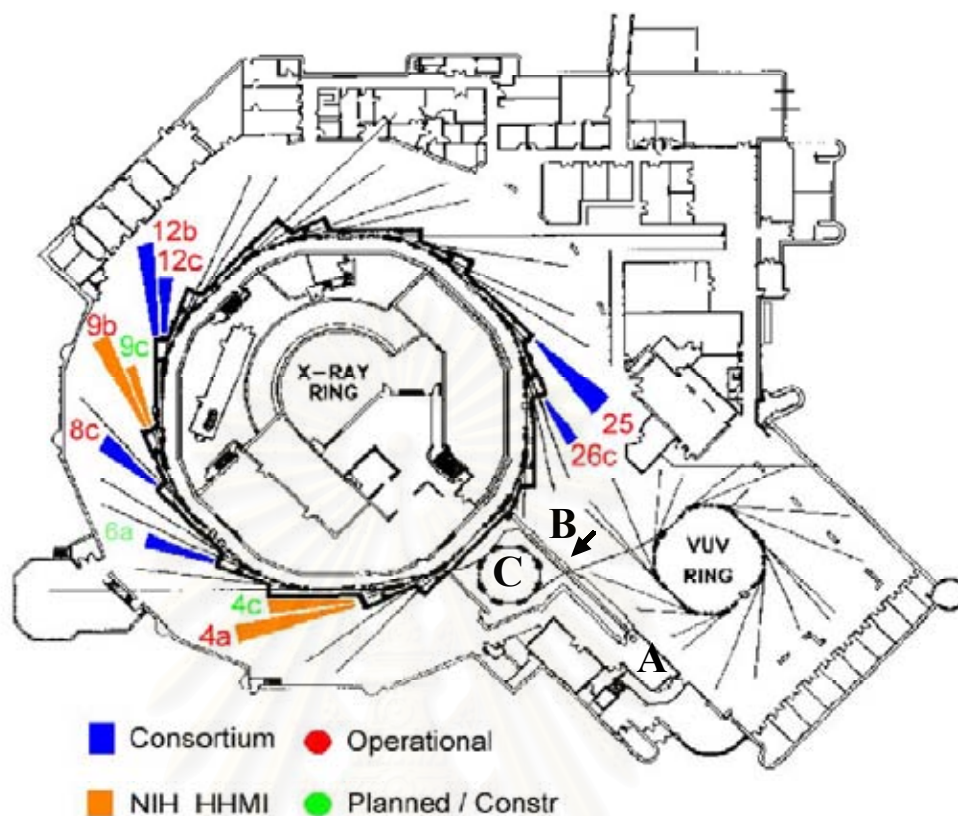


**Figure 2.9** Diagram of the synchrotron at NSLS/BNL showing the (A) electron source, (B) linear accelerator, and (C) booster ring, as well as the VUV storage ring and beamlines.

Bunches of electrons orbiting in a VUV storage ring emit radiation that is directed from the ring port into beamlines in proximity to various bending magnets. The emitted light is given by incoherent superposition of the emissions from individual electrons. The total output is proportional to the number of electrons in the bunch, which is as high as  $10^{12}$  at NSLS [40]. In fact, the radiation extracted from the VUV ring to the beamlines contains soft X-rays and vacuum ultraviolet radiation in addition to that in the IR region. In consideration of this, the optical system between the synchrotron beam port and IR instruments necessarily includes a standard plane copper-coated laser mirror as a first reflecting optic. The mirror absorbs X-rays and the VUV flux, and reflects the IR beam at the right angles from the incident radiation to several mirrors prior to entering an evacuated tube at the end of the interface. At the Albert Einstein Center of Synchrotron Biosciences's U2B

beamline (NSLS), a special interface of the ring and an evacuated tube allows an introduction of the synchrotron beam into FT-IR instruments by a total angular acceptance of 45 mrad horizontally by 45 mrad vertically [41]. This angular aperture meets (or exceeds) the natural opening angle for IR frequencies down to  $250\text{ cm}^{-1}$ , and thus delivers the highly collimated synchrotron radiation across the overall MIR spectral range without degrading the brightness.

### 2.4.3 Synchrotron Characteristics

To specify the intensity level emitted by an IR source, the term “brightness” (also called brilliance, or spectral radiance) is in general the proper parameter, which can be defined as power/(area  $\times$  solid angle). The product of the beam area and its solid angle in steradians (sr) is known as *étendue*. According to this definition, the brightness of a 1200 K thermal source (e.g., Globar<sup>TM</sup>) having a beam area of  $10 \times 1\text{ mm}$ , which emits into an angle of  $2\pi\text{ sr}$ , is roughly  $30\text{ }\mu\text{W cm mm}^{-2}\text{ sr}^{-1}$  for 20 W total IR power. In contrast, a synchrotron radiation source emits 100 mW into the same bandwidth (namely  $10,000\text{ cm}^{-1}$ ), but from a source size of  $330 \times 330\text{ }\mu\text{m}$  into a solid angle of 1 msr, which consequently produces a brightness in the range of  $100\text{ mW cm mm}^{-2}\text{ sr}^{-1}$ . By a comparison, the synchrotron brightness is a factor of 3000 higher than that generated by a thermal source [40]. Regarding the power through a  $10\text{-}\mu\text{m}$  pinhole illuminated with  $f/1$  optics, a Globar<sup>TM</sup> source provides about 1 nW cm onto a sample with respect to that of  $1\text{ }\mu\text{W cm}$  from the synchrotron [42]. Therefore, the primary advantage of a synchrotron IR radiation is its high brightness, which is apparently 100–1000 times greater than the conventional sources. Such a source is absolutely free of thermal noise. Given typical MCT detector noise characteristics of  $10^{-11}\text{ W}$ , the SNR advantage of the synchrotron is distinctively clear. Accordingly, high-quality spectra can be achieved without excessive co-addition of scans, in relatively short acquisition time.

Of note is that the superior brightness is not because the synchrotron produces more power, but because the effective source size is small and the light is emitted into a narrow range of angles as highly collimated rays. This non-divergent characteristic of the synchrotron beam with a high flux greatly improves the spatial

resolution at the diffraction limit, enabling inhomogeneous areas as small as a few  $\mu\text{m}^2$  to be efficiently probed and resolved. Although a laser IR source is also bright and can supply a high photon flux onto a small aperture, the synchrotron source on the other hand is broadband in nature allowing the broadband spectroscopy to the far-IR region to be readily performed. As a result, synchrotron IR sources are an ideal solution for measurements with a limited throughput, meaning either a small sample area, the requirement of a narrow beam, or the combination of both.



สถาบันวิทยบริการ  
จุฬาลงกรณ์มหาวิทยาลัย

## CHAPTER III

### EXPERIMENTAL SECTION

#### 3.1 Fabrication of the Tapered Quasi-Planar Waveguides and Its Optics

##### 3.1.1 Materials and Equipment

1. Single-crystalline germanium (Ge) disk with a diameter of 70 mm, and 3 mm in thickness (Lattice Materials Corp., Bozeman, MT); see Table 3.1 for physical and optical properties of the material
2. Zinc sulfide (ZnS) with  $n_{\text{ZnS}} = 2.2$
3. Epothin® epoxide resin (Buehler Ltd., Lake Bluff, IL)
4. Optical polishing kit including:
  - 4.1 Silicon carbide (SiC) grinding compounds of 400 and 600 grit
  - 4.2 Aluminum oxide ( $\text{Al}_2\text{O}_3$ ) abrasive powders of 25- and 12.5- $\mu\text{m}$  particle sizes
  - 4.3  $\text{Al}_2\text{O}_3$  grinding discs and diamond lapping films with particle sizes of 9, 6, 3, 1, 0.5, 0.3, and 0.1  $\mu\text{m}$
  - 4.4 Ground glass plates and self-adhesive polishing pads

**Table 3.1** Physical and optical properties of crystalline Ge.

##### Physical Properties

Atomic mass average	72.61
Boiling / melting points	2830 °C / 937.4 °C
Density	5.323 g/cm <sup>3</sup> at 300 K
Hardness (Knoop #)	550
Appearance	hard brittle grayish-white metal

##### Optical Properties

Transmission range	5500–600 cm <sup>-1</sup>
Useful range for ATR	5500–830 cm <sup>-1</sup>
Refractive index	4.0

### 3.1.2 Instruments

1. Automated grinding/polishing machine equipped with a cylindrical aluminum grinding tool of 600-mm curvature diameter (K & S Optics, Binghamton, NY)
2. Vertical band saw (Materials Facility, Cornell Center for Materials Research, Cornell University, Ithaca, NY)
3. Chemical vapor deposition (CVD) instrument
4. IR-Plan<sup>TM</sup> Infrared Microscope Accessory (Spectra-Tech, Stamford, CT)
5. FT-IR interferometer (Illuminator, Midac Corp., Irvine, CA)
6. HgCdTe (MCT) immersion detector (MOD-O2S1, Remspec Corp., Sturbridge, MA)
7. Single off-axis paraboloid mirror with 19.1-mm focal length (Melles Griot, Irvine, CA)

### 3.1.3 Fabrication Procedure

Fabrication of the tapered quasi-planar waveguides was previously reported [33]. A schematic procedure is illustrated in Figure 3.1. Briefly, the disk was first symmetrically tapered and polished on a grinding machine with a cylindrical aluminum grinding tool of 600-mm curvature diameter (i.e.,  $R = 300$  mm), to produce a curved surface on one side of the disk. The polished curved surface was then coated with a 2- $\mu\text{m}$ -thick ZnS cladding layer by using a CVD process at a relatively low temperature ( $<150$  °C). This proprietary deposition method (by Hughes-Santa Barbara Research Corporation, Santa Barbara, CA) was found to be necessary to provide an adequate mechanical adhesion of the ZnS layer on Ge surface particularly for the subsequent grinding and polishing to the minimum thickness of  $<30$   $\mu\text{m}$ . The cladding layer essentially prevents IR light from being absorbed by the supporting epoxide substrate. The ZnS-coated round Ge disk was then diced into 2-mm-wide strips using a vertical band saw. Each of these strips was ground on its two parallel planar sides, to a final width of 0.5–1 mm.



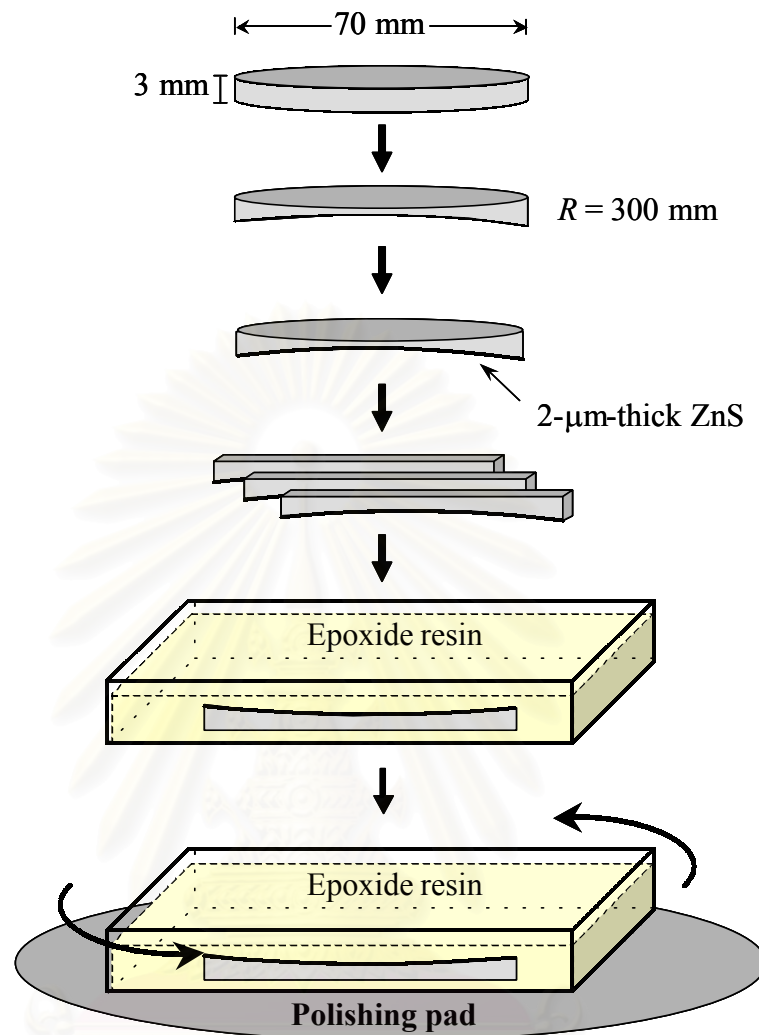


**Figure 3.1** Experimental outline of the fabrication procedure of the symmetrically tapered  $<30\text{-}\mu\text{m}</math>-thick quasi-planar Ge waveguides.$

In the next step, each ZnS-coated tapered Ge strip was individually embedded into a specific epoxide resin (Epothin<sup>®</sup>). The epoxide resin and hardener was mixed in the manufacturer's recommended proportion prior to pouring a well-blended mixture onto the Ge strip which was held, flat side down, in a disk-shaped mold. After the epoxide resin was completely polymerized and fully hardened, the minimum thickness of the waveguide was subsequently reduced from its initial value ( $\sim 2\text{ mm}$ ) down to the final tapered thicknesses of  $<30\text{ }\mu\text{m}$ , by grinding and polishing its exposed flat surface. When the fabrication process was accomplished, the top flat surface of the finished waveguide performs as a sensing area, while its ZnS-coated

curved bottom helps increase the number of total internal reflections resulting in enhanced sensitivity particularly in the middle part of the waveguide. Of note is that the quality of spectra taken with these tapered Ge waveguides depends strongly on the quality of the final polished sensing surfaces, because surface scratches cause light scattering and thereby result in less total energy throughput and a correspondingly poor SNR.

In case of the experiments to determine the effect of surface-finish quality on waveguide transmittance, hand grinding and polishing were performed by utilizing various polishing compounds and polishing disks manufactured by Buehler Ltd. A careful fine-polishing down to a 0.1- $\mu\text{m}$  finish was crucial for minimizing light scattering from imperfections in the planar surface. For all other experiments, on the other hand, this procedure was performed at a commercial optics house equipped with automated grinding/polishing machines, in order to obtain a high-quality finish.

#### **3.1.4 Thickness Determination Based on Interference Fringes**

Towards the end of this process, the thickness of the supported waveguide was determined periodically during grinding and polishing by rinsing and drying the waveguide prior to a measurement of the interference pattern (“channeling”) that appears on the single beam spectrum (*vide infra*). In practice, the incident IR beam was transmitted perpendicular onto the planar (flat) surface of central part of the waveguide, using an IR-Plan<sup>TM</sup> microscope connected to a Midac FT-IR interferometer. Spectra were then measured in reflectance mode. The instrumental parameters used for data acquisition are as listed below. An estimate of the thickness can be obtained based upon the principle of interference in thin films caused by reflections from the front and back surfaces of the Ge waveguides, as depicted in Figure 3.2 [43]. Using particular expressions below, the thickness of a waveguide can be calculated either from spacing of the interference pattern in a single-beam spectrum (Figure 3.3), or from the distance between the centerburst to spikes obtained in the observed interferogram (Figure 3.4).

### Instrumental Setup

Source	Standard Globar™
Beam splitter	KBr
Detector	MCT

### Acquisition Parameters

Spectral resolution	1 $\text{cm}^{-1}$
Number of coadded scans	256 scans
Signal gain	1
Spectral format	Reflectance

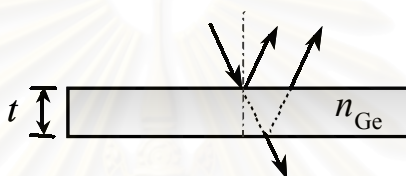


**Figure 3.2** Reflections at the front and the back of a thin Ge film resulting in the oscillatory interference fringes.

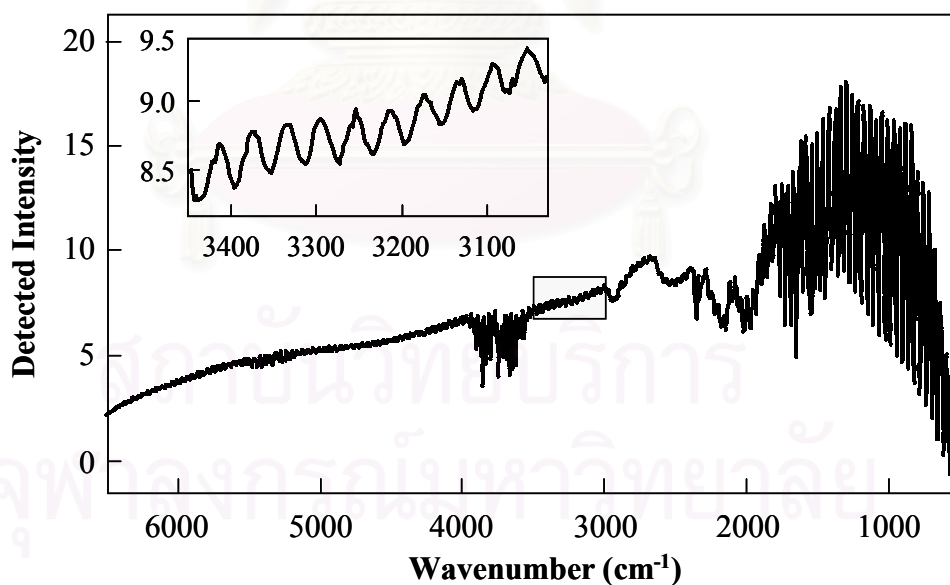


**Figure 3.3** FT-IR single-beam spectrum obtained from IR microscopy, by impinging the incident IR beam transverse the thinnest central part of the waveguide's sensing surface. **Inset:** Expanded range of the periodic oscillatory interference pattern.

$$t = \frac{n_{\text{fringes}}}{2n_{\text{Ge}}(\nu_2 - \nu_1)} \quad (3.1)$$

where  $t$  is the thickness (in cm) of the Ge waveguide having refractive index  $n_{\text{Ge}}$ , and  $n_{\text{fringes}}$  is the number of full fringes in the wavenumber range between  $\nu_2$  and  $\nu_1$ . Note that the precision will be improved if  $n_{\text{fringes}}$  is as large as possible.

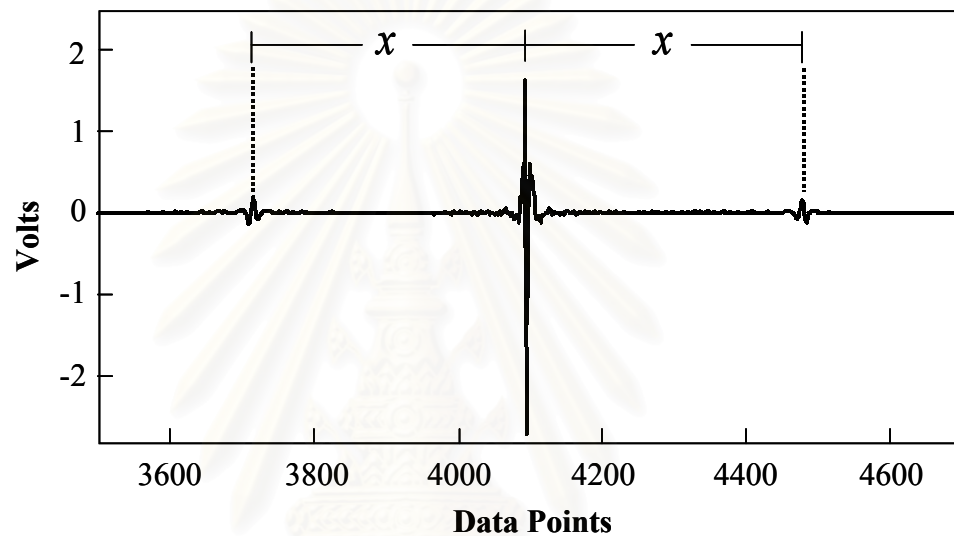


**Figure 3.4** Symmetrical spikes in a FT-IR interferogram used for determination of the waveguide thickness.

$$t = \frac{0.6328 x}{2n_{\text{Ge}}} \quad (3.2)$$

where  $t$  is the thickness (in  $\mu\text{m}$ ) of the Ge waveguide having refractive index  $n_{\text{Ge}}$ , and  $x$  is the distance between the centerburst to spike (in unit of data point) as shown in Figure 3.4. The number “0.6328” is the reference wavelength of a He-Ne laser, in  $\mu\text{m}$ .

### 3.1.5 Optical Alignment of the Tapered Waveguide

As illustrated in Figure 3.5, broadband IR light from the spectrometer's external beam port is focused onto the entrance end of the waveguide. The output end of the waveguide is butt-coupled against the window of a liquid-N<sub>2</sub>-cooled (Remspec) MCT immersion detector. The collimated beam exiting the external output port of the spectrometer is simply focused onto the entrance end of the waveguide by using a single off-axis paraboloid mirror with 19.1-mm focal length.

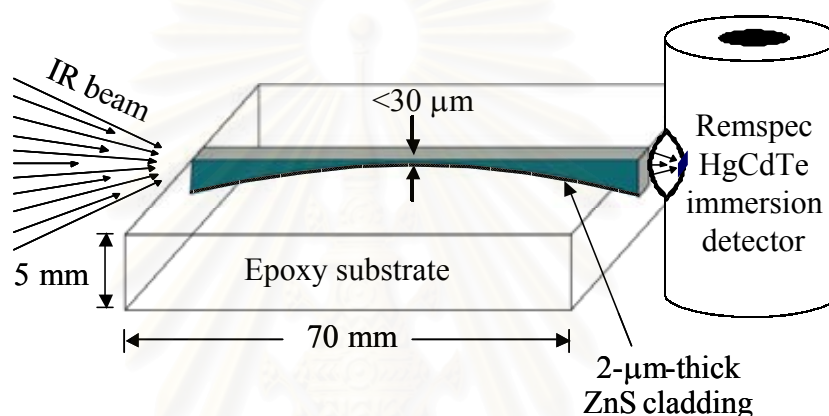


**Figure 3.5** Optical layout of a symmetrically tapered  $<30\text{-}\mu\text{m}$ -thick Ge waveguide with respect to IR source and detector. Incident light, indicated at left, is typically generated from a standard Global<sup>TM</sup> source of an FT-IR spectrometer, and the output is coupled onto a liquid-N<sub>2</sub>-cooled MCT immersion detector placed as close as possible to the exit end of the waveguide. The detector window, outside the lens, is not shown.

## 3.2 Potential Applications of the Tapered Quasi-Planar Ge Waveguides

### 3.2.1 Samples of Interest

1. Volatile solvents in analytical grade: methanol, ethanol, *i*-propanol, acetone, hexane, and double-distilled water
2. Non-volatile thin film: Nujol
3. D96N mutant of protein bR (D96N-bR) in the form of purple membranes
4. Single human hairs

### 3.2.2 Instruments for Data Acquisition

1. Bruker IFS66 FT-IR spectrometer equipped with a standard internal Global<sup>TM</sup> source
2. Out-of-Compartment Contact Sampler<sup>TM</sup> with 45° Ge Trough Plate Kit (Spectra-Tech, Shelton, CT, USA)
3. MCT immersion detectors with different active areas:
  - 3.1 Kolmar (internal) MCT detector with an active area 0.785 mm<sup>2</sup>, and a specified  $D^*$  value at 10 kHz of  $3.23 \times 10^{10}$  cm Hz<sup>1/2</sup> W<sup>-1</sup> (Model KMPV11-1-LJ2/239, Kolmar Technologies Inc., Conyers, GA)
  - 3.2 Remspec (portable) MCT detector with an active area of 0.50×0.50 mm<sup>2</sup> and a specified  $D^*$  value at 10 kHz of  $\geq 4 \times 10^{10}$  cm Hz<sup>1/2</sup> W<sup>-1</sup> (MOD-O2S1, Remspec Corp., Sturbridge, MA)
  - 3.3 Graseby MCT detector with an active area of 0.15 × 0.15 mm<sup>2</sup> and a specified  $D^*$  value at 10 kHz of  $\geq 4 \times 10^{10}$  cm Hz<sup>1/2</sup> W<sup>-1</sup> (FTIR-M 16-0.10, Graseby Infrared)
4. Single off-axis paraboloid mirror with 19.1-mm focal length (Melles Griot, Irvine, CA)
5. Shimadzu UV/Vis Spectrometer
6. Standard 150-Watt quartz-halogen fiber-optic illuminator (Model 180, Dolan-Jenner Industries Inc., Lawrence, MA)

### 3.2.3 Default Instrumental Parameters

#### Instrumental Setup

Source	Standard Global <sup>TM</sup>
Beam splitter	KBr
Detector	MCT

**Acquisition Parameters**

Spectral resolution	8 cm <sup>-1</sup>
Number of coadded scans	as mentioned in each figure
Signal gain	1
Spectral format	Absorbance

**Advanced Parameters**

Bandwidth	7800 cm <sup>-1</sup>
Mirror velocity*	3.164 cm s <sup>-1</sup>
Zero filling	2
Apodization	Blackman-Harris 3-Term
Phase correction	Mertz

\*giving optical retardation velocity (ORV) of 100 kHz for the HeNe reference beam.

**3.2.4 Experimental Procedure**

The ATR measurements obtained with the tapered Ge waveguides were compared with those obtained by using a commercially available macroscopic ATR accessory (Out-of-Compartment Contact Sampler<sup>TM</sup> with 45° Ge Trough Plate Kit). For experiments with the commercial ATR accessory, an internal (Kolmar) MCT detector was utilized, instead of the externally mountable (Remspec) one which was utilized with the tapered waveguides. In order to maximize absorption intensity, as well as to increase reproducibility, every sample applied onto the tapered waveguides must be carefully placed in contact with the sensing surface at the thinnest (center) point on the waveguide.

For purposes of spectral comparisons between waveguide and commercial ATR accessory, the same experimental parameters were utilized on a Bruker IFS66 FTIR spectrometer. Data collection was performed under Opus software with parameters mentioned above.

### 3.2.4.1 Preparation of D96N-bR Films for Light-Dark Experiments

The D96N mutant of bacteriorhodopsin (D96N-bR) was used in the form of purple membranes. The concentration measurement was acquired by UV-visible spectroscopy using the absorption intensity at 560 nm ( $\epsilon_{560} \approx 60,000 \text{ M}^{-1} \text{ cm}^{-1}$ ) as a reference peak. For the ATR-IR measurements, 1  $\mu\text{L}$  of unbuffered D96N-bR suspension with a protein concentration of 1.3 mg/mL was placed on the central 2–3 mm portion of the waveguide and completely air-dried for  $\sim 20$  min prior to pH adjustment. A droplet of 25 mM TRIS buffer at pH 9.5 was subsequently applied on the thin purple film and dried again. The sample preparation was the same for both the commercial ATR accessory and the 14- $\mu\text{m}$ -thick tapered Ge waveguide. Only the total volume of sample solution applied was different in each experiment.

Infrared spectra were collected with either the commercial ATR accessory or the 14- $\mu\text{m}$ -thick tapered Ge waveguide, always using the Bruker IFS66 FT-IR spectrometer. The D96N purple membrane film was illuminated with a standard 150-Watt quartz-halogen fiber-optic illuminator. The illumination and data collection were automatically controlled by rapid-scan time-resolved spectroscopy mode under Opus software. The loop started by taking a background spectrum in dark conditions for 30 s (= 192 scans), and then turning on the illuminator to expose the D96N purple membrane film to bright light for 20 s. A sample spectrum, representing D96N-bR in the so-called M state, was initiated  $\sim 1$  s after the lamp was turned off, and lasted for a duration of 10 s (= 64 scans), to complete one loop. The next loop was started after a 1-minute delay in order to let the sample relax back to the unphotolyzed state. Averaging many dark/light cycles was necessary to obtain an adequate SNR in the difference IR spectrum. After finishing all the loops, the alternately collected single-beam spectra of background (i.e., unphotolyzed bR state) and sample (i.e., photolyzed M state) were coadded separately. The final static FT-IR difference spectrum is the ratio of coadded sample and background spectra, converted to absorbance units.



### 3.3 Characterization of the Waveguides with Synchrotron IR Radiation

#### 3.3.1 Sample of Interest: Double-distilled water

#### 3.3.2 Instruments for Data Acquisition

1. FT-IR spectrometers:
  - 1.1 Bruker IFS66 FT-IR spectrometer
  - 1.2 Nicolet 860 FT-IR spectrometer
2. Remspec MCT detector with an active area of  $0.50 \times 0.50 \text{ mm}^2$  and a specified  $D^*$  value at 10 kHz of  $\geq 4 \times 10^{10} \text{ cm Hz}^{1/2} \text{ W}^{-1}$  (MOD-O2S1, Remspec Corp., Sturbridge, MA)
3. Single off-axis paraboloid mirror with 19.1-mm focal length (Melles Griot, Irvine, CA)

#### 3.3.3 Default Instrumental Parameters

##### Instrumental Setup

Source	Global <sup>TM</sup> / Synchrotron IR
Beam splitter	KBr
Detector	MCT

##### Acquisition Parameters

Spectral resolution	$8 \text{ cm}^{-1}$
Number of coadded scans	5-minute scans
Signal gain	1
Spectral format	Absorbance

##### Advanced Parameters

Bandwidth	$7800 \text{ cm}^{-1}$
Mirror velocity*	$3.164 \text{ cm s}^{-1}$
Zero filling	2

**Advanced Parameters (contd.)**

Apodization	Blackman-Harris 3-Term (Bruker) Happ-Genzel (Nicolet)
Phase correction	Mertz

\*giving optical retardation velocity (ORV) of 100 kHz for the HeNe reference beam.

**3.3.4 Experimental Procedure**

Two different FT-IR spectrometers equipped with different IR sources were employed for spectral collections with the same tapered Ge waveguide, in order to determine how the waveguide functions under different throughput conditions. The first was a Bruker IFS66 FT-IR spectrometer with the standard internal Globar™ source. The second was Nicolet 860 FT-IR spectrometer interfaced with a synchrotron light source (U2B Beamline at National Synchrotron Light Source, Brookhaven National Laboratory, Upton, NY). The latter spectrometer was additionally equipped with a standard internal Globar™ source that could be selected by switching a single computer-controlled mirror.

With both spectrometers, it was possible to configure the optical system to allow use of the tapered Ge waveguide either outside the spectrometer (i.e., via the external output port) or inside the main sample compartment as a traditional ATR accessory. In case of the out-of-compartment setup, the incident light exiting the external output port of the spectrometer was simply focused onto the entrance end of the waveguide, by using a single off-axis paraboloid mirror with 19.1-mm focal length. It should be noted that, in case of the in-compartment setup, use of a ZnSe lens for directly focusing the light onto the waveguide's input end helps us to simplify the optics but, on the other hand, results in substantial energy loss due to reflections from the high-index ZnSe lens surfaces. Alternatively, several mirrors could be utilized to function as a periscope inside the sample compartment of the spectrometer, in order to efficiently focus the light onto the input end of the waveguide.

With either in-compartment or out-of-compartment setup, a liquid-N<sub>2</sub>-cooled Remspec MCT immersion detector, with an active area of  $0.50 \times 0.50 \text{ mm}^2$ , was mounted with its window directly against the output end of the waveguide. For some experiments investigating mode-specific behavior, the Graseby MCT immersion detector, with an active area of  $0.15 \times 0.15 \text{ mm}^2$  and similar  $D^*$ , was utilized. The detector's angle was always fixed perpendicular to the top and side surfaces of the waveguide (i.e., its immersion lens optical axis was parallel to the waveguide axis), while its position was adjusted both horizontally and vertically to maximize the measured throughput of broadband IR light.

### 3.4 Ray-Tracing Calculations

#### 3.4.1 Software and Requirements

1. MATLAB<sup>®</sup> version 5.3.1 (The Mathworks Inc., Natick, MA)
2. Minimum system specifications
  - 2.1 Operating system: Microsoft Windows 95, Windows 98 (original and Second Edition), Windows Millennium Edition, Windows NT 4.0 or Windows 2000
  - 2.2 Processors: Pentium, Pentium Pro, Pentium II, Pentium III, Pentium IV or AMD Athlon-based personal computer
  - 2.3 RAM: 64 MB (minimum), 128 MB (recommended)
  - 2.4 Disk space: 340 MB (depending on size of partition and installation)

#### 3.4.2 Strategic Approach

A series of input rays impinging on the end of the waveguide through its entire length was traced. This required calculating many reflections (typically several hundreds) for each input ray. The analytical geometry required is rather simple, but solution of this type of problem (multiple internal reflections between a planar and cylinder surface) is not included in commercial ray-tracing programs. Therefore we wrote our own program using MATLAB<sup>®</sup>.

We simplified the problem by limiting ourselves to two dimensions. The trajectories of all incoming rays are assumed to be confined to a plane that is perpendicular to the waveguide's upper planar surface as well as to the (axis of) the lower cylinder surface. The traced rays that are restricted to this plane are then calculated as a series of reflections from a line and a circular arc. Each input ray, impinging on the end of the waveguide at angle  $\theta$  with respect to the waveguide axis and at a depth  $y$  below the planar surface, first has its refraction angle  $\theta'$  into the high-index waveguide calculated according to Snell's law (Eq. 2.1).

The program then propagates the ray (by setting the reflected angle equal to the incident angle at each internal reflection point) until it reaches the exit end of the waveguide, or else exceeds the critical angle for reflection from the upper or lower surfaces. The program reduces the problem to a very elementary treatment with ray optics, omitting features (such as the displacement of the reflected ray along the dielectric boundary) that have been shown to be required for a more accurate treatment of the ray-tracing problem for a multi-reflection waveguide.

The main output of the routine is the maximum sensing angle  $\varphi$  achieved inside the waveguide for each pair of input parameters ( $y$ ,  $\theta$ ). One of the additional inputs required for the program is a subroutine defining the height and slope of the lower curved surface as a function of horizontal distance from the center of the waveguide. In this study, this subroutine was set to define only a circular arc in order to compare results with those obtained by experiments, but it could alternatively be set to other functional forms of curve of interest. Almost any differentiable function gives accurate ray-trace calculations with the routines, as long as the function is sufficiently smooth (i.e., having no point with a radius of curvature less than  $\sim 2$  mm).

## CHAPTER IV

### RESULTS AND DISCUSSION

#### 4.1 Symmetrically Tapered <30- $\mu\text{m}$ -thick Quasi-Planar Ge Waveguides and Their Coupling Efficiency

As predicted by theory, the large differences in refractive indices enable the thin Ge layer ( $n_{\text{Ge}} = 4.0$ ), sandwiched between ZnS cladding ( $n_{\text{ZnS}} = 2.2$ ) and air ( $n_{\text{air}} = 1.0$ ) or sample (e.g. water,  $n_{\text{water}} = 1.34$ ), to serve as a waveguide for broadband MIR light. Previous theoretical calculations, based on a planar waveguide extending to infinity in two dimensions and with a finite thickness in the third, indicate that the highest absorbance sensitivities should be achieved from waveguides with a thickness in the range of 0.5–1  $\mu\text{m}$  [23]. Such waveguides are not yet realized due to the brittleness of Ge and other fabrication difficulties.

However, we have now successfully fabricated <30- $\mu\text{m}$ -thick symmetrically tapered Ge waveguides, which are the thinnest direct-coupled IREs demonstrated to date. These waveguides are designated as quasi-planar—more specifically, as cylinder-planar—because while one surface is planar, the other is ground and polished as a cylinder surface, resulting in a gradual, symmetrical taper away from the central minimum in thickness (see Figures 1.4 and 3.5). The fabrication and coupling methods differ somewhat from those described in our historical developments of thin Ge waveguides [24–28], in order to eliminate several difficulties. The particular advantages of the present quasi-planar waveguides can be categorized as follows.

- ✓ Using a waveguide with symmetrical tapering helps simplify the alignment of the beam and detector when using a direct coupling method, as illustrated in Figure 3.5.

- ✓ The taper yields sufficient throughput energy to come close to saturating a 0.25 mm<sup>2</sup> (Remspec) MCT immersion detector without requiring an IR microscope as a focusing optical element.
- ✓ The 1-mm<sup>2</sup> ends of the waveguide are large enough to make initial alignment by eye possible.
- ✓ The taper simultaneously keeps high the number of reflections in the middle sensing region, where the waveguide is thinnest, yielding an excellent improvement of surface sensitivity (*vide infra*).
- ✓ The flat and flush horizontal sensing area of the epoxide-embedded tapered waveguides results in easy sampling and cleaning.
- ✓ Completely embedding the Ge strip in the epoxide substrate, instead of cementing just one surface onto a quartz substrate as described previously [24–28], provides more mechanical support for the waveguide—it reduces the possibility of damage to the waveguide during grinding and polishing procedures.

Comparing to other kinds of miniature waveguides, there are three particularly novel aspects to our fabrication and use of the thin supported quasi-planar IR waveguides. First, we have generated the waveguides by mechanically whittling away at a macroscopic piece of highly transparent single-crystalline Ge, rather than by attempting either to deposit or to modify chemically a thin film of transmissive material. The latter are the most common approaches for producing thin-film waveguides, in part because they can more easily provide reproducible waveguide thicknesses than a subtractive hand grinding-polishing process such as which described herein. To our knowledge, sputtering was the only method used previously to fabricate thin-film Ge light guides for wavelengths in the range of 2–10 μm [44]. However, this approach resulted in a waveguide with a rather high attenuation of ~20 dB/cm, caused by scattering from the non-uniformly deposited Ge layer. Although it was possible to detect transmission of CO<sub>2</sub> laser light through such a waveguide, combining this sputtered thin-film Ge waveguide (i.e., on a CaF<sub>2</sub> substrate) to a broadband light source in practice failed to generate an observable transmission. This is most likely because of the much lower luminosity of the broadband light source, relative to the CO<sub>2</sub> laser.

A second innovation is that we have added a cladding for the waveguide's supported cylindrical surface, in the form of a rather thick vacuum-deposited layer of ZnS. This turns out to be a crucial for fabrication and use, because this cladding layer prevents the broadband IR light from being absorbed by the supporting epoxide substrate. A significant amount of light is thereby capable of propagating throughout the Ge strip, which is embedded in the epoxide resin.

The final novel aspect of our waveguides is the direct method operated to couple light into and out of the waveguide's ends. Such direct coupling is generally not performed for monochromatic (e.g., laser) light; prism or grating coupling schemes are instead ideal for coupling monochromatic light into waveguides. In contrast, our attempts to perform broadband IR spectroscopy utilized a single off-axis paraboloid mirror having a suitable focal length (i.e.,  $f = 19.1$  mm) to focus the collimated broadband light from a commercial FT-IR spectrometer along a horizontal optical axis, into the  $1\text{-mm}^2$  entrance aperture of the waveguide. In particular, alignment at the output end of the waveguide is greatly simplified by using a Remspec immersion detector that is composed of an IR-transmitting lens, having a relatively short focal length, in a direct contact to its active element. In most respects, this optical scheme is the useful means of coupling a broad bandwidth of light, which is similar to those of macroscopic IREs in EWS.

#### **4.1.1 Dependence of Total Throughput on Coupling Efficiency**

The evanescent-wave absorption properties of symmetrically tapered Ge waveguides were always investigated after careful optical alignments, to ensure an optimal coupling efficiency for individual experiments. In general, the coupling quality can be simply determined by measuring the transmitted intensity present in the collected single-beam spectrum. Although the coupling method is simple in description, adjusting the optics in practice is very delicate. A small shift in position of any component (e.g., paraboloid mirror, waveguide, or detector) may give rise to a drastic change in total energy throughput. To maximize all broadband IR light coming through the waveguide, the detector mount was positioned with the lens's optical axis along the waveguide, and the Dewar window in front of the lens within

~100  $\mu\text{m}$  of the output end of the waveguide. Continual careful adjustment of the overall optical alignment is required to ensure the optimal amount of output light, prior to repeated measurements.

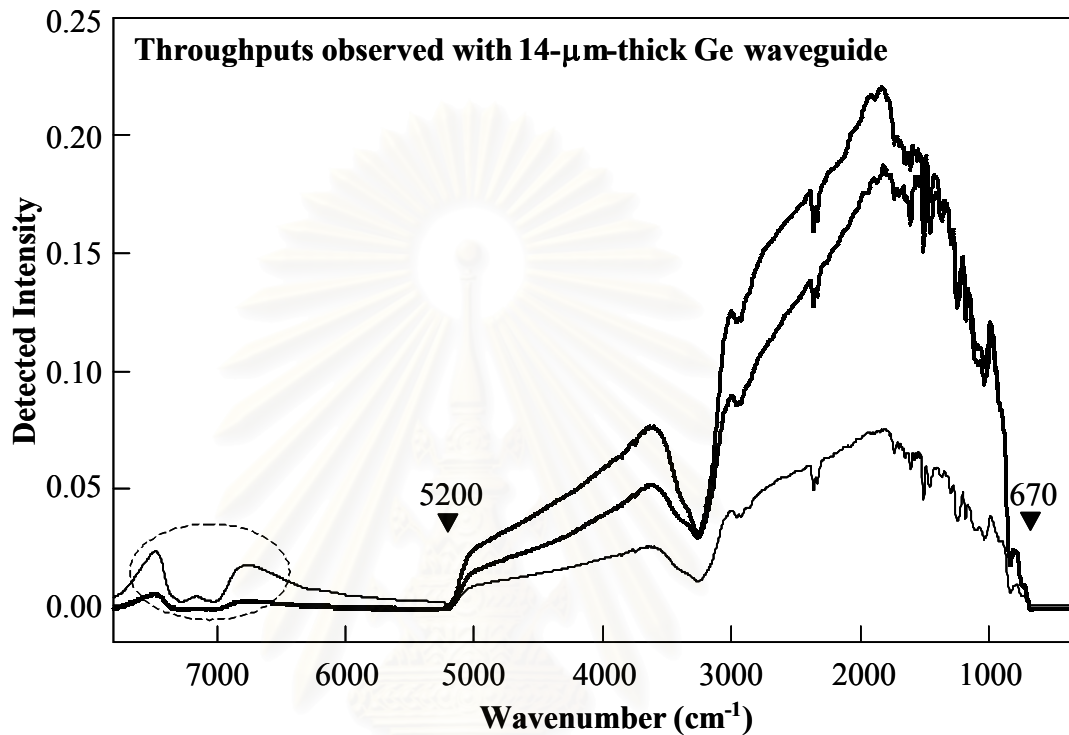


**Figure 4.1** FT-IR single-beam spectra observed during an alignment procedure of a symmetrically tapered 14- $\mu\text{m}$ -thick Ge waveguide. All spectra were collected with 1-minute scans. The y-axis scale stands for arbitrary intensity units, which are the same for all plots shown here.

Figure 4.1 shows levels of the throughput observed with a 14- $\mu\text{m}$ -thick waveguide, during adjustments of the optical alignment. Higher intensities represent a better coupling efficiency. As indicated by the circle, an unusual absorption in the spectral range of 6500–7700  $\text{cm}^{-1}$  is evident when the propagating beam leaks through the epoxide substrate by the lateral surfaces. This feature is commonly present in association with a substantial decrease in total intensity detected, indicating an insufficient coupling quality (see the thin line). Maximizing the optical throughput, along with a proper propagation of the light ray through the waveguide, is thus of crucial requirement to optimize the waveguide performance. It is



noteworthy that even after assuming a  $\sim 40\%$  reflection loss at the Ge/air interface, the transmitted light obtained with this waveguide configuration exhibits an exquisite increase in total transmission energy, which allows measurements with a satisfactory spectral SNR in a shorter length of time, as compared to those previously obtained in conjunction with an IR microscope [25–27].

In addition, the single-beam spectra reveal the characteristic frequency cut-offs of Ge at  $5200$  and  $670\text{ cm}^{-1}$ , indicating that light is genuinely guided through the thin Ge layer. The lower frequency cut-off demonstrates a benefit of using Ge waveguides. In contrast, there is a lack of transparency with silicon (Si) waveguides in the IR region  $1500\text{--}700\text{ cm}^{-1}$ , where there is rich spectral information for most organic compounds. The spectral feature centered at  $1550$  and  $3700\text{ cm}^{-1}$  obviously comes from gaseous water, while the narrow broken peak at  $2350\text{ cm}^{-1}$  is an absorption band caused by carbon dioxide.

#### 4.1.2 Variation of Waveguide Thickness

We subsequently analyzed the throughput as a function of decreasing waveguide thickness. Figure 4.2 displays several FT-IR single-beam spectra acquired from thin symmetrically tapered Ge waveguides with different thicknesses in the range of  $7\text{--}27\text{ }\mu\text{m}$ . As can clearly be seen, the observed throughput diminishes with decreasing thickness, due to cut-off of higher-order modes (i.e., modes propagating near to the critical angle) [39, 45–46]. The inset illustrates plots of the detected intensity at  $1850\text{ cm}^{-1}$  as a function of the waveguide thickness with a correlation coefficient of  $R^2 = 0.9999$  and  $0.9956$  for quadratic and linear relationships, respectively. Regarding the  $R^2$  value, the plot suggests a (almost) perfect fitting with the quadratic equation of  $y = -0.0002x^2 + 0.0292x - 0.1352$ .

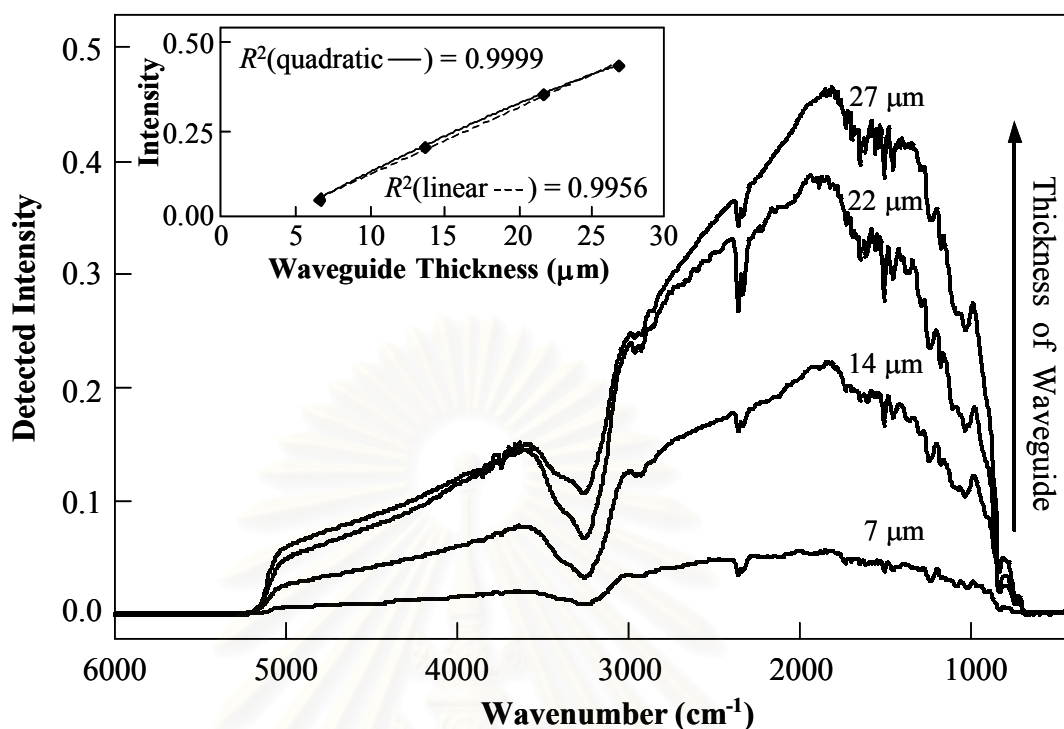


**Figure 4.2** FT-IR single-beam spectra of symmetrically tapered Ge waveguides with different thicknesses (i.e., 7, 14, 22, and 27  $\mu\text{m}$  from lower to upper lines, respectively). All spectra were collected with 1-minute scans and under identical conditions. The y-axis scale stands for arbitrary intensity units, which are the same for all plots shown here. **Inset:** Plot of the detected intensity at  $1850\text{ cm}^{-1}$  as a function of the waveguide thickness.

In order to investigate the effect of the tapered thickness on waveguide sensitivity, a 1-mm-diameter ( $= 1\ \mu\text{L}$ ) water droplet covering the  $1 \times 1\ \text{mm}^2$  sensing area was carefully sampled at the same (thinnest) part of each of several waveguides. Original single-beam sample spectra were converted to absorbances by ratioing to the corresponding background spectra shown in Figure 4.2 at the same thickness with the same experimental parameters. The resulting absorbance spectra are presented in Figure 4.3.

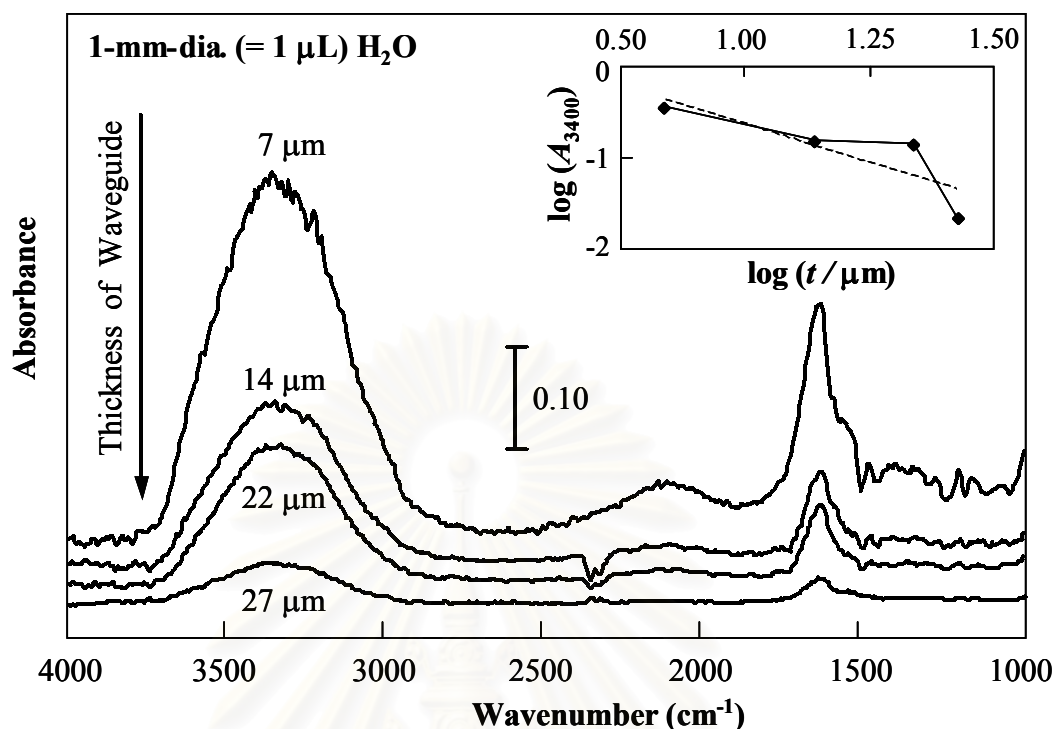


**Figure 4.3** ATR FT-IR Spectra of 1- $\mu\text{L}$  water droplet, covering an  $\sim 1 \text{ mm}^2$  sensing area, acquired by using symmetrically tapered Ge waveguides with different thicknesses (i.e., 7, 14, 22, and 27  $\mu\text{m}$  from upper to lower lines, respectively). **Inset:** Plot between the logarithm of the absorption intensity at 3400  $\text{cm}^{-1}$  ( $\log(A_{3400})$ ), due to the O-H stretching vibration, vs. the logarithm of waveguide thickness ( $\log(t)$ ).

It can be seen that the waveguide's sensitivity, in terms of absorbance for a particular small-area liquid sample, increases as waveguide thickness decreases. This enhanced sensitivity with decreasing thickness is due both to the increase in number of internal reflections per mm of waveguide length, and to the increase in the average evanescent-wave surface intensity of the transmitted modes. The inset of Figure 4.3 indicates a drastic increase in absorption intensity when the waveguide thickness is  $< 10 \mu\text{m}$ . On the other hand, a very thin waveguide (i.e.,  $< 10 \mu\text{m}$ ) results in distinctively lower total throughput (see Figure 4.2) and a noticeable increase in spectral noise level. To improve the spectral quality, a higher number of scans must be used.

### 4.1.3 Variations in Optical Coupling with Sample

#### 4.1.3.1 Sampling Length of the Sample

We additionally observed the dependence of absorption intensity on sampling length by varying the size of a water droplet placed on the central part of the sensing surface. A successive data collection was performed under identical conditions for both waveguides with different thicknesses. Figure 4.4 shows spectra with increasing the droplet size, observed for a 7- $\mu\text{m}$ -thick and a 27- $\mu\text{m}$ -thick waveguides. It should be noted that data plotted on each graph coincide with the value of absorption intensity at  $3400\text{ cm}^{-1}$  (i.e., O–H stretching vibration) appearing on each sub-figure.

With a planar waveguide, absorbance is expected to increase in direct proportion to sample contact length. With a tapered waveguide, on the other hand, the increase in absorbance as a function of contact length is expected to be sub-linear because the average number of reflections per unit length of sample contact decreases as sample is added to regions of the waveguide away from its central minimum. This was observed, as shown in the inset of Figure 4.4. Each plot of absorption intensity at  $3400\text{ cm}^{-1}$  ( $A_{3400}$ ) as a function of contact length ( $l$ ) was fitted to a quadratic relationship. The optimized quadratic coefficients gave  $A_{3400} = -0.0009l^2 + 0.0316l + 0.3218$  for the 7- $\mu\text{m}$ -thick waveguide and  $A_{3400} = -0.0001l^2 + 0.0073l + 0.0533$  for the 27- $\mu\text{m}$ -thick waveguide. The quadratic fit is good only up to  $\sim 2$  cm of contact length, after which point the absorbance approaches an asymptotic value monotonically. This observation elucidates that one advantage of using these  $<30\text{-}\mu\text{m}$ -thick tapered Ge waveguides is that only molecules in contact with the thinnest part of the waveguide significantly influence the absorbance spectrum.

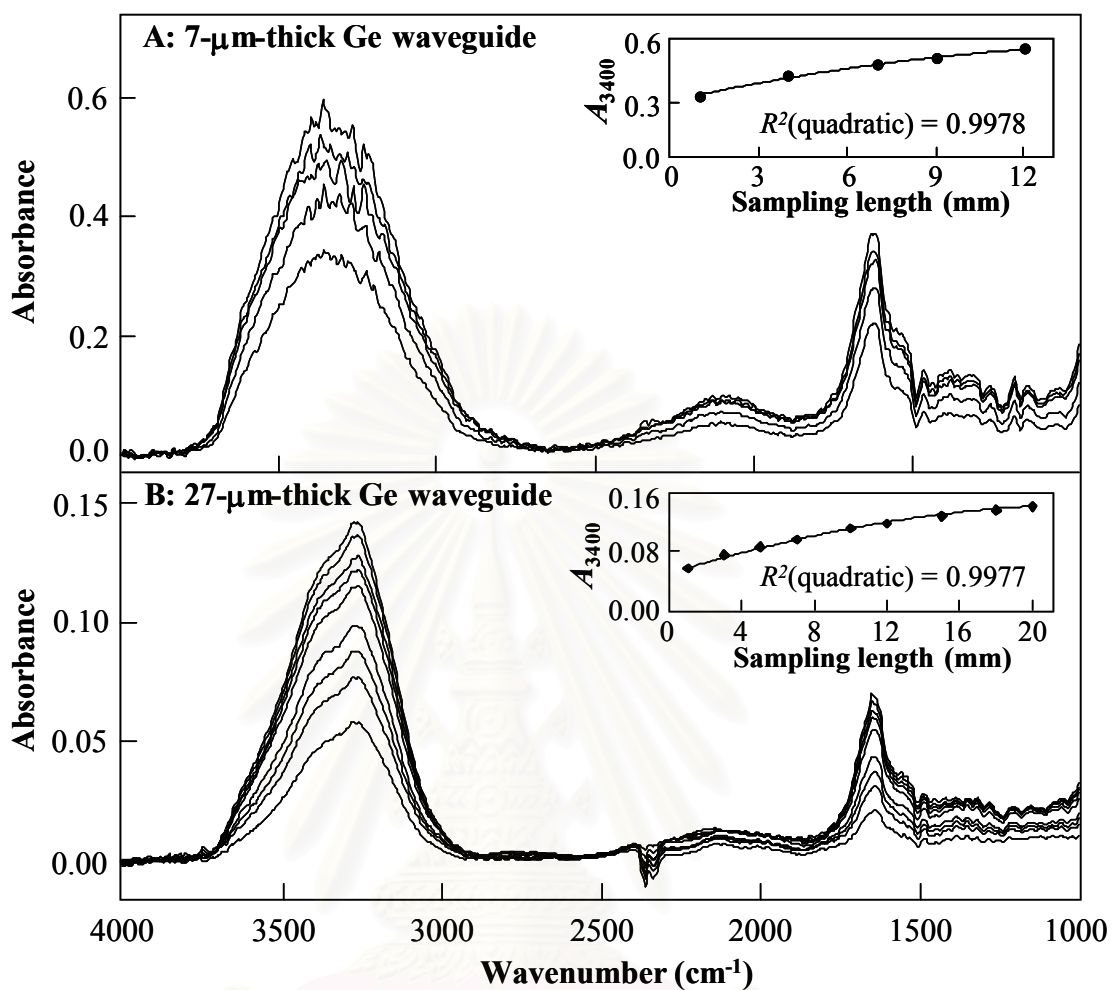


**Figure 4.4** ATR FT-IR Spectra of water droplets with different lengths contacting the sensing surface of the waveguide. (A) Spectra were obtained by using a 7- $\mu\text{m}$ -thick Ge waveguide, with sampling lengths of 1, 4, 7, 9, and 12 mm from lower to upper lines, respectively; (B) spectra acquired with 27- $\mu\text{m}$ -thick waveguide with sampling lengths of 1, 3, 5, 7, 10, 12, 15, 18, and 20 mm from lower to upper lines, respectively. All spectra were taken with 1-minute scans. **Insets:** Plot of the absorption intensity at  $3400\text{ cm}^{-1}$  ( $A_{3400}$ ), vs. the sampling length (mm) with a constant width of the waveguide (i.e., 1 mm), for different waveguide thicknesses.

#### 4.1.3.2 Quality of the Polished Sensing Surface

In an attempt to further improve the waveguide's sensitivity, we explored several additional variations in optical coupling through the waveguide and sample. Effect of the surface quality was also investigated by hand grinding/polishing rather than the machine polishing. Each spectrum in Figure 4.5 represents the same waveguide with progressively smaller particle sizes (i.e., 15, 3, and 0.1  $\mu\text{m}$  from lower to upper lines, respectively). All polishing compounds used are manufactured by Buehler Ltd., as described in Chapter 3 (Experimental Section).

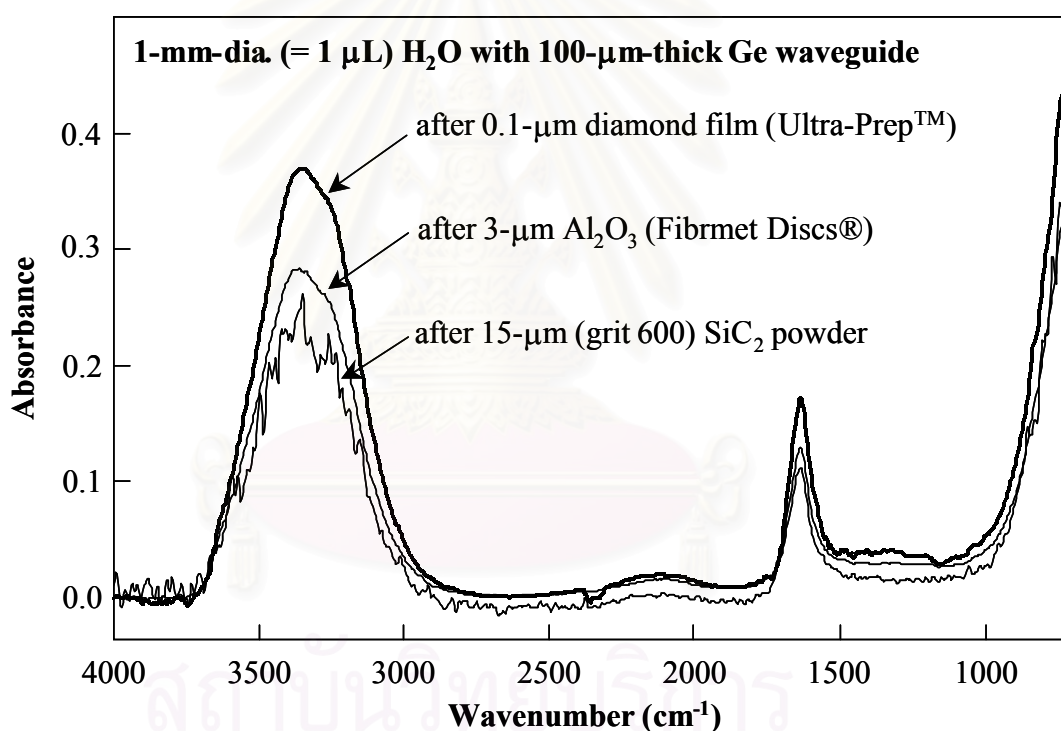


**Figure 4.5** Effect of the surface quality on absorbance spectral features observed from a 1-cm-diameter water droplet sample. These spectra were collected by using a 100- $\mu\text{m}$ -thick tapered Ge waveguide with  $45^\circ$  bevel angle at both ends with 1-minute scans.

As clearly seen in Figure 4.5, the overall spectral quality obtained from tapered Ge waveguides depends strongly on the quality of the polished sensing surfaces. A better optical-finished surface gives not only a higher absorbance

due to the better optical contact between sample and waveguide's surface. The spectral quality is also distinctively improved because of lower scattering losses caused by surface scratches, resulting in substantially greater throughput. Conclusively, the more thoroughly the surface was polished, the lower the spectral noise (and therefore the better the limit of detection) of the waveguide.

#### 4.1.3.3 Effects of Central Beam Blocking

Substantially greater detected absorption intensity can sometimes be achieved as a consequence of beam blocking of the on-axis waveguide modes. In this study, such an approach was demonstrated by using a ~6-mm-diameter aluminum rod held horizontally transverse to the IR beam where it fills an aperture of ~30 mm, in order to partially obstruct the beam. Light rays with low propagation angles (i.e., lower-order modes) in the vertical direction are thus blocked by the aluminum rod. At the selected distance from the waveguide, this rod eliminates rays that would enter the waveguide at an approximate angle of  $<17^\circ$  away from horizontal, relative to the waveguide axis.

Blocked-beam spectra shown in Figure 4.6 were recorded after the beam path was obstructed by the same rod, regardless of the waveguide thickness. With both waveguide thicknesses investigated, the spectra taken with the centrally blocked beam gave higher absorbance readings than those with an open beam, substantially so in the case of the 22- $\mu\text{m}$ -thick Ge waveguide. The increase in absorption intensity results from selection of the only higher-order modes (i.e., light propagating closer to the normal of the waveguide interface at the points of internal reflection). This is theoretically expected to increase (1) the average number of reflections per unit length; (2) the average evanescent field strength at the sensing area; and (3) the effective average penetration depth into the media beyond the interface.

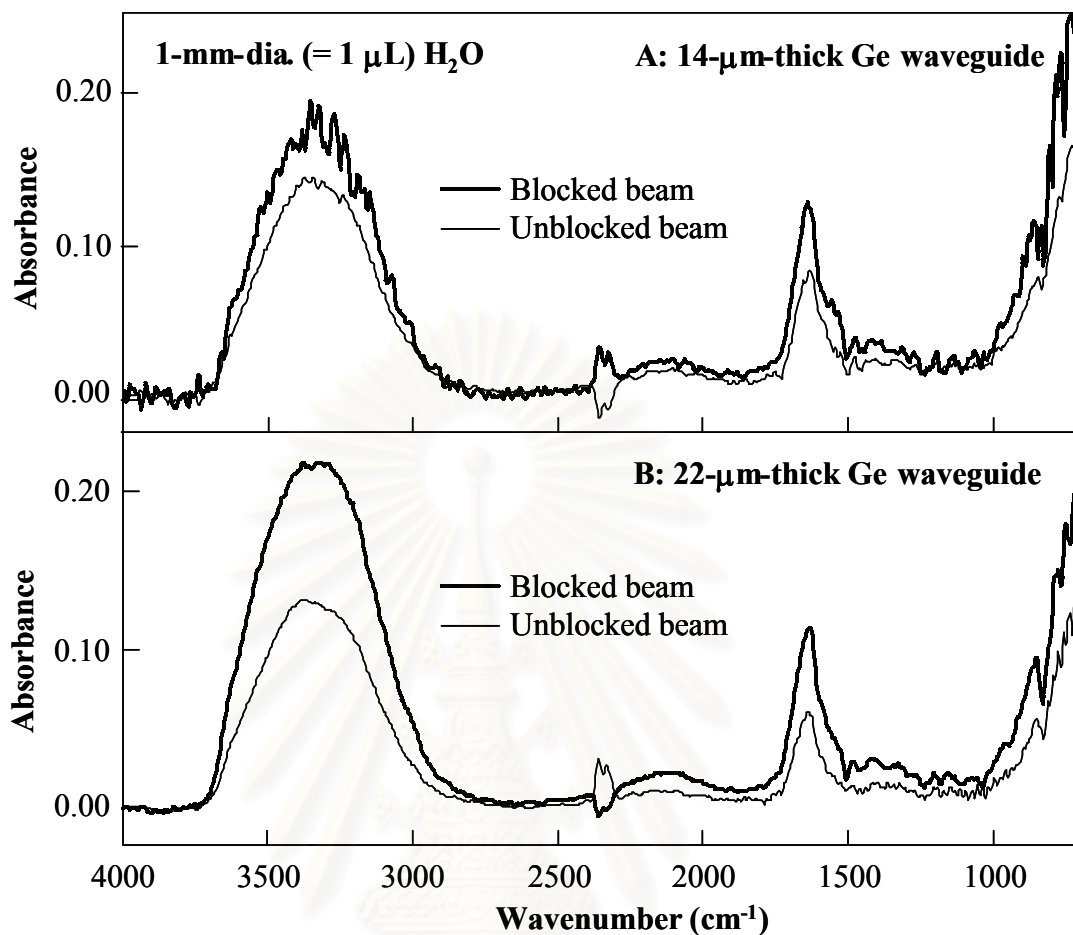


**Figure 4.6** Effect of central beam blocking on absorption intensity of 1-mm-diameter (= 1  $\mu\text{L}$ ) water droplet investigated by (A) 14- and (B) 22- $\mu\text{m}$ -thick Ge waveguides with 5-minute scans. Thick lines represent results with the blocked beam in comparison to those with unblocked one (thin lines).

The improvement in absorption intensity is nevertheless greater with the 22- $\mu\text{m}$ -thick waveguide than the 14- $\mu\text{m}$ -thick one. This is probably because the coupling efficiency of the highest-order modes to the detector is always decreased with the thinner waveguide, whether or not the central beam is blocked. This observation indicates that blocking even more of the central rays might further increase the absorbance enhancement factor, but it would likely give rise to a higher noise level due to the lower total throughput, particularly with thinner waveguides, as clearly seen by comparing the spectral quality in Figures 4.6 (A) and 4.6 (B).



#### 4.1.3.4 Effects of Detector Dimensions

There are a number of changes in optical coupling that are likely to afford substantial additional improvement in sensitivity, but that we have been unable to investigate so far. Ultimately, the most important of these is likely to be optimization of the detector dimensions. Using a MCT immersion detector with a smaller-area rectangular active element whose aspect ratio is more closely matched to the thinnest part of the waveguide is in theory expected to give somewhat better results than we have so far obtained. By limiting ourselves thus far to a square detector, we were faced with the tradeoff between going to the smallest possible detector, leading to an expected noise reduction in proportion to the square-root of the detector area (see Eq. 1.2 in Chapter 1); and keeping the output of the entire width of the waveguide imaged onto the detector, which is necessary for maintaining the largest response.

Accordingly, an alternative approach that we additionally investigated for improving the spectral SNR was to use a smaller-area detector, since the manufacturer's specifications sheet of the current (Remspec) detector indicated that the optical design of the  $(0.5\text{-mm})^2$  detector element was optimized for collecting light from the output of an optical fiber somewhat larger than  $1\text{ mm}^2$ . Therefore the same experimental procedure was carried out with the Graseby MCT detector, equipped with a  $(0.15\text{-mm})^2$  detector element and the same immersion lens as the former detector. Results obtained for both detectors are demonstrated in Figure 4.7 under the same scale for a comparison purpose.

The observation shows that use of a smaller (Graseby) MCT detector failed to produce absorbance spectra with a higher SNR. Furthermore, the use of this detector resulted in the observation of a stronger periodic oscillation pattern on the spectrum as compared to the larger immersion detector (i.e., Remspec). This oscillatory interference pattern is similar to what was observed for the synchrotron-generated spectra (*vide infra*). From these observations, we conclude that the smaller detector area results in detection of only a selected portion of the IR throughput of the waveguide. The smaller detector appears to

be functioning as a spatial filter, selectively observing a limited range of the optical modes that are transmitted through the waveguide. The particular vertical alignment of the detector determines which modes are detected.

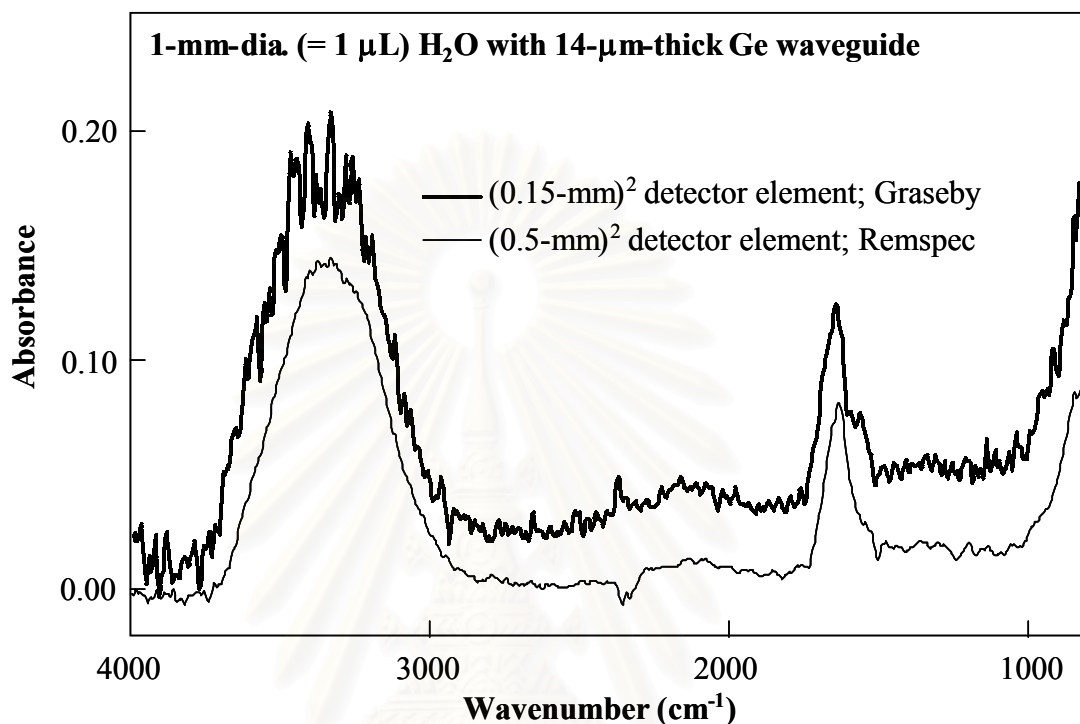


**Figure 4.7** Effect of size of the detector element on spectral SNR measured from a 1-mm-diameter (= 1  $\mu$ L) water droplet. Both spectra were collected by using 5-minute scans with a 14- $\mu$ m-thick Ge waveguide, but with different lensed detectors carrying MCT active elements either 0.50 or 0.15 mm on a side, as indicated.

สถาบันวิทยบริการ  
จุฬาลงกรณ์มหาวิทยาลัย

## 4.2 Applications and Comparisons with a Commercial Ge ATR Accessory

To evaluate the sensitivity improvement achieved by use of the tapered Ge waveguides, a commercial macroscopic ATR accessory, i.e., (\*) Out-of-Compartment Contact Sampler<sup>TM</sup> with 45° Ge Trough Plate Kit, was employed for comparison purposes. In case of the tapered waveguide, every sample used in this study was carefully applied at the central part of its sensing surface to ensure the maximum sensitivity and reproducibility.

### 4.2.1 Small Volumes of Volatile Solvents

Figure 4.8 is the evanescent-wave IR spectra of a 1-mm-diameter (= 1  $\mu$ L) water droplet in contact with a 14- $\mu$ m-thick tapered Ge waveguide, compared to that observed with a macroscopic ATR accessory shown in the same figure. The sample covered the sensing surface with a total area of 1 mm<sup>2</sup>.

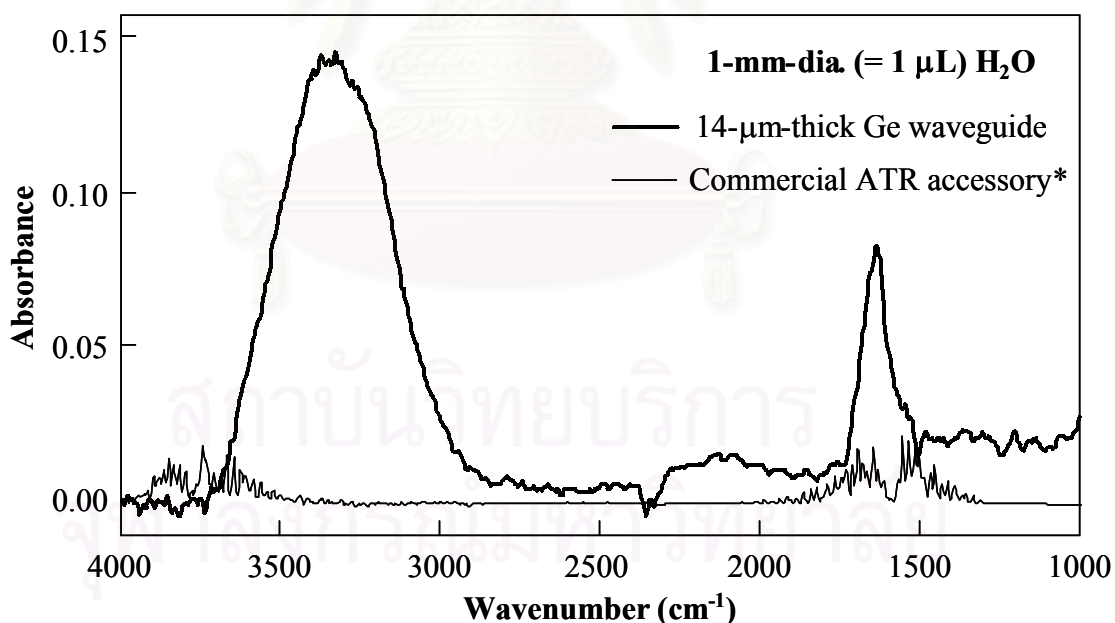


**Figure 4.8** Comparison of absorption intensities of 1-mm-diameter (= 1  $\mu$ L) water droplet observed by 14- $\mu$ m-thick tapered Ge waveguide to that with a commercial macroscopic ATR accessory. Both spectra represent 5-minute scan times.

By comparison, the absorption intensity of the O–H vibration at  $3400\text{ cm}^{-1}$  acquired with the thin tapered waveguide is enhanced by a factor of  $>50$  folds, due to the increase in total internal reflections achieved by tapering method. Thus, small volumes of volatile solvents such as water that cannot easily be spread out in a thin film on a macroscopic ATR prism can still be sampled using the waveguide.

Accordingly, volatile organic solvents are particularly applicable samples for the thin tapered waveguides. Figure 4.9 sequentially demonstrates a variety of volatile organic solvents investigated by a  $14\text{-}\mu\text{m}$ -thick tapered Ge waveguide, with only a few  $\mu\text{L}$  sample volume applied. Although these solvents by nature evaporate rapidly at room temperature, the characteristic features of individual solvents can be readily distinguishable using the waveguides with 64 scans only (i.e.,  $\sim 50\text{ s}$ ). In contrast, with similarly small samples of these volatile samples the macroscopic Ge ATR accessory does not afford any spectral information, other than from the water vapor contaminant at  $\sim 1550$  and  $\sim 3700\text{ cm}^{-1}$ , which is similar to that shown in Figure 4.8. Because of their rapid evaporation that can be completed within less than a minute, an optimum scanning time must be found that represents a compromise between the increased SNR and the loss of sample that both occur with longer measurement times. Nevertheless, these spectra perceptibly demonstrate the convenience, speed, and sensitivity of such thin tapered waveguides for obtaining spectra of microvolumes of volatile organic liquids.

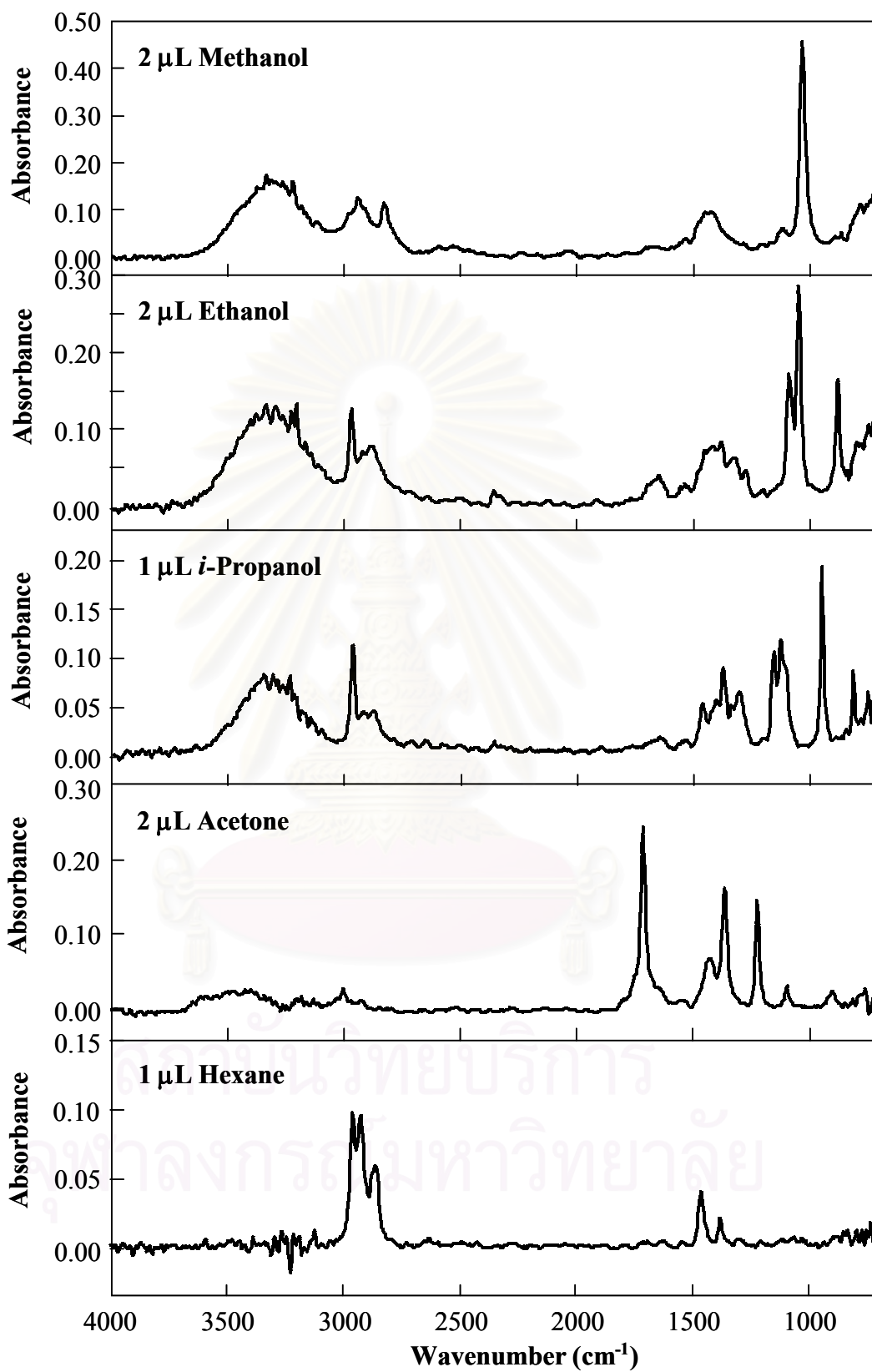


**Figure 4.9** ATR FT-IR spectra of some volatile solvents in a few  $\mu\text{L}$  of applied volume. Data were acquired by a 14- $\mu\text{m}$ -thick tapered Ge waveguide with 64 scans.

#### 4.2.2 Small Quantities of Non-Volatile Thin Films

Figure 4.10 shows spectral results of 850 and 85 ng Nujol deposited as thin films from hexane solution onto the sensing surfaces of either the commercial ATR accessory or the 14- $\mu\text{m}$ -thick tapered Ge waveguide. The spectra were recorded  $>1$  h after the hexane was visibly evaporated and the films were left exposed to room air.

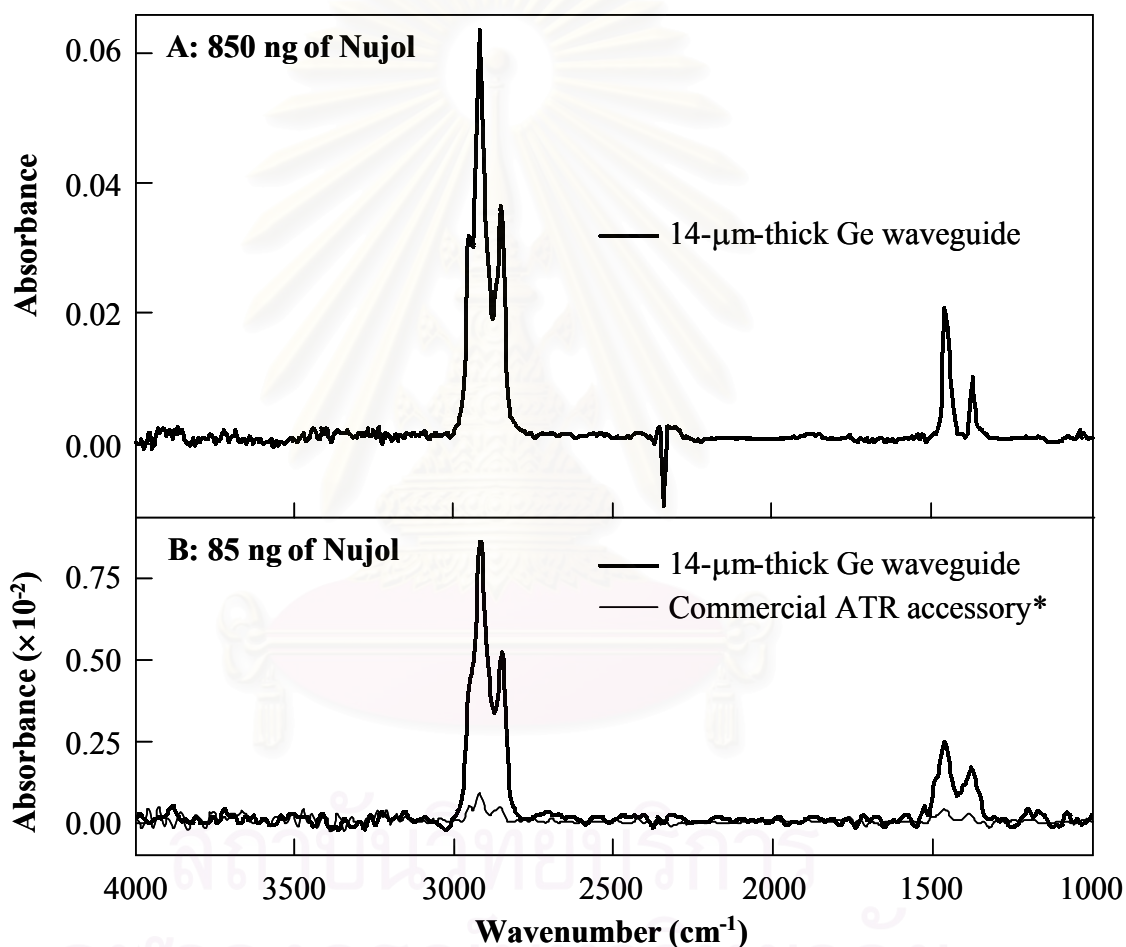


**Figure 4.10** ATR FT-IR spectra of Nujol thin films with different quantities deposited on the sensing surface, i.e., (A) 850 ng and (B) 85 ng. The thick lines represent the results observed by a 14- $\mu\text{m}$ -thick tapered Ge waveguide, while the thin one was collected with the commercial ATR accessory. All spectra were taken after hexane was completely evaporated, and with 5-minute scan times.

Once again, the 14- $\mu\text{m}$ -thick tapered Ge waveguide exhibits substantially higher sensitivity than the commercial ATR accessory. The relative absorbance factor observed at  $2922\text{ cm}^{-1}$  was 13.6 for the 85-ng Nujol sample. This clearly demonstrates the advantage of the thin tapered waveguides for measuring sample-limited thin films. With the traditional Ge ATR accessory, the 85 ng sample size gives absorbance signals that are barely above the noise with a 5-minute scan time, whereas with our thin tapered waveguides the SNR of the strongest bands in the absorbance spectrum substantially exceeds 20. Characteristic peaks of Nujol can therefore be easily identified. The estimated detection limit with a 5-minute scan time is 85 ng Nujol deposited on the waveguide's sensing surface. This is of course substantially higher than the detection limit for a droplet of pure Nujol measured in transmission mode by a microscope. Nevertheless, for small quantities of poorly-soluble samples that can only be deposited uniformly as films under  $\sim 1\text{ }\mu\text{m}$  in thickness, the miniature waveguide is likely to afford a superior sampling method.

#### **4.2.3 Light-Dark Difference Spectra of Biological Film Samples**

FT-IR spectroscopy is particularly well suited for studying biological membranes, which are often not amenable to study with other currently available techniques. Even for proteins with known atomic-resolution structures, FT-IR difference spectroscopy can provide useful information about changes in the local environment for chemical groups that would not likely be detected by crystallographic techniques. Much FT-IR work on membrane proteins has involved difference spectroscopy, since the absorptions of the numerous residues within even a moderately sized protein are rarely resolved from one another in the unsubtracted IR absorption spectrum. However, careful FT-IR difference spectroscopy can resolve individual vibrational bands, which correspond to structural changes occurring in the parts of a protein that are directly involved in its physical function.

Bacteriorhodopsin (bR) is a transmembrane protein complex that functions as a light-driven proton pump in the plasma membrane of the archaebacterium *Halobacterium salinarium*. The photocycle of bR is in nature initiated by absorption of a photon, producing a proton transfer from the inner side of the cell membrane to the outer medium. This process subsequently induces a sequence of transitions, which can be distinguished by means of transient changes in vibrational difference bands [47–49]. In this study, the D96N-bR in the form of purple membranes was chosen as a model sample for studying the triggered structural change of the protein conformation. This mutant was selected because it has a greatly slowed photocycle when dried from a buffer at an elevated pH, permitting light-dark difference measurements at room temperature simply by using a fiber-optic illuminator.

With our experimental design described in Chapter 2 (Experimental Section), a thin tapered Ge waveguide is able to detect the structural conformation of the purple transmembrane protein of D96N-bR, in the form of a dried film, covering only 1 mm<sup>2</sup> on the thinnest middle part of its sensing surface. Figure 4.11A clearly presents the strong bands centered at 1650, 1550 and 1160 cm<sup>-1</sup>, which are assigned to the respective amide (I), amide (II), and amide (III) vibrations of the predominantly  $\alpha$ -helical peptide backbone in the purple membrane of D96N-bR. As expected, these characteristic spectral features of the peptide backbone can be detected by using a 14- $\mu$ m-thick waveguide with just 1.25 pmol (37.5 ng) of protein sample.

Light-dark difference measurements on D96N-bR require somewhat larger samples (50 pmol bR) deposited as a thin film on a 14- $\mu$ m-thick waveguide. However, this amount is 3000 times less than the  $1.5 \times 10^5$  pmol of D96N-bR required for similar light-dark difference measurements using a macroscopic Ge ATR accessory. The light-dark difference spectrum obtained with a 14- $\mu$ m-thick waveguide (Figure 4.11B) is ultimately very similar to that observed for a much larger sample with a macroscopic ATR accessory (Figure 4.11C), supporting the reliability of spectral changes detected by the waveguide. Note that a poor SNR of the final averaged difference spectrum, due to a small quantity of protein sample, can be improved by increasing the number of data sets used in the averaging process.



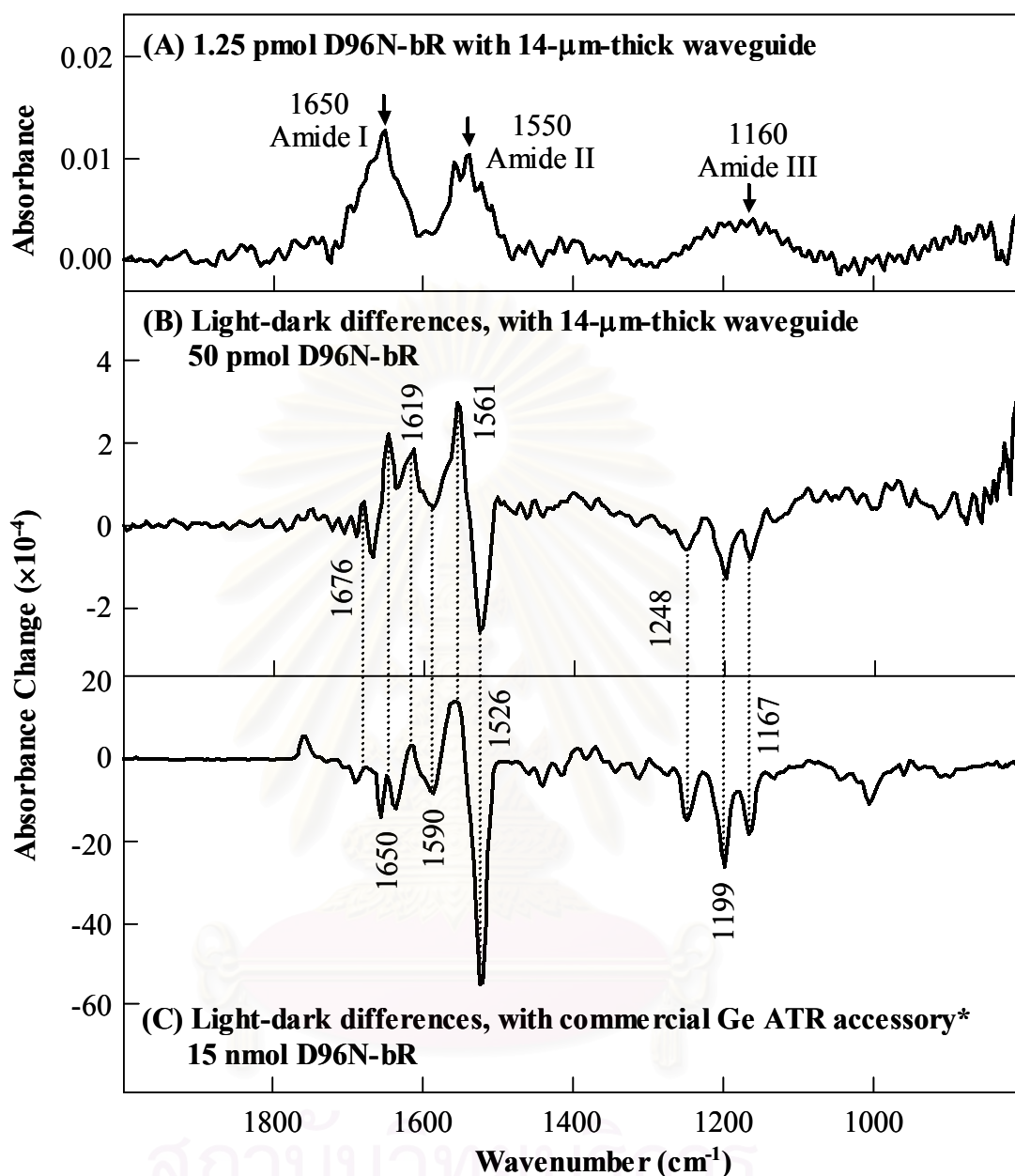


**Figure 4.11** (A) ATR FT-IR spectrum of D96N-bR film with a total amount of 1.25 pmol (37.5 ng) of protein. The spectrum was acquired with a 14- $\mu\text{m}$ -thick tapered Ge waveguide with 5-minute scan times. (B,C) ATR FT-IR difference spectra of D96N-bR using light-dark subtraction at room temperature (25°C): (B) 128 averaged data sets, total measurement time  $\sim 4$  h, using 14- $\mu\text{m}$ -thick tapered Ge waveguide and 50 pmol protein; (C) 64 averaged data sets, total measurement time  $\sim 2$  h, using the commercial ATR accessory and 15 nmol protein.

#### 4.2.4 Hair analysis

Vibrational spectroscopy is a crucial tool in hair analysis since the structure and chemical composition of hairs are the main focus for numerous fields of research and development. Due to their relatively small size (i.e., 50–100  $\mu\text{m}$  in diameter), single human hairs represent a challenging type of IR sample that has been investigated mainly with ATR and FT-IR microspectroscopic techniques [50–51]. On the other hand, we performed the single-hair analysis simply by uses of the thin tapered waveguide, with no sample preparation required.

In our measurements, a single hair obtained from either an African-West Indian female or a Caucasian male was squeezed against the center of the waveguide sensing area with a ratcheting micrometer, in order to obtain reproducible sample contact. Typical results are shown in Figure 4.12. Each spectrum observed shows a broad band at  $3250\text{ cm}^{-1}$  attributable to water absorption. The predominant absorption bands centered at  $1650$  and  $1550\text{ cm}^{-1}$  on both single-hair spectra in the figure arise from amide (I) and amide (II) vibrations, respectively. The amide (I) band is particularly diagnostic for secondary structure, and in this case is at a wavenumber characteristic of the known  $\alpha$ -helical structure of hair keratin [50].

By comparing the spectra of each individual's hair with pure samples of the respective styling gels each had applied several hours previously, it is clearly seen that even a tiny amount of chemicals deposited on a 2-mm length of hair surface can be detected. In each case, there are several peaks on the measured hair spectrum corresponding to the strongest bands in the spectrum of the corresponding pure styling gel. This indicates the potential utility of the  $<30\text{-}\mu\text{m}$ -thick tapered waveguides as a new tool for forensic analysis.

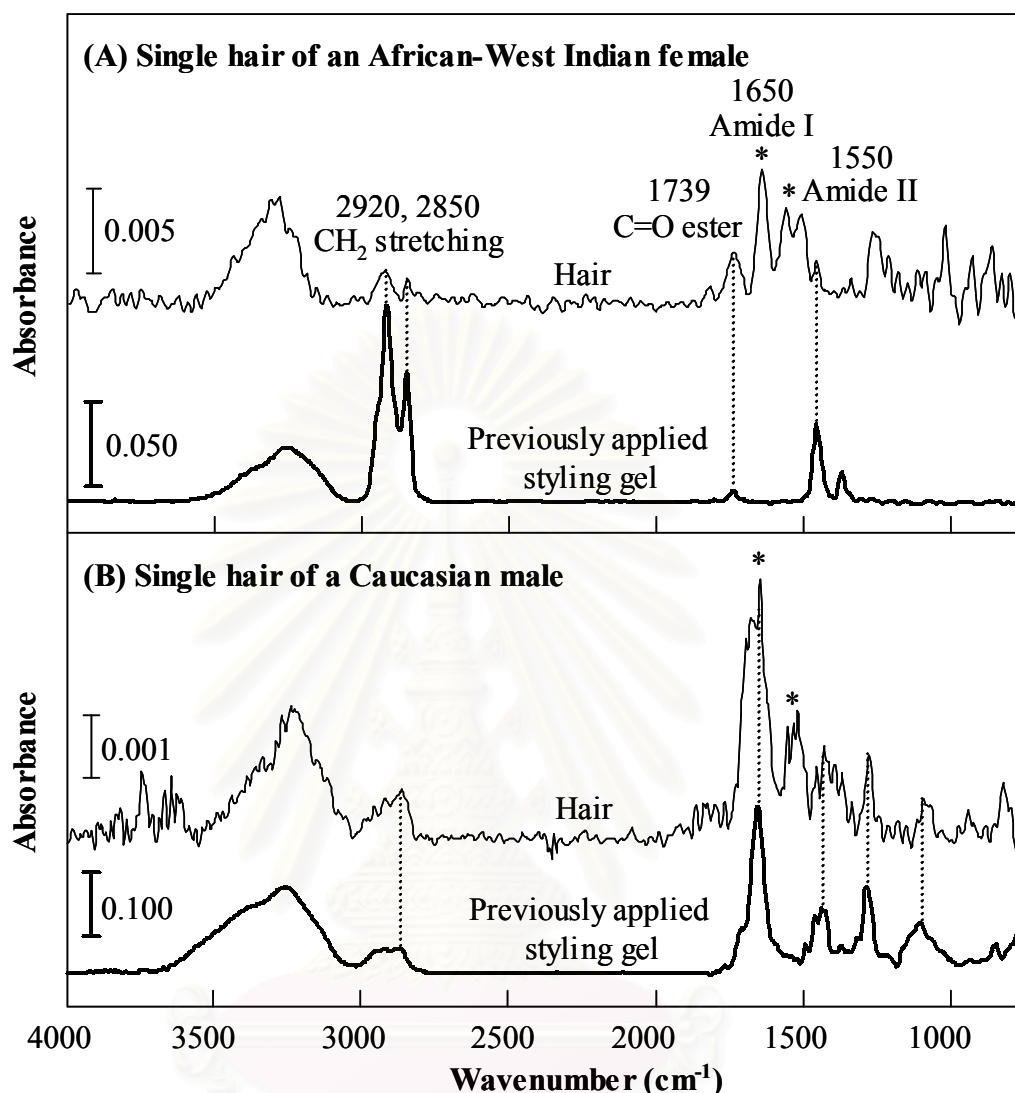


**Figure 4.12** Baseline-corrected ATR FT-IR spectra of single hairs (upper thin line) taken from two different people: (A) an African-West Indian female, and (B) a Caucasian male. The lower (thick line) spectrum in each sub-figure represents the styling gel applied earlier in the day by each person (i.e., Magnificent<sup>®</sup> Hair Food manufactured by Magnificent Products Division, Memphis, TN, for donor A; and Aussie Mega Styling Gel<sup>®</sup> manufactured by Redmond Products, Inc. Dist., Stamford, CT, for donor B). Films were dried ~1 h prior to spectral measurement. All spectra were acquired with a 14- $\mu\text{m}$ -thick tapered Ge waveguide with 5-minute scans.

### 4.3 Ray-Tracing Calculations of Supported Ge Waveguides

Regarding the overall observations reported above, we have successfully accomplished a substantial improvement in sensitivity achieved by symmetrically tapering Ge waveguide evanescent-wave sensors and decreasing their central thickness to 7–15  $\mu\text{m}$  [33]. Absorption intensities of spectra acquired with thinner waveguides are enhanced as an inverse function of the waveguide thickness raised to a power greater than 1, due to increases both in the number of internal reflections per unit length and in the amount of electromagnetic energy contained within the evanescent wave at each reflection. Tapering also simplifies the optical alignment since only common focusing optics (i.e., off-axis paraboloid mirrors) are needed. As a consequence, spectral absorption measurements on even tiny (nanogram) samples are simple and quick.

Nevertheless, the absorption intensities observed corresponded only to those expected for 3–5 reflections, rather than >25 reflections expected for a 20- $\mu\text{m}$ -thick waveguide with an average internal propagation angle of  $45^\circ$  and a sensing length of  $\sim 1\text{--}2$  mm. Furthermore, these thin tapered Ge waveguides have in practice not afforded as high spectral SNR in observed broadband FT-IR spectra as was predicted theoretically by using standard approximations and simplifying assumptions in order to predict the range of modes that would be excited [23]. In an attempt to evaluate how light focused onto the end of the waveguide is coupled into modes with varying propagation angles, we have now performed both ray-tracing calculations and measurements at selected angles using the highly-collimated broadband light available from a synchrotron IR radiation to carry out mode-specific measurements [52]. Reasons for the discrepancy between the theoretical and observed performances have thus been investigated in more detail towards results obtained with both the calculations and experimental investigations.

#### 4.3.1 Ray Tracing of Cylinder-Planar Waveguides

A series of input rays impinging onto the waveguide's end face were traced by using the program written in MATLAB<sup>®</sup> (see Appendix C for the program routines).

A typical traced ray is shown in Figure 4.13 for a cylinder-planar Ge waveguide with a total length  $L$  of 70, an entrance/exit height ratio of 1 (i.e., symmetrical tapering), and a minimum thickness  $t$  of 0.010 (i.e., 10  $\mu\text{m}$ ). This corresponds to a circular radius  $R$  of 300. These dimensions (assuming units of mm) match quite closely to those of the physically realized waveguides we have utilized for evanescent-wave sensing measurements. Note that the vertical scale in Figure 4.13 is greatly exaggerated relative to the horizontal scale. This creates the illusion that wherever the curved waveguide surface is sloped (i.e., non-horizontal), the incident and reflection angles are unequal.

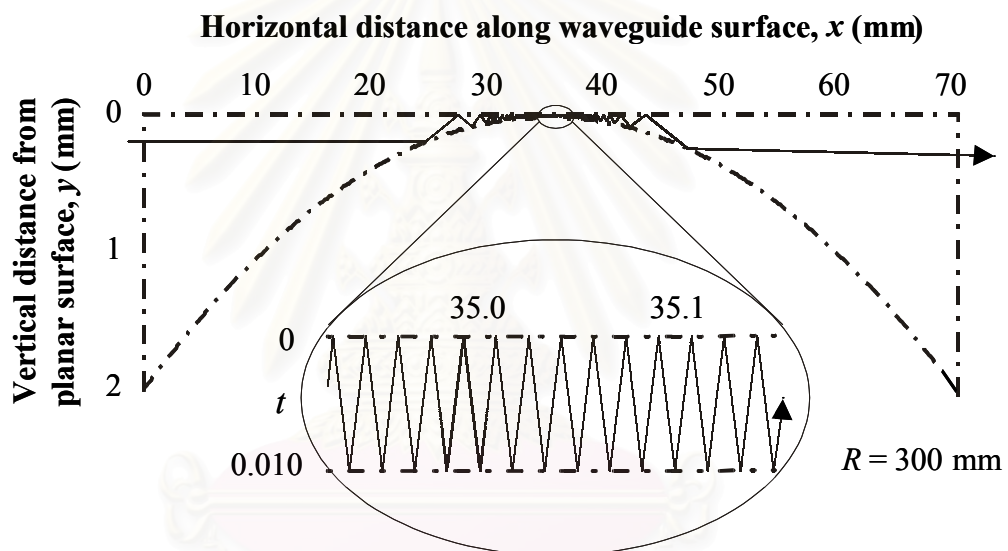
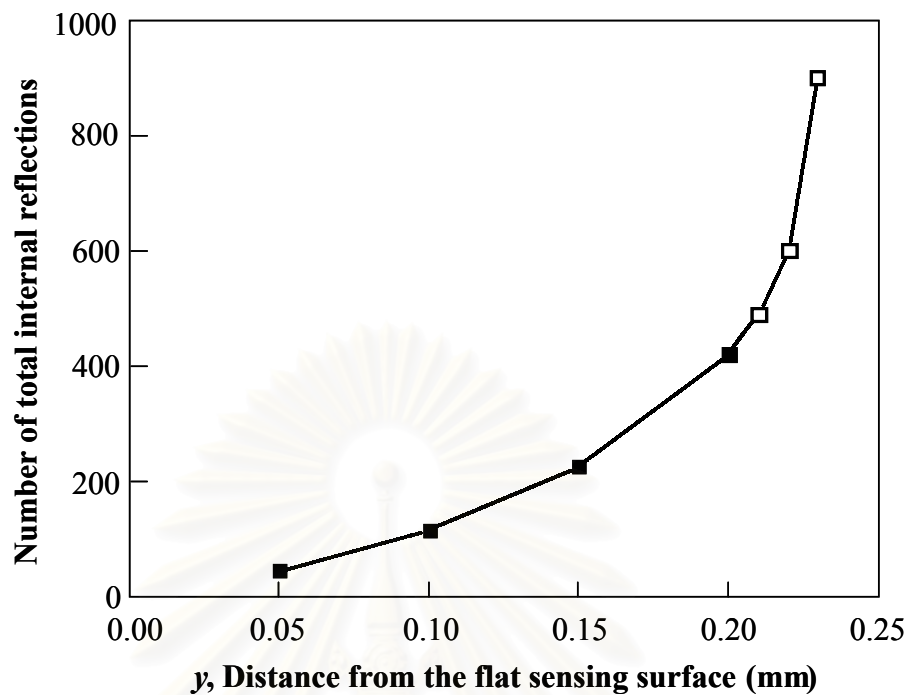


**Figure 4.13** Typical calculated reflection pattern of a light ray propagating through a symmetrically tapered cylinder-planar waveguide with a total length  $L$  of 70 mm, a circular radius  $R$  of 300 mm for the cylinder surface, and a minimum thickness  $t$  of 10  $\mu\text{m}$ . Note that the exaggerated vertical scale in both the main figure and the inset results in distorted apparent reflection angles.

As shown in Figure 4.13, this particular ray was assumed to impinge perpendicular onto the waveguide's  $\sim 2$ -mm-high entrance face ( $\theta = 0^\circ$ ), at a distance  $y$  of 0.20 mm from the flat surface. Near the center of the waveguide, the particular ray propagates very close to the critical off-axis angle of  $\phi = 56.6^\circ$  for propagation of light through a ZnS-clad Ge waveguide, ( $n_{21} = 2.2/4.0$ ), indicating total internal

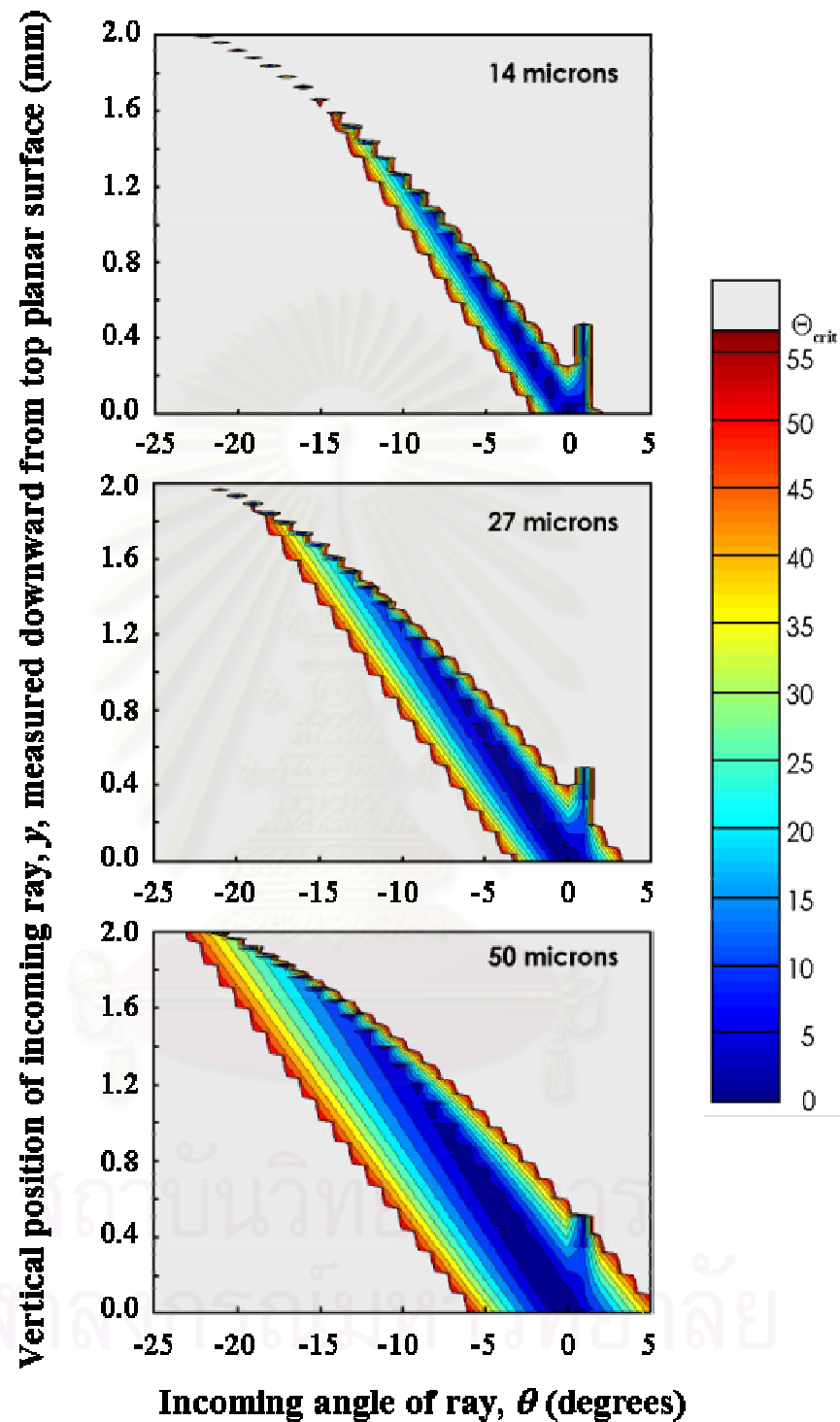
reflection at the Ge-ZnS interface. For this critical ray, there are a very large number of internal reflections (133 per mm of travel; 67 per mm for only the sensing surface) at the thinnest central sensing region, as shown in the expansion (inset) of the centermost 0.10 mm of the waveguide. At  $x = 0$  (i.e., the entrance end of the waveguide), this ray has a  $y$  value of 0.20 mm and an initial angle inside the waveguide of  $\theta' = 0^\circ$ . Using Snell's law ( $n_{\text{Ge}} \sin\theta' = n_{\text{air}} \sin\theta$ ), this also corresponds to an impinging angle of  $\theta = 0^\circ$  (i.e., perpendicular to the entrance face) for the ray propagating in air prior to entering the waveguide. Generally speaking, the calculated reflection patterns schematically illustrate that off-axis light rays entering the waveguide at left undergo multiple internal reflections at successively steeper angles due to the convergent taper. The maximum angle  $\varphi$  (with respect to the waveguide axis) is reached at the thinnest central part of the tapered waveguide. In principle, this maximum angle  $\varphi$  largely defines the sensitivity of the measuring light to evanescent-wave absorption by materials in contact with the upper sensing surface of the waveguide, since most internal reflections occur where the propagation angle is greatest.

Figure 4.14 shows the variation of number of total internal reflections within the 0.010-mm-thick cylinder-planar waveguide as a function of  $y$ , holding the impinging angle  $\theta$  constant at  $0^\circ$ . As clearly seen, there is a substantial increase in number of total internal reflections as  $y$  is increased. However, propagation via total internal reflection is allowed only for  $y \leq 0.20$  mm, i.e., only for rays entering the waveguide along the 10% of its entrance face closest to the planar surface. For an on-axis ray entering farther than this from the waveguide's flat sensing surface (i.e.,  $y > 0.20$  mm, as indicated by  $\square$ ), the propagation angle exceeds the critical angle for a Ge-ZnS interface before the ray reaches the center of the waveguide. As a consequence, for  $\theta = 0^\circ$ , only light rays entering within 0.20 mm of the flat surface contribute to the detected light. At this  $y$  value, the number of total internal reflections in the model waveguide described is  $\sim 400$ , and this turns out to be (approximately) the maximum number of internal reflections allowed for this tapered waveguide at any combination of  $y$  and  $\theta$ .



**Figure 4.14** Plot of the calculated number of total internal reflections vs. vertical distance ( $y$ ) of the impinging ray from the upper planar surface of a 70-mm-long, symmetrically-tapered, cylinder-planar waveguide with a minimum thickness of 10  $\mu\text{m}$ . The light rays are assumed to enter the waveguide on-axis ( $\theta = 0^\circ$ ).

By calculating ray-traces such as those in Figure 4.13 while varying both  $\theta$  and  $y$ , it was possible to determine all possible combinations of these two parameters for which light can propagate through a particular waveguide. As mentioned previously, the sensing angle  $\varphi$ , defined as the maximum angle that the ray makes with respect to the planar surface of the waveguide at the thinnest (sensing) portion of the waveguide, is the crucial indicator for the sensitivity of an incoming ray (in terms of evanescent-wave absorption). Therefore, the ray-trace program was also instructed to provide the sensing angle  $\varphi(\theta, y)$  for each of the allowed rays. These results are schematically demonstrated in Figure 4.15 for various central thicknesses of cylinder-planar waveguide (including several that match those used in experimental measurements).



**Figure 4.15** Summary of results of 10,251 ray-trace calculations on each of three different cylinder-planar waveguide sensors, all having a circular radius  $R$  of 300 mm but different minimum thicknesses  $t$  (i.e., 14, 27, and 50  $\mu\text{m}$ ) as indicated.



According to Figure 4.15, the contour plots show on the horizontal and vertical axes the initial conditions for each calculated ray (respectively  $\theta$ , the entrance angle in air prior to entering into the waveguide; and  $y$ , the distance measured downward from the top planar surface). The  $z$ -axis corresponds to the maximum angle  $\varphi$  at which the ray is calculated to propagate in the thinnest (sensing) region of the waveguide. Contours are given at  $5^\circ$  intervals. The  $z$ -levels are also color-coded according to the key at right.

A somewhat surprising result is that the dependence of this sensing angle  $\varphi$  on the impinging angle  $\theta$  of a light ray is not close to linear. In fact, it is not even monotonic. It is also strongly dependent on the height ( $y$ ) of the ray on the input face of the waveguide. The contour plots, based on thousands of individual ray-trace calculations, show just how nonlinear this dependence is. Colors close to red represent the highest sensing angles, i.e., closest to the critical angle  $\varphi_{\text{crit}} = \arccos(2.2/4.0)$  for reflection at the Ge-ZnS interface. The grey regions, on the other hand, correspond to all initial conditions that result in the ray exceeding the critical angle for a Ge-ZnS interface of the waveguide, i.e., rays that fail to propagate all the way through the waveguide.

As expected, with decreasing waveguide thickness there is a corresponding decrease in the range of allowed  $(\theta, y)$  pairs, corresponding to a decrease in total throughput. However, there is also the evolution of fascinating structure in the contour plots as the waveguides get thinner, including the gradual pinching-off of isolated “islands” at very specific combinations of  $\theta$  and  $y$ , and the clear appearance of a thumb-like protrusion that indicates a large throughput allowed for light entering the waveguide from a specific angle just above  $0^\circ$ . We speculate that these regions may be the characteristics of mathematical “attractors”, and therefore signs of chaotic (or near-chaotic) behavior for rays reflecting from such closely apposed non-parallel surfaces.

The optical invariant (one-dimensional version of the étendue) of a cylinder-planar waveguide in the vertical direction is normally calculated as the product of the numerical aperture (NA) and the thickness  $t$ . In order to estimate a value of the numerical aperture, let us consider the waveguide configuration. In brief, the Ge stripe ( $n_{\text{Ge}} = 4.0$ ) is adjacent to materials of lower refractive indices. The outer material on the sensing side consists of either the sample used in the study ( $n_{\text{organic}} \cong 1.5$ ) or air ( $n_{\text{air}} = 1.0$ ), while it faces a ZnS layer ( $n_{\text{ZnS}} = 2.26$ ) on the substrate side. According to Eq. 2.4, the ZnS possesses the higher of the two outer refractive indices and therefore determines the numerical aperture of the waveguide.

$$\text{NA} = \sqrt{n_{\text{Ge}}^2 - n_{\text{ZnS}}^2} = \sqrt{(4.0)^2 - (2.26)^2} = 3.3 \quad (4.1)$$

For a simple planar waveguide, the étendue value is equal to:

$$\text{étendue} = t\sqrt{n_1^2 - n_2^2} = t \times \text{NA} \quad (4.2)$$

where  $n_1$  and  $n_2$  are the refractive indices of the waveguide ( $n_{\text{Ge}}$ ) and cladding materials ( $n_{\text{ZnS}}$ ), respectively.

In more general terms, and in particular at the entrance end of the waveguide, the optical invariant should be given by the following integral over the thickness  $t$  of the waveguide:

$$\text{étendue} = \frac{1}{2} \cdot \left\{ \int_0^{t=2\text{mm}} \left[ \int_{\theta_{\min}(y)}^{\theta_{\max}(y)} \cos \theta \, d\theta \right] dy \right\} \quad (4.3)$$

In Eq. 4.3,  $\theta_{\max}$  and  $\theta_{\min}$  are the extreme values of impinging angle  $\theta$  that can successfully propagate through the entire waveguide from a vertical position  $y$  within a cross-section at a specific horizontal position  $x$  where the optical invariant is being calculated. In this case, the étendue value was calculated at the entrance of the waveguide (i.e.,  $x = 0$ ). The refractive index  $n$  should in most generality appear inside the integral, but it is assumed in Eq. 4.3 to be 1.0 at the entrance of the

waveguide, which faces air. It can readily be seen that if all entering rays in a range of  $\pm\psi$  are allowed to propagate through a waveguide of constant thickness  $t$ , this formula gives étendue =  $t \sin\psi$  (i.e., the thickness times the numerical aperture, as it should).

Using Eq. 4.3 and setting the integral limits according to the allowed rays from the ray-tracing calculations, the étendue value of the 0.014-mm-thick Ge waveguide for the data matrix in Figure 4.15 is 0.0510 mm ( $\sim 51.0 \mu\text{m}$ ). This is remarkably close to that given by the simple formula for planar waveguides in Eq. 4.2, which gives the value of  $46.7 \mu\text{m}$ . The closeness of the two values suggests that light illuminating the end face uniformly and then propagating to the center of the waveguide could be accurately represented as a bundle of rays filling the numerical aperture of 3.3 (i.e., according to Eq. 4.1), at uniform density.

However, the hypothesis that the numerical aperture of the sensing region of the waveguide gets filled uniformly is contradicted by a more careful analysis based on the contour plots calculated. Figure 4.15 clearly shows that the distribution of intensity as a function of angle is far from uniform. In particular, rays that approach close to the critical angle (red-green colors) are somewhat under-represented. This is undesirable behavior for an evanescent-wave sensor, because the on-axis rays undergo relatively few internal reflections and have a lower evanescent-wave electric-field strength than rays near the critical angle. Unfortunately, it is completely consistent with the experimental results on the cylinder-planar waveguides, which show substantially lower evanescent-wave absorption intensities than would be predicted for modes evenly distributed over all the “allowed” angles for the cylinder-planar sensing region at the center of the waveguide (*vide infra*).

For a more advanced treatment of waveguide design, it is of interest to consider how changes in the shape of the waveguide might affect this result. In particular, we examined how it depends on the curvature radius  $R$  of the cylindrical bottom surface, at a constant waveguide center thickness  $t$  of  $14 \mu\text{m}$ . We hoped this might provide some useful clues for improving waveguide’s performance.

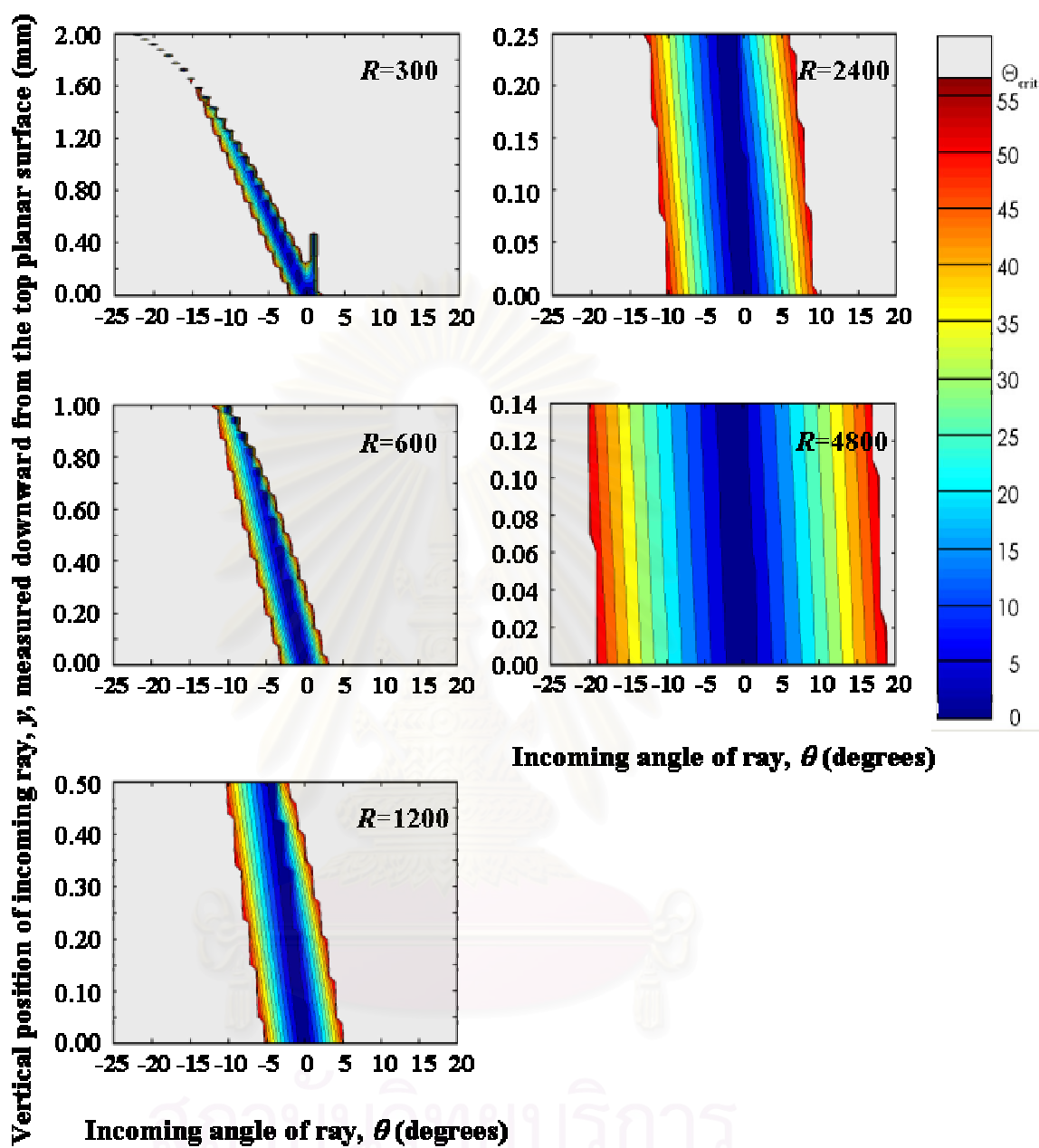


**Figure 4.16** Sensing-angle plots for rays impinging on the entrance faces of 14- $\mu\text{m}$ -thick cylinder-planar waveguides with different values of circular radius  $R$  (i.e., 300, 600, 1200, 2400, and 4800 mm) as indicated. As in Figure 4.15,  $z$ -axis contours are always calculated at  $5^\circ$  intervals. The color bar shown at right is applicable to all plots.

Figure 4.16 presents contour plots of cylinder-planar waveguides having the same length (70 mm) and center thickness (14  $\mu\text{m}$ ) as the top plot in Figure 4.15, but with various values of  $R$ . By holding the waveguide length constant at 70 mm, a larger  $R$  results in thinner end faces, as indicated in the figure by the correspondingly smaller range for the  $y$ -axis scale. Although increasing  $R$  causes a reduction of the end heights of the 70-mm-long waveguides, our calculations indicate that waveguides with  $R$  values in a range of 1200–2500 reveal only a small decrease in throughput relative to that for  $R = 300$  mm. Of note is that a waveguide with a larger radius of the curvature reveals a wider range of incoming angles with allowed sensing angles. This consequently leads to excitation of the far-off-axis modes in the sensing region of the tapered waveguide—the modes that are in fact useful for evanescent-wave absorptions. Thus we can in theory obtain a significant improvement in the waveguide performance, simply by increasing the circular radius of waveguides' curved bottom.

In order to investigate how the total étendue varies with  $R$  values, we performed étendue calculations, based on Eq. 4.3, to the entire data matrix of individual waveguides at different radii of curvature which correspond to those contours in Figure 4.16. A summary of calculations of the étendue obtained with these waveguides is illustrated in Figure 4.17. In practice, each value of total étendue was calculated from Eq. 4.3, by taking appropriate limits for the double integral from the data matrix that gave the corresponding plot in Figure 4.16. Because  $\cos \theta \approx 1$  for most of the allowed input rays, each calculated total étendue (■) roughly equals the total colored (non-gray) area of the plot in Figure 4.16. For the high-sensing-angle étendue (●), on the other hand, the range of the double integral was limited to just those plotted elements that correspond to sensing angles in the range of  $25^\circ$  to the critical angle ( $56.6^\circ$ ), giving roughly the green-to-red area of the each plot in Figure 4.16.

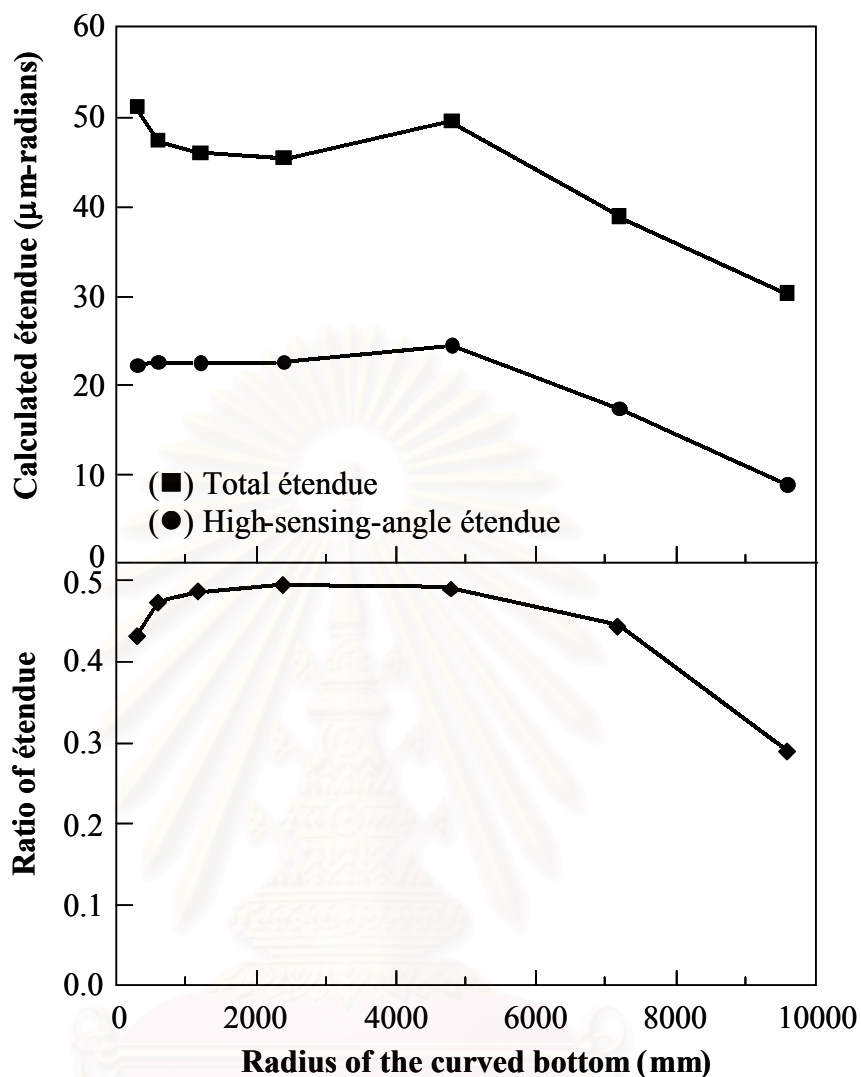


**Figure 4.17** (*Upper*) Plot of calculated total étendue (■) and high-sensing-angle étendue (●) of a 14- $\mu\text{m}$ -thick cylinder-planar waveguide vs. curvature radius  $R$  of the bottom cylinder surface. (*Lower*) Ratio of the high-sensing-angle étendue to the total étendue as a function of the curvature radius  $R$ , based on plots in the upper part of the figure.

The plot shows the largest total étendue at the smallest  $R$  value (300 mm) as a result of the largest entrance aperture ( $2 \text{ mm}^2$ ) into the waveguide. In fact, it is impressive that the calculated étendue for all the  $R$  values indeed end up being so close to each other, because this is a clear demonstration of the validity of the étendue as an optical constant. However, the étendue is not monotonic with  $R$ —it rises again at  $R = 4800 \text{ mm}$  and drastically goes down afterwards.

In addition, we determined the fraction of the étendue associated with light rays that propagate at high angles in the sensing area. Therefore, a filter based on maximum sensing angle was applied to the data matrices in order to exclude those elements containing sensing angles less than an arbitrary angle (i.e.,  $25^\circ$  for this present work), from the calculation. The result of high-sensing-angle étendue, as represented by (●) in Figure 4.17, approaches the maximum theoretical value at  $R = 4800$  mm, instead of the value of  $R = 300$  mm obtained by the full calculation without filtering the data matrix. By ratioing the high-sensing-angle étendue to the total étendue, the lower curve (◆) in the same figure reveals that waveguide sensors have optimum performance at radius of curvature in a range of 2000–3000 mm, rather than 300-mm-radius waveguide sensor used in the practical measurements. This can be attributed to two reasons: (1) somewhat higher fractional throughput for higher-sensing angles, i.e., above  $25^\circ$ , with no loss of total throughput; and (2) an ability to selectively excite modes with high sensing angles by illuminating the end face of the waveguide with off-axis rays. By comparison, the calculations show that there was a little or no selective excitation possible with the 300-mm-radius waveguide, in contrast to the contour lines of the 4800-mm-radius waveguide, which are almost perfectly vertical. This suggests that we could obtain exclusive light propagation with sensing angles greater than  $25^\circ$  by limiting input angles to be larger than  $10^\circ$ . As a consequence, sensitivity of the waveguide should be significantly improved.

#### 4.3.1.1 Contour Features of Cylinder-Planar Waveguides at Higher Resolution

In the later time, we have performed the contour calculations using a higher resolution of the incoming angle  $\theta$  on the  $x$ -axis. Based on the program input “RayTraceWG\_Data.m” as seen in Appendix C, the actual resolution of the input angle  $\theta$  for calculation process depends on two variables (*ThetaRange* and *Theta\_Res*), and can be simply determined by  $(2 \times \text{ThetaRange})/\text{Theta\_Res}$ . In fact, the contour calculations in Figures 4.15 and 4.16 were previously carried out at  $1^\circ$  interval for the  $x$ -axis. On the other hand, the following contour features shown in Figures 4.17 and 4.18 are the re-calculated plots at a higher  $\theta$

resolution of  $0.25^\circ$  using all other similar conditions as those in Figures 4.15 and 4.16, respectively. By comparison, the higher-resolution calculations apparently reveal the interesting new information that slightly conflicts with those contours at low resolution. Of interest is that the separate "islands" of allowed ray parameters  $(\theta, y)$  are not really islands, but instead a long connected "isthmus" or "sandbar". In addition, the anomaly at small negative angle is actually a very tall, narrow peak, indicating that the low-resolution plot truncates these features a third of the way to its top. However, both figures of the high-resolution give rise to the similar conclusions as those at lower resolution.

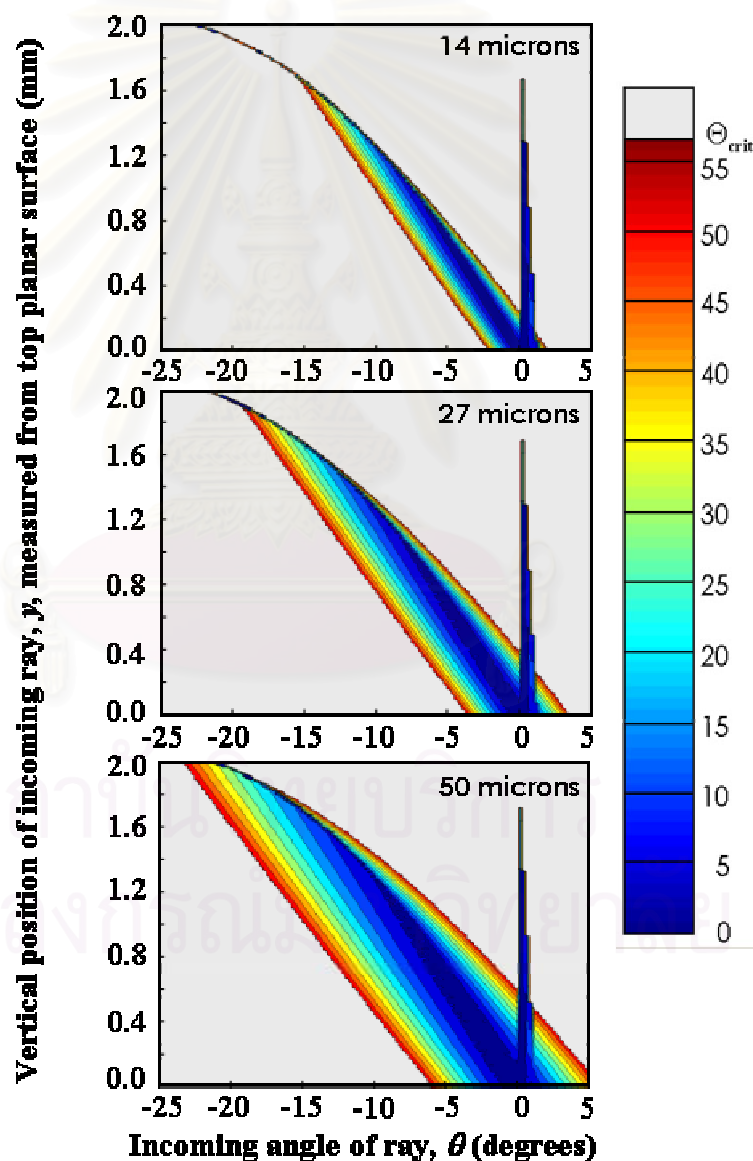


**Figure 4.18** Ray-trace calculations at the higher resolution of incoming angle  $\theta$  on each of cylinder-planar waveguides, having a circular radius  $R$  of 300 mm, with different minimum thicknesses  $t$  (i.e., 14, 27, and 50  $\mu\text{m}$ ) as indicated.



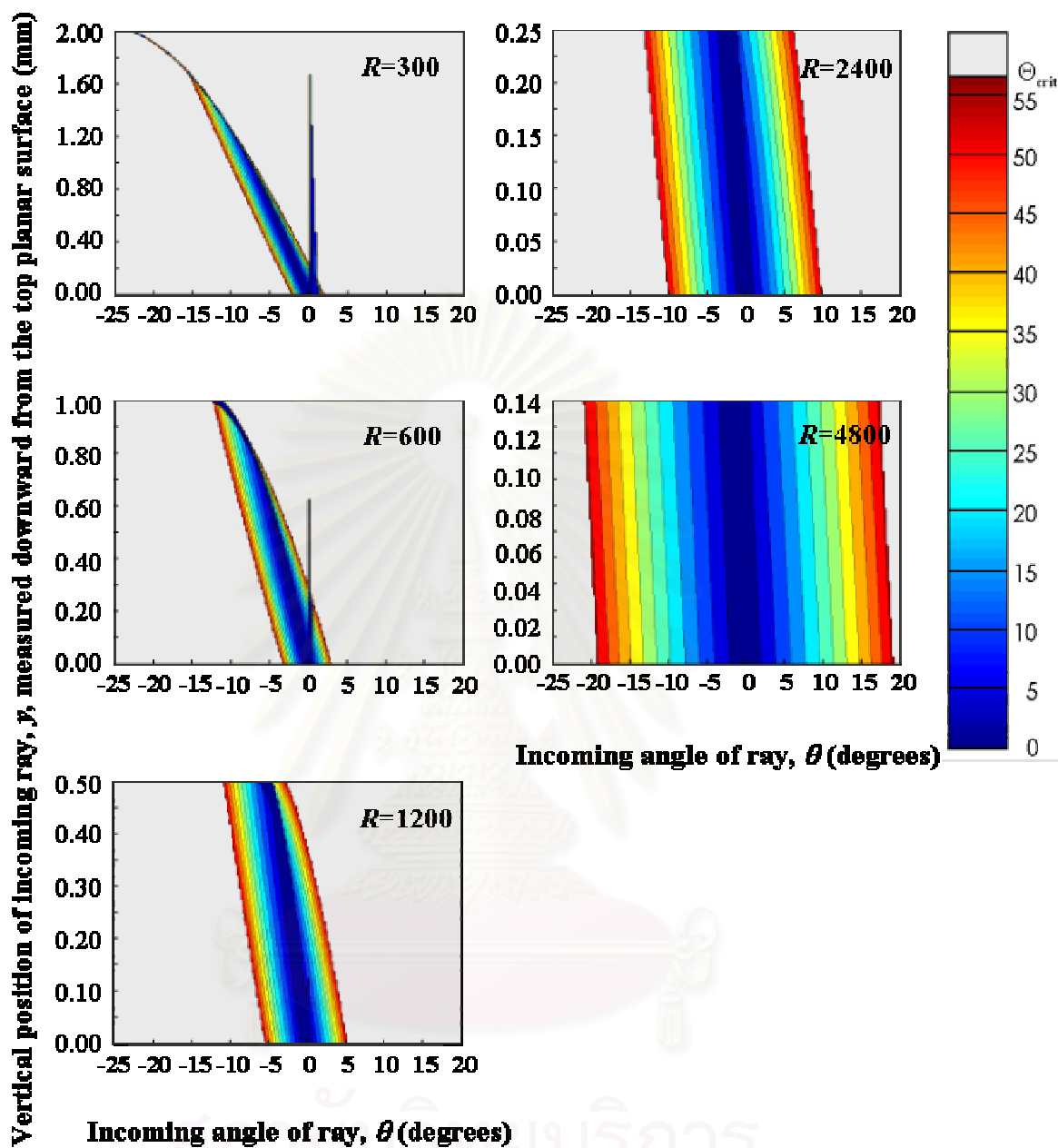


**Figure 4.19** Sensing-angle plots at the higher resolution of incoming angle  $\theta$  for rays impinging on the entrance faces of 14- $\mu\text{m}$ -thick cylinder-planar waveguides with different values of circular radius  $R$  (i.e., 300, 600, 1200, 2400, and 4800 mm) as indicated.

### 4.3.2 Ray Tracing for Waveguides with a More Complicated (Gaussian) Curved Surface

The ray-tracing computational method clearly reveals significant information about light propagation inside particular waveguide designs. With the modification of a subroutine in the ray-tracing program, the shape of the curved bottom of a waveguide sensor can be simply altered to other functional forms besides circular. This procedure allows ones to study changes in distribution of sensing angles at the tapered center of the waveguide, which might lead to the optimization of the waveguide design in order to achieve better performance than other devices currently on the market.

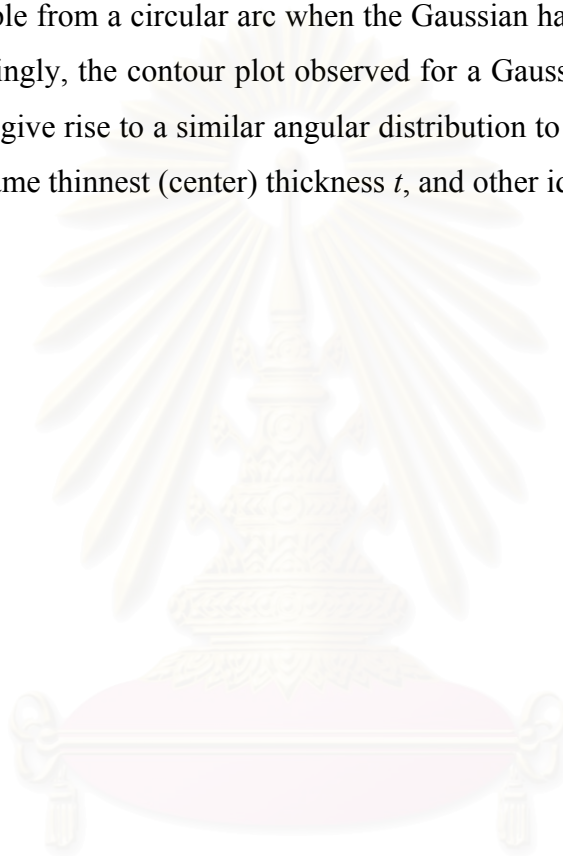
In particular, the subroutine “curve.m” (see Appendix C) was originally set to define a circular arc for a cylinder-planar waveguide, using a simple equation of circle (i.e.,  $y_i = \sqrt{R^2 - x_i^2}$  at any specified radius). We hypothesized that changes in shape of the curved bottom of the waveguide could improve the throughput of light rays that propagate close to the critical angle at the center of the tapered region. This would subsequently enhance its sensitivity both by increasing the total throughput, and by increasing the strength of evanescent wave absorptions. With this regard, our initial hypothesis was that a curve that included both concave as well as convex surfaces (i.e., curvatures both upward and downward) might provide an improved performance. Therefore, we replaced the bottom circular curve with an equation of Gaussian curve-shape, as follows:

$$y = t + \left[ \frac{(e-t)}{1 - \exp\left(-\frac{1}{2}\left(\frac{Li}{w}\right)^2\right)} \right] - \left[ \frac{(e-t)}{1 - \exp\left(-\frac{1}{2}\left(\frac{Li}{w}\right)^2\right)} \right] \exp\left[ -\frac{1}{2}\left(\frac{x-Li}{w}\right)^2 \right] \quad (4.4)$$

Here  $y$  represents the waveguide thickness as a function of horizontal distance  $x$  from the entrance face of the waveguide. The thickness of the waveguide at the entrance face is given by the fixed parameter  $e$ , while the minimum (center) thickness is given by  $t$ . The other two fixed parameters,  $Li$  and  $w$ , represent the

horizontal distances from the center of the Gaussian curve to the end of the waveguide, and to the inflection point of the curved surface, respectively.

Prior to the investigation of sensing angle, it is desirable to verify the definition of the Gaussian curved surface in the subroutine “curve.m”. On a basis of the fundamental geometry, the Gaussian curve-shape should gradually transform to be indistinguishable from a circular arc when the Gaussian half-width  $w$  value gets very large. Accordingly, the contour plot observed for a Gaussian-planar waveguide at a large  $w$  would give rise to a similar angular distribution to that of the cylinder-planar one with the same thinnest (center) thickness  $t$ , and other identical variables.



สถาบันวิทยบริการ  
จุฬาลงกรณ์มหาวิทยาลัย

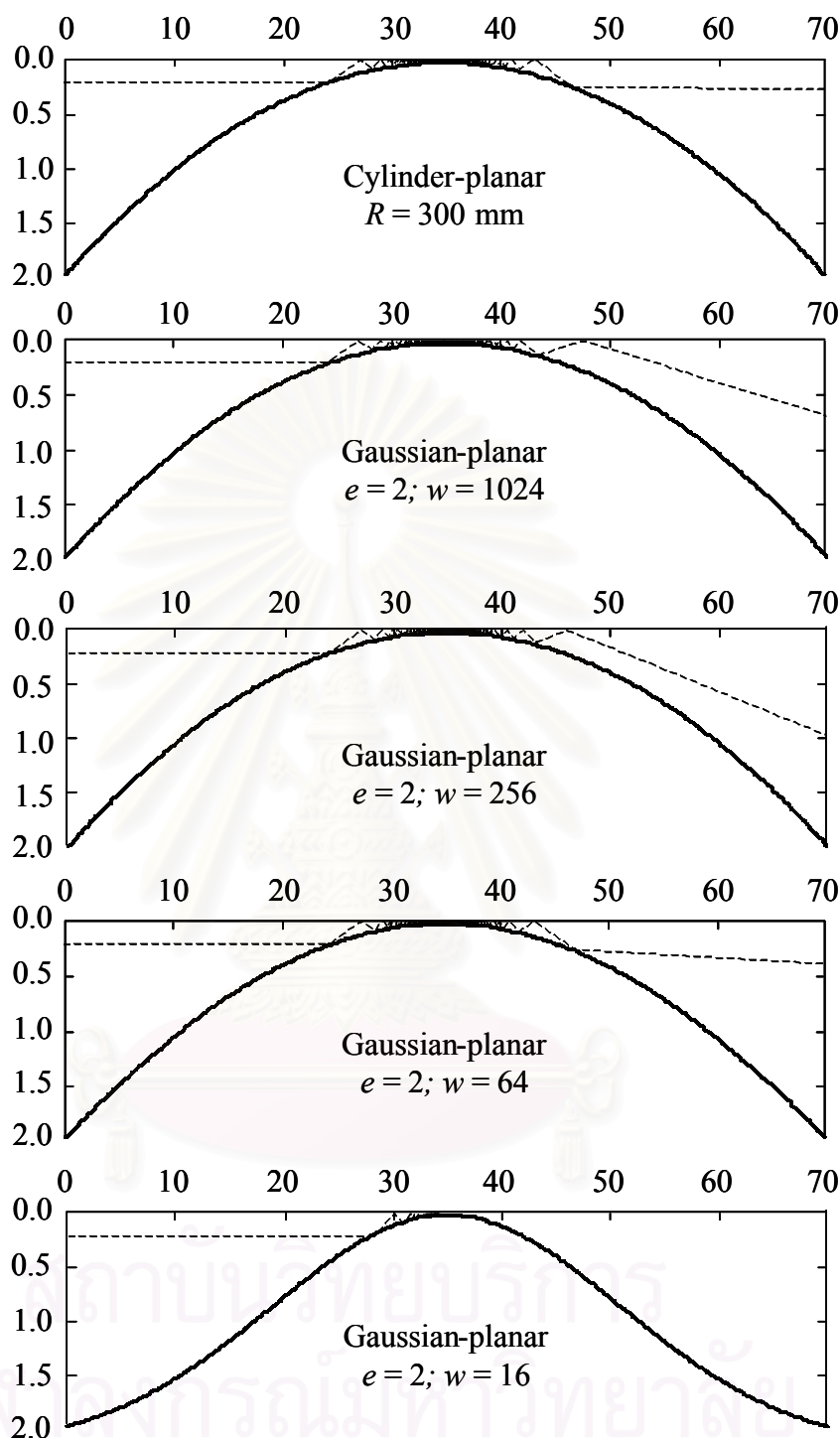


**Figure 4.20** Changes in Gaussian curvatures of the bottom surface observed for 14- $\mu\text{m}$ -thick waveguides with increasing  $w$  values (i.e., 16, 64, 256, and 1024 mm) from lower to upper lines, respectively, at a fixed  $e$  of 2 mm. The circular arc of  $R = 300$  mm with the same center thickness  $t = 14$   $\mu\text{m}$  is shown as a reference curve on the top. The ray traces were simulated using the distance away from the flat sensing surface ( $y$ ) of 0.2 mm and an impinging  $\theta = 0^\circ$ .

Figure 4.20 reveals changes in the Gaussian curve-shape with increasing values of  $w$  by a factor of four (i.e., 16, 64, 256, and 1024 mm), in comparison to the circular arc shown on the top of the figure. Every curve in the figure has the same center thickness  $t$  of 14  $\mu\text{m}$  with its length  $L$  and entrance height  $e$  held constant at 70 and 2 mm, respectively. The Gaussian curve-shape at the smallest  $w$  clearly reveals its characteristics of both upward and downward curvatures. Increasing  $w$  causes a longer distance from the waveguide center to the inflection point of the curved bottom surface. As a consequence, the entire length of the Gaussian-shaped waveguide at  $w \geq 16$  has only a downward curving surface, which is almost identical to a circular arc. With  $w \geq 256$ , the Gaussian curves are essentially superimposable on the circular arc of  $R = 300$  mm.

To test the subroutine “curve.m”, the calculations of sensing angle were subsequently performed as a function of both the incoming angle (in air)  $\theta$ , and the distance measured from the flat surface  $y$ , by using the corresponding variables to those in Figure 4.20. As predicted, the contour results in Figure 4.21 clearly demonstrate the validity of the program by obtaining a very similar contour feature for the Gaussian-planar waveguides with  $w \geq 64$ , in which only downward curvature is composed, relative to that of the cylinder-planar waveguide. In addition, the contours in Figure 4.21 suggest that most of the sensing angles observed for  $w$  as small as 16 mm are nearly close to  $0^\circ$  (i.e., the blue regions), which is not the desirable mode for evanescent-wave spectroscopy. Therefore, the combination of both upward and downward curvatures likely results in insignificant improvement in waveguide performance for both means of throughput energy and its sensitivity. Accordingly, we performed the consecutive calculations on Gaussian-shaped waveguide using only a large value of  $w$ .

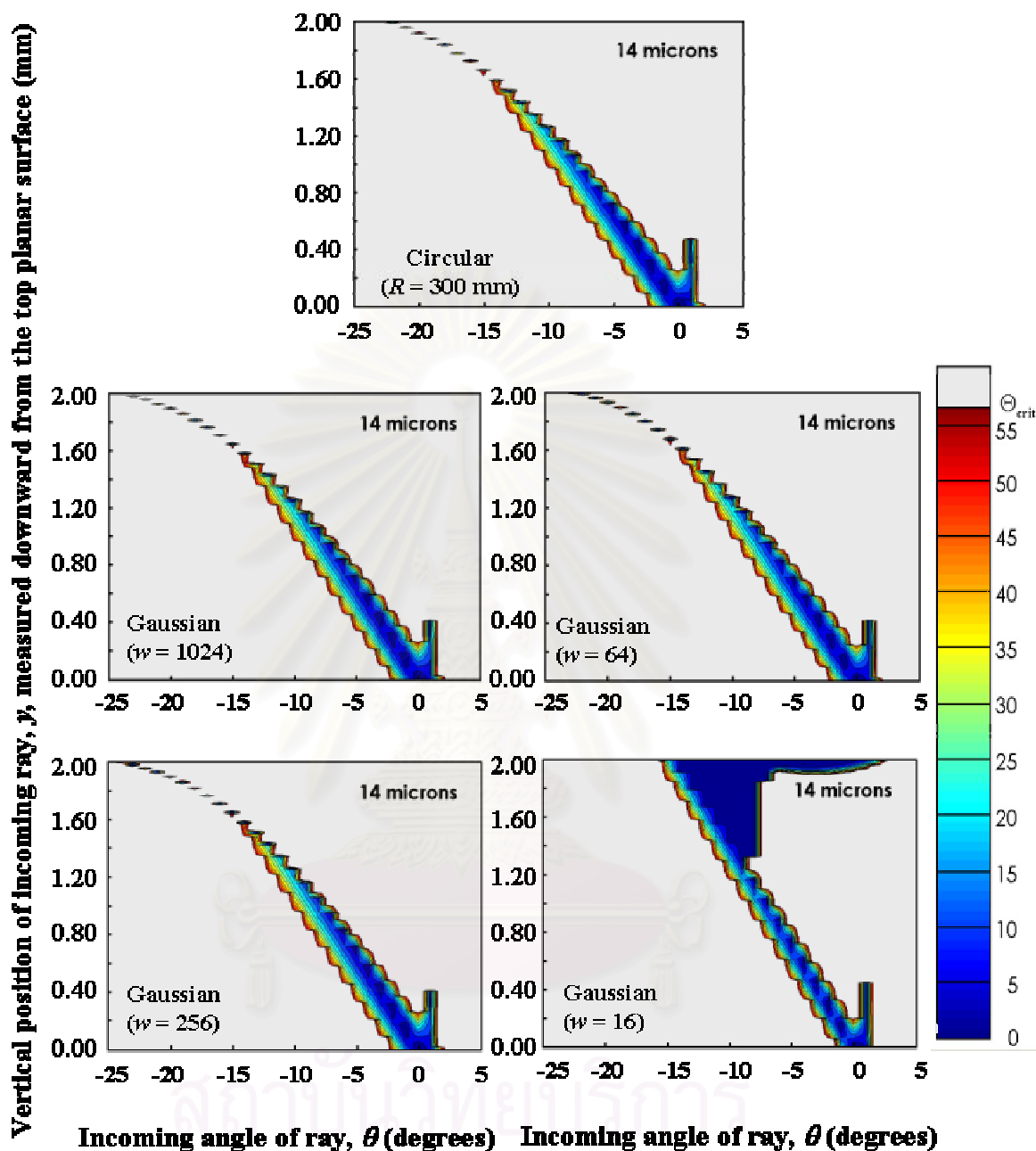


**Figure 4.21** Contour plots of Gaussian-planar waveguides with identical variables as those in Figure 4.20, in comparison to that of cylinder-planar waveguide with  $R = 300$  mm shown on the top. The  $z$ -axis contours are calculated at  $5^\circ$  intervals as represented by the color bar at right.

In an attempt to gain more off-axis rays from a Gaussian-planar waveguide, the variation of the thinnest center thickness  $t$  was investigated by holding the Gaussian half-width  $w$  constant at 1024 mm for all cases. The thicknesses were defined in accordance with those used in the experimental measurements. As shown in Figure 4.22, plots at the left side correspond to Gaussian-planar waveguides having the same 2-mm-high entrance face ( $e$ ) as the plots for the cylinder-planar waveguides in Figure 4.15. Comparison of these two figures shows that use of an identical entrance height ( $e = 2$  mm) for Gaussian-shaped waveguides results in similar contour patterns to those for the corresponding cylinder-planar waveguides. These similar features suggest no variance in waveguide performance.

On the other hand, the Gaussian-shaped waveguide with a shorter end height of  $e = 1$  (see the right column) interestingly exhibits a throughput enhancement by means of a substantially larger angular distribution of sensing angles of light being able to propagate through the tapered region of the waveguide, although a narrower range of incoming angles is allowed. Nevertheless, the fraction of high-angle rays (red-to-green regions) leading to excitation of the far-off-axis modes (i.e., the most useful modes for the evanescent-wave sensing) is insignificantly improved, relative to either waveguides with the entrance height of 2 mm. Only by use of a thinner entrance face (i.e., a vertically shrunken Gaussian shape for the curved surface with less extreme values), it is thus possible to achieve high-quality spectra (i.e., better SNR) with a reduced number of co-added scans, even though it would in practice turn out to be extremely difficult to fabricate a waveguide with such a shape. The computational ray-tracing method nevertheless demonstrates herein a crucial role in waveguide's design for a better performance.

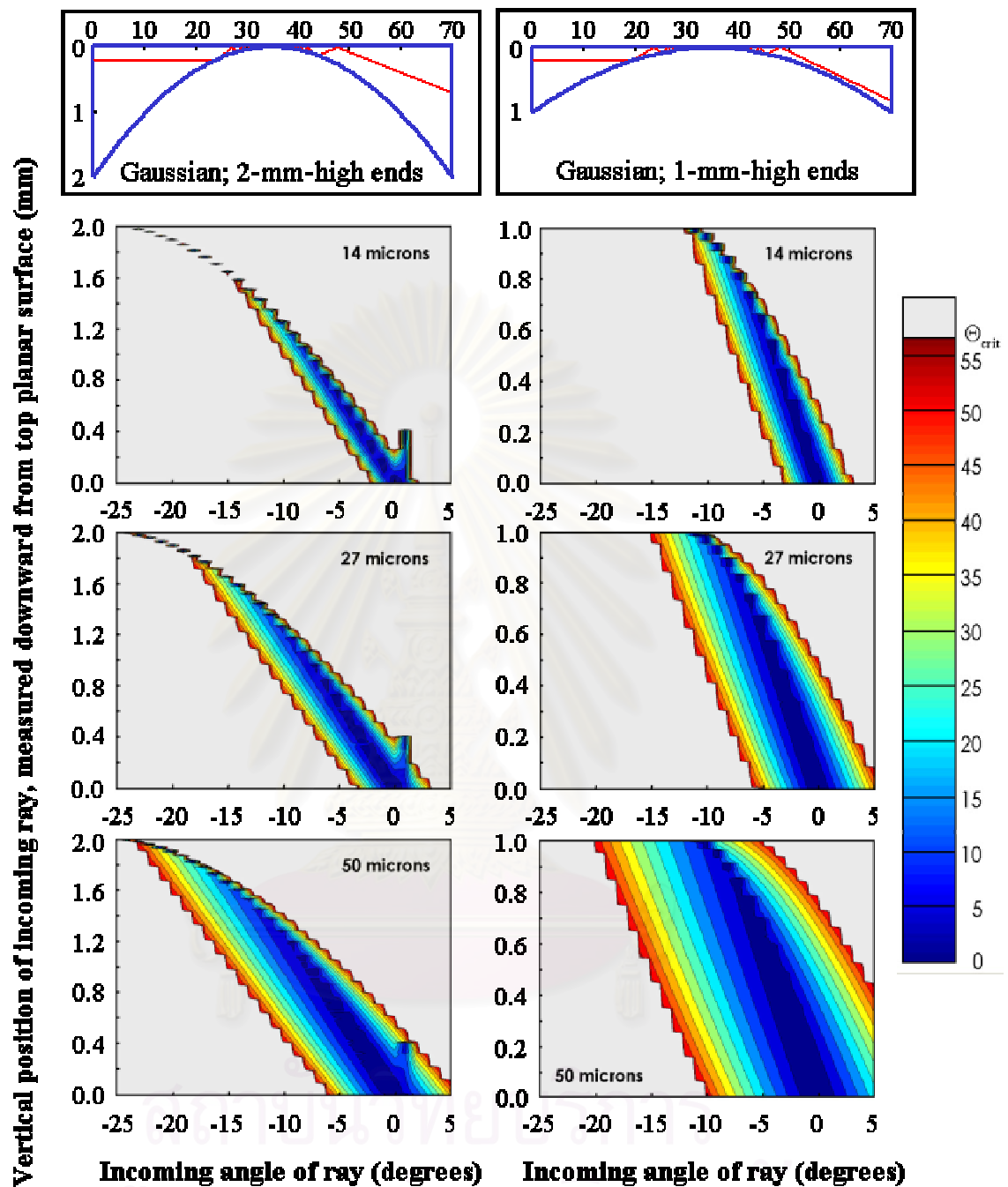


**Figure 4.22** Sensing-angle plots of rays impinging on each of three different Gaussian-planar waveguides, having the same length and half-width but different central thicknesses (i.e., 14, 27, and 50  $\mu\text{m}$ ) as indicated. Contours in each column reflect Gaussian-planar waveguides with (*left*) 2-mm-high and (*right*) 1-mm-high entrance ends, which correspond to the respective ray-trace pattern shown on the top. The 5°-interval color bar at right is applicable to all plots.



## 4.4 Characterization of Supported Cylinder-Planar Ge Waveguides with Synchrotron IR Radiation

### 4.4.1 Throughput Measurements with Synchrotron IR Radiation

As mentioned in Section 4.1, the SNR in absorbance spectra acquired by the waveguides is limited by the total throughput detected. Because of the high brightness (flux per unit area) of the synchrotron radiation, it turns to be of interest to determine how the waveguide functions under higher-throughput condition of synchrotron IR radiation. In an effort to improve the waveguide performance, the waveguides were investigated under the intense-throughput condition of synchrotron light source in comparison to those using the standard internal Global<sup>TM</sup> source. Figure 4.23 compares single-beam spectra of symmetrically tapered 14- and 27- $\mu\text{m}$ -thick Ge waveguides obtained both with synchrotron IR radiation and with a standard blackbody (Global<sup>TM</sup>) source. Throughput in each case was maximized by shifting the relative horizontal and vertical positions of the IR beam, waveguide, and detector.

For the synchrotron beam, the optics were aligned in two different setups utilizing the Nicolet 860 FT-IR spectrometer: (1) using the external output port with an out-of-compartment setup; or (2) with the Remspec immersion detector and waveguide both mounted inside the internal sample compartment. The spectral series in Figure 4.23 demonstrate that the synchrotron radiation input beam does not exceed the numerical aperture of even the smallest of our waveguides, because the detected throughputs are independent of waveguide thickness. As expected, the small effective source size of the synchrotron can totally pass through the minimum 46- $\mu\text{m}$  étendue of the 14- $\mu\text{m}$ -thick waveguide. The calculated one-dimensional étendue of the output of the U2B beamline at the National Synchrotron Light Source (NSLS) is far below 14- $\mu\text{m}$ ; in fact, it is somewhat under 0.1  $\mu\text{m}$ , based on the published VUV parameters at NSLS as of December 2002 [53].

The results in Figure 4.23 show that indeed there is a higher total energy throughput when using the synchrotron radiation, as compared to a blackbody Globar<sup>TM</sup> source, for both 14- and 27- $\mu\text{m}$ -thick waveguides. For the thicker (27- $\mu\text{m}$ -thick) waveguide, the increase in throughput intensity for the synchrotron, relative to the Globar<sup>TM</sup>, is significant only above 2500  $\text{cm}^{-1}$  (and up to 5000  $\text{cm}^{-1}$  where the cut-off due to the Ge bandgap blocks all transmission in either case). In contrast, for the 14- $\mu\text{m}$ -thick waveguide, the synchrotron affords higher throughput over all MIR frequencies.

Therefore, using synchrotron radiation can clearly help to increase the total light energy throughput with such thin waveguides. Furthermore, the use of synchrotron IR radiation allows a simple in-compartment set-up configuration using only flat mirrors, with no loss of energy. This is because the  $\sim 100\text{-mm}$ -focal-length mirror that the spectrometer uses to focus the beam into the sample compartment is adequate to focus the highly collimated synchrotron beam into the  $\sim 1\text{-mm}^2$  end of the waveguide. On the other hand, it can only focus a small portion of the Globar<sup>TM</sup> intensity into such a minute aperture.

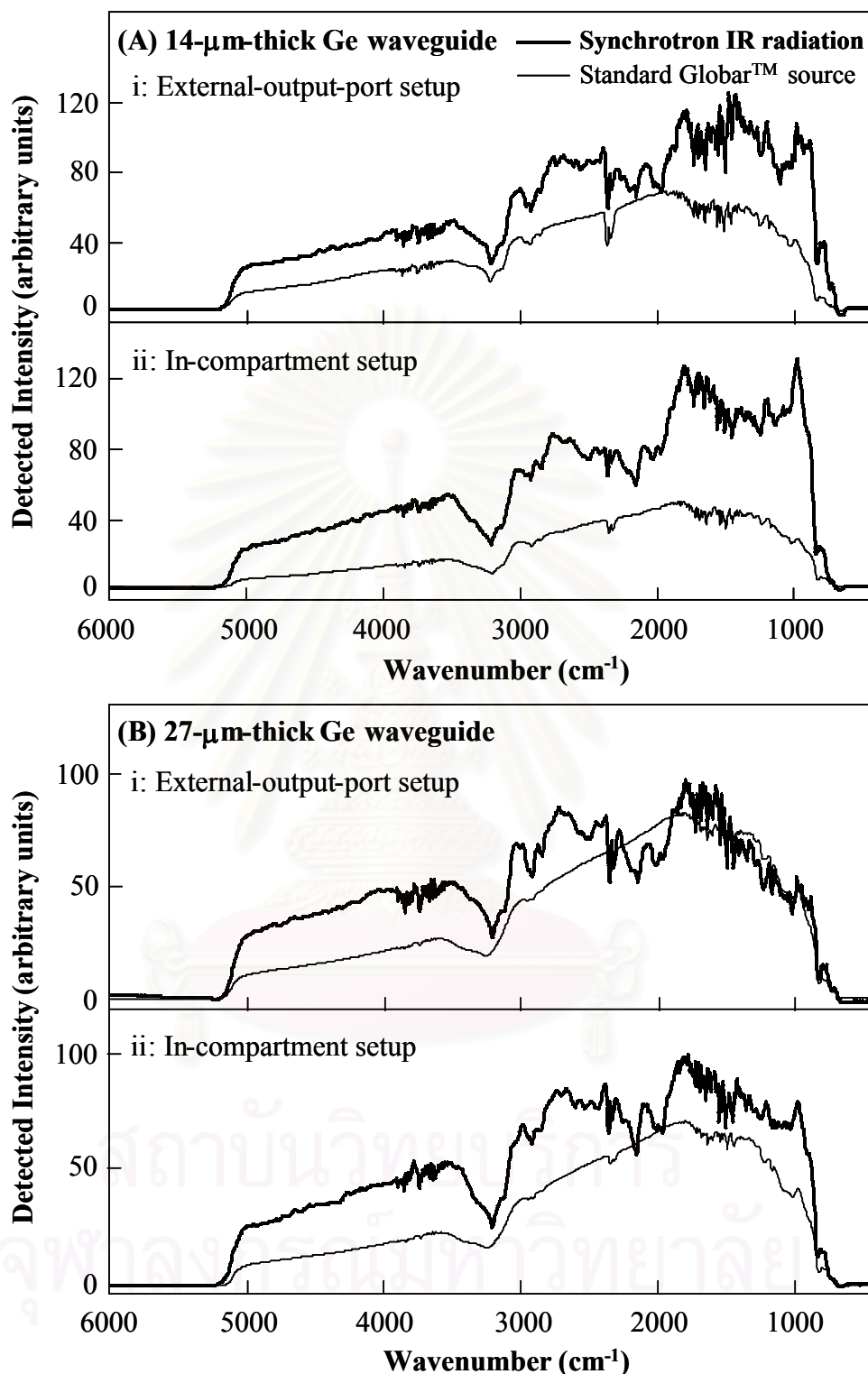


**Figure 4.23** FT-IR single-beam spectra of (A) a 14- $\mu\text{m}$ -thick and (B) a 27- $\mu\text{m}$ -thick Ge waveguides observed with synchrotron IR radiation, compared to those observed with a standard blackbody (Globar<sup>TM</sup>) source. With each waveguide thickness, two different on-axis setups were examined: (i) using the external output port; and (ii) using the internal sample compartment.

#### 4.4.2 Angle Dependence of Throughput and Absorbance Signals with Synchrotron IR Radiation

We also measured the total synchrotron-generated IR energy throughput of the 27- $\mu\text{m}$ -thick waveguide, and the water absorbance signal at  $3400\text{ cm}^{-1}$  for a standard 1-mm-diameter droplet of water, at different external incident angles. Figure 4.24 presents a summary of integrated energy throughputs and absorption intensities of the water droplet as a function of external incident angle  $\theta$ . Note that the throughputs mentioned on the  $x$ -axis are relative values of the observed throughput at a certain input angle to that of total transmission acquired when the light was directed on-axis ( $\theta = 0^\circ$ ).

As can be seen, the results apparently revealed a great variability. In particular, the energy throughput and the absorption intensity are clearly sensitive to the input angle  $\theta$ . Nevertheless, these experimental observations are consistent with the ray-tracing computations summarized in Figure 4.15. They confirm that at any value of the external incident angle  $\theta$ , widely different results can be expected depending on other aspects of the optical alignment of the waveguide relative to the synchrotron beam, specifically, entrance height  $y$  on the waveguide end face and the relative vertical displacement of the output end of the waveguide and the detector's immersion lens. This displacement determines the efficiency of coupling light to the detector. There is thus a significant error in the  $y$  values in this plot arising from uncertainty in knowing that the alignment was fully optimized. At the time that measurements were made at the synchrotron (prior to performing the ray-trace calculations), we did not suspect such a strong dependence of throughput and absorbance signal on these beam height parameters.

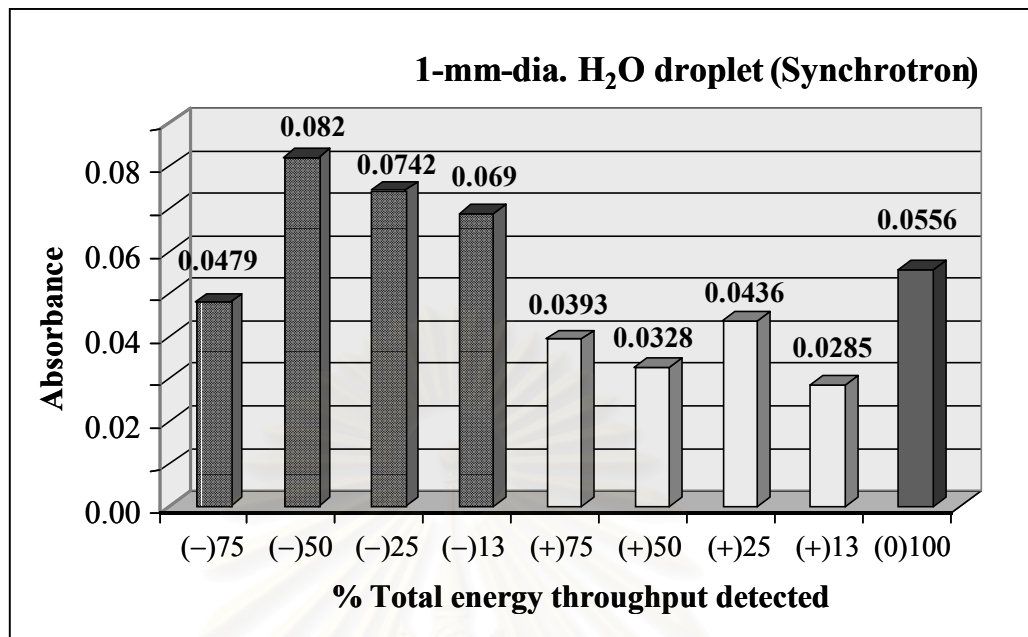


**Figure 4.24** Correlation of changes in % total energy throughput and absorption intensity of a 1-mm-diameter water droplet observed at different external incident angles by using the synchrotron IR radiation with a 27- $\mu\text{m}$ -thick Ge waveguide. The +/- signs indicated on the  $x$ -axis represent the direction from where the input light was focused, i.e., below (-) and above (+) the waveguide plane, as presented in black and white columns, respectively. The throughput value observed at each input angle was ratioed to the reference value of the total transmission detected with no input angle ( $0^\circ$ ) when the light was directed on-axis shown in the last (shaded) column. Numbers indicated over the columns are the actual absorption intensities.

Nevertheless, we made enough measurements on both 14- and 27- $\mu\text{m}$ -thick waveguides (at  $\sim 10$  different beam angles in the range  $-20^\circ$  to  $+20^\circ$ ) to draw some useful generalizations that both support the ray-tracing calculations, and are explained (*a posteriori*) by them. In particular, we observed that for any absolute value of the incident angle  $\theta$ , the energy throughput obtained when light is directed from a small but substantial angle below the waveguide surface ( $-10^\circ < \theta < -3^\circ$ ) is substantially greater than the near-zero throughput obtained when the light is directed at a similar angle from above the waveguide surface plane, and typically up to  $\sim 20\%$  greater than the throughput obtained when the synchrotron light is directed strictly

on-axis ( $\theta = 0^\circ$ ). However, it was also found that the detected throughput drops off gradually as the input angle increases in the negative direction ( $\theta > -10^\circ$ ). On the other hand, almost no transmission is obtained if the input angle is more than just a few degrees positive from above the waveguide's plane. This empirical observation, which was very confusing at first, makes perfect sense in light of the subsequent ray-trace calculations shown in Figure 4.15. This calculation demonstrates that negative values of  $\theta$  in the range of  $-3^\circ$  to  $-10^\circ$  contribute far more to the total throughput of the waveguide than similar-magnitude positive angles, and slightly more than on-axis rays. As a consequence, the optimum vertical position of the detector element changes with input angle, but is always *below* the waveguide (i.e., displaced towards its curved surface).

Furthermore, the absorption intensities of a 1-mm-diameter water droplet are also variable even for any particular input angle (see Figure 4.24). The observation shows that the absorbance of a standard sample (e.g. the  $3400\text{-cm}^{-1}$  peak for a 1-mm-diameter water droplet at the center of the waveguide sensing region) was only up to  $\sim 50\%$  larger when the measuring synchrotron IR light impinged on the waveguide entrance face from  $4^\circ - 10^\circ$  below the waveguide plane, than for light impinging on-axis, as evidenced in Figure 4.24. We had qualitatively expected that we would selectively excite high-angle modes at the sensing region of the waveguide by using light impinging off-axis onto the end face. However, the graphs in Figure 4.15 contradict this expectation, and instead support our empirical observation that it becomes only slightly easier to excite off-axis modes as the impinging angle is increased.

This explains why we found no input angle conditions for which we could get the water absorbance signal to approach that expected for light propagating at the critical angle. Figure 4.15 indicates that we might have been able to do this only if we had tightly focused the synchrotron beam at just the right entrance height (one of a few  $\sim 10\text{-}\mu\text{m}$ -high "sweet spots") on the entrance face of the cylinder-planar waveguide.

#### 4.4.3 Oscillatory Signal on Absorbance Spectra Measured with Synchrotron IR Radiation

In general, the absorption intensity and band shape measured for the broad  $\nu_{\text{OH}}$  band at  $3400\text{ cm}^{-1}$  by using synchrotron radiation is similar to that measured by using a standard Global<sup>TM</sup> source (Figure 4.25). However, the spectra observed with the synchrotron show intense oscillatory interference patterns, regardless of the waveguide thickness. These oscillations arise from a fixed frequency separation between the allowed waveguide modes when the light is required to propagate between two planar surfaces with a well-defined propagation angle (*vide infra*).

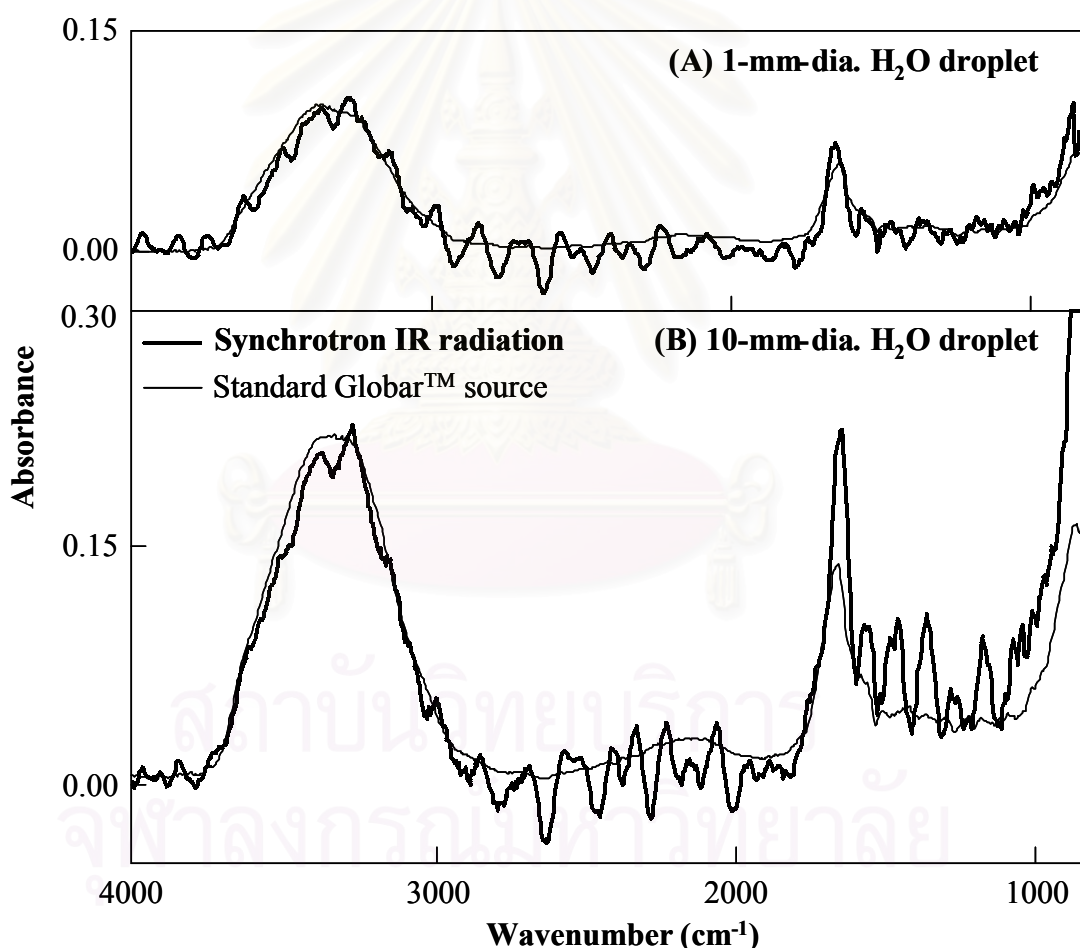


**Figure 4.25** Comparison of evanescent-wave absorbance spectra measured with a  $14\text{-}\mu\text{m}$ -thick Ge waveguide, by using either synchrotron IR radiation (bold lines) or a standard blackbody (Global<sup>TM</sup>) source (thin lines). Samples were water droplets covering either (A) 1 mm or (B) 10 mm of the central part of the waveguide's sensing surface.

The strength of the interference phenomenon is greatly increased for the synchrotron-produced light, due to its much greater spatial coherence (i.e., its ability to be simultaneously well-collimated and focused to a narrow beam diameter), relative to blackbody-generated irradiation. As a result, the entire synchrotron IR beam is propagated through the thinnest part of the waveguide at a single well-defined angle  $\theta'$ , which can be determined from the following formula giving the separation between allowed frequencies:

$$\Delta\nu = \frac{1}{(2nt \sin \theta')} \quad (4.5)$$

where  $n$  is the refractive index (4.0 for Ge) and  $t$  is the separation between the (approximately) planar surfaces.

As described in Chapter 2 (Experimental Section), the thickness of each waveguide was initially measured using a variant of Eq. 4.5, with IR light directed vertically through the waveguide from above, corresponding to  $\theta' = 90^\circ$ . For the oscillating interference pattern in Figure 4.25A, the calculated value of  $\theta'$  corresponding to the measured  $\Delta\nu = 125 \text{ cm}^{-1}$  was  $45.6^\circ$ . This is a reasonable value, and indicates that the propagation of the synchrotron IR light through the Ge obeys well-understood equations.

In addition, the oscillating patterns observed with synchrotron light in Figure 4.25 are very different from the much smoother baselines obtained with blackbody light, which propagates through the thinnest part of the tapered waveguide with a wide range of angles as shown in Figures 4.13 and 4.15. This can be explained based on a fixed frequency separation between allowed waveguide modes [16,27]. Generally speaking, such small spot size of the synchrotron radiation can only excite a small fraction of the allowed modes of the waveguides. When the synchrotron is coupled into the waveguide, it covers only an extremely limited range of angles, and the propagation angle of the propagating light is subsequently fixed. The fixed propagation angle is identical to an allowed waveguide mode only for the set of evenly spaced light frequencies. In contrast, the standard Global<sup>TM</sup> source consists



of a wide range of propagation angles, which result in a superposition of continuous oscillating patterns over a wide range of different periods. This consequently produces a smooth baseline on the observed Global<sup>TM</sup> spectra. Nevertheless, it seems a bit strange at first glance that the oscillation of Figure 4.25 is not as marked in the single-beam spectra from which it was calculated (e.g., Figure 4.23). Presumably this is because in single-beam spectra measured with the waveguide, there is a superposition of different oscillation frequencies resulting from its tapered shape. This taper creates a wide range of separations between the two surfaces of the waveguide as the light propagates down to its length.

In the case of absorbance measurements, however, the effects of the sample are concentrated in the region of minimum thickness, where the vast majority of the internal reflections occur (see Figure 4.13). The main effect of the sample on the oscillation is simply a phase shift (without any frequency shift). The size of the phase shift is proportional to the number of internal reflections at the Ge-water interface. Thus, the oscillation frequency corresponding to the propagation angle at the minimum waveguide thickness is selected out of the superposition of oscillations corresponding to a range of greater thicknesses and shallower propagation angles. The superposition of the latter obscures the oscillations, which must nevertheless be present in the single-beam spectrum (Figure 4.23).

From a practical point of view, the sharp oscillatory feature in the collected spectrum could be easily mistaken for absorption bands of a material present at the waveguide surface. This indicates an advantage of using the waveguide sensors with a standard blackbody Global<sup>TM</sup> source, rather than with synchrotron IR radiation. However, in some circumstances, the wide range of propagation angles at the sensing region produces a fundamental disadvantage. The presence of multiple propagation angles in the waveguide results in a non-logarithmic response to increasing numbers of absorbing molecules, i.e., the absorbance non-linearities deviated from Beer's law. The more complicated (but still monotonic) spectral response, as seen in Figure 4.4, makes the waveguide generally inappropriate for quantitative analysis over wide ranges of analyte surface concentration. However, such nonlinear behavior may be

an insignificant aspect in some experiments in which a single known analyte and a calibration curve can be established in practice.



สถาบันวิทยบริการ  
จุฬาลงกรณ์มหาวิทยาลัย

## CHAPTER V

### CONCLUSIONS

FT-IR spectroscopy has proven itself to be a valuable contributor to the study of material characterization, due to the molecular specific fingerprints provided on vibrational spectra. Uses of FT-IR spectroscopy coupled with the thin waveguides have enabled spectroscopists to probe even smaller, and thinner, samples in the ways that were unthinkable decades ago.

#### **5.1 Symmetrically Tapered <30- $\mu\text{m}$ -thick Quasi-Planar Ge Waveguides as Chemical Sensors for Microanalysis**

Symmetrically tapered Ge waveguides with thicknesses down to  $\sim 7 \mu\text{m}$  have been successfully fabricated and utilized as MIR evanescent-wave sensors. Tapering in this way helps eliminate several problems previously discussed [16–20]. Firstly, a high total throughput can be achieved with an uncomplicated optical alignment procedure and without requiring an IR microscope, by using only a single off-axis paraboloid mirror. The larger cross-sectional area at the waveguide ends provides an ease to achieve an optimal coupling efficiency of the waveguide, with respect to both the focused IR beam and the detector. In addition, a flat horizontal sensing area provides convenience in sampling—the most useful for typical sensing applications. It allows for better contact of solid samples such as human hairs, resulting in higher sensitivity and better spectral SNR. As expected, reducing the tapered thickness of the waveguide to  $<30 \mu\text{m}$  produces substantially higher absorbance per unit weight of sample, particularly as compared to a macroscopic Ge ATR accessory. However, this measured increase in absorbance is not yet as great as that which was predicted for waveguides of this thickness; and it must also be balanced against the significantly lower total throughput that is also not yet close to that which was predicted to be theoretically achievable [16].

Nevertheless, we have demonstrated that these <30- $\mu\text{m}$ -thick tapered Ge waveguides have the potential to become a useful technique for at least 3 types of application that are currently difficult with commercial ATR accessories: (1) sub-microliter quantities of volatile liquids; (2) ng-quantity thin-film samples; and (3) coatings and surface layers on small fibrous samples such as individual human hairs. The last application especially indicates the possible utility of these miniature Ge waveguides in non-destructive forensic analysis.

## **5.2 Characterization of Supported Cylinder-Planar Ge Waveguides with Synchrotron IR Radiation**

Combining synchrotron-based IR spectroscopy with thin cylinder-planar Ge waveguides does not yet result in any overall improvement in the sensitivity of either technology for sensing small quantities of samples. However, there is clearly a throughput increase available with the synchrotron source, which is greater for thinner waveguides. Of course, for a sufficiently thick waveguide, a blackbody source can provide a greater total light energy flux than the synchrotron. The exact crossover thickness is dependent on the size of the detector element and focusing optics, but is typically somewhere in the range of 30–50  $\mu\text{m}$ . Unfortunately, with waveguides in the range of 14–30  $\mu\text{m}$  in thickness, the closer one approaches to single-angle operation (by using either highly-collimated source such as a synchrotron or a very small detector), the more deleterious is an oscillatory interference pattern that appears in the spectrum. This limits the applications of synchrotron light source to investigate samples with such thin Ge waveguides. Thus, even for cylinder-planar waveguides as thin as 10  $\mu\text{m}$ , a standard Global<sup>TM</sup> source turns out to be more useful than the synchrotron, even though it cannot achieve quite such a high total energy throughput. However, for cylinder-planar waveguide sensors that are thinner than 10  $\mu\text{m}$  or that have a non-cylindrical shape for their curved surface, the synchrotron may yet turn out to have important uses.

### 5.3 Ray-Tracing Calculations of Supported Ge Waveguides

The ray-tracing computational method clearly presents a potential to use as a tool for optimizing the waveguide performance. The calculations suggest that the better performance (i.e., both for improved spectral quality and enhanced sensitivity) can be achieved by the cylinder-planar waveguides with a radius of curvature, at its bottom surface, in the range of 2000–3000 mm. This would consequently give rise to more powerful evanescent-wave sensors, particularly for microanalysis, in the near future.

Finally, the additional results of ray-tracing calculations indicate that even for thicker tapered waveguides, changes in the waveguide shape may lead to increased utility. For example, a Gaussian shape for the bottom surface is expected to result in an increase in the average off-axis angle of propagation at the waveguide center, as compared to the cylinder-planar waveguides fabricated so far (which have a standard cylindrical surface). If such a waveguide shape can be fabricated, it is expected to lead to improved spectral quality (i.e., spectral SNR) by giving higher evanescent-wave absorption signals due to the presence of a larger average number of internal reflections. Such ray-trace calculations is substantially crucial in explaining the properties of evanescent-wave absorption spectra measured with a particular Ge waveguide sensors using multimode light as well as with synchrotron radiation.

## REFERENCES

1. Griffiths, P. R.; and de Haseth, J. A. Fourier Transform Infrared Spectrometry. In Elving, P. J.; Winefordner, J. D.; and Kolthoff, I. M. (eds.), Chemical Analysis Vol. 83. New York: John Wiley & Sons, 1986.
2. Niemela, P.; and Suhonen, J. Rugged Fiber-Optic Raman Probe for Process Monitoring Applications. Appl. Spectrosc. 55 (2001): 1337–1340.
3. Blair, D. S.; Burgess, L. W.; and Brodsky, A. M. Study of Analyte Diffusion into a Silicone-Clad Fiber-Optic Chemical Sensor by Evanescent Wave Spectroscopy. Appl. Spectrosc. 49 (1995): 1636–1645.
4. Walker, D. S.; Reichert, W. M.; and Berry, C. J. Corning 7059, Silicon Oxynitride, and Silicon Dioxide Thin-Film Integrated Optical Waveguides: In Search of Low Loss, Nonfluorescent, Reusable Glass Waveguides. Appl. Spectrosc. 46 (1992): 1437–1441.
5. Han, L.; Niemczyk, T. M.; Lu, Y.; and Lopez, G. P. Chemical Sensors Based on Surface-Modified Sol-Gel-Coated Infrared Waveguides. Appl. Spectrosc. 52 (1998): 119–122.
6. Han, L.; Niemczyk, T. M.; Haaland, D. M.; and Lopez, G. P. Enhancing IR Detection Limits for Trace Polar Organics in Aqueous Solution with Surface-Modified Sol-Gel-Coated ATR Sensors. Appl. Spectrosc. 53 (1999): 381–389.
7. Frank, J.; Schindler, R.; Lendl, O.; and Lendl, B. Improved Fiber-Detector Coupling for MIR Spectroscopy Employing Shaped Silver Halide Fibers. Appl. Spectrosc. 54 (2000): 1417–1422.
8. Karlowatz, M.; Kraft, M.; Eitenberger, E.; Mizaikoff, B.; and Katzir, A. Chemically Tapered Silver Halide Fibers: An Approach for Increasing the Sensitivity of Mid-Infrared Evanescent Wave Sensors. Appl. Spectrosc. 54 (2000): 1629–1633.
9. Han, P.; Tacke, M.; Jakusch, M.; Mizaikoff, B.; Spector, O.; and Katzir, A. Detection of Hydrocarbons in Water by MIR Evanescent-Wave Spectroscopy with Flatten Silver Halide Fibers. Appl. Spectrosc. 55 (2001): 39–43.

10. Yeh, T.-C.; Tien, P.; and Chau, L.-K. Fiber-Optic Evanescent-Wave Absorption Copper (II) Sensor Based on Sol-Gel-Derived Organofunctionalized Silica Cladding. *Appl. Spectrosc.* 55 (2001): 1320–1326.
11. Haibach, F. G.; Sanchez, A.; Floro, J. A.; and Niemczyk, T. M. Extended Spectral Range Surface-Modified Sol-Gel Coated Infrared Waveguide Sensors. *Appl. Spectrosc.* 56 (2002): 398–400.
12. Dekel, B.; and Katzir, A. Mid-Infrared Diffused Planar Waveguides Made of Silver Halide Chloro-Bromide. *Appl. Opt.* 41 (2002): 3622–3627.
13. Kraft, M.; Jakusch, M.; Karlowatz, M.; Katzir, A.; and Mizaikoff, B. New Frontiers for Mid-Infrared Sensors: Towards Deep Sea Monitoring with a Submarine FT-IR Sensor System. *Appl. Spectrosc.* 57 (2003): 591–599.
14. Steiner, H.; Jakusch, M.; Kraft, M.; Karlowatz, M.; Baumann, T.; Niessner, R.; Konz, W.; Brandenburg, A.; Michel, K.; Boussard-Pledel, C.; Bureau, B.; Lucas, J.; Raichlin, Y.; Katzir, A.; Fleischmann, N.; Staubmann, K.; Allabashi, R.; Bayona, J. M.; and Mizaikoff, B. In-situ Sensing of Volatile Organic Compounds in Groundwater: First Field Tests of a Mid-Infrared Fiber-Optic Sensing System. *Appl. Spectrosc.* 57 (2003): 607–613.
15. Janotta, M.; Katzir, A.; and Mizaikoff, B. Sol-Gel-Coated Mid-Infrared Fiber-Optic Sensors. *Appl. Spectrosc.* 57 (2003): 823–828.
16. Raichlin, Y.; Fel, L.; and Katzir, A. Evanescent-Wave Infrared Spectroscopy with Flattened Fibers as Sensing Elements. *Opt. Lett.* 28 (2003): 2297–2299.
17. Rave, E.; Ephrat, P.; Goldberg, M.; Kedmi, E.; and Katzir, A. Silver Halide Photonic Crystal Fibers for the Middle Infrared. *Appl. Opt.* 43 (2004): 2236–2241.
18. Raichlin, Y.; Milo, A.; and Katzir, A. Investigations of the Structure of Water Using Mid-IR Fiberoptic Evanescent Wave Spectroscopy. *Phys. Rev. Lett.* 93 (2004): 185703-1–185703-4.
19. Harrick, N. J. *Internal Reflection Spectroscopy*. 2<sup>nd</sup> ed. New York: Interscience, 1979.

20. Harrick, N. J. Surface Chemistry from Spectral Analysis of Totally Internally Reflected Radiation. J. Phys. Chem. 64 (1960): 1110–1114.
21. Ekgasit, S.; and Ishida, H. Optical Depth Profiling by Multiple Angle Attenuated Total Reflection Fourier Transform Infrared Spectroscopy: A New Approach. Appl. Spectrosc. 50 (1996): 1187–1195.
22. Jonas, R. E.; and Braiman, M. S. Efficient Source-to-Fiber Coupling Method Using a Diamond Rod: Theory and Application to Multimode Evanescent-Wave IR Absorption Spectroscopy. Appl. Spectrosc. 47 (1993): 1751–1759.
23. Braiman, M. S.; and Plunkett, S. E. Design for Supported Planar Waveguides for Obtaining Mid-IR Evanescent-Wave Absorption Spectra from Biomembranes of Individual Cells. Appl. Spectrosc. 51 (1997): 592–597.
24. Plunkett, S. E.; Propst, S.; and Braiman, M. S. Supported Planar Germanium Waveguides for Infrared Evanescent-Wave Sensing. Appl. Opt. 36 (1997): 4055–4061.
25. Plunkett, S. E.; Jonas, R. E.; and Braiman, M. S. Vibrational Spectra of Individual Millimeter-Size Membrane Patches Using Miniature Infrared Waveguides. Biophys. J. 73 (1997): 2235–2240.
26. Stone, J. J.; Braiman, M. S.; and Plunkett, S. E. Mid-IR Evanescent-Wave Absorption Spectra of Thin Films and Coatings Measured with a ~50- $\mu\text{m}$ -thick Planar Ge Waveguide Sensors. Proc. SPIE-Int. Soc. Opt. Eng. 3105 (1997): 371–377.
27. Braiman, M. S.; Plunkett, S. E.; and Stone, J. J. Surface-Sensitive FTIR Spectral Measurement of Nanogram Samples Using 30-100- $\mu\text{m}$ -thick Planar Ge Waveguides. AIP Conf. Proc. 430 (1998): 577–580.
28. Braiman, M. S.; and Mi, L.-Z. Tapered Quasi-Planar Germanium Waveguides for Mid-IR Chemical and Biochemical Sensing. Proc. SPIE-Int. Soc. Opt. Eng. 3540 (1999): 146–152.
29. Shilov, S. V.; Braiman, M. S.; and Mi, L.-Z. Mid-IR Evanescent-Wave Sensors for Tiny Biological Samples. Proc. SPIE-Int. Soc. Opt. Eng. 3918 (2000): 202–207.



30. White, S. R.; and Nave, S. E. Spectrometric Temperature Measurement Using a Zinc Selenide-Based Fiber-Optic Sensor. Appl. Spectrosc. 53 (1999): 1138–1142.
31. Burger, R. J.; Melling, P. J.; Moser, W. A.; and Berard, J.-R. Remote Spectroscopy Using Mid-IR Fiber-Coupled Laboratory Apparatus. Proc. SPIE-Int. Soc. Opt. Eng. 1591 (1991): 246–255.
32. Bornstein, A.; Katz, M.; Baram, A.; and Wolfman, D. Attenuated Total Reflection Spectroscopy with Chalcogenide Bi-Tapered Fibers. Proc. SPIE-Int. Soc. Opt. Eng. 1591 (1991): 256–262.
33. Vongsvivut, J.; Shilov, S. V.; Ekgasit, S.; and Braiman, M. S. Symmetrically Tapered <math><30\text{-}\mu\text{m}</math>-thick Quasi-Planar Germanium Waveguides as Chemical Sensors for Microanalysis. Appl. Spectrosc. 56 (2002): 1552–1561.
34. Theocharous, E.; and Birch, J. R. Detectors for Mid- and Far-infrared Spectrometry: Selection and Use. In Chalmers, J. M.; and Griffiths, P. R. (eds.), Handbook of Vibrational Spectroscopy Vol. 1 (Theory and Instrumentation), pp. 349–367. New York: John Wiley & Sons, 2002.
35. Lee, D. L. Electromagnetic Principles of Integrated Optics. New York: John Wiley & Sons, 1986.
36. Urban, M. W. Attenuated Total Reflectance Spectroscopy of Polymer: Theory and Practice. Washington: American Chemical Society, 1996.
37. Biran, I.; and Walt, D. R. Optrode-Based Fiber Optic Biosensors (Bio-Optrode). In Ligler, F. S.; and Rowe-Taitt, C. A. (eds.), Optical Biosensors: Present and Future, pp. 5–56. Amsterdam, The Netherlands: Elsevier Science, 2002.
38. Nishihara, H.; Haruna, M.; and Suhara, T. Optical Integrated Circuits. In Fischer, R. E.; and Smith, W. J. (eds.), McGraw-Hill Optical and Electro-Optical Engineering Series, New York: McGraw-Hill, 1985.
39. Marcuse, D. Theory of Dielectric Optical Waveguides. 2<sup>nd</sup> ed. New York: Academic Press, 1991.

40. William, G. P. Synchrotron and Free Electron Laser Sources of Infrared Radiation. In Chalmers, J. M.; and Griffiths, P. R. (eds.), Handbook of Vibrational Spectroscopy Vol. 1 (Theory and Instrumentation), pp. 341–348. New York: John Wiley & Sons, 2002.
41. Marinkovic, N. S.; Huang, R.; Bromberg, P.; Sullivan, M.; Toomey, J.; Miller, L. M.; Sperber, E.; Mosche, S.; Jones, K. W.; Chouparova, E.; Lappi, S.; Franzen, S.; and Chance, M. R. Center for Synchrotron Biosciences' U2B Beamline: An International Resource for Biological Infrared Spectroscopy. J. Synchrotron Rad. 58 (2002): 1–10.
42. Wetzel, D. L.; and LeVine, S. M. Biological Applications of Infrared Microspectroscopy. In Gremlich, H.-U.; and Yan, B. (eds.), Infrared and Raman Spectroscopy of Biological Materials, pp. 101–142. New York: Marcel Dekker, 2000.
43. Harrick, N. J. Determination of Refractive Index and Film Thickness from Interference Fringes. Appl. Opt. 10 (1971): 2344–2349.
44. Chang, W. S. C.; and Loh, K. W. Experimental Observation of 10.6-micron Guided Wave in Ge Thin Films. Appl. Opt. 10 (1971): 2361–2362.
45. Ferrell, D. J.; Lerner, J. M.; Lieberman, R. A.; Quintana, T.; Schmidlin, E. M.; and Syracuse, S. J. Instrumentation Systems for Passive Fiber Optic Chemical Sensors. Opt. Eng. 32 (1993): 504–507.
46. Abramson, N. H. Holography as a Teaching Tool. Opt. Eng. 32 (1993): 508–513.
47. Braiman, M. S.; Mogi, T.; Marti, Th.; Stern, L. J.; Khorana, H. G.; and Rothschild, K. J. Vibrational Spectroscopy of Bacteriorhodopsin Mutants. Light-Driven Proton Transport Involves Protonation Changes of Aspartic Acid Residues 85, 96, and 212. Biochemistry 27 (1988): 8516–8520.
48. Dioumaev, A. K.; and Braiman, M. S. Two Bathointermediates of the Bacteriorhodopsin Photocycle, Distinguished by Nanosecond Time-Resolved FTIR Spectroscopy at Room Temperature. J. Phys. Chem. B 101 (1997): 1655–1662.

49. Hutson, M. S.; Alexiev, U.; Shilov, S. V.; Wise, K. J.; and Braiman, M. S. Evidence for a Perturbation of Arginine-82 in the Bacteriorhodopsin Photocycle from Time-Resolved Infrared Spectra. Biochemistry 39 (2000): 13189–131200.
50. Lyman, D. J.; Murray-Wijelath, J.; and Feughelman, M. Effect of Temperature on the Conformation of Extended  $\alpha$ -Keratin. Appl. Spectrosc. 55 (2001): 552–554.
51. Küpper, L.; Heise, H. M.; Bechara, F.-G.; and Stücker, M. Micro-Domain Analysis of Skin Samples of Moor-Mummified Corpses by Evanescent Wave Infrared Spectroscopy Using Silver Halide Fibers. J. Mol. Struct. 565–566 (2001): 497–504.
52. Vongsvivut, J.; Fernandez, J.; Ekgasit, S.; and Braiman, M. S. Characterization of Supported Cylinder-Planar Germanium Waveguide Sensors with Synchrotron Infrared Radiation. Appl. Spectrosc. 58 (2004): 143–151.
53. Tang, Y. N.; and Pearson, P. VUV Storage Ring Parameters as of December 2002 [Online]. 2002. Available from: [http://nslsweb.nsls.bnl.gov/nsls/org/AccPhys/vuv/vuv\\_parameters.pdf](http://nslsweb.nsls.bnl.gov/nsls/org/AccPhys/vuv/vuv_parameters.pdf) [2003, March 1].



**APPENDICES**

สถาบันวิทยบริการ  
จุฬาลงกรณ์มหาวิทยาลัย

## APPENDIX A

Symmetrically Tapered  $<30\text{-}\mu\text{m}$ -thick Quasi-Planar  
Germanium Waveguides as Chemical Sensors  
for Microanalysis

Jitraporn Vongsvivut, Sergey V. Shilov,  
Sanong Ekgasit, and Mark S. Braiman

*Applied Spectroscopy* (2002) 56: 1552 – 1561.

สถาบันวิทยบริการ  
จุฬาลงกรณ์มหาวิทยาลัย

# Symmetrically Tapered <math><30\text{-}\mu\text{m}</math>-thick Quasi-Planar Germanium Waveguides as Chemical Sensors for Microanalysis

JITRAPORN VONGSVIVUT, SERGEY V. SHILOV,\* SANONG EKGASIT, and MARK S. BRAIMAN<sup>2</sup>

Department of Chemistry, Faculty of Science, Chulalongkorn University, Bangkok 10330 Thailand (J.V., S.E.); and Chemistry Department, Syracuse University, Syracuse, New York 13244-4100 (S.V.S., M.S.B.)

Symmetrically tapered planar IR waveguides have been fabricated by starting with a ZnS coated concave piece of single-crystal Ge, embedding it in an epoxide resin as a supporting substrate, and then grinding and polishing a planar surface until the thickness at the taper minimum is <math><30\ \mu\text{m}</math>. Such tapering is expected to enhance a waveguide's sensitivity as an evanescent wave sensor by maximizing the amount of evanescent wave energy present at the thinnest part of the waveguide. As predicted by theory, the surface sensitivity, i.e., the absorbance signal per molecule in contact with the sensing region, increases with decreasing thickness of the tapered region even while the total energy throughput decreases. The signal-to-noise ratio obtained depends very strongly on the quality of the polished surfaces of the waveguides. The surface sensitivity is superior to that obtained with a commercial Ge attenuated total reflection (ATR) accessory for several types of sample, including thin films (<math><10\ \text{ng}</math>) and small volumes (<math><1\ \mu\text{L}</math>) of volatile solvents. By using the waveguides, light-induced structural changes in the protein bacteriorhodopsin were observable using samples as small as <math>\sim 50\ \text{pmol}</math> (<math>\sim 1\ \mu\text{g}</math>). In addition, the waveguide sensors can reveal the surface compositions on a single human hair, pointing to their promise as a tool for forensic fiber analysis.

Index Headings: Tapered Ge waveguides; Evanescent wave sensor; Throughput; Sensitivity; Nujol; D96N mutant; Bacteriorhodopsin (bR); Hair analysis.

## INTRODUCTION

Attempts to develop compact chemical sensors based on optical fibers and other types of miniature waveguides have been driven by increasing demands to handle very small-sized samples in microanalysis and trace analysis. The greatest progress on development of waveguide sensors based on vibrational spectroscopy has been in the near-infrared (NIR), due to greater manufacturing experience with silica and other optical glasses that transmit in the visible and NIR. Due to significantly stronger and more easily interpreted fundamental absorption bands in the mid-infrared (MIR) region, as compared to the overtones or combination bands appearing in the NIR region, it is desirable to develop alternative waveguides for the MIR spectral range. MIR optical waveguides have been fabricated from IR-transparent materials with high refractive index such as germanium (Ge), zinc selenide (ZnSe), and chalcogenide.<sup>1-11</sup> MIR optical sensors have been demonstrated to be a potentially powerful chemical

sensing tool, as seen in many publications over the past few years.<sup>12-18</sup>

Whether a cylindrical optical fiber or a planar waveguide in various shapes is utilized, the technique can generally be referred to as either attenuated total reflection (ATR) or evanescent wave absorption. This phenomenon is well known in MIR spectroscopy and has successfully become a widespread technique for both qualitative and quantitative measurements. In this case, the measured absorption spectrum is the result of attenuation of the evanescent wave accompanying an incident IR beam traveling through the high-index waveguide. At the interface of two media with different refractive indices, the evanescent field penetrates a fraction of a wavelength beyond the waveguide into the lower-index sample layer. It decays exponentially within a shallow region, defined by the penetration depth ( $d_p$ ). For MIR light, the penetration depth is generally in the range of 0.5–5  $\mu\text{m}$  depending on both experimental conditions (e.g., angle of incidence) and material characteristics (i.e., refractive indices of waveguide and sample).<sup>19</sup> In general, the limits of detection for various MIR sensing systems have been too high for use as a trace method. Hence, there is substantial interest in improvements in the design and optical configuration of waveguide sensors in order to enhance their sensitivity.

Use of some optical fibers made of IR-transmitting glasses have been published.<sup>2-11</sup> More recently, methods of fabricating supported thin planar germanium (Ge) waveguides have already been published by our laboratory.<sup>2-8</sup> These  $\sim 50\text{-}\mu\text{m}$ -thick supported planar Ge waveguides have also previously been presented as chemical tools for applications with biomolecules,<sup>3,4</sup> but the use of IR microscopes with the waveguide created a substantial restriction on sample handling and also limited the waveguide length to the range of <math><12\ \text{mm}</math>, the maximum adjustable distance between the focal points of objective and condenser in commercial FT-IR microscopes. In order to eliminate the IR microscope, several new designs of thin Ge waveguides have been presented that rely on particular fabrication processes.<sup>7,8</sup>

One difficulty in fabricating Ge waveguides as thin as <math><30\ \mu\text{m}</math> is the poor mechanical stability of Ge, i.e., it can be easily broken during a grinding or polishing process. However, its property of chemical inertness, particularly with biochemical molecules in picomolar quantities, is a continued impetus for choosing this material. For development studies, an additional advantage is the

Received 13 May 2002; accepted 18 August 2002.

\* Current address: Bruker Optics Inc., Manning Park, Billerica, MA 01821.

<sup>2</sup> Author to whom correspondence should be sent.

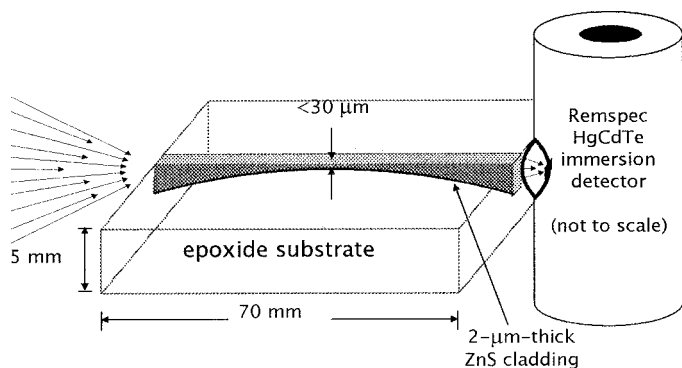


FIG. 1. Schematic configuration of the  $<30\text{-}\mu\text{m}$ -thick symmetrically tapered Ge waveguide supported by epoxide substrate and used as miniature internal reflection element (IRE). The top planar surface of the waveguide acts as a sensing area, while its bottom is a cylindrical sector with a diameter of 600 mm, coated with a  $2\text{-}\mu\text{m}$ -thick ZnS cladding layer. Incident light, indicated at left, was typically generated from the IR source of an FT-IR spectrometer, and the output was coupled onto a liquid  $\text{N}_2$  cooled HgCdTe immersion detector placed as close as possible to the exit end of the waveguide. The detector window, outside the lens, is not shown.

presence of characteristic high- and low-frequency Ge cut-offs at  $5200$  and  $670\text{ cm}^{-1}$ , respectively. The presence of these cut-off frequencies provides useful evidence for propagation of broadband IR light through the waveguide.

In the work described here, we reduce the sensor-region thickness of symmetrically tapered Ge waveguides (see Fig. 1) to  $7\text{--}30\text{ }\mu\text{m}$  in order to achieve further sensitivity enhancements. Tapering allows the use of common focusing optical elements without an IR microscope. Substantially higher total energy throughput can then be achieved with very simple optical alignment procedures, as illustrated in Fig. 1. The tapered waveguides have a planar upper surface and a gently curved lower surface that is parallel to the upper surface only near the line segment corresponding to the thinnest region of the waveguide. Lacking a planar lower surface, these waveguides do not meet the standard definition of planar waveguides; but because of their near-parallelism at the sensing region, we refer to them as quasi-planar.

Tapering to such a thin dimension is expected to result in enhanced sensitivity through an increase in the detected absorption intensity per unit area of sample-waveguide contact. The challenge addressed in the current work was in maintaining adequate throughput of light to be able to take advantage of the high surface sensitivity. We present a number of potential new applications for the waveguide sensors, including light-dark difference spectroscopy of picomolar quantities of the purple membrane protein, bacteriorhodopsin (bR), and the nondestructive surface layers of short pieces of human hairs.

## EXPERIMENTAL

**Waveguide Fabrication.** The raw material utilized for fabrication of waveguides was a  $70\text{-mm}$ -diameter,  $3\text{-mm}$ -thick single-crystalline Ge disk (Lattice Materials Corp., Bozeman, MT). The disk was first symmetrically tapered and polished on a grinding machine (K & S Optics, Binghamton, NY) with a cylindrical aluminum grinding tool with a  $600\text{-mm}$  curvature diameter, producing a curved

surface on one side of the disk as depicted in Fig. 1. The polished curved surface was then coated with a  $2\text{-}\mu\text{m}$ -thick ZnS cladding layer by using a chemical vapor deposition (CVD) process. This cladding layer prevents IR light from being absorbed by the supporting substrate. The ZnS coated round Ge disk was then diced into  $2\text{-mm}$ -wide strips using a vertical band saw (Materials Facility, Cornell Center for Materials Research, Cornell University, Ithaca, NY). Each of these strips was ground on its two parallel planar sides, to a final width of  $0.5\text{--}1\text{ mm}$ .

In the next step, each ZnS coated tapered Ge strip was individually embedded into epoxide resin (Epothin<sup>®</sup>, Buehler Ltd., Lake Bluff, IL) by pouring a well-blended mixture of epoxide resin and hardener in the manufacturer's recommended proportion onto the Ge strip held, flat side down, in a disk-shaped mold. After the epoxide resin was completely polymerized and fully hardened, the bottom (flat) side of the Ge and epoxide was ground and polished to the desired thickness, i.e.,  $<30\text{ }\mu\text{m}$ . For experiments to determine the effect of surface-finish quality on waveguide transmittance, hand grinding and polishing utilized various polishing compounds and polishing disks manufactured by Buehler Ltd. (Lake Bluff, IL). For all other experiments, in order to obtain a high-quality finish, waveguides were sent to a commercial optics house (K & S Optics, Binghamton, NY) equipped with automated grinding/polishing machines.

The quality of spectra taken with these tapered Ge waveguides depends strongly on the quality of the final polished sensing surfaces because surface scratches cause light scattering and thereby result in less total energy throughput and a correspondingly poor signal-to-noise (S/N) ratio. The thickness of the waveguide was determined periodically during grinding and polishing by rinsing and drying the waveguide, then measuring the interference pattern ("channeling") that appears on the single beam spectrum taken transverse to the thinnest part of the waveguide with an IR microscope (IR-Plan Infrared Microscope Accessory, Spectra-Tech, Stamford, CT) connected to an FT-IR interferometer (Illuminator, Midac Corp., Irvine, CA) in reflectance mode with a  $1\text{ cm}^{-1}$  spectral resolution and 256 scans.<sup>20</sup>

**Waveguide Optical Alignment.** Figure 1 shows a schematic of a  $<30\text{-}\mu\text{m}$ -thick symmetrically tapered Ge waveguide. The top flat surface of the waveguide acts as a sensing area, while its ZnSe coated curved bottom helps increase the number of total internal reflections, resulting in enhanced sensitivity, particularly in the middle part of the waveguide.

Broadband IR light from the spectrometer's external beam port is focused onto the entrance end of the waveguide. The output end of the waveguide is butt-coupled against the window of a liquid  $\text{N}_2$  cooled HgCdTe immersion detector (MOD-O2S1, Remspec Corp., Sturbridge, MA). The collimated beam exiting the external output port of the spectrometer was simply focused onto the entrance end of the waveguide by using a single off-axis paraboloid mirror with a  $19.1\text{-mm}$  focal length. In order to maximize absorption intensity as well as to increase reproducibility, every sample applied in the experiment must be carefully placed in contact with the

sensing surface at the thinnest (center) point on the waveguide.

**Comparisons to Standard Attenuated Total Reflection Measurements.** Attenuated total reflection measurements obtained with the tapered Ge waveguides were compared with those obtained by using a commercially available macroscopic ATR accessory (Out-of-Compartment Contact Sampler™ with 45° Ge Trough Plate Kit, Spectra-Tech, Shelton, CT). For experiments with the commercial ATR accessory, a photodiode HgCdTe detector (Model KMPV11-1-LJ2/239 with 0.785 mm<sup>2</sup> active area, Kolmar Technologies Inc., Conyers, GA) internal to the spectrometer was utilized. The manufacturer's specified  $D^*$  value of this detector at 10 kHz was  $3.23 \times 10^{10}$  cm Hz<sup>1/2</sup> W<sup>-1</sup>, compared to  $\geq 4 \times 10^{10}$  cm Hz<sup>1/2</sup> W<sup>-1</sup> for the Remspec immersion detector.

For purposes of spectral comparisons between waveguide and commercial ATR accessory, the same experimental parameters were utilized on a Bruker IFS66 FT-IR spectrometer. All IR spectra shown below were acquired by using an 8 cm<sup>-1</sup> resolution and a 7800 cm<sup>-1</sup> bandwidth. The mirror velocity was 3.164 cm s<sup>-1</sup>, giving an optical retardation velocity (ORV) of 100 kHz for the HeNe reference beam. The number of coadded scans is mentioned individually in each figure. Blackman-Harris 3-Term apodization, Mertz phase correction, and zeroing of 2 were set as default acquisition parameters with the gain of 1 under Opus software.

**Preparation of Bacteriorhodopsin Film for Light-Dark Experiments.** The D96N mutant of bacteriorhodopsin (D96N-bR) used was in the form of purple membranes. This mutant was selected because it has a greatly slowed photocycle when dried from a buffer at an elevated pH, permitting light-dark difference measurements at room temperature. For the ATR-IR experiment, 1  $\mu$ L of unbuffered D96N-bR suspension with a concentration of 1.3 mg/mL was placed on the central 2–3 mm portion of the waveguide and completely air-dried for ~20 min prior to pH adjustment. A droplet of 25 mM TRIS buffer at pH 9.5 was subsequently applied on the thin purple film and dried again. The sample preparation was the same for both the commercial ATR accessory and the 14- $\mu$ m-thick tapered Ge waveguide. Only the total volume of sample solution applied is different in each experiment.

Infrared spectra were collected with either the commercial ATR accessory or the 14- $\mu$ m-thick tapered Ge waveguide, always using the Bruker IFS66 FT-IR spectrometer. The D96N purple membrane film was illuminated with a standard 150 watt quartz-halogen fiber-optic illuminator (Model 180, Dolan-Jenner Industries Inc., Lawrence, MA). The illumination and data collection were automatically controlled by rapid-scan time-resolved spectroscopy mode under Opus software. The loop started by taking a background spectrum in dark conditions for 30 s (=192 scans), and then turning on the illuminator to expose the D96N purple membrane film for 20 s. A sample spectrum, representing D96N-bR in the so-called M state, was initiated ~1 s after the lamp was turned off and lasted for a duration of 10 s (=64 scans) to complete one loop. The next loop was started after a 1-min delay in order to let the sample relax back to the unphotolyzed state. Averaging many dark/light cycles

was necessary to obtain an adequate S/N ratio in the difference IR spectrum. After finishing all the loops, the alternately collected single-beam spectra of background (i.e., unphotolyzed bR state) and sample (i.e., photolyzed M state) were coadded separately. The final static FT-IR difference spectrum is the ratio of coadded sample and background spectra, converted to absorbance units.

## RESULTS AND DISCUSSION

Previous theoretical calculations, based on a planar waveguide extending to infinity in two dimensions and with a finite thickness in the third,<sup>2</sup> indicate that the highest absorbance sensitivities should be achieved from waveguides with a thickness in the range of 0.5–1  $\mu$ m. Such waveguides are not yet realized due to the brittleness of Ge and other fabrication difficulties.

However, we have now successfully fabricated <30- $\mu$ m-thick symmetrically tapered Ge waveguides, which are the thinnest direct-coupled IREs demonstrated to date. The fabrication and coupling methods differ somewhat from those described in previous publications<sup>2–7</sup> in order to eliminate several difficulties. First, using a waveguide with symmetrical tapering helps simplify the alignment of the beam and detector when using a direct coupling method, as illustrated in Fig. 1. In particular, the taper yields sufficient throughput energy to come close to saturating a 0.25 mm<sup>2</sup> HgCdTe detector without requiring an IR microscope as a focusing optical element. The 1-mm<sup>2</sup> ends of the waveguide are large enough to make initial alignment by eye possible. Simultaneously, the taper keeps high the number of reflections in the middle sensing region, where the waveguide is thinnest. In addition, the flat and flush horizontal sensing area of the epoxide-embedded tapered waveguides results in easy sampling and cleaning. Furthermore, completely embedding the Ge strip in the epoxide substrate, instead of cementing just one surface to a quartz substrate as described previously,<sup>3–7</sup> provides more mechanical support for the waveguide. In particular, it reduces the possibility of damage to the waveguide during grinding and polishing.

**Variation of Waveguide Thickness.** The evanescent wave absorption properties of symmetrically tapered Ge waveguides were investigated after careful alignment, as determined by detected throughput. We first analyzed the throughput as a function of decreasing waveguide thickness. Figure 2 displays several FT-IR single-beam spectra acquired from thin symmetrically tapered Ge waveguides with different thicknesses. As can clearly be seen, the observed throughput diminishes with decreasing thickness, due to cut-off of higher-order modes.<sup>21–23</sup>

The single-beam spectra (Fig. 2) reveal the characteristic frequency cut-offs of Ge at 5200 and 670 cm<sup>-1</sup> and demonstrate that light is genuinely guided through the thin Ge layer. The lower-frequency cut-off demonstrates a benefit of using Ge waveguides. In contrast, there is a lack of transparency with silicon (Si) waveguides in the IR region 1500–700 cm<sup>-1</sup>, where there is rich spectral information for most organic compounds.

In order to investigate the effect of the tapered thickness on waveguide sensitivity, a 1-mm-diameter (~1  $\mu$ L) water droplet covering the 1  $\times$  1 mm<sup>2</sup> sensing area was



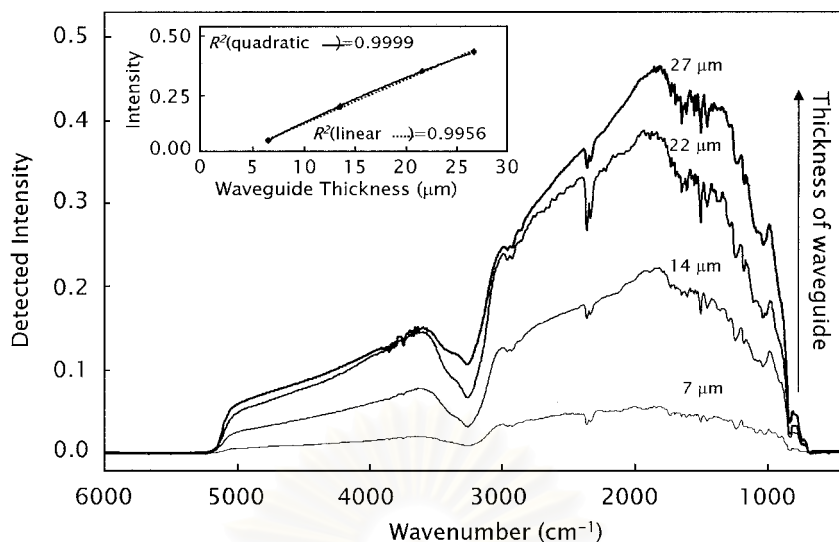


FIG. 2. FT-IR single-beam spectra of symmetrically tapered Ge waveguides with different thicknesses (i.e., 7, 14, 22, and 27  $\mu\text{m}$  from lower to upper lines, respectively). All spectra were collected with 1-min scans and under identical conditions. The y-axis scale stands for arbitrary intensity units, which are the same for all plots shown here. As clearly seen, the throughput diminishes with decreasing thickness, with a correlation coefficient of  $R^2 = 0.9999$  and  $0.9956$  for quadratic and linear relationships, respectively (see Inset). The plot fits with the quadratic equation of  $y = -0.0002x^2 + 0.0292x - 0.1352$ . **Inset:** Plot of the detected intensity at  $1850\text{ cm}^{-1}$  as a function of the waveguide thickness.

carefully sampled at the same (thinnest) part of each of several waveguides. The resulting absorbance spectra are presented in Fig. 3. It can be seen that the waveguide's sensitivity, in terms of absorbance for a particular small-area liquid sample, increases as waveguide thickness decreases. This enhanced sensitivity with decreasing thickness is due both to the increase in number of internal reflections per mm of waveguide length and to the increase in the average evanescent wave surface intensity of the transmitted modes.<sup>2</sup> The inset of Fig. 3 indicates a drastic increase in absorbance when the waveguide thickness is  $<10\ \mu\text{m}$ . On the other hand, a very thin waveguide (i.e.,  $<10\ \mu\text{m}$ ) results in distinctly lower total throughput and an increase in spectral noise level. To

improve the spectral quality, a higher number of scans must be used.

**Variations in Optical Coupling with Sample.** We additionally observed the dependence of absorption intensity on sampling length as shown in Fig. 4. With a planar waveguide, absorbance is expected to increase in direct proportion to sample contact length. With a tapered waveguide, on the other hand, the increase in absorbance as a function of contact length is expected to be sub-linear because the average number of reflections per unit length of sample contact decreases as sample is added to regions of the waveguide away from its central minimum. This was observed, as shown in the inset of Fig. 4. Each plot of absorbance at  $3400\text{ cm}^{-1}$  ( $A_{3400}$ ) as a function of

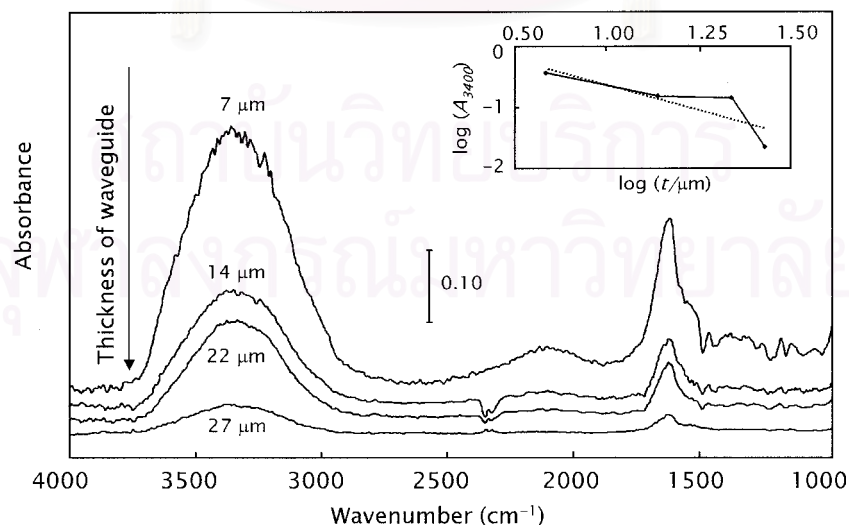


FIG. 3. ATR-IR spectra of a  $1\text{-}\mu\text{L}$  water droplet, covering an  $\sim 1\text{ mm}^2$  sensing area, acquired by using symmetrically tapered Ge waveguides with different thicknesses (i.e., 7, 14, 22, and 27  $\mu\text{m}$  from upper to lower lines, respectively). Original single-beam sample spectra were converted to absorbances by ratioing to the corresponding background spectra shown in Fig. 2 at the same thickness with the same experimental parameters. The spectra with higher absorbances correspond to measurements using thinner waveguides. **Inset:** Plot between the logarithm of the absorption intensity at  $3400\text{ cm}^{-1}$  [ $\log(A_{3400})$ ], due to the O-H stretching vibration, vs. the logarithm of waveguide thickness [ $\log(t)$ ].

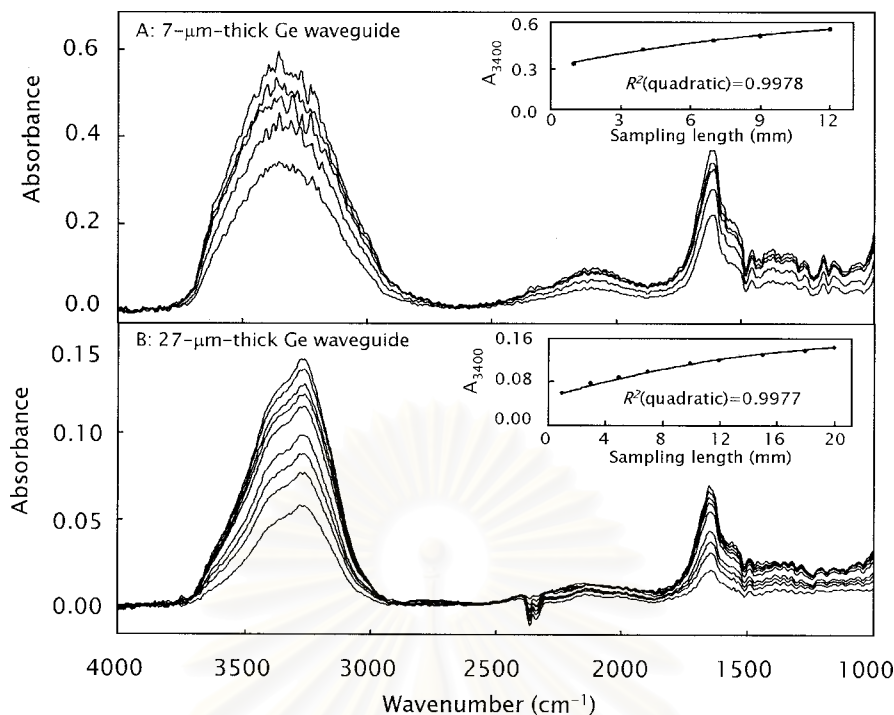


FIG. 4. ATR-IR spectra of water droplets of different lengths contacting the sensing surface of the waveguide. (A) Spectra were obtained by using a 7- $\mu\text{m}$ -thick Ge waveguide, with sampling lengths of 1, 4, 7, 9, and 12 mm from lower to upper lines, respectively; (B) spectra obtained with a 27- $\mu\text{m}$ -thick waveguide with sampling lengths of 1, 3, 5, 7, 10, 12, 15, 18, and 20 mm from lower to upper lines, respectively. All spectra were taken with 1-min scans. Both data sets over this limited range could easily be fit to quadratic relationships between absorption intensity at 3400  $\text{cm}^{-1}$  (i.e., O-H stretching) and sampling length covered by the water droplet. **Insets:** Plot of the absorption intensity at 3400  $\text{cm}^{-1}$  ( $A_{3400}$ ) vs. the sampling length (mm) with a constant width of the waveguide (i.e., 1 mm), for different waveguide thicknesses. Data plotted on each graph coincide with the value of  $A_{3400}$  appearing on each sub-figure.

contact length ( $l$ ) was fitted to a quadratic relationship. The optimized quadratic coefficients gave  $A_{3400} = -0.0009l^2 + 0.0316l + 0.3218$  for the 7- $\mu\text{m}$ -thick waveguide and  $A_{3400} = -0.0001l^2 + 0.0073l + 0.0533$  for the 27- $\mu\text{m}$ -thick waveguide. The quadratic fit is good only up to  $\sim 2$  cm of contact length, after which point the absorbance approaches an asymptotic value monotonically. This observation shows that one advantage of using these  $<30$ - $\mu\text{m}$ -thick tapered Ge waveguides is that only molecules in contact with the thinnest part of the waveguide significantly influence the absorbance spectrum.

In an attempt to further improve the waveguide's sensitivity, we explored several additional variations in optical coupling through the waveguide and sample. First, the overall spectral quality obtained from tapered Ge waveguides depends strongly on the quality of the polished sensing surfaces (see Fig. 5). A better optical-finished surface gives not only a higher absorbance due to the better optical contact between sample and waveguide's surface, but the spectral quality is also distinctively improved because of lower scattering losses caused by surface scratches, resulting in substantially greater throughput. The more thoroughly the surface was polished, the lower the absorbance noise (and therefore the limit of detection) of the waveguide.

Substantially greater detected absorption intensity can sometimes be achieved as a consequence of beam blocking of the on-axis waveguide modes (see Fig. 6). This was demonstrated by using an  $\sim 6$ -mm-diameter aluminum rod held horizontally transverse to the IR beam where it fills an aperture of  $\sim 30$  mm, in order to partially

obstruct the beam. Light rays with low propagation angles in the vertical direction are thus blocked by the aluminum rod. At the selected distance from the waveguide, this rod eliminates rays that would enter the waveguide at an angle of  $<17^\circ$  away from horizontal.

With both waveguide thicknesses investigated, the spectra taken with the centrally blocked beam gave higher absorbance readings than those with an open beam, substantially so in the case of the 22- $\mu\text{m}$ -thick Ge waveguide. The increase in absorption intensity results from selection of only the higher-order modes (i.e., light propagating closer to the normal of the waveguide interface at the points of internal reflection). This is theoretically expected to increase (1) the average number of reflections per unit length; (2) the average evanescent field strength at the sensing area; and (3) the effective average penetration depth into the media beyond the interface. The improvement in absorption intensity is greater with the 22- $\mu\text{m}$ -thick waveguide than with the 14- $\mu\text{m}$ -thick one, probably because the coupling efficiency of the highest-order modes to the detector is always decreased with the thinner waveguide whether or not the central beam is blocked. This observation indicates that blocking even more of the central rays might further increase the absorbance enhancement factor, but would likely give rise to a higher noise level due to the lower total throughput, particularly with thinner waveguides, as clearly seen by comparing the spectral quality in Figs. 6A and 6B.

There are a number of changes in optical coupling that are likely to afford substantial additional improvement in sensitivity, but that we have been unable to investigate

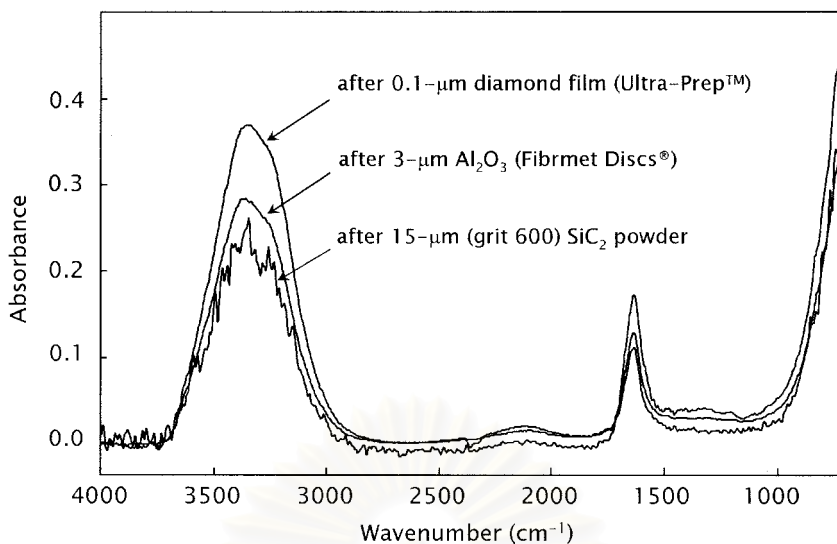


FIG. 5. Effect of the surface quality on absorbance spectral features observed from a 1-cm-diameter water droplet sample. These spectra were collected by using a 100- $\mu\text{m}$ -thick tapered Ge waveguide with  $45^\circ$  bevel angle at both ends with 1-min scans. Data were obtained by hand-polishing the same waveguide with progressively smaller particle sizes (i.e., 15, 3, and 0.1  $\mu\text{m}$  from lower to upper lines, respectively).

so far. Ultimately, the most important of these is likely to be optimization of the detector dimensions. Using a HgCdTe detector with a smaller-area rectangular active element whose aspect ratio is more closely matched to the thinnest part of the waveguide is in theory expected to give somewhat better results than we have so far obtained. By limiting ourselves thus far to a square detector, we were faced with the tradeoff between going to the smallest possible detector, leading to an expected noise

reduction in proportion to the square-root of the detector area, and keeping the output of the entire width of the waveguide imaged onto the detector, which is necessary for maintaining the largest response.

**Applications and Comparisons with a Commercial Ge ATR Accessory. *Small Volumes of Volatile Solvent.*** Figure 7 is the evanescent wave IR spectra of a 1-mm-diameter ( $=1 \mu\text{L}$ ) water droplet in contact with the 14- $\mu\text{m}$ -thick tapered Ge waveguide, compared to that ob-

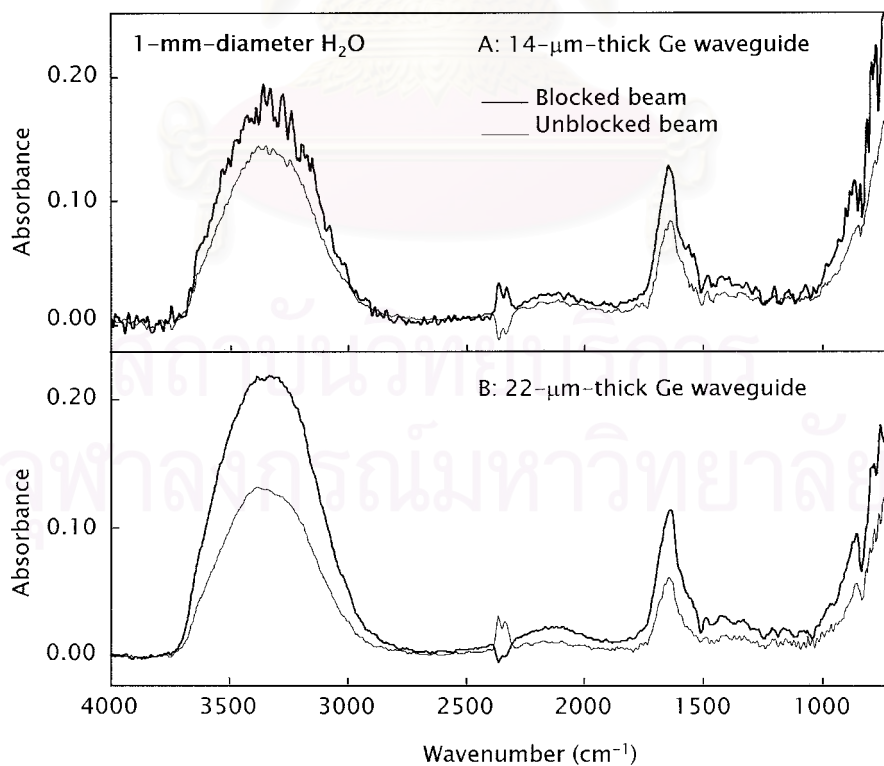


FIG. 6. Effect of central beam blocking on absorption intensity of 1-mm-diameter ( $=1 \mu\text{L}$ ) water droplet investigated by (A) 14- and (B) 22- $\mu\text{m}$ -thick Ge waveguides with 5-min scans. Blocked-beam spectra were recorded after the beam path was obstructed for rays deviating  $<17^\circ$  vertically away from the waveguide axis. In both cases, the spectra exhibit substantially greater absorption intensity enhancement with blocked beam (thick lines) as compared to those with unblocked one (thin lines).

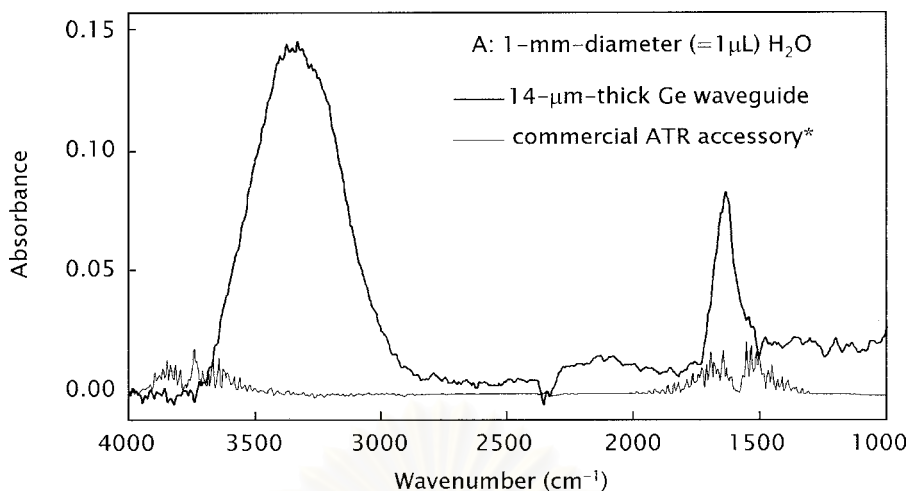


FIG. 7. Comparison of absorption intensities of a 1-mm-diameter water droplet ( $=1 \mu\text{L}$ ) observed by the 14- $\mu\text{m}$ -thick tapered Ge waveguide to those with a commercial macroscopic ATR accessory (\*Out-of-Compartment Contact Sampler<sup>®</sup> with 45° Ge Trough Plate Kit, Spectra-Tech). The sample covered the sensing surface with a total area of 1 mm<sup>2</sup> at the central point. Both spectra represent 5-min scan times.

served with a macroscopic ATR accessory shown in the same figure. By comparison, the absorption intensity of the O–H vibration at 3400 cm<sup>-1</sup> acquired with the thin tapered waveguide is enhanced by a factor of 37 due to the increase in total internal reflections achieved by the tapering method. Thus, small volumes of volatile solvents such as water that cannot easily be spread out in a thin film on a macroscopic ATR can still be sampled using the waveguide.

**Small Quantities of Non-volatile Thin Films.** Figure 8 shows spectral results of 85 ng Nujol deposited as a thin film from hexane solution onto the sensing surfaces of either the commercial ATR accessory or the 14- $\mu\text{m}$ -thick tapered Ge waveguide. The spectra were recorded >1 h after the hexane was visibly evaporated and the film was left exposed to room air. Once again, the 14-

$\mu\text{m}$ -thick tapered Ge waveguide exhibits substantially higher sensitivity than the commercial ATR accessory. The relative absorbance factor observed at 2922 cm<sup>-1</sup> was 13.6 for the 85-ng Nujol sample. This clearly demonstrates the advantage of the thin tapered waveguides for measuring sample-limited thin films. With the traditional Ge ATR accessory, the 85 ng sample size gives absorbance signals that are barely above the noise with a 5-min scan time, whereas with our thin tapered waveguides, the S/N ratio of the strongest bands in the absorbance spectrum substantially exceeds 20. Characteristic peaks of Nujol can therefore be easily identified. The estimated detection limit with a 5-min scan time is 85 ng Nujol deposited on the waveguide's sensing surface. This is, of course, substantially higher than the detection limit for a droplet of pure Nujol measured in transmission

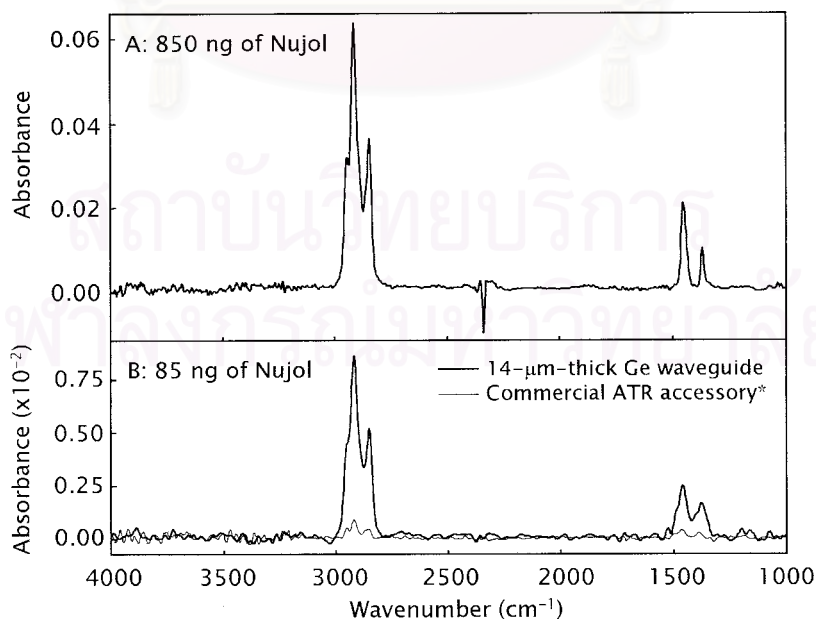


FIG. 8. ATR FT-IR spectra of Nujol thin films with different quantities deposited on the sensing surface, i.e., (A) 850 ng and (B) 85 ng. The thick lines represent the results observed by the 14- $\mu\text{m}$ -thick symmetrically tapered Ge waveguide, while the thin one was collected with the commercial ATR accessory (\*Out-of-Compartment Contact Sampler<sup>®</sup> with 45° Ge Trough Plate Kit, Spectra-Tech). All spectra were taken after hexane was completely evaporated and with 5-min scan times.

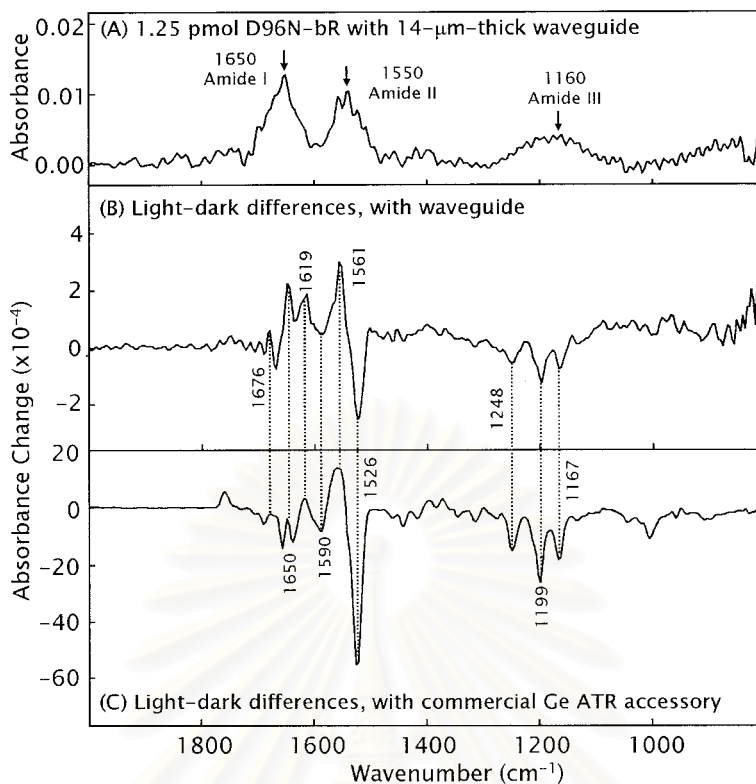


Fig. 9. (A) ATR FT-IR spectrum of D96N mutant of bacteriorhodopsin (D96N-bR) in the form of a dried film with a total amount of 1.25 pmol (37.5 ng) of protein. The spectrum was acquired with a 14- $\mu\text{m}$ -thick tapered Ge waveguide with 5-min scan times. The strong bands centered at 1650, 1550, and 1160  $\text{cm}^{-1}$  represent amide(I), amide(II), and amide(III) vibrations, respectively, which are the characteristic spectral features of the peptide backbone. (B, C) ATR FT-IR difference spectra of D96N-bR using light-dark subtraction at room temperature (25  $^{\circ}\text{C}$ ). (B) 128 averaged data sets, total measurement time,  $\sim 4$  h, using the 14- $\mu\text{m}$ -thick tapered Ge waveguide and 50 pmol protein. (C) 64 averaged data sets, total measurement time,  $\sim 2$  h, using the Out-of-Compartment Contact Sampler<sup>TM</sup> with 45 $^{\circ}$  Ge Trough Plate Kit, Spectra-Tech (\*) and 15 nmol protein.

mode by a microscope. Nevertheless, for small quantities of poorly soluble samples that can only be deposited uniformly as films under  $\sim 1$   $\mu\text{m}$  in thickness, the miniature waveguide is likely to afford a superior sampling method.

**Light-Dark Difference Spectra of Biological Film Samples.** A thin tapered Ge waveguide is able to detect a structural conformation of biological sample covering only 1  $\text{mm}^2$  on the thinnest middle part of its sensing surface. The D96N mutant of bacteriorhodopsin (D96N-bR) was chosen as a model sample for studying the triggered structural change of the protein conformation. As expected, the characteristic spectral features of the peptide backbone (i.e., amide(I), (II), and (III) vibrations) in the purple membrane of D96N-bR can be successfully sensed by using a 14- $\mu\text{m}$ -thick waveguide with just 1.25 pmol (37.5 ng) of protein sample (see Fig. 9A). Light-dark difference measurements on D96N-bR require somewhat larger samples (50 pmol bR) deposited as a thin film on a 14- $\mu\text{m}$ -thick waveguide. However, this amount is 3000 times less than the  $1.5 \times 10^5$  pmol of D96N-bR required for similar light-dark difference measurements using a macroscopic Ge ATR accessory. The light-dark difference spectrum obtained with a 14- $\mu\text{m}$ -thick waveguide (Fig. 9B) is very similar to that obtained on a much larger sample with a macroscopic ATR accessory (Fig. 9C).

**Hair Analysis.** Single human hairs represent a challenging type of IR sample that has been investigated with both ATR and FT-IR microscope methods.<sup>24,25</sup> In our

measurements, a single hair obtained from either an African-West Indian female or a Caucasian male was squeezed against the center of the waveguide sensing area with a ratcheting micrometer in order to obtain reproducible sample contact. Typical results are shown in Fig. 10. Each spectrum observed showed a broad band at 3250  $\text{cm}^{-1}$  attributable to water absorption. The predominant absorption bands centered at 1650 and 1550  $\text{cm}^{-1}$  on both single-hair spectra in Fig. 10 arise from amide(I) and amide(II) vibrations, respectively. The amide(I) band is particularly diagnostic for secondary structure and in this case, is at a wavenumber characteristic of the known  $\alpha$ -helical structure of hair keratin.<sup>24</sup>

By comparing the spectra of each individual's hair with pure samples of the respective styling gels each had applied several hours previously, it is clearly seen that even a tiny amount of chemicals deposited on a 2-mm length of hair surface can be detected. In each case, there are several peaks on the measured hair spectrum corresponding to the strongest bands in the spectrum of the corresponding pure styling gel. This indicates the potential utility of the  $<30$ - $\mu\text{m}$ -thick tapered waveguides as a new tool for forensic analysis.

## CONCLUSION

Symmetrically tapered Ge waveguides with thicknesses down to  $\sim 7$   $\mu\text{m}$  have been successfully fabricated and utilized as MIR evanescent wave sensors. Tapering in this

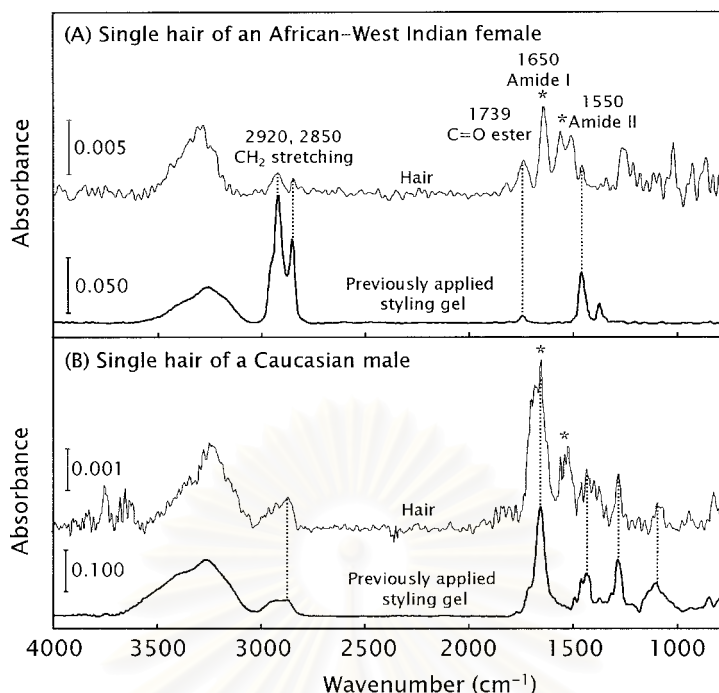


FIG. 10. Baseline-corrected ATR FT-IR spectra of single hairs (upper thin line) taken from two different people, (A) an African-West Indian female, and (B) a Caucasian male. The lower (thick line) spectrum in each sub-figure represents the styling gel applied earlier in the day by each person (i.e., Magnificen<sup>®</sup> Hair Food manufactured by Magnificen Products Division, Memphis, TN, for donor A, and Aussie Mega Styling Ge<sup>®</sup> manufactured by Redmond Products, Inc. Dist., Stamford, CT, for donor B). Films were dried ~1 h prior to spectral measurement. All spectra were acquired with a 14- $\mu\text{m}$ -thick tapered Ge waveguide with 5-min scan times. The strong bands centered at 1650 and 1550  $\text{cm}^{-1}$  on both single hair spectra arise from amide (I) and amide (II) vibrations, respectively

way helps eliminate several problems previously discussed.<sup>2-6</sup> First, a high total throughput can be achieved with an uncomplicated optical alignment procedure and without requiring an IR microscope by using only a single off-axis paraboloid mirror. In addition, a flat horizontal sensing area provides convenience in sampling. It allows for better contact of solid samples such as human hairs, resulting in higher sensitivity and better spectral S/N ratio. As expected, reducing the tapered thickness of the waveguide to  $<30 \mu\text{m}$  produces substantially higher absorbance per unit weight of sample, particularly as compared to a macroscopic Ge ATR accessory. However, this measured increase in absorbance is not yet as great as that predicted for waveguides of this thickness; and it must also be balanced against the significantly lower total throughput that is also not yet close to that predicted to be theoretically achievable.<sup>2</sup>

Nevertheless, we have demonstrated that these  $<30\text{-}\mu\text{m}$ -thick tapered Ge waveguides have the potential to become a useful technique for at least three types of application that are currently difficult with commercial ATR accessories: (1) sub-microliter quantities of volatile liquids; (2) ng-quantity thin-film samples; and (3) coatings and surface layers on small fibrous samples such as individual human hairs. The last application especially indicates the possible utility of these miniature Ge waveguides in nondestructive forensic analysis.

#### ACKNOWLEDGMENTS

This research was supported by National Science Foundation (NSF) grant MCB-9722887 to M.S.B. and by additional funding from the Keck Center for Molecular Electronics at Syracuse University. Jitraporn Vongsivut was supported by a fellowship from the Thailand Research

Fund (TRF) via The Royal Golden Jubilee (RGJ) Program 3-C-CU-43-P-1 to Dr. Sanong Ekgasit (Chulalongkorn University, Bangkok, Thailand). We also gratefully acknowledge the assistance of William F. Kutz, K & S Optics, who did most of the work involved in fabricating the waveguides.

1. R. E. Jonas and M. S. Braiman, *Appl. Spectrosc.* **47**, 1751 (1993).
2. M. S. Braiman and S. E. Plunkett, *Appl. Spectrosc.* **51**, 592 (1997).
3. S. E. Plunkett, S. Propst, and M. S. Braiman, *Appl. Opt.* **36**, 4055 (1997).
4. S. E. Plunkett, R. E. Jonas, and M. S. Braiman, *Biophys. J.* **73**, 2235 (1997).
5. J. J. Stone, M. S. Braiman, and S. E. Plunkett, *Proc. SPIE-Int. Soc. Opt. Eng.* **3105**, 371 (1997).
6. M. S. Braiman, S. E. Plunkett, and J. J. Stone, *AIP Conf. Proc.* **430**, 577 (1998).
7. M. S. Braiman and L.-Z. Mi, *Proc. SPIE-Int. Soc. Opt. Eng.* **3540**, 146 (1999).
8. S. V. Shilov, M. S. Braiman, and L.-Z. Mi, *Proc. SPIE-Int. Soc. Opt. Eng.* **3918**, 202 (2000).
9. S. R. White and S. E. Nave, *Appl. Spectrosc.* **53**, 1138 (1999).
10. R. J. Burger, P. J. Melling, W. A. Moser, and J.-R. Berard, *Proc. SPIE-Int. Soc. Opt. Eng.* **1591**, 246 (1991).
11. A. Bornstein, M. Katz, A. Baram, and D. Wolfman, *Proc. SPIE-Int. Soc. Opt. Eng.* **1591**, 256 (1991).
12. L. Han, T. M. Niemczyk, Y. Lu, and G. P. Lopez, *Appl. Spectrosc.* **52**, 119 (1998).
13. L. Han, T. M. Niemczyk, D. M. Haaland, and G. P. Lopez, *Appl. Spectrosc.* **53**, 381 (1999).
14. J. Frank, R. Schindler, O. Lendl, and B. Lendl, *Appl. Spectrosc.* **54**, 1417 (2000).
15. M. Karlowatz, M. Kraft, E. Eitenberger, B. Mizaikoff, and A. Katzir, *Appl. Spectrosc.* **54**, 1629 (2000).
16. P. Hahn, M. Tacke, M. Jakusch, B. Mizaikoff, O. Spector, and A. Katzir, *Appl. Spectrosc.* **55**, 39 (2001).
17. T.-C. Yeh, P. Tien, and L.-K. Chau, *Appl. Spectrosc.* **55**, 1320 (2001).
18. F. G. Haibach, A. Sanchez, J. A. Floro, and T. M. Niemczyk, *Appl. Spectrosc.* **56**, 398 (2002).

19. N. J. Harrick, *Internal Reflection Spectroscopy* (Harrick Scientific Corporation, Ossining, New York, 1979).
20. N. J. Harrick, *Appl. Opt.* **10**, 2344 (1971).
21. D. J. Ferrell, J. M. Lerner, R. A. Lieberman, T. Quintana, E. M. Schmidlin, and S. J. Syracuse, *Opt. Eng.* **32**, 504 (1993).
22. N. H. Abramson, *Opt. Eng.* **32**, 508 (1993).
23. D. Marcuse, *Theory of Dielectric Optical Waveguides* (Academic Press, New York, 1991).
24. D. J. Lyman, J. Murray-Wijelath, and M. Feughelman, *Appl. Spectrosc.* **55**, 552 (2001).
25. L. Küpper, H. M. Heise, F.-G. Bechara, and M. Stücker, *J. Mol. Struct.* **565-566**, 497 (2001).



สถาบันวิทยบริการ  
จุฬาลงกรณ์มหาวิทยาลัย

**APPENDIX B**

Characterization of Supported Cylinder-Planar  
Germanium Waveguides Sensors  
with Synchrotron Infrared Radiation

Jitraporn Vongsvivut, Jason Fernandez,  
Sanong Ekgasit, and Mark S. Braiman

Applied Spectroscopy (2004) 58: 143 – 151.

สถาบันวิทยบริการ  
จุฬาลงกรณ์มหาวิทยาลัย



# Characterization of Supported Cylinder–Planar Germanium Waveguide Sensors with Synchrotron Infrared Radiation

JITRAPORN VONGSVIVUT, JASON FERNANDEZ, SANONG EKGASIT, and MARK S. BRAIMAN\*

*Department of Chemistry, Faculty of Science, Chulalongkorn University, Bangkok 10330 Thailand (J.V., S.E.); and Chemistry Department, Syracuse University, Syracuse, New York 13244-4100 (J.F., M.S.B.)*

Cylinder–planar Ge waveguides are being developed as evanescent-wave sensors for chemical microanalysis. The only non-planar surface is a cylinder section having a 300-mm radius of curvature. This confers a symmetric taper, allowing for direct coupling into and out of the waveguide's 1-mm<sup>2</sup> end faces while obtaining multiple reflections at the central <30- $\mu$ m-thick sensing region. Ray-optic calculations indicate that the propagation angle at the central minimum has a strong nonlinear dependence on both angle and vertical position of the input ray. This results in rather inefficient coupling of input light into the off-axis modes that are most useful for evanescent-wave absorption spectroscopy. Mode-specific performance of the cylinder–planar waveguides has also been investigated experimentally. As compared to a blackbody source, the much greater brightness of synchrotron-generated infrared (IR) radiation allows a similar total energy throughput, but restricted to a smaller fraction of the allowed waveguide modes. However, such angle-selective excitation results in a strong oscillatory interference pattern in the transmission spectra. These spectral oscillations are the principal technical limitation on using synchrotron radiation to measure evanescent-wave absorption spectra with the thin waveguides.

Index Headings: Tapered waveguides; Evanescent wave absorption spectroscopy; Synchrotron IR radiation; Blackbody IR source; Throughput.

## INTRODUCTION

Development of mid-infrared (MIR) waveguides fabricated from various IR-transparent materials has been driven by the goal of performing surface-sensitive chemical analysis. The general approach is known as attenuated total reflection (ATR) or evanescent-wave spectroscopy (EWS).<sup>1</sup> With this technique, the waveguide can be regarded as an internal reflection element (IRE) wherein the incident light experiences total internal reflection at the interface between media of different refractive indices. At each reflection, the evanescent wave penetrates a fraction of wavelength beyond the high-index waveguide into the lower-index medium (i.e., the sample). The penetration depth of the evanescent wave is typically in the range of 0.5–5  $\mu$ m for MIR light propagating through useful IREs. As a consequence, only a thin layer of the sample is probed.

The detection limit of ATR spectroscopy is as yet insufficient for it to be considered generally suitable as a trace method. Hence, there is substantial interest in novel methods for improving the surface sensitivity of MIR waveguides. One approach, for both fiber optics and planar waveguides, has been to reduce the cross-sectional

area of the sensor. This tends to increase the fraction of the total energy carried in the evanescent wave, but has the limitation of reducing the optical power available for detection.

The greatest achievements in developing chemical sensors for tiny samples have been carried out with silica-based fibers and planar waveguides, which are useful in the near-infrared (NIR) spectral region.<sup>2–4</sup> However, much useful chemical information is lost due to the opacity of silica composites in the MIR spectral range (i.e., 400–4000  $\text{cm}^{-1}$ ), where specific molecular fundamental vibrational fingerprints are more readily interpreted, compared to the overtone and combination bands at NIR frequencies.

We have instead focused on single-crystal germanium (Ge) as an IRE for the MIR region because of its relatively low cost, its transparency from 5000–800  $\text{cm}^{-1}$ , and its high refractive index (4.0), as well as its excellent chemical and biochemical inertness. A significant drawback of Ge is its brittleness and relatively low mechanical strength, leading to significant challenges in fabrication. However, several types of thin planar Ge waveguides under 50  $\mu$ m in thickness have now successfully been fabricated and applied in EWS analysis of sub- $\mu$ L volatile liquids, ng-quantity thin films, coatings on fibrous samples, and single- and multilayer biological membranes covering small (<1  $\text{mm}^2$ ) areas.<sup>5–12</sup> These studies demonstrated a significant improvement in sensitivity for such small samples as a result of the larger number of internal reflections per unit length.

Most recently, the development of tapered cylinder–planar Ge waveguides has simplified the coupling of broadband IR light from the blackbody source of commercial FT-IR spectrometers into the waveguide.<sup>10–12</sup> These waveguides are designated as cylinder–planar because while one surface is planar, the other is ground and polished as a cylinder surface, resulting in a gradual, symmetrical taper away from the central minimum in thickness (see Fig. 1). The larger cross-sectional area at the ends of the waveguides makes it easy to align them with respect to both the focused IR beam and the detector, eliminating the need for an IR microscope and permitting the use of the waveguides in a horizontal configuration, the most useful for typical sensing applications.<sup>12</sup>

However, these thin tapered Ge waveguides have in practice not afforded as high a spectral signal-to-noise (S/N) ratio in observed broadband FT-IR spectra as was predicted theoretically by using standard approximations and simplifying assumptions in order to predict the range of modes that would be excited.<sup>5</sup> In the current work, the

Received 21 August 2003; accepted 2 October 2003.

\* Author to whom correspondence should be sent. E-mail: mbraiman@syr.edu.

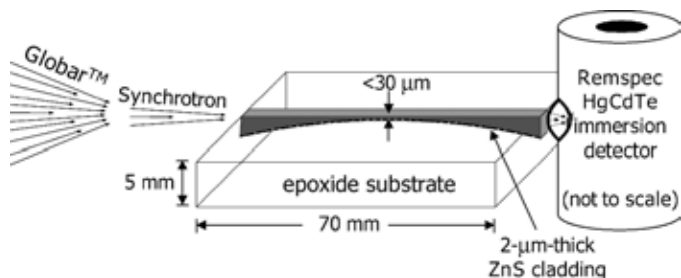


FIG. 1. Schematic configuration of cylinder-planar tapered Ge waveguide used as a miniature evanescent-wave sensor. The waveguide is mechanically supported by a cast epoxide substrate. The top flat surface near the  $<30\text{-}\mu\text{m}$ -thick central region of the waveguide is the sensing area. The bottom surface of the waveguide is a cylindrical sector with a radius of 300 mm, coated with a  $2\text{-}\mu\text{m}$ -thick ZnS cladding layer. Incident light indicated at left is generated from a broadband IR source, either a standard blackbody (Globar<sup>TM</sup>) internal to the spectrometer, or an external synchrotron (U2B beamline at NSLS, Brookhaven National Laboratory). A liquid-N<sub>2</sub>-cooled HgCdTe immersion detector, placed as close as possible to the exit end of the waveguide, is used to measure the transmitted IR radiation.

reasons for the discrepancy between the theoretical and observed performances have been investigated in more detail, both with calculations and by using broadband synchrotron IR radiation to carry out mode-specific measurements.

Our original hope was that a combination of synchrotron-based IR spectroscopy with the symmetrically tapered  $<30\text{-}\mu\text{m}$ -thick Ge waveguides would create a new opportunity for analyzing tiny samples with improved spectral quality. This goal has not yet been realized due to the strong interference patterns produced by combining highly spatially coherent synchrotron light with thin waveguides. Nevertheless, the results with the synchrotron radiation lead to useful conclusions that are likely to result in improved designs for MIR waveguide sensors.

## EXPERIMENTAL

**Waveguide Fabrication.** Fabrication of cylinder-planar tapered waveguides was carried out as described previously.<sup>12</sup> In brief, a 70-mm-diameter, 3-mm-thick single-crystalline Ge disk was first cylindrically ground and polished to a 600-mm-diameter curvature at a commercial optical polishing house (K & S Optics, Binghamton, NY), producing a curved surface on one side of the disk (see Fig. 1). The curved surface was then coated with a  $2\text{-}\mu\text{m}$ -thick ZnS cladding layer using chemical vapor deposition. The ZnS-coated Ge disk was diced into 2-mm-wide strips, and the parallel-diced sides were ground to give a final width of 1–1.5 mm. A single Ge strip was embedded into an  $\sim 1\text{-cm}$ -thick epoxide substrate by casting it, planar-side down, into the freshly mixed resin and hardener (Buehler Ltd., Lake Bluff, IL). The minimum thickness of the waveguide was subsequently reduced from its initial value ( $\sim 2\text{ mm}$ ) down to the final tapered thicknesses of  $<30\ \mu\text{m}$ , by grinding and polishing its exposed flat surface. Towards the end of this process, the thickness was periodically measured by using the interference pattern appearing on the reflectance spectrum<sup>13</sup> obtained with the IR beam perpendicular to the waveguide's planar (flat) surface. This reflectance spectrum was obtained by using an IR microscope (IR-Plan Infra-

red Microscope Accessory, Spectra-Tech, Stamford, CT) coupled to an FT-IR spectrometer (Midac Illuminator) operating with  $1\text{-cm}^{-1}$  resolution and 256 scans.

**Optical Alignment and Conditions for Spectral Data Collection.** Figure 1 shows schematically the optical configuration of the cylinder-planar Ge waveguide with respect to the IR source and detector. The large differences in refractive indices enable the thin Ge layer ( $n_{\text{Ge}} = 4.0$ ), sandwiched between ZnS cladding ( $n_{\text{ZnS}} = 2.2$ ) and air ( $n_{\text{air}} = 1.0$ ) or sample (e.g., water,  $n_{\text{H}_2\text{O}} = 1.34$ ), to serve as a waveguide for MIR light.

Two different FT-IR spectrometers equipped with different IR sources were employed for spectral collections with the same cylinder-planar Ge waveguide in order to determine how the waveguide functions under different throughput conditions. The first was a Bruker IFS66 FT-IR spectrometer with the standard internal Globar<sup>TM</sup> source. The second was a Nicolet 860 FT-IR spectrometer interfaced with a synchrotron light source (U2B Beamline at National Synchrotron Light Source, Brookhaven National Laboratory). The latter spectrometer was additionally equipped with a standard internal Globar<sup>TM</sup> source that could be selected by switching a single computer-controlled mirror.

With both spectrometers, it was possible to configure the optical system to allow use of the tapered Ge waveguide either outside the spectrometer (i.e., via the external output port) or inside the main sample compartment as a traditional ATR accessory. For the out-of-compartment setup, the incident light exiting the external output port of the spectrometer was simply focused onto the entrance end of the waveguide by using a single off-axis paraboloid mirror with a 19.1-mm focal length (Melles Griot, Irvine, CA). Alternatively, several mirrors could be utilized inside the sample compartment of the spectrometer in order to focus the light onto the input end of the waveguide.

With either in-compartment or out-of-compartment setup, a liquid-N<sub>2</sub>-cooled HgCdTe immersion detector (MOD-O2S1, Remspec Corp., Sturbridge, MA), with an active area of  $0.50 \times 0.50\ \text{mm}^2$  and  $D^* (10\ \text{kHz}) \geq 4 \times 10^{10}\ \text{cm Hz}^{1/2}\ \text{W}^{-1}$ , was mounted with its window directly against the output end of the waveguide. For some experiments investigating mode-specific behavior, an alternative immersion detector (FTIR-M16-0.10, Graseby Infrared), with an active area of  $0.15 \times 0.15\ \text{mm}^2$  and similar  $D^*$ , was utilized. The detector's angle was always fixed perpendicular to the top and side surfaces of the waveguide (i.e., the immersion lens optical axis was parallel to the waveguide axis), while its position was adjusted both horizontally and vertically to maximize the measured throughput of broadband IR light.

The same spectrometer parameters were utilized in comparisons between measurements with the standard Globar<sup>TM</sup> source and those with synchrotron IR radiation. All spectra shown below were acquired at a gain of 1, resolution of  $8\ \text{cm}^{-1}$ , and measurement bandwidth of  $7800\ \text{cm}^{-1}$ . The moving mirror of the interferometer had its optical retardation velocity set to give a modulation frequency of 100 kHz for the HeNe reference beam. The coadded scan time was 5 min for all measurements. Mertz phase correction and zero-filling of 2 were set as default acquisition parameters. Happ-Genzel and Black-

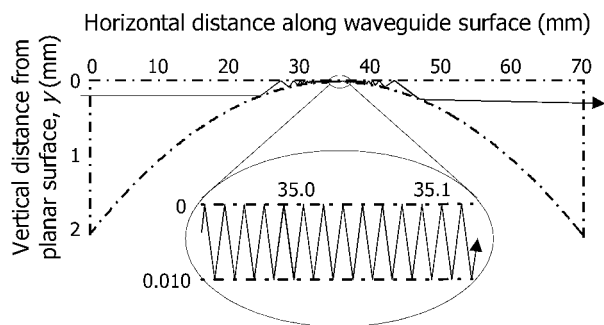


FIG. 2. Typical calculated reflection pattern of a light ray propagating through a symmetrically tapered cylinder-planar waveguide with a total length of 70 mm, a circular radius of 300 mm for the cylinder surface, and a minimum thickness  $t$  of 10  $\mu\text{m}$ . This particular ray was assumed to impinge perpendicular onto the waveguide's  $\sim 2$ -mm-high entrance face ( $\theta = 0^\circ$ ), at a distance  $y$  of 0.20 mm from the flat surface. This results in this ray's propagation through the thinnest part of the waveguide near the critical angle for total internal reflection at a Ge-ZnS interface. Note that the exaggerated vertical scale in both the main figure and the inset results in distorted apparent reflection angles.

man-Harris three-term apodization functions were applied for Nicolet and Bruker instruments, respectively.

**Ray-Tracing Calculations.** We traced a series of input rays impinging on the end of the waveguide through its entire length. This required calculating many reflections (typically several hundreds) for each input ray. The analytical geometry required is rather simple, but solution of this type of problem (multiple internal reflections between a planar and cylinder surface) is not included in commercial ray-tracing programs. Therefore, we wrote our own program using MATLAB<sup>®</sup> (The Mathworks Inc., Natick, MA, version 5.3.1).

We simplified the problem by limiting ourselves to two dimensions. The trajectories of all incoming rays are assumed to be confined to a plane that is perpendicular to the waveguide's upper planar surface as well as to the (axis of) the lower cylinder surface. The traced rays that are restricted to this plane are then calculated as a series of reflections from a line and a circular arc (see Fig. 2). Each input ray, impinging on the end of the waveguide at angle  $\theta$  with respect to the waveguide axis and at a depth  $y$  below the planar surface, first has its refraction angle  $\theta'$  into the high-index waveguide calculated according to Snell's law. The program then propagates the ray (by setting the reflected angle equal to the incident angle at each internal reflection point) until it reaches the exit end of the waveguide or else exceeds the critical angle for reflection from the upper or lower surfaces. Our program reduces the problem to a very elementary treatment with ray optics, omitting features (such as the displacement of the reflected ray along the dielectric boundary) that have been shown to be required for a more accurate treatment of the ray-tracing problem for a multi-reflection waveguide. The main output of the routine is the maximum sensing angle  $\varphi$  achieved inside the waveguide for each pair of input parameters ( $y, \theta$ ). One of the additional inputs required for the program is a subroutine defining the height and slope of the lower curved surface as a function of horizontal distance from the center of the waveguide. In the present work, this subroutine was set to define only a circular arc in order to compare results with those obtained by experiments, but it could

alternatively be set to other functional forms of curves of interest. Almost any differentiable function gives accurate ray-trace calculations with the routines, as long as the function is sufficiently smooth (i.e., having no point with a radius of curvature less than  $\sim 2$  mm).

## RESULTS AND DISCUSSION

We have recently reported a substantial improvement in sensitivity achieved by symmetrically tapering Ge waveguide evanescent-wave sensors and decreasing their central thickness to 7–15  $\mu\text{m}$ .<sup>12</sup> Absorption intensities of spectra acquired with thinner waveguides are enhanced to a power greater than 1, due to increases both in the number of internal reflections per unit length and in the amount of electromagnetic energy contained within the evanescent wave at each reflection. Tapering also simplifies the optical alignment since only common focusing optics (off-axis paraboloid mirrors) are needed. As a result, spectral absorption measurements on even tiny (nanogram) samples are simple and quick.

Nevertheless, the absorption intensities observed<sup>12</sup> corresponded only to those expected for 3–5 reflections, rather than  $>25$  reflections expected for a 20- $\mu\text{m}$ -thick waveguide with an average internal propagation angle of  $45^\circ$  and a sensing length of  $\sim 1$ –2 mm. In an attempt to evaluate how light focused onto the end of the waveguide is coupled into modes with varying propagation angles, we have performed both ray-tracing calculations and measurements at selected angles using the highly collimated broadband light available from a synchrotron.

**Ray Tracing of Cylinder-Planar Waveguides.** A typical traced ray is shown in Fig. 2 for a cylinder-planar Ge waveguide with a total length of 70, an entrance/exit height ratio of 1 (i.e., symmetrical tapering), and a minimum thickness of 0.010. This corresponds to a circular radius of 300. These dimensions (assuming units of mm) match quite closely to those of the physically realized waveguides that we have utilized for evanescent-wave sensing measurements. Note that the vertical scale in Fig. 2 is greatly exaggerated relative to the horizontal scale. This creates the illusion that wherever the curved waveguide surface is sloped (i.e., non-horizontal), the incident and reflection angles are unequal.

Near the center of the waveguide, the particular ray shown in Fig. 2 propagates very close to the critical off-axis angle of  $\varphi = 56.6^\circ$  for propagation of light through a ZnS-clad Ge waveguide, ( $n_{21} = 2.2/4.0$ ). For this critical ray, there are a very large number of internal reflections (133 per mm of travel; 67 per mm for only the sensing surface) at the thinnest central sensing region, as shown in the expansion (inset) of the centermost 0.1 mm of the waveguide. At  $x = 0$  (i.e., the entrance end of the waveguide), this ray has a  $y$  value of 0.2 mm and an initial angle inside the waveguide of  $\theta' = 0^\circ$ . Using Snell's law ( $n_{\text{Ge}} \sin \theta' = n_{\text{air}} \sin \theta$ ), this also corresponds to an impinging angle of  $\theta = 0^\circ$  (i.e., perpendicular to the entrance face) for the ray propagating in air prior to entering the waveguide.

Figure 3 shows the variation of number of total internal reflections within the 0.010-mm-thick waveguide as a function of  $y$ , holding the impinging angle  $\theta$  constant at

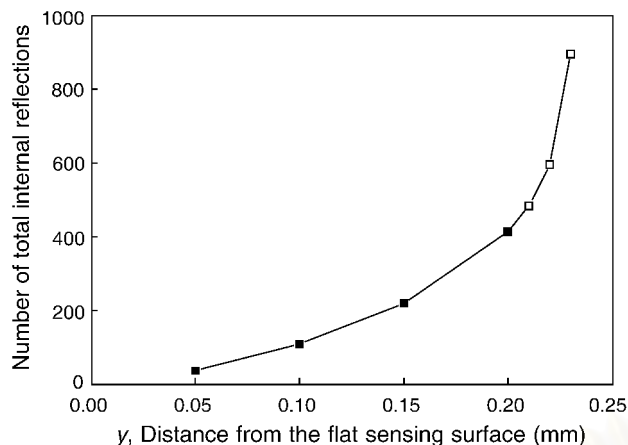


FIG. 3. Plot of the calculated number of total internal reflections vs. vertical distance ( $y$ ) of the impinging ray from the upper planar surface of a 70-mm-long, symmetrically-tapered, cylinder-planar waveguide with a minimum thickness of 10  $\mu\text{m}$ . The light ray is assumed to enter the waveguide on-axis ( $\theta = 0^\circ$ ). Values of  $y$  above 0.20 mm ( $\square$ ) give reflections that exceed the critical angle for a Ge-ZnS interface. Therefore, the maximum number of total internal reflections in a ZnS-clad Ge waveguide of these dimensions is approximately 400, and is achieved at  $y = 0.20$  mm.

$0^\circ$ . There is a substantial increase in number of total internal reflections as  $y$  is increased. However, propagation via total internal reflection is allowed only for  $y \leq 0.20$  mm, i.e., only for rays entering the waveguide along the 10% of its entrance face closest to the planar surface. For an on-axis ray entering farther than this from the waveguide's flat surface, the propagation angle exceeds the critical angle for a Ge-ZnS interface before the ray reaches the center of the waveguide. As a consequence, for  $\theta = 0^\circ$ , only light rays entering within 0.20 mm of the flat surface contribute to the detected light. At this  $y$  value, the number of total internal reflections in the model waveguide described is  $\sim 400$ , and this turns out to be (approximately) the maximum number of internal reflections allowed for this tapered waveguide at any combination of  $y$  and  $\theta$ .

By calculating ray-traces such as those in Fig. 2 while varying both  $\theta$  and  $y$ , it was possible to determine all possible combinations of these two parameters for which light can propagate through a particular waveguide. For each of the allowed rays, the ray-trace program also provided the sensing angle  $\varphi(\theta, y)$ , which is the maximum angle that the ray makes with respect to the planar surface of the waveguide at the thinnest (sensing) portion of the waveguide. These results are shown schematically in Fig. 4 for various thicknesses of the cylinder-planar waveguide (including several that match those used in experimental measurements). As expected, with decreasing waveguide thickness there is a corresponding decrease in the range of allowed ( $\theta, y$ ) pairs, corresponding to a decrease in total throughput. However, there is also the evolution of fascinating structure in the contour plots as the waveguides get thinner, including the gradual pinching-off of isolated "islands" at very specific combinations of  $\theta$  and  $y$  and the clear appearance of a thumb-like protrusion that indicates a large throughput allowed for light entering the waveguide from a specific angle just above  $0^\circ$ . We speculate that these regions may be mathematical

"attractors", and therefore signs of chaotic (or near-chaotic) behavior for rays reflecting from such closely apposed non-parallel surfaces.

The optical invariant (one-dimensional version of the étendue) of a cylinder-planar waveguide in the vertical direction is normally calculated as the product of the numerical aperture (NA) and the thickness  $t$ . For a simple planar waveguide, this is equal to  $t\sqrt{n_1^2 - n_2^2}$ , where  $n_1$  and  $n_2$  are the refractive indices of the waveguide and cladding materials, respectively. In more general terms, and in particular at the entrance end of the waveguide, the optical invariant should be given by the following integral over the thickness  $t$  of the waveguide:

$$\text{étendue} = \frac{1}{2} \left\{ \int_0^{t=2\text{mm}} \left[ \int_{\theta_{\min}(y)}^{\theta_{\max}(y)} \cos \theta \, d\theta \right] dy \right\} \quad (1)$$

In this formula,  $\theta_{\max}$  and  $\theta_{\min}$  are the extreme values of  $\theta$  that can successfully propagate through the entire waveguide from a vertical position  $y$  within a cross-section at a specific horizontal position  $x$  where the optical invariant is being calculated, in this case, at the entrance of the waveguide. The refractive index  $n$  should in most generality appear inside the integral, but it is assumed in Eq. 1 to be 1.0 at the entrance of the waveguide, which faces air. (It can readily be seen that if all entering rays in a range of  $\pm\psi$  are allowed to propagate through a waveguide of constant thickness  $t$ , this formula gives  $\text{étendue} = t \sin \psi$ , i.e., the thickness times the numerical aperture, as it should.)

Using Eq. 1 and setting the integral limits according to the allowed rays from the ray-tracing calculations, the étendue value for the 0.014-mm-thick Ge waveguide for the data matrix in Fig. 4 is 0.0510 mm ( $\sim 51.0 \mu\text{m}$ ). This is remarkably close to that given by the simple formula for planar waveguides ( $\text{étendue} = t\sqrt{n_1^2 - n_2^2}$ ), which gives the value of 46.7  $\mu\text{m}$ . The closeness of the two values suggests that light illuminating the end face uniformly and then propagating to the center of the waveguide could be accurately represented as a bundle of rays filling the numerical aperture of 3.3 (i.e., according to the formula  $\text{NA} = \sqrt{n_{\text{Ge}}^2 - n_{\text{ZnS}}^2} = \sqrt{(4.0)^2 - (2.26)^2}$  for a Ge-ZnS interface), at uniform density.

However, the hypothesis that the numerical aperture of the sensing region of the waveguide gets filled uniformly is contradicted by a more careful analysis, which shows that the distribution of intensity as a function of angle is far from uniform (Fig. 4). In particular, rays that approach close to the critical angle (red-green colors) are somewhat under-represented. This is undesirable behavior for an evanescent-wave sensor, because the on-axis rays undergo relatively few internal reflections and have a lower evanescent-wave electric-field strength than rays near the critical angle. Unfortunately, it is completely consistent with the experimental results on the cylinder-planar waveguides, which show substantially lower evanescent-wave absorption intensities than would be predicted for modes evenly distributed over all the "allowed" angles for the cylinder-planar sensing region at the center of the waveguide<sup>12</sup> (see below).

It is of interest to consider how changes in the shape of the waveguide might affect this result. In particular, we examined how it depends on the curvature radius  $R$

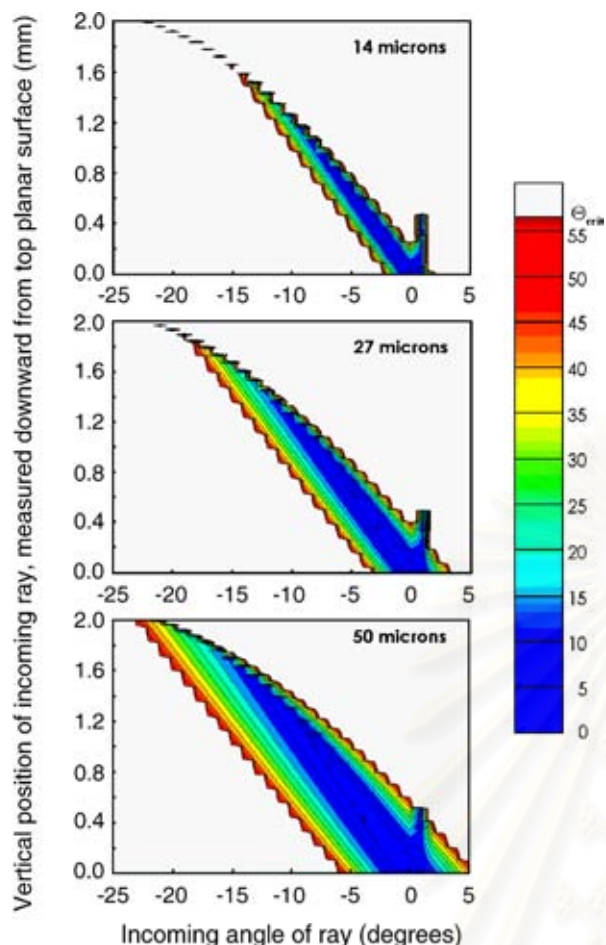


FIG. 4. Summary of results of 10251 ray-trace calculations on each of three different cylinder-planar waveguide sensors, all having a circular radius of 300 mm but different minimum thicknesses (14, 27, and 50  $\mu\text{m}$ ) as indicated. These contour plots show on the horizontal and vertical axes the initial conditions for each calculated ray (respectively,  $\theta$ , the entrance angle in air prior to entering into the waveguide; and  $y$ , the distance measured downward from the top planar surface). The  $z$ -axis corresponds to the maximum angle  $\varphi$  at which the ray is calculated to propagate in the thinnest (sensing) region of the waveguide. Contours are given at  $5^\circ$  intervals. The  $z$ -levels are also color-coded according to the key at right, with gray indicating all initial conditions that result in the ray exceeding  $\varphi_{\text{crit}} = \arccos(2.2/4)$  for a Ge/ZnS interface of the waveguide.

of the cylindrical bottom surface, at a constant waveguide center thickness  $t$  of 14  $\mu\text{m}$ . We hoped this might provide some useful clues for improving the waveguide's performance. Figure 5 presents contour plots of cylinder-planar waveguides having the same length (70 mm) and center thickness (14  $\mu\text{m}$ ) as the top plot in Fig. 4, but with various values of  $R$ . Figure 6 presents a summary of calculations of the étendue of these waveguides. Although increasing  $R$  results in a reduction of the end heights of the 70-mm-long waveguides, our calculation indicates that waveguides with  $R$  values in a range of 1200–2500 show only a small decrease in throughput relative to that for  $R = 300$  mm. In addition, a wider range of incoming angles with allowed sensing angles, achieved by a waveguide with a larger radius of curvature, leads to excitation of the far-off-axis modes in the sensing region of the tapered waveguide, the modes that are in fact useful for evanescent-wave absorptions. Thus we can in theory ob-

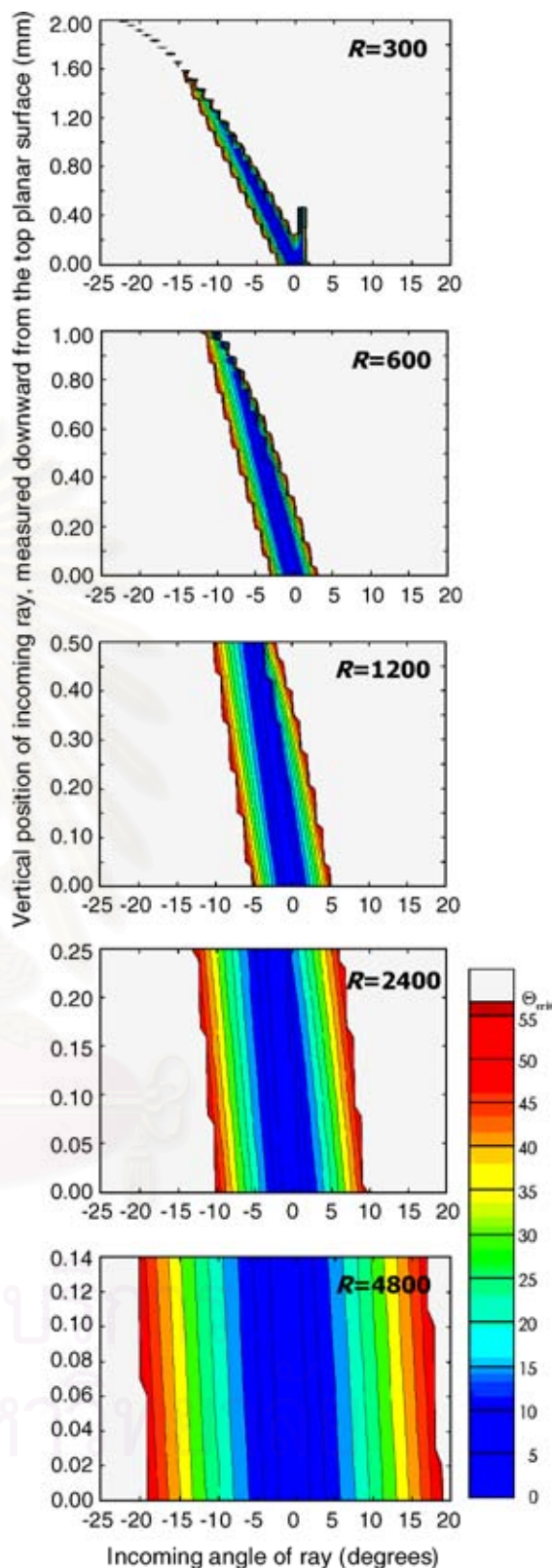


FIG. 5. Sensing-angle plots for rays impinging on the entrance faces of 14- $\mu\text{m}$ -thick cylinder-planar waveguides with different values of circular radius  $R$  (300, 600, 1200, 2400, and 4800 mm) as indicated. A larger radius of curvature results in thinner end faces, as indicated by the correspondingly smaller range for the  $y$ -axis scale. As in Fig. 4,  $z$ -axis contours are always calculated at  $5^\circ$  intervals. The color bar shown at right is applicable to all plots.

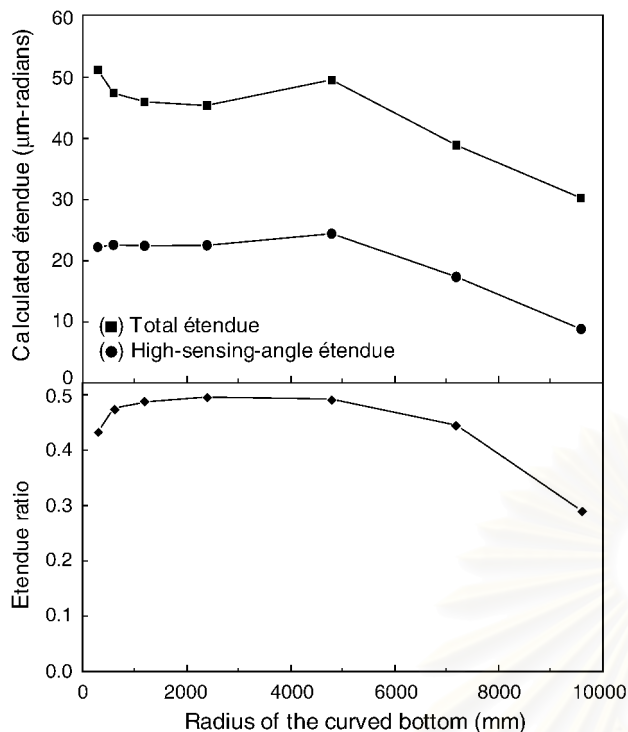


FIG. 6. (Upper) Plot of calculated total étendue (■) and high-sensing-angle étendue (●) of a 14- $\mu\text{m}$ -thick cylinder-planar waveguide vs. curvature radius  $R$  of the bottom cylinder surface. Each value of total étendue was calculated from Eq. 1 (see text), taking appropriate limits for the double integral from the data matrix that gave the corresponding plot in Fig. 5. Because  $\cos \theta \approx 1$  for most of the allowed input rays, each calculated étendue roughly equals the total colored (non-gray) area of the plot in Fig. 5. For the high-sensing-angle étendue, on the other hand, the range of the double integral was limited to just those plotted elements that correspond to sensing angles in the range of  $25^\circ$  to the critical angle ( $56.6^\circ$ ), giving roughly the green-to-red area of each plot in Fig. 5. (Lower) Ratio of the high-sensing-angle étendue to the total étendue as a function of the curvature radius  $R$ , based on plots in the upper part of the figure.

tain a significant improvement in the waveguide performance, simply by increasing the circular radius of the waveguide's curved bottom.

In order to investigate how the total étendue varies with  $R$  values, we performed étendue calculations, based on Eq. 1, on the entire data matrix of individual waveguides at different radii of curvature, which correspond to those contours in Fig. 5. The calculated total étendue are represented by (■) in Fig. 6. The plot shows the largest total étendue at the smallest  $R$  value (300 mm) as a result of the largest entrance aperture ( $2 \text{ mm}^2$ ) into the waveguide. In fact, it is impressive that the calculated étendue for all the  $R$  values indeed end up being so close to each other because this is a clear demonstration of the validity of the étendue as an optical constant. However, the étendue is not monotonic with  $R$ : it rises again at  $R = 4800 \text{ mm}$  and drastically goes down afterwards.

In addition, we determined the fraction of the étendue associated with light rays that propagate at high angles in the sensing area. Therefore, a filter based on maximum sensing angle was applied to the data matrices in order to exclude those elements containing sensing angles less than an arbitrary angle (i.e.,  $25^\circ$  for the present work)

from calculation. The result of high-sensing-angle étendue, as shown in Fig. 6 (●), approaches the maximum theoretical value at  $R = 4800 \text{ mm}$ , instead of the value of  $R = 300 \text{ mm}$  obtained by the full calculation without filtering the data matrix. By ratioing the high-sensing-angle étendue to the total étendue, the lower curve (◆) in the same figure reveals waveguide sensors have optimum performance at a radius of curvature in a range of 2000–3000 mm, rather than the 300-mm-radius waveguide sensor used in practical measurements, for two reasons: (1) somewhat higher fractional throughput for higher-sensing angles, i.e., above  $25^\circ$ , with no loss of total throughput; and (2) an ability to selectively excite modes with high sensing angles by illuminating the end face of the waveguide with off-axis rays. By comparison, the calculations show that there is little or no selective excitation possible with the 300-mm-radius waveguide, in contrast to the contour lines of the 4800-mm-radius waveguide, which are almost perfectly vertical. This suggests that we could obtain exclusive light propagation with sensing angles greater than  $25^\circ$  by limiting input angles to be larger than  $10^\circ$ . As a consequence, the sensitivity of the waveguide should be significantly improved.

**Throughput Measurements with Synchrotron Radiation.** Figure 7 compares single-beam spectra of symmetrically tapered 14- and 27- $\mu\text{m}$ -thick Ge waveguides obtained both with synchrotron IR radiation and with a standard blackbody (GloBar™) source. For the synchrotron beam, the optics were aligned in two different setups along with the Nicolet 860 FT-IR spectrometer: (1) using the external output port with an out-of-compartment setup; or (2) with the Remspec immersion detector and waveguide both mounted inside the internal sample compartment. The results demonstrate that the synchrotron radiation does not exceed the numerical aperture of the waveguides, because the detected throughputs are independent of waveguide thickness. As expected, the small effective source size of the synchrotron can totally pass through the minimum 46- $\mu\text{m}$  étendue of the 14- $\mu\text{m}$ -thick waveguide. The calculated one-dimensional étendue of the output of the U2B beamline at the National Synchrotron Light Source is far below 46  $\mu\text{m}$ ; in fact, it is somewhat under 0.1  $\mu\text{m}$ , based on the published VUV parameters at NSLS as of December 2002.<sup>14</sup>

The results in Fig. 7 show that indeed there is a higher total energy throughput when using the synchrotron radiation, as compared to a blackbody GloBar™ source, for both 14- and 27- $\mu\text{m}$ -thick waveguides. For the thicker (27- $\mu\text{m}$ -thick) waveguide, the increase in throughput intensity for the synchrotron, relative to the GloBar™, is significant only above  $2500 \text{ cm}^{-1}$  (and up to  $5000 \text{ cm}^{-1}$  where the cutoff due to the Ge bandgap blocks all transmission in either case). In contrast, for the 14- $\mu\text{m}$ -thick waveguide, the synchrotron affords higher throughput over all MIR frequencies.

Therefore, using synchrotron radiation can clearly help to increase the total light energy throughput with such thin waveguides. Furthermore, the use of synchrotron IR radiation allows a simple in-compartment set-up configuration using only flat mirrors, with no loss of energy. This is because the  $\sim 100\text{-mm}$ -focal-length mirror that the spectrometer uses to focus the beam into the sample com-

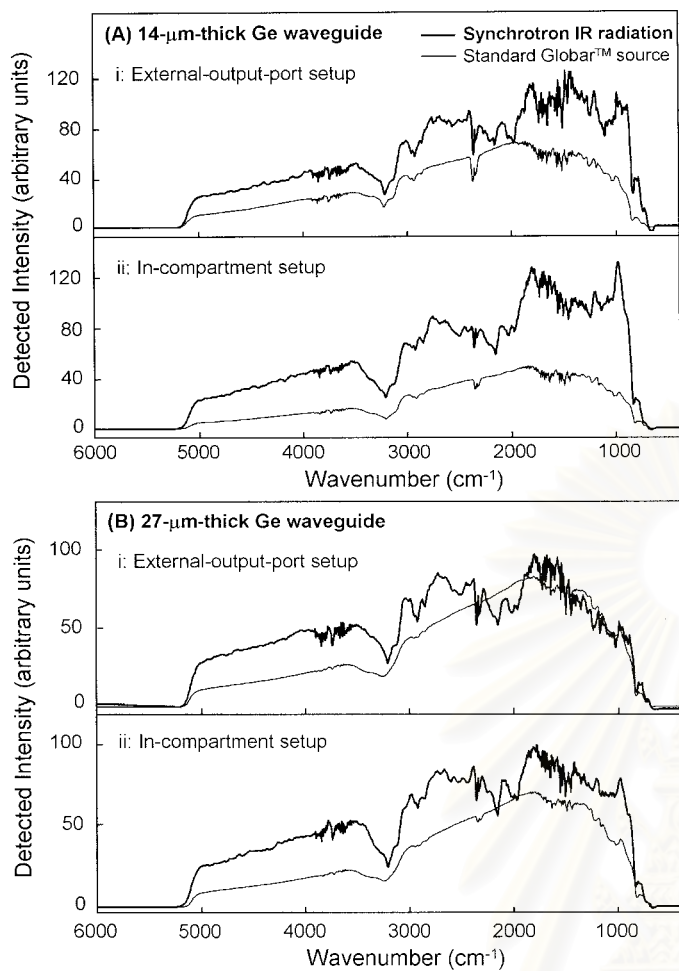


FIG. 7. FT-IR single-beam spectra of (A) a 14- $\mu\text{m}$ -thick and (B) a 27- $\mu\text{m}$ -thick Ge waveguide observed with synchrotron IR radiation, compared to those observed with a standard blackbody (Global<sup>TM</sup>) source. With each waveguide thickness, two different on-axis setups were examined: (i) using the external output port; and (ii) using the internal sample compartment. Throughput in each case was maximized by shifting the relative horizontal and vertical positions of the IR beam, waveguide, and detector.

partment is adequate to focus the highly collimated synchrotron beam into the  $\sim 1\text{-mm}^2$  end of the waveguide. On the other hand, it can only focus a small portion of the Global<sup>TM</sup> intensity into such a minute aperture.

**Angle Dependence of Throughput and Absorbance Signals with Synchrotron Radiation.** We measured the total synchrotron-generated IR energy throughput of the 27- $\mu\text{m}$ -thick waveguide and the water absorbance signal at  $3400\text{ cm}^{-1}$  for a standard 1-mm-diameter droplet of water as a function of the external incident angle  $\theta$ . However, the results showed great variability. The ray-trace calculations in Fig. 4 help to explain this. They show that at any value of  $\theta$ , widely different results can be expected depending on other aspects of the optical alignment of the waveguide relative to the synchrotron beam, specifically, entrance height  $y$  on the waveguide end face and the relative vertical displacement of the output end of the waveguide and the detector's immersion lens. At the time that measurements were made at the synchrotron (prior to performing the ray-trace calculations), we did not sus-

pect such a strong dependence of throughput and absorbance signal on these beam height parameters.

Nevertheless, we made enough measurements on both 14- and 27- $\mu\text{m}$ -thick waveguides (at  $\sim 10$  different beam angles in the range  $-20^\circ$  to  $+20^\circ$ ) to draw some useful generalizations that both support the ray-tracing calculations and are explained (*a posteriori*) by them. In particular, we observed that for any absolute value of the incident angle  $\theta$ , the energy throughput obtained when light is directed from a small but substantial angle below the waveguide surface ( $-10^\circ < \theta < -3^\circ$ ) is substantially greater than the near-zero throughput obtained when the light is directed at a similar angle from above the waveguide surface plane, and typically up to  $\sim 20\%$  greater than the throughput obtained when the synchrotron light is directed strictly on-axis ( $\theta = 0^\circ$ ). This empirical observation, which was very confusing at first, makes perfect sense in light of the subsequent ray-trace calculations shown in Fig. 4. This calculation demonstrates that negative values of  $\theta$  in the range of  $-3^\circ$  to  $-10^\circ$  contribute far more to the total throughput of the waveguide than similar-magnitude positive angles, and slightly more than on-axis rays.

We also observed that the absorbance of a standard sample (e.g., the  $3400\text{ cm}^{-1}$  peak for a 1-mm-diameter water droplet at the center of the waveguide sensing region) was only up to  $\sim 50\%$  larger when the measuring synchrotron IR light impinged on the waveguide entrance face from  $4^\circ$ – $10^\circ$  below the waveguide plane than for light impinging on-axis. We had qualitatively expected that we would selectively excite high-angle modes at the sensing region of the waveguide by using light impinging off-axis onto the end face. However, the graphs in Fig. 4 contradict this expectation and instead support our empirical observation that it becomes only slightly easier to excite off-axis modes as the impinging angle is increased.

This explains why we found no input angle conditions for which we could get the water absorbance signal to approach that expected for light propagating at the critical angle. Figure 4 indicates that we might have been able to do this only if we had tightly focused the synchrotron beam at just the right entrance height (one of a few  $\sim 10\text{-}\mu\text{m}$ -high "sweet spots") on the entrance face of the cylinder-planar waveguide.

**Oscillatory Signal on Absorbance Spectra Measured with Synchrotron Radiation.** In general, the absorption intensity and band shape measured for the broad  $\nu_{\text{OH}}$  band at  $3400\text{ cm}^{-1}$  by using synchrotron radiation is similar to that measured by using a standard Global<sup>TM</sup> source (Fig. 8). However, the spectra observed with the synchrotron show intense oscillatory interference patterns. As discussed previously for planar waveguides,<sup>6</sup> these oscillations arise from a fixed frequency separation between the allowed waveguide modes when the light is required to propagate between two planar surfaces with a well-defined propagation angle.

The strength of the interference phenomenon is greatly increased for the synchrotron-produced light due to its much greater spatial coherence (i.e., its ability to be simultaneously well-collimated and focused to a narrow beam diameter), relative to blackbody-generated irradiation. As a result, the entire synchrotron IR beam is propagated through the thinnest part of the waveguide at a

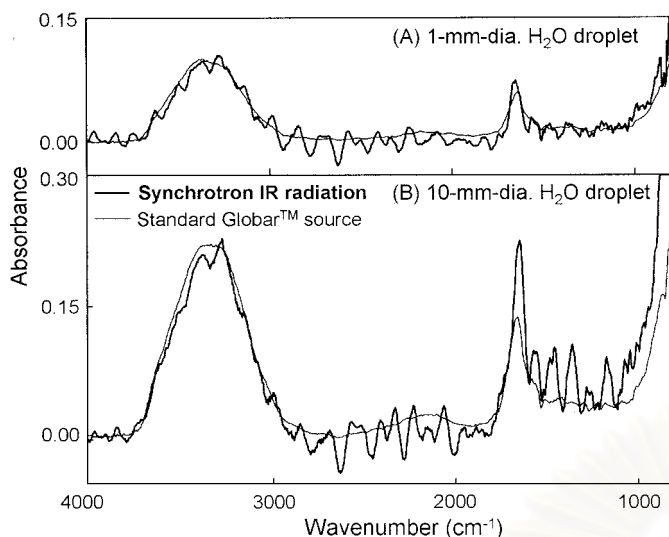


FIG. 8. Comparison of evanescent-wave absorbance spectra measured with a 14- $\mu\text{m}$ -thick Ge waveguide, by using either synchrotron IR radiation (bold lines) or a standard blackbody (Globar<sup>™</sup>) source (thin lines). Samples were water droplets covering either (A) 1 mm or (B) 10 mm of the central part of the waveguide's sensing surface. These spectra were all collected with the in-compartment setup. The oscillatory interference pattern appears only with the synchrotron radiation, regardless of the waveguide thickness.

single well-defined angle  $\theta'$ , which can be determined from the following formula giving the separation between allowed frequencies:  $\Delta\nu = 1/(2nt \sin \theta')$ , where  $n$  is the refractive index (4.0 for Ge) and  $t$  is the separation between the (approximately) planar surfaces. As discussed in the Experimental section, the thickness of each waveguide was previously measured using a variant of this equation, with IR light directed vertically through the waveguide from above, corresponding to  $\theta' = 90^\circ$ . For the oscillating interference pattern in Fig. 8A, the calculated value of  $\theta'$  corresponding to the measured  $\Delta\nu = 125 \text{ cm}^{-1}$  was  $45.6^\circ$ . This is a reasonable value and indicates that the propagation of the synchrotron IR light through the Ge obeys well-understood equations.

In addition, the oscillating patterns observed with synchrotron light in Fig. 8 are very different from the much smoother baselines obtained with blackbody light, which propagates through the thinnest part of the tapered waveguide with a wide range of angles as shown in Figs. 2 and 4. It seems a bit strange at first glance that the oscillation of Fig. 8B is not as marked in the single-beam spectra from which it was calculated (e.g., Fig. 7). Presumably this is because in single-beam spectra measured with the waveguide, there is a superposition of different oscillation frequencies resulting from its tapered shape. This taper creates a wide range of separations between the two surfaces of the waveguide as the light propagates down its length.

In the case of absorbance measurements, however, the effects of the sample are concentrated in the region of minimum thickness, where the vast majority of the internal reflections occur (see Fig. 2). The main effect of the sample on the oscillation is simply a phase shift (without any frequency shift). The size of the phase shift is proportional to the number of internal reflections at the Ge-water interface. Thus, the oscillation frequency corre-

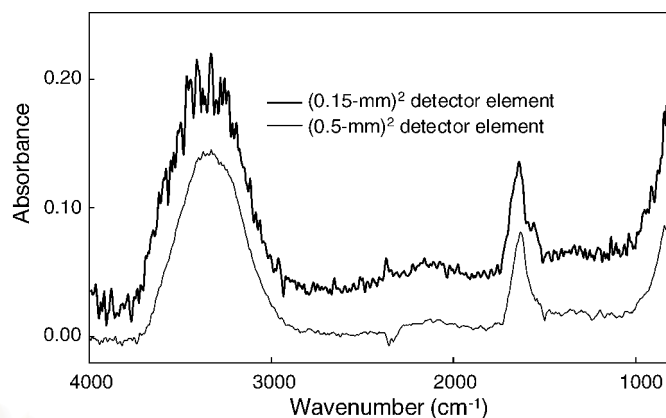


FIG. 9. Effect of size of the detector element on spectral signal-to-noise ratio observed for evanescent-wave absorbance measured from a 1-mm-diameter ( $\sim 1 \mu\text{L}$ ) water droplet. Both spectra were collected by using 5-min sample and background scans, with the same standard Globar<sup>™</sup> source and 14- $\mu\text{m}$ -thick Ge waveguide, but with different lensed detectors carrying HgCdTe active elements either 0.50 or 0.15 mm on a side, as indicated.

sponding to the propagation angle at the minimum waveguide thickness is selected out of the superposition of oscillations corresponding to a range of greater thicknesses and shallower propagation angles. The superposition of the latter obscures the oscillations, which must nevertheless be present in the single-beam spectrum (Fig. 7).

An alternative approach that we additionally investigated for improving signal/noise ratio in our spectra was to use a smaller-area detector, since the manufacturer's spec sheet of the current detector indicated that the optical design of the 0.5-mm<sup>2</sup> detector element was optimized for collecting light from the output of an optical fiber somewhat larger than 1 mm<sup>2</sup>. However, use of a different HgCdTe detector (FTIR-M16-0.10, Graseby Infrared), equipped with a 0.15-mm<sup>2</sup> detector element and the same immersion lens as the other detector, failed to produce absorbance spectra with a higher signal-to-noise ratio, at least when a Globar<sup>™</sup> source was used (Fig. 9). Furthermore, the use of this detector also resulted in the observation of a stronger oscillation pattern on the spectrum as compared to the larger immersion detector, similar to what was observed for the synchrotron-generated spectra (Fig. 8). From these observations, we conclude that the smaller detector area results in detection of only a selected portion of the IR throughput of the waveguide. The smaller detector appears to be functioning as a spatial filter, selectively observing a limited range of the optical modes that are transmitted through the waveguide. The particular vertical alignment of the detector determines which modes are detected.

## CONCLUSION

Combining synchrotron-based IR spectroscopy with thin cylinder-planar Ge waveguides does not yet result in any overall improvement in the sensitivity of either technology for sensing small quantities of samples. However, there is clearly a throughput increase available with the synchrotron source, which is greater for thinner waveguides. Of course, for a sufficiently thick waveguide, a



blackbody source can provide a greater total light energy flux than the synchrotron. The exact crossover thickness is dependent on the size of the detector element and focusing optics, but is typically somewhere in the range of 30–50  $\mu\text{m}$ . Unfortunately, with waveguides in the range of 14–30  $\mu\text{m}$  in thickness, the closer one approaches to single-angle operation (by using either a highly collimated source such as a synchrotron or a very small detector), the more deleterious is the oscillatory interference pattern that appears in the spectrum. This limits the application of synchrotron source light to the investigation of samples with such thin Ge waveguides. Thus, even for cylinder–planar waveguides as thin as 10  $\mu\text{m}$ , a standard Globalar<sup>TM</sup> source turns out to be more useful than the synchrotron, even though it cannot achieve quite such a high total energy throughput. However, for cylinder–planar waveguide sensors that are thinner than 10  $\mu\text{m}$  or that have a non-cylindrical shape for their curved surface, the synchrotron may yet turn out to have important uses.

Furthermore, the ray-tracing computational method may potentially be used as a tool for optimizing the waveguide performance. The calculations suggest that the better performance (i.e., both for improved spectral quality and enhanced sensitivity) can be achieved by the cylinder–planar waveguides with a radius of curvature, at its bottom surface, in the range of 2000–3000 mm. This would consequently give rise to more powerful evanescent-wave sensors, particularly for microanalysis, in the near future.

#### ACKNOWLEDGMENTS

This research was supported by National Science Foundation (NSF) grant MCB-9722887 to M.S.B. and by additional funding from the

Keck Center for Molecular Electronics at Syracuse University. Jitraporn Vongsvivut was supported by a fellowship from the Thailand Research Fund (TRF) via The Royal Golden Jubilee (RGJ) Program 3-C-CU-43-P-1 to Dr. Sanong Ekgasit (Chulalongkorn University, Bangkok, Thailand). We also would like to thank William F. Kutz of K & S Optics, who did most of the work involved in the fabrication process. In addition, it is a great pleasure to acknowledge the Center for Synchrotron Biosciences (U2B Beamline) at National Synchrotron Light Source (NSLS) in Brookhaven National Laboratory (BNL, Upton, Long Island) for financial and instrumental supports via NIH grant RR-01633, as well as help and technical support from Dr. Nebojsa Marinkovic at U2B beamline.

1. N. J. Harrick, *Internal Reflection Spectroscopy* (Harrick Scientific Corporation, Ossining, New York, 1979).
2. P. Niemela and J. Suhonen, *Appl. Spectrosc.* **55**, 1337 (2001).
3. D. S. Blair, L. W. Burgess, and A. M. Brodsky, *Appl. Spectrosc.* **49**, 1636 (1995).
4. D. S. Walker, W. M. Reichert, and C. J. Berry, *Appl. Spectrosc.* **46**, 1437 (1994).
5. M. S. Braiman and S. E. Plunkett, *Appl. Spectrosc.* **51**, 592 (1997).
6. S. E. Plunkett, S. Propst, and M. S. Braiman, *Appl. Opt.* **36**, 4055 (1997).
7. S. E. Plunkett, R. E. Jonas, and M. S. Braiman, *Biophys. J.* **73**, 2235 (1997).
8. J. J. Stone, M. S. Braiman, and S. E. Plunkett, *Proc. SPIE-Int. Soc. Opt. Eng.* **3105**, 371 (1997).
9. M. S. Braiman, S. E. Plunkett, and J. J. Stone, *AIP Conf. Proc.* **430**, 577 (1998).
10. M. S. Braiman and L.-Z. Mi, *Proc. SPIE-Int. Soc. Opt. Eng.* **3540**, 146 (1999).
11. S. V. Shilov, M. S. Braiman, and L.-Z. Mi, *Proc. SPIE-Int. Soc. Opt. Eng.* **3918**, 202 (2000).
12. J. Vongsvivut, S. V. Shilov, S. Ekgasit, and M. S. Braiman, *Appl. Spectrosc.* **56**, 1552 (2002).
13. N. J. Harrick, *Appl. Opt.* **10**, 2344 (1971).
14. *VUV Storage Ring Parameters as of December 2002*, retrieved March 1, 2003, from <http://nslsweb.nsls.bnl.gov/nsls/org/AccPhys/vuv/vuv-parameters.pdf>.
15. D. Marcuse, *Theory of Dielectric Optical Waveguides* (Academic Press, New York, 1991).

สถาบันวิทยบริการ  
จุฬาลงกรณ์มหาวิทยาลัย

## APPENDIX C

### RAY-TRACING PROGRAM

#### RayTraceWG\_Data.m

```
% FILENAME: RayTraceWG_Data.m
% MAINFILE: RayTraceWG_Plot.m (for a reflection pattern of the ray)
%           PlotAngles.m (for a contour plot)
% This is the data file for a one-side-curved waveguide.
% Parameters:
% file_out: filename for output
% L: full length of the waveguide
% LRatio: ratio of the length (before center)/(after center)
% t: minimum thickness of the waveguide
% n_2: refractive index of the waveguide
% n_21: ratio of refractive index of waveguide to index of cladding
% y_In: distance from flat surface where ray enters the one-side-curved waveguide
% m_In: initial slope of the ray inside the waveguide
% Theta_In: input angle of a ray in air prior to entering the waveguide
% ContourInt: interval of contours in plot of sensing angle, in degrees
% y_In_Res: number of points plotted along y_In-axis of a contour plot
% Theta_Res: number of points plotted along Theta-axis of a contour plot
% ThetaRange: Range of Theta values, in degrees, for a contour plot
% Minimum of contour plot will be (-ThetaRange), maximum will be (ThetaRange).
% Notes:
% 1. Lengths are all assumed to be in mm.
% 2. The curved surface is assumed to be symmetric about the x-value defined to be
%    the center.
% 3. Number of elements of array used in contour plot will be given by
%    Theta_Res*y_In_Res.
```

```

file_out='RayTrace.';
L=70;
LRatio=1;
t=0.014;
n_2=4.0;
n_21=4.0/2.2;
y_In=0.20;
m_In=-0.0;
ContourInt=5;
ThetaRange=25;
Theta_Res=50;
y_In_Res=201;
y_In_Range=2.01;

*****

RayTraceWG_Plot.m

% This is the routine for calculating propagation of a beam within a one-side-curved
% waveguide. The waveguide is symmetry with the thickness at center of  $t$  mm.
clear;
RayTraceWG_Data;
[tracegood,xi,yi,thetai,delta_x]=RayTraceWG(L,LRatio,t,n_21,y_In,m_In);
disp('Plotting') %Plot the results.
clf;
xarray=[0:0.01:L];
yarray=xarray;
for i=1:size(xarray,2)
    [yarray(i),deriv]=curve(xarray(i));
end
subplot(2,1,1); plot(xi,yi,'-',xarray,yarray,'b-.');
title ('impinge position on waveguide');
subplot(2,1,2); plot(xi,thetai);
title ('angle of incidence');

*****

```

**PlotAngles.m**

```

function [ThetaSensing]=PlotAngles
% This is the routine for making a contour plot showing the sensing angle at the
% thinnest part of the waveguide, as a function of y_In and Theta_In.
clear;
RayTraceWG_Data;
Theta_Step=2*ThetaRange/Theta_Res;
[y_In_max,slope]=curve(0);
if y_In_Range>y_In_max;
    y_In_Range=y_In_max;
end
y_In_Step=y_In_Range/y_In_Res;
Theta_Crit=(acos(n_21))*180/pi;
v= 0:ContourInt:Theta_Crit ;
v= [v ; Theta_Crit ] ;
theta= -ThetaRange:Theta_Step:ThetaRange;
y= 0:y_In_Step:y_In_Range-y_In_Step;
[Theta,Y]=meshgrid(theta,y);
ThetaSensing=maxthetai(Theta,Y);
save SensingAngles ThetaSensing -ascii % Angle at sensing region of waveguide.
                                     % It's the highest angle during propagation.
contourf(ThetaSensing,v);           % Do the contour plot.
xlabel('Input angle in air')
ylabel('Distance of input ray from planar surface')

```

\*\*\*\*\*

**RayTraceWG.m**

```

function [tracegood,xi,yi,thetai,delta_x]=RayTraceWG(L,LRatio,t,n_21,y_In,m_In)
[yIn_max,slope]=curve(0); % Thickness and slope of the waveguide at entrance.
m_crit=sqrt(n_21^2-1); % Absolute value of slope of ray at critical angle.
thetaIn=atan(m_In)*180/pi; % Angle of entering ray (in degrees).
% Determine if bogus data was entered for starting position.

```

```

if y_In > yIn_max
    disp('Invalid Beam Entrance Position: Too far from planar surface');
    disp('Press CTRL-c');
    tracegood=0; pause;
end
if m_In >= m_crit
    disp('Invalid Initial Beam Angle: Exceeds critical angle');
    disp('Press CTRL-c');
    tracegood=0; pause;
end
% Start the arrays that hold the final data.
if m_In <= 0
    deltax=0;
else
    deltax=(yIn_max-y_In)/m_In;% Estimate for how long it will take to reach the
    % curved surface,
end
% assuming m_In is positive.
xi=[0;0]; % Same values repeated twice at start to define an array.
yi=[y_In;y_In];
thetai=[abs(thetaIn);abs(thetaIn)];
delta_x=[0;0];
x1=0;
y1=y_In;
m1=m_In;
tracegood=1; % Tracegood is set to 0 if ray fails to propagate all the way
% through the waveguide.
% Determine whether a planar horizontal surface is the first encountered by the ray.
if m_In >= 0 % If the slope of incoming ray is positive,
    FirstReflFlat=0; % flat surface can't be the first encountered.
else
    FirstReflFlat=1; % But if the slope is negative, it may be.
    x=0; % To make sure, start at end of waveguide.
    y=y_In;

```

```

while y>0
    [ycurve,slope]=curve(x);
    if y>=ycurve;    % See if ray penetrates above curved surface.
        FirstReflFlat=0;
        deltax=x-0.01; % This first penetration point should be
                        % where the intersection is sought using fzero.
        y=-1;        % It did penetrate, so stop the test.
    else
        x=x+0.01;    % Go a little further into the waveguide.
        y=y_In+m_In*x;
    end              % And check again to be sure.
end
end
% First reflection from flat surface, if needed to get to curved surface.
if FirstReflFlat==1;
    tracegood=dotests(x1,y1,m1,m_crit); % See if critical angle was exceeded,
    y2=0;                               % trace ray to its intersection with line y=0.
    x2=x1-y1/m1;
    m2=-m1;                             % Reflect the ray upwards.
    [deltax,xi,yi,thetai,delta_x]=writearrays(x1,x2,y2,m2,xi,yi,thetai,delta_x);
    x1=x2;                               % Reset the values for next point.
    y1=y2;
    m1=m2;
end
% Further propagation down the waveguide.
while x1<L
    while x1+deltax/10<L;
        OPTIONS=OPTIMSET('display','off','MaxIter',100);
        x2=fsolve('curvdist',x1+deltax/10,OPTIONS,x1,y1,m1);
        % Find the intersection of the ray with the upper curved surface nearest
        % to x1+deltax (most recent displacement).
    end
end

```

```

    if abs(x2-x1) < 0.001; % Only found the same point over again.
        deltax=deltax+10;
    else
        break; % Found a different point; get out of loop!
    end
    x2=L+1; % Get out of both "while" loops.
end
if abs(curvdist(x2,x1,y1,m1)) > .0001; % In this case, ray apparently
    % doesn't intersect
    x2=L+1; % upper surface at all.
    y2=m1*(x2-x1); % So just show the ray exiting past x=L.
    doublehit=-1; % It won't hit upper surface twice (not even once!).
else
    [y2,yprime]=curve(x2); % yprime is the slope of the curve.
    denom=1-yprime^2+2*yprime*m1; % Denominator of slope calculation.
    if denom==0;
        tracegood=0; break; % Means ray escaped waveguide.
    end;
    if abs(m1-yprime)<0.01 % If ray is tangent to waveguide,
        tracegood=1; break; % stop trying to trace it; assume it's good.
    end;
    m2=(2*yprime-m1+m1*yprime^2)/denom;
    % From formulas for adding tangents.
    [deltax,xi,yi,thetai,delta_x]=writearrays(x1,x2,y2,m2,xi,yi,thetai,delta_x);
    doublehit=sign(m2); % If ray comes off curved surface with positive slope,
    % then it will not hit flat surface next; keep track of this.
    x1=x2; % Reset the values for next point.
    y1=y2;
    m1=m2;
    tracegood=dotests(x1,y1,m1,m_crit); % See if critical angle was exceeded.
    if tracegood==0
        break;
    end
    % Assuming it wasn't,

```

```

    y2=0;                % trace ray to its intersection
    x2=x1-y1/m1;        % with the planar surface (y=0).
end
if doublehit==-1
    m2=-m1;            % Reflect the ray upwards.
    [deltax,xi,yi,thetai,delta_x]=writearrays(x1,x2,y2,m2,xi,yi,thetai,delta_x);
    x1=x2;             % Reset the values for next point.
    y1=y2;
    m1=m2;
end
end
maxthetai=max(thetai);

*****

curve.m (for Cylinder-Planar Waveguide)
function [y,yprime]=curve(x)
% This function must define the upper curved surface of the waveguide as a function
% of x, the horizontal distance from the entrance end of the waveguide, and the
% function includes no features smaller than about 1 mm (i.e., the radius of
% curvature never gets close to 1 mm).
% The values of y and yprime should be defined in a way that makes yprime(x)
% equal to the derivative of the function y(x), using the rules of calculus.
% Parameters used for a "Circular Arc":
% Li: length of the waveguide before the center
% t: minimum thickness of the waveguide
% R: radius of curvature
t=0.014;
R=300;
Li=35;
xcirc=x-Li;
ycirc=sqrt(R^2-xcirc^2);
y=R+t-ycirc;          % yIn_max
yprime=xcirc/ycirc;  % Slope

```



**curve.m (for Gaussian-Planar Waveguide)**

```

function [y,yprime]=curve(x)
% Parameters used for a "Gaussian curve":
%   Li: length of the waveguide before the center
%   t: minimum thickness of the waveguide
%   e: maximum thickness of the waveguide at the entrance
%   w: distance to inflection point from the waveguide center
Li=35;
t=0.014;
e=2;
w=1024;
Lratio=Li/w;
Lixponent=-0.5*Lratio^2;
Amax=(e-t)/(1-exp(Lixponent));
xcent=x-Li;
xscaled=xcent/w;
xponent=-0.5*xscaled^2;
yinvert=Amax*exp(xponent);
y=t+Amax-yinvert;
yprime=yinvert*xcent/(w^2);

*****

curvtest.m
function delta_y=curvtest(x)
yvalue=cos(x) % [yvalue,deriv]=curve(x);
delta_y=yvalue-.2 % y1-m1*(x-x1);
% delta_y is the vertical distance between the current ray and
% the curved upper surface.

*****

```

**curvdist.m**

```
function delta_y=curvdist(x,x1,y1,m1)
[yvalue,yprime]=curve(x);
delta_y=yvalue-y1-m1*(x-x1);
```

\*\*\*\*\*

**maxthetai.m**

```
function maxthetai=maxthetai(theta_array,y_In_array)
% This function determines the maximum propagation angle inside a waveguide
% using the function RayTraceWG. Besides an input angle (in air) of Theta_In and
% an input vertical position of y_In that are parameters of the function call,
% maxthetai, depends on being able to pass several other parameters to the
% subroutine RayTraceWG, that are determined from a shared data file
% RayTraceWG_Data, as well as a pre-defined function "curve(x)" for the curved
% surface of the waveguide.
RayTraceWG_Data; % Read the shared data file.
disp('Allowed values of y and theta, and resulting sensing angle.')
y_In_array=[];
theta_array=[];
for j=1:size(y_In_array,1);
    for i=1:size(theta_array,2);
        y_In=y_In_array(j,i)
        theta=theta_array(j,i)
        m_In=tan(asin(sin(theta*pi/180)/n_2))
        % Initial slope of the ray INSIDE the waveguide.
        % Must use Snell's law to calculate this from the input angle.
        [tracegood,xi,yi,thetai,delta_x]=RayTraceWG(L,LRatio,t,n_21,y_In,m_In);
        if tracegood==0;
            maxthetai(j,i)=90
        else
            y_In
            theta
            max(thetai)
```

```

        maxthetai(j,i)=max(thetai);
    end
end
end

```

\*\*\*\*\*

### **AcceptAngles.m**

```

function [zeta_min,zeta_max]=AcceptAngles(y_In)
% This is the routine for calculating the maximum and minimum angles for external
% rays impinging at position y_In.
clear;
RayTraceWG_Data;
[tracegood,xi,yi,thetai,delta_x]=RayTraceWG(L,LRatio,t,n_2l,y_In,m_In);
if tracegood=1;
    zeta=thetai;
end

```

\*\*\*\*\*

### **dotests.m**

```

function tracegood=dotests(x,y,m1,m_crit)
% This function determines if the trace is still a valid raytrace for a total internal
% reflection. The outputs are tracegood=1 if the trace is OK
%
% tracegood=0 if the critical angle has been exceeded.
tracegood=1;
if abs(m1)>=m_crit;
    tracegood=0; % It's all over.
end

```

\*\*\*\*\*

### **writearrays.m**

```

function [deltax,xi,yi,thetai,delta_x]=writearrays(x1,x2,y2,m2,xi,yi,thetai,delta_x)
% This function adds the most recent values to the arrays containing the x and y
% values for the reflection points, the slopes m and angles theta for the rays, and
% the values of delta_x for the separation between successive reflections.

```

```
xi = [xi; x2]; % Append values onto the existing arrays.
yi = [yi; y2];
thetai = [thetai; atan(abs(m2))*180/pi]; % theta is the arctan of the slope.
deltax=x2-x1;
delta_x = [delta_x; deltax]; % delta_x is the distance between successive
% reflections along the x-axis.
```

\*\*\*\*\*



สถาบันวิทยบริการ  
จุฬาลงกรณ์มหาวิทยาลัย

## CURRICULUM VITAE

**Date of Birth:** November 18, 1978

**Birth Place:** Trang, Thailand

**Address:** 97, Ratchadomnoen Road, Muang, Trang 92000, Thailand

### Educations:

Ph.D. / Chemistry	2004	Chulalongkorn University/Thailand
B.Sc. (hons) / Chemistry	1998	Chulalongkorn University/Thailand

### Research Publications:

1. Sompornpisut, P.; Deechalao, N.; and **Vongsvivut, J.** An Inclusion Complex of  $\beta$ -Cyclodextrin-*L*-Phenylalanine:  $^1\text{H}$  NMR and Molecular Docking Studies. *Science Asia* 28 (2002): 263–270.
2. **Vongsvivut, J.**; Shilov, S. V.; Ekgasit, S.; and Braiman, M. S. Symmetrically Tapered <30- $\mu\text{m}$ -thick Quasi-Planar Germanium Waveguides as Chemical Sensors for Microanalysis. *Applied Spectroscopy* 56 (2002): 1552–1561.
3. **Vongsvivut, J.**; Fernandez, J.; Ekgasit, S.; and Braiman, M. S. Characterization of Supported Cylinder-Planar Germanium Waveguide Sensors with Synchrotron Infrared Radiation. *Applied Spectroscopy* 58 (2004): 143–151.\*  
*\*The article was appeared on the journal cover.*
4. **Vongsvivut, J.**; Itoh, T.; Ikehata, A.; Wood, B. R.; Ekgasit, S.; and Ozaki, Y. Anomalous Surface-Enhanced Infrared Spectra of Manganese (III) Tetraphenylporphine Chloride Physisorbed on Gold Island Films. submitted for publication in *Applied Spectroscopy*.

### Scholarships and Awards:

- 2000 – 2004 : *The Royal Golden Jubilee (RGJ) Ph.D. Scholarship* supported by Thailand Research Fund
- October 2002 : *Certificate for Outstanding (Oral) Presentation* issued by Science Society of Thailand at 28<sup>th</sup> Congress on Science and Technology of Thailand (STT)
- October 2001 : *2001 Student Poster Presentation Award* issued by Society for Applied Spectroscopy at 2001 FACSS Conference
- 1999 : *Teaching Assistant (TA)* supported by Department of Chemistry, Faculty of Science, Chulalongkorn University

1995 – 1998 : *Additional Scholarship for Excellent Students in Science* promoted by  
Faculty of Science, Chulalongkorn University

**International Conferences:**

February 3-7, 2003 : *The Inaugural Austral-Asian Biospectroscopy Conference (ABC)* at  
Suranaree University of Technology, Nakhon Ratchasima, Thailand

May 21-22, 2002 : *Annual National Synchrotron Light Source (NSLS) Users' Meeting  
2002* at Brookhaven National Laboratory (BNL), Upton, NY, USA

March 17-22, 2002 : *The 53<sup>rd</sup> Pittsburgh Conference (PITTCON 2002)* at Morial Convention  
Center, New Orleans, LA, USA

October 7-12, 2001 : *The 28<sup>th</sup> Annual Conference of the Federation of Analytical Chemistry  
and Spectroscopy (FACSS 2001)* at Cobo Conference and Exhibition  
Center, Detroit, MI, USA



สถาบันวิทยบริการ  
จุฬาลงกรณ์มหาวิทยาลัย